Perfusion imaging in the peripheral vasculature using interventional C-arm systems

Marco Giordano

Colophon

This book was typeset by the author using LaTeX2$_\varepsilon$. All graphics and images were included formatted as Encapsulated PostScript (^{TM}Adobe Systems Incorporated). The final PostScript output was converted to Portable Document Format (PDF) and transferred to film for printing.

Cover designed by Maria Lina Crobeddu using Adobe Photoshop Elements 8.0. The illustration on the cover represents the perfusion through an analogy with natural elements. The hard-working men close to the trees symbolize the efforts of the medical and scientific community to study the perfusion. The C-arm, which is the X-ray system used to assess the perfusion, is represented by the sun illuminating the landscape.

The research described in this thesis was carried out at Philips Research Laboratories, Aachen, Germany, and at the Image Sciences Institute - UMC Utrecht, Utrecht, The Netherlands. The project was financially supported by the European Commission under a Marie Curie Host Fellowship for Early Stage Researchers Training, MEST-CT-2005-020424.

Financial support for the publication of this thesis was kindly provided by Philips Research Laboratories, Aachen, Germany, ImagO and Röntgen Stichting Utrecht.

ISBN 978-90-393-5922-8

Printed by Ridderprint BV

Perfusion imaging in the peripheral vasculature using interventional C-arm systems

Perfusie beeldvorming in het perifere vaatstelsel
met interventionele C-boog systemen

(met een samenvatting in het Nederlands)

Proefschrift

ter verkrijging van de graad van doctor aan de
Universiteit Utrecht op gezag van de rector magnificus,
prof.dr. G.J. van der Zwaan,
ingevolge het besluit van het college voor promoties
in het openbaar te verdedigen op
vrijdag 22 maart 2013 des middags te 12.45 uur

door

Marco Giordano

geboren op 8 augustus 1981, te Rome, Italië

Promotoren:	**Prof.dr.ir. M.A. Viergever**
	Prof.dr. W.P.Th.M. Mali
Co-promotoren:	**Dr. C. Neukirchen**
	Dr.ir. E.P.A. Vonken

Contents

Chapter One

Introduction

It's a gross oversimplification, of course, but what it means to me is that if a plumber can do it to pipes, we can do it to blood vessels.

— Charles Dotter (1920-1985)

1.1 Introduction to interventional radiology

The discovery of X-rays in 1895 by the german physicist Wilhelm Conrad Röntgen [101] has revolutionarized modern medicine. The possibility to image internal organs and characterize their structure proved to have enormous potential applications in medicine. In 1896 only, almost 1000 articles were published on the potential applications of 'new light' [31]. In particular, the possibility to visualize blood vessels in humans had interested the medical community since the first x-ray images were shown. Already in January 1896, Hascheck & Lindenthal obtained the first angiogram by injection of a mixture of chalk, red mercury and petroleum into an amputated hand, followed by an hour exposure to X-rays [43]. In this first acquisition the detected radiation was captured on a silver-impregnated film.

Figure 1.1. Wall painting of Wilhelm Conrad Röntgen on the external wall of the house in Utrecht where he used to live during his studies at Utrecht University. The painting depicts Wilhelm Conrad Röntgen (on the right) and the first X-ray image ever acquired (on the left).

After the first acquisition, continuous technological improvements were made in acquisition and processing techniques. In 1927 the Portuguese physician and neurologist Egas Moniz acquired the first contrasted x-ray cerebral angiography in a living patient allowing the visualization of cerebral blood vessels [83]. In order to capture the rapid flow of contrast medium,

Moniz mounted his films on a turntable operating on the principle of a revolver. Moniz injected sodium iodide directly into the carotid artery which allowed to show structures that were previously invisible. However, the images of the structures under examination were often obscured by the overlying bones of the skull and of the spinal column. To overcome this issue, B.G. Ziedses des Plantes in 1934 proposed to subtract one radiograph from another so that only the differences between them could be visualized [10]. Originally, subtraction was performed photographically but in the late 1950s films were substituted by image intensifiers combined with a TV camera allowing for much faster subtraction.

In 1953, the swedish radiologist Dr. Sven-Ivar Seldinger introduced a technique to insert catheters into blood vessels through needles and wires [105]. With this technique the access to blood vessels became easier and much safer as no sharp introductory devices needed to remain inside the vascular lumen. For the first 10 years, the catheters were used for diagnostic angiography in order to define the location of lesions of vessels or organs so that surgery could be undertaken. In June 1963 Charles Dotter, a vascular radiologist at the University of Oregon in Portland, during his presentation at the Czechoslovak Radiologic Congress in Karlovy Vary, announced that: "the diagnostic catheter can be more than a tool for passive means for diagnostic observation; used with imagination, the catheter can become an important therapeutic tool and replace the surgical scalpel" [12]. Dotter's idea to unblock occluded arteries was to insert, with the help of a guide-wire, multiple catheters of increasing diameters up to the point of the occlusion. This technique will be later known as percutaneous transluminal angioplasty (PTA). On 16 January 1964, he experimented PTA on Laura Shaw, an 82-years-old woman who had a non-healing ulcer and gangrenous toes due to short segmental stenosis of the superficial femoral artery. The treatment was successful, the flow was restored and the ulcer healed within few weeks [13]. Disregarding the demonstrated success, the surgical community in the United States was initially reluctant in adopting Dotter's new technique [102]. In contrast, European angiographers adopted Dotter's technique shortly after its introduction. The greatest credit for disseminating PTA throughout Europe belongs to Dr. Eberhart Zeitler from Germany. Thanks to his work, many European angiographers accepted PTA and began treating diseased arteries [123] with Dotter's technique. Notably, the German cardiologist Andreas Grüntzig improved Dootter's technique in 1974 by introducing a balloon catheter capable of dilating peripheral arteries [37]. The success of PTA in Europe aroused the interest of a new generation of angiographers in the U.S.: some went to Europe to see Grüntzig at work and upon returning they brought the improved PTA procedure back to the United States [102].

The introduction of PTA marked the birth of interventional radiology and Charles Dotter was appointed the "Father of Interventional Radiology" [94]. Dotter revolutionized radiology and moved it toward non-surgical, i.e. minimally invasive, interventions. In this new way of operating, X-ray images play an important role since they are necessary to direct interventional instruments throughout the body and to assess the technical success of the procedures.

Parallel to the progresses in interventional procedures, also acquisition techniques underwent a series of improvements. One remarkably technological improvement was the introduction of digital computers in the 1970s which gave rise to the development of digital subtraction angiography (DSA) considered still by many the 'gold standard' for quantification and detection of vascular abnormalities [68]. In DSA, a mask image obtained before the arrival of contrast material is stored in a digital memory, then subsequent images are obtained after arrival of a contrast bolus and are stored on a separate memory. The mask image is digitally subtracted from the succeeding contrast images resulting in images showing the contrasted structures with the background removed.

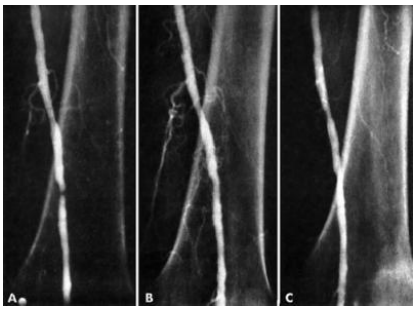

Figure 1.2. Angiograms of Dotter's first catheter patient, Laura Shaw: A) before transluminal dilation of the left superficial femoral artery, B) immediately after dilation, and C) 3 weeks after the procedure. (Image taken from [13])

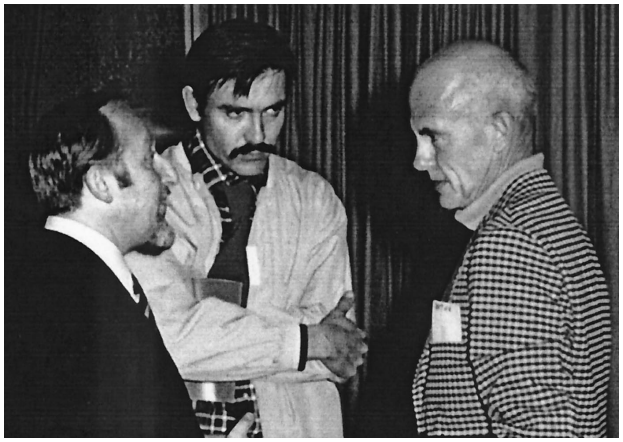

Figure 1.3. From left to right, Eberhardt Zeitler, Andreas Grüntzig, and Charles Dotter in 1975 discussing angioplasty techniques at the symposium in Cologne, Germany (Image taken from [102]).

Further technological improvements have lead to the introduction of mobile C-arm systems capable of acquiring images from different angular views during the procedure. The last generation of C-arm system introduced in the early 2000s have been equipped with Flat-panel detectors which offer higher performance with respect to image intensifiers: higher contrast resolution, faster frame-rates, reduced dose and also the possibility for three-dimensional tomographic imaging [62]. These features have opened the possibility of visualizing contrast information not only in large vessels but also in soft tissue [125]. Soft tissue contrast information could be used to measure the tissue blood flow (i.e. perfusion) which could help the interventional radiologist to assess the success of the treatment.

The subject of this thesis is the development of image processing methods to calculate the perfusion from angiographic images acquired during revascularization procedures in the legs. Most of the methods that we have developed can be implemented on most interventional flat-panel C-arm systems currently available in many operating rooms. The main focus of the

thesis is on the technical implementation of the methods and on their evaluation on phantom and clinical data.

This chapter is organized as follows: to understand more clearly the clinical benefit obtained from the calculation of perfusion during the revascularization procedure, in Sec. 1.2.1 we provide some clinical background on peripheral arterial disease and on peripheral revascularization procedures. In Sec. 1.3.1 we provide some background on perfusion imaging. In Sec. 1.3.2 we discuss the characteristics and limitations of C-arm systems. In Sec. 1.3.3 we discuss some previous attempts in C-arm based perfusion imaging. Finally in Sec. 1.4 the outline of the thesis is presented.

1.2 Clinical background

1.2.1 Peripheral vascular disease: assessment and treatment

Peripheral arterial disease (PAD) is a growing health care concern that places a considerable burden on both afflicted patients and health care systems. PAD prevalence has been evaluated in several epidemiologic studies and is in the range 3-10%, increasing to 15-20% in individuals aged over 70 years [92].

PAD is caused by partial or total blockage of the peripheral arteries which results in decreased blood flow to the limbs. PAD is one of the most common diabetes-induced cardiovascular complications. In diabetic patients, arterial blockages are typically located in the vessels below the knee resulting in most cases in ulcers on the toes and heels which may become infected and gangrenous and may even require amputation.

Atherosclerosis, the gradual build up of cholesterol and scar tissue in arteries, is the most common cause of PAD. Athereosclerotical PAD is often located in the vessels above the knee, and results in restriction of blood flow limiting the supply of nutrients and oxygen to the various parts of the leg. Lifestyle choices such as smoking, poor diet and lack of exercise are among the main causes of atherosclerosis and Type 2 diabetes.

Peripheral artery disease is commonly divided in the Fontaine stages, introduced by René Fontaine in 1954 [23]:

- i) mild pain when walking (claudication), incomplete blood vessel obstruction;
- ii) severe pain when walking relatively short distances (intermittent claudication), pain triggered by walking "after a distance of > 150 m in stage iia and after < 150 m in stage iib";
- iii) pain while resting (rest pain), mostly in the feet, increasing when the limb is raised;
- iv) biological tissue loss (gangrene) and difficulty walking.

The initial assessment for patients with suspected PAD includes a physical examination to look for signs of acute or chronic peripheral ischaemia and to determine the status of the peripheral pulses. An initial screening test is the anklebrachial systolic pressure index (ABI) based on the measurement of the systolic blood pressure in the ankle via Doppler. Based on the ABI measurements, physical findings and the patient symptoms, different workflows apply. Patient with suspected critical limb ischemia (CLI) are generally selected for surgical treatment or revascularization while patients with milder diagnosis are prescribed for exercise

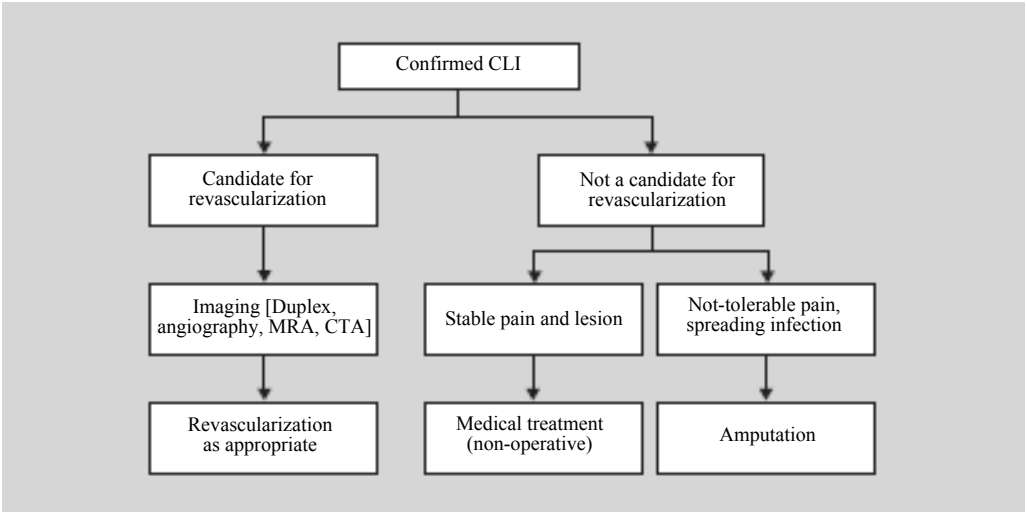

Figure 1.4. Algorithm for the treatment of patients with critical limb ischaemia (from [92])

rehabilitation and pharmacotherapy [47, 92]. In patients where the infection is overwhelming and patients life is threatened amputation is necessary. The algorithm for the treatment of patients with critical limb ischaemia is illustrated in Fig. 1.4. Magnetic resonance angiography (MRA), computed tomography angiography (CTA) or Duplex ultrasound are performed to define the severity of the disease and to plan intervention. In general two revascularization approaches are possible according to the cases: surgical bypass or catheter-based endovascular procedures like balloon angioplasty and stenting. For patients in whom catheter-based intervention is the likely treatment, a diagnostic DSA immediately followed by a catheter-based treatment in the same procedure is the preferred approach [98]. Depending on the anatomical location and complexity of the lesion, a combination of angioplasty and/or stenting is performed. Stenting consists of inserting into the artery a mesh 'tube' that keeps the artery open. Stents are usually applied after balloon angioplasty and are mostly used after suboptimal result or where there is expected early restenosis. Self-expanding nitinol stents provide good scaffolding and seal dissections after PTA. Covered stents efficaciously seal perforations. The TASC II [92] provides guidelines for endovascular treatment of peripheral vascular disease.

Recently the angiosome concept was proposed to guide the vascular specialist to choose the optimal target vessel for re-establishing perfusion of the ischaemic tissue area. The angiosome concept, introduced by Taylor and Palmer in 1987 [112], in a description where the human body is partitioned into three-dimensional blocks of tissue fed by specific arterial sources named 'angiosomes'. The mapping between feeding arteries and tissue perfusion blocks may help the clinician to better refine vessel selection by targeting the angiosome supplying the area of the tissue lesion. A few dedicated studies proved that the angiosome model can achieve better reperfusion of ulcers resulting in better healing and higher limb preservation rates than classical revascularization in which a non-angiosome-based vessel is targeted [2, 3].

The distribution of the angiosomes in the foot and in the ankle is illustrated in Fig.1.5: a) the posterior tibial artery subdivides into the medial calcaneal artery (MCA), the medial plantar artery (MPA), and the lateral plantar (lP) artery angiosomes which supply the entire

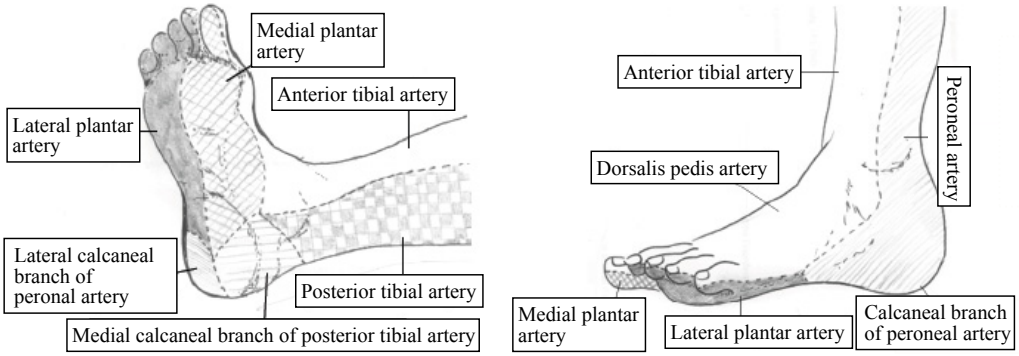

Figure 1.5. Distribution of the main foot and lower ankle angiosomes (taken from [3])

plantar heel and the medial and lateral plantar surface of the toes; b) the anterior tibial artery prolonges into the dorsalis pedis artery (DPA) angiosome which nourishes the dorsum of the foot and toes as well as the upper anterior; c) the peroneal artery becomes the lateral calcaneal artery (lCA) angiosome and supplies the lateral and plantar aspects of the heel.

1.2.2 Benefits of perfusion imaging

Since the target of the potential application of the angiosome model is the re-perfusion of the diseased tissue area, the quantification of tissue perfusion in the diseased areas is crucial to establish the success of the revascularization procedure. In an ideal scenario, the perfusion in the diseased tissue area would be estimated before and after revascularization and the difference would be used to assess the effective restoration of blood flow to the diseased area. Currently the post-treatment assessment is performed by planar DSA which shows only qualitative arterial blood flow information. With DSA it is currently not possible to assess quantitative tissue blood flow. In this thesis a set of methods to quantify tissue perfusion based on angiographic images is proposed.

1.3 Perfusion Imaging with interventional C-arm systems

1.3.1 Principles of Perfusion imaging

Perfusion is the process of blood supply to the biological tissue via the capillary network. Through the perfusion process nutrients are delivered to the cells of an organ. The level of perfusion determines whether the energy status of the tissue is likely to become compromised, therefore, perfusion is an essential indicator of tissue viability.

The measurement of perfusion are based on the quantification of the displacement of blood over a certain time interval. To compute perfusion therefore, measurements over a certain time interval are required. Several imaging modalities like positron emission tomography (PET) [53], single photon emission computed tomography (SPECT), contrast-enhanced magnetic resonance, arterial spin labeling MR, ultrasound and contrast-enhanced computed tomography

(CT) [118], can applied for in vivo perfusion measurements. Since our main focus is perfusion imaging with X-ray systems, here we will only discuss the basic concepts of CT perfusion (CTP).

In CTP, tissue perfusion is determined from dynamic contrast-enhanced CT data [4]. A contrast agent bolus is injected into a vein or an artery followed by repeated and fast scanning of the organ of interest. During the scan, the x-ray source and the detector are repeatedly rotated around the patient to acquire a large number of x-ray projection images from different angular views. The acquired projection images are used to reconstruct 3D dimensional images by applying a reconstruction algorithm. The collection of all reconstructed 3D images is used to generate a time sequence showing the temporal evolution of contrast in tissue and vessels.

In most commercially available CT systems the reconstruction is performed by applying methods based on the filtered-back projection [61] algorithm. The main assumption of this algorithm is that the object attenuation remains constant during the acquisition of projections. However, due to the passage of contrast in vessels and tissues, the attenuation changes over time. Therefore, in order to fulfill the assumption on constant attenuation, rotation times in the order of 0.3-0.6 s are used.

After reconstruction of the time sequence of images, a time attenuation curve (TAC) is obtained at each voxel to describe the temporal change of contrast agent concentration. From the TACs, a set of perfusion parameters is calculated such as blood flow, blood volume and mean transit time [80]. For the calculation of perfusion parameters from the TACs several models have been proposed. Among the most established methods are those based on compartmental analysis and linear systems theory [22]. Since the methods used in this thesis are based on compartmental models, in the following we introduce the concept of compartmental analysis.

In compartmental analysis the contrast material is modeled as entering an organ via an artery, rapidly distributing uniformly within the blood vessels and extracellular space, and then leaving the organ via a vein. Compartmental analysis in based on three main assumptions:

- the contrast does not affect the blood flow
- the tissue is homogeneous, i.e. no concentrations gradient is present
- the contrast mixes instantaneously with blood after inflow

In this thesis, in order to quantify perfusion, we apply a method based on a one compartmental model which is referred to as the 'slope method' [66]. Although this method is known to provide less accurate results, it has the advantage that it requires less input data.

A one compartmental model assumes that the contrast remains intravascular and does not diffuse in the interstitium. The perfusion parameters based on compartmental models have been largely used to quantify cerebral perfusion [72], however, their definition can be be extended also to leg perfusion. Typically, the most clinically relevant perfusion parameter is the blood flow which describes the tissue viability. The blood flow is defined as the blood volume displacement per temporal unit (i.e. flow) and tissue volume.

The simplest approach to calculate perfusion is the conservation of mass within the system [60]: typically the same amount of contrast that is injected into the system, leaves the system after a certain time. Let $a(t)$ be the arterial concentration of iodine, $v(t)$ the venous concentration and $c(t)$ the tissue concentration within a volume of tissue being examined. Let V be the volume of a voxel and F the flow into the volume. Then by definition, the perfusion is F/V. If we consider the time interval $(t, t+\delta t)$, the amount of contrast arriving in the voxel

is $F\delta t[a(t)-v(t)]$. This equals the change in the amount of iodine in the voxel: $Vc(t)$. If we go to the limit, integrate with respect to t and rearrange, we can express the perfusion as follows:

$$\frac{F}{V} = \frac{c(t')}{\int_0^{t'} a(t)dt - \int_0^{t'} v(t)dt} \tag{1.1}$$

In practice, Eq. 1.1 is generally not applicable due to the requirement to determine TACs for the artery, the tissue and the vein for all voxels at each instance of time. The 'Mullani-Gould formulation' or 'No Venous Out Flow Method' [89] has been developed to avoid the need for venous measurements by analyzing tissue and arterial TACs prior to the time the contrast agent flows out of the organ of interest. If we call this time t_{ven}, for $t' < t_{ven}$ the venous term in the denominator of Eq. 1.1 becomes zero:

$$\frac{F}{V} = \frac{c(t')}{\int_0^{t'} a(t)dt} \qquad with \qquad t' < t_{ven} \tag{1.2}$$

Equation 1.2 holds for any time $t < t_{ven}$ and therefore also for the time of maximum slope of the tissue TAC:

$$\frac{F}{V} = \frac{c(t')|_{max}}{\int_0^{t'} a(t)dt} \tag{1.3}$$

The formula of the slope method for the calculation of perfusion is given by differentiation of Eq.1.3:

$$\frac{F}{V} = \frac{\frac{d}{dt}c(t')|_{max}}{a(t)|_{max}} \tag{1.4}$$

One of the main advantages of the slope method is that it allows the calculation at the time point when the tissue TAC reaches its peak gradient, thus well before its peak enhancement value. This reduces the chance of the no venous out flow assumption being broken. Another advantage is that it uses only the first data points of the contrast enhancement curves, therefore artifacts due to patient motion are less probable. The main disadvantage is that it is very noise sensitive as the data is differentiated and only a few data points are used for perfusion evaluation.

Another parameter relevant for perfusion evaluation is that of blood volume V which is calculated as follows:

$$V = \frac{\int_0^{\infty} c(t)dt}{\int_0^{\infty} a(t)dt} \tag{1.5}$$

In clinical terms, V does not describe an absolute volume but the fraction within tissue that is occupied by blood vessels [77]. To be more precise, the values of cerebral blood volume are often divided by a haematocrit correction value, since the contrast material only mixes up with the blood plasma [113]. In our studies however the haematocrit correction was not applied.

The mean transit time relates to the time taken by the blood to cross the local capillary network. In the classical papers on cerebral perfusion [4,77] the mean transit time is calculated as:

$$MTT = MTT_v - MTT_a = \frac{\int_0^\infty tv(t)dt}{\int_0^\infty v(t)dt} - \frac{\int_0^\infty ta(t)dt}{\int_0^\infty a(t)dt} \tag{1.6}$$

Finally, the relationship between the three parameters blood flow F, blood volume V and mean transit time MTT is described by the central volume principle or 'Stewart-Hamilton' equation:

$$F = \frac{V}{MTT} \tag{1.7}$$

In perfusion analysis typically a blood flow map, blood volume map and mean transit time map are presented to provide information on tissue viability at different spatial locations. In this thesis we focus mainly on the analysis of the blood flow maps.

1.3.2 Characteristics and limitations of C-arm systems

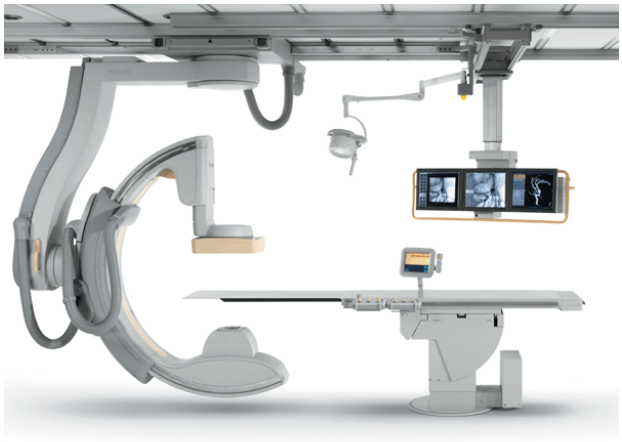

Figure 1.6. Interventional X-ray C-arm system with flat detector: Philips Allura XPER FD20

Since the topic of this thesis is the estimation of perfusion with C-arm systems, in this section we discuss the characteristics and the limitations in terms of acquisition speed of the C-arm systems.

A C-arm system (Fig. 1.6) is an X-ray apparatus which allows for fast imaging and easy patient access during interventions. An X-ray source and a detector are mounted on a moving arch which can be rotated over different axes to obtain images of the object from different angles. X-rays are emitted from the X-ray source and detected using a flat panel detector after being attenuated by the object of interest. The patient is held by a moving table which can be shifted so to obtain the best view of the organ of interest.

The main application of C-arms is to obtain fast, typically 160 frames per second, planar images during interventional procedures. When used in low-dose fluoroscopic mode, real time images are used to navigate the catheters or other instruments through the vasculature. When used in angiographic mode, a temporal sequence of 2D images is acquired after short bolus

injection to assess blood flow in arteries. However, since the 2D images are projections of the 3D organ, the longitudinal information of the object is lost and the images show only qualitative contrast enhancement information. In particular the contrast enhancement in tissue areas, which is crucial to calculate tissue blood perfusion, can not be measured by standard angiography .

In addition to 2D imaging, recent C-arms have also been provided with volumetric functionalities. Thanks to the flat detector technology, which provides high contrast dynamic ranges, the contrast resolution in the 3D reconstructed image is nearly as that for CT. The concept of 3D imaging with C-arms is similar to that of CT, however some differences occur in terms of acquisition protocol: i) the acquisition time for C-arms is around 5 s while for CT systems is in the range $0.3 - 0.6$ s; ii) the angular range in C-arms is limited to $220°$ while for CT scanners is $360°$ iii) currently, due to mechanical limitations, C-arm systems are not capable of performing continuous rotations as in CTP but can only perform single rotations.

To sequentially acquire several reconstructed volumes, recently new acquisition protocols have been proposed which are based on repeated forward and backward rotations of the C-arm [25]. Therefore, in theory perfusion quantification could be obtained with a C-arm by acquiring reconstructed 3D images using alternating forward and backward C-arm rotations after a contrast agent bolus injection. However, there are two major challenges mainly due to the long rotation time:

- Because of the long sample period ($\sim 5s$), temporal undersampling of the dynamic contrast curves may lead to incorrect perfusion quantification.
- In CTP the rotation time is sufficiently short such that the change of attenuation in the vasculature due to the contrast propagation is negligible. When using a C-arm, due to the long rotation time, the assumption on constant attenuation during the acquisition of projections is violated resulting in image reconstruction artifacts

1.3.3 Previous attempts in C-arm perfusion imaging

A series of methods has been proposed in the past to derive blood flow information using interventional C-arm systems. The methods can be classified into two groups:

- (Tomographic 3D perfusion estimation) : These methods aim at dynamic reconstruction of the 3D object based on projection data acquired over multiple forward/backward sweeps (i.e. multisweeps) of the C-arm during bolus injection. In [86] Montes *et al.* introduced a dynamic Feldkamp-type reconstruction algorithm for TACs estimation in the brain where the missing projection data due to the slow temporal sampling are computed by interpolation of projections acquired at the two closest point in time. This method was initially meant to reduce dose in CT acquisitions and assumed continuous rotations of the CT gantry. Neukirchen [91] extended this method to work with data acquired using bi-directional C-arm rotations. However the accuracy of the reconstructed TACs was limited due to the low number of sample points. In order to increase the sampling density of projections, Ganguly *et al.* [25] proposed an interleaved scanning protocol consisting of several multisweep acquisitions. For each multisweep acquisition an identical contrast injection is performed using a different delay time between the start of the bolus injection and the start of the scanning. Results obtained on animal models

were promising however the high X-ray dose and the high volume of contrast required limit the usability in a clinical environment.

- (Combined 2D/3D blood flow estimation) : These methods rely on the combination of a temporal sequence of X-ray angiograms acquired from a fixed viewing angle and an additional anatomical 3D dataset. This concept was initially investigated by Schmitt *et al.* [103] for the calculation of contrast agent propagation in arteries. The vessel morphology is derived from a 3D rotational angiography (3D-RA) scan. Then, the propagation of the bolus in 3D is obtained by mapping the grey values in the projections to the 3D vessel tree. Since gray values in 2D projections provide only qualitative contrast information, this method is not quantitative. In addition the contrast propagation can be derived only for vessels and not for tissues.

  Taguchi *et al.* [109,110] proposed a method to derive TACs from angiography to calculate liver perfusion. They assume a segmentation of the liver in spatially homogeneous regions which follow the same TAC. The region-related TACs are estimated from the projection angiograms by solving a least-squares problem. However, in their simulations the regions are assumed perfectly defined which limits the feasibility of the method in reality.

1.4 Outline of the thesis

In this thesis we present a set of methods for perfusion estimation which can be implemented on C-arm systems. To overcome the limitations of the C-arm in terms of amount of acquired temporal and spatial information, we exploit prior knowledge on the spatial and temporal distribution of contrast in the tissue and integrate this knowledge in the estimation procedure. In particular, in Chapter 2 we assume smoothness of the time attenuation curves to estimate fully spatially resolved perfusion. Even though the method was tested on brain perfusion data, it can easily be applied to perfusion estimation in legs. In Chapters 3, 4 and 5 we assume that in legs the perfusion is spatially homogeneous over volumetric regions which resemble muscle blocks and vessels. By making the assumption, the spatially averaged perfusion in the regions can be estimated by combination of simple 2D and 3D angiographic acquisitions. The thesis focuses on the implementation of the mathematical methods to calculate the perfusion from the angiographic images and on the evaluation of the methods on phantom data and on clinical data.

In the following we present the thesis outline.

In Chapter 2 we present an iterative tomographic perfusion estimation method which exploits prior knowledge about the expected contrast dynamics. This method aims at fully 3D spatially resolved perfusion estimation from projections data acquired over multiple C-arm rotations. The prior knowledge about the expected contrast dynamics is implemented as a temporal decomposition model based on a set of smooth basis functions which aim at approximating TACs. The temporal model is integrated into an iterative tomographic reconstruction algorithm which is flexible in terms of acquisition protocol. Since the key operations consist of spatial forward and backward projections and simple scalar products, the recovery of TACs can be performed computationally efficient. The issue of noise propagating from the projections to the reconstructed TACs is tackled by the use of smooth basis function and by regularization realized by early stopping of the iteration cycles. The quantitative accuracy of the proposed method is evaluated in a simulation study on dynamic brain phantom data and

aims at assessing the influence of noise propagation, regularization, different basis functions and type of acquisition mode. Two acquisition modes are compared in the study: the multi-sweep (i.e. repeated forward backward movement) acquisition mode using a single injection, and the multiple full rotation acquisition mode which is used as a reference.

In Chapter 3 we propose a method for spatially averaged perfusion estimation in the lower leg. This method is based on a temporal angiographic sequence acquired from a fixed angle, and two 3D images reconstructed from C-arm rotational scans. The temporal information derived from the angiography is combined with the spatial information derived from the 3D images to obtain perfusion information spatially averaged along the direction of the x-rays. The main assumption of the method is that perfusion is spatially homogeneous along the projection rays and within a single large 3D tissue area. The spatially averaged perfusion along the x-rays is obtained by normalizing the projection line integrals in the DSA by the contrast length along the rays. The contrast lengths are derived by segmentation of a single perfused area derived from the 3D reconstructed images. To derive the area subject to contrast propagation we introduce a segmentation algorithm which is tailored to the estimation procedure. The accuracy of the method with respect to the 3D perfusion values is evaluated in a simulation study on CTP data acquired on patients undergoing peripheral revascularization. In addition the validity of the assumption on spatial homogeneity is assessed on the same CTP dataset.

In Chapter 4 we propose method for 3D region-based perfusion estimation which extends the 2D perfusion estimation method proposed in Chapter 3 by relaxing the assumption on orientation of homogeneity. In the method proposed here we assume a set of multiple 3D regions related to local contrast homogeneity. By using a sufficiently high number of segmented regions, the perfusion homogeneity within the regions can be increased allowing a better modeling of the spatial distribution of contrast concentration. To identify homogeneous regions from the 3D reconstructed images we introduce a segmentation method which exploits contrast homogeneity and connectivity of the anatomical structures. The contrast TACs in the regions are estimated by mapping the 2D blood flow information from the angiograms to the 3D reconstructed images regions. The mapping is achieved by solving an inverse problem. Instability in the solution of the inverse problem due to overlap of the regions in projection space is tackled by the use of temporal and spatial regularization. A quantitative assessment of the estimation accuracy and of the error sources is carried out on data simulated from CTP scans.

In Chapter 5 we evaluate the feasibility of the region-based perfusion method on C-arm data acquired on patients during their revascularization procedures. In this chapter the practical issues related to the implementation of the method in a clinical environment are tackled. In particular we define the injection protocol used for the acquisition of the 3D contrasted rotational scans. This is defined such as to optimize the balance between contrast enhancement and image reconstruction artifacts. Furthermore we provide a strategy for the registration of the 3D images to the 2D angiogram which is necessary to obtain a motion-free mapping of the 2D blood flow into the 3D segmented regions. The feasibility of the method is evaluated with respect to three main aspects: i) capability in detecting low contrast differences as those occurring in hypo-perfused regions ii) correlation of 3D estimated TACs with the corresponding 2D TACs in DSA iii) correlation of the estimated perfusion maps with maps obtained with contrast enhanced MR on the same patients.

Contrast enhancement measurements performed using common energy integrating detectors assume a linear relation between the measured attenuation and the contrast concentration in the object. However due to the polychromatic nature of x-rays and the energy dependency of the different body materials, the relation is not linear and the so called beam hardening

effect occurs. In Chapter 6 therefore we analyze the the effect of beam hardening on the measurement of contrast enhancement by DSA. This is relevant to assess the impact of beam hardening on the perfusion estimation methods proposed in Chapters 2, 3 and 4 which are all based on the contrast enhancement information measured via DSA. In particular in presence of contrast agents, the spectra of the measured x-ray signal is modified resulting in errors on the quantification of contrasts attenuation. A simulation study was carried out to assess: i) the impact of the modeling assumptions on the monochromatic nature of the x-ray beam on the beam hardening error ii) the influence of the different body materials and contrast concentrations on the beam hardening error. The simulations were carried out on a simple 1D object and on a geometrical leg phantom.

In Chapter 7 a summary and an outlook of the work presented in this thesis are provided.

Chapter Two

An iterative method for tomographic x-ray perfusion estimation in a decomposition model-based approach

With four parameters I can fit an elephant, and with five I can make him wiggle his trunk.

— John von Neumann (1903-1957)

Abstract — X-ray based tomographic blood perfusion imaging requires recovery of contrast time-attenuation-curves from dynamic projection data. When using slowly rotating imaging systems this task is challenging due to non-simultaneous projection acquisition. A dynamic reconstruction method is proposed that aims at compensating the lack of simultaneously acquired information by incorporating prior knowledge about the expected temporal contrast dynamics.

A decomposition model using temporal basis functions to approximate time-attenuation-curves is integrated into an iterative tomographic reconstruction method. The computationally efficient implementation of the proposed approach makes use of standard forward- and back-projections as well as scalar products in image space. The critical issue of projection noise propagation is tackled by application of regularization which is realized by early stopping of iteration cycles and by proper selection of smooth temporal basis functions. The performance of the proposed dynamic reconstruction approach is evaluated in a simulation study concerning various aspects: noise propagation and regularization, specification of temporal model, and type of acquisition mode.

The evaluation based on dynamic phantom data indicates that tomographic recovery of contrast time-attenuation-curves in tissue can be achieved with an average range of accuracy of ca. 2% (with respect to dynamic peak attenuation) under ideal noise-free conditions. The relative estimation error for arterial time-attenuation-curves is in the range of 8%, which is due to faster contrast dynamics in the artery. In general, performance depends on the level of acquired information contained in the projection data which is mainly influenced by the type of rotational acquisition mode; restrictions in angular range and speed can lead to limited accuracy. The analysis of propagated projection noise in a statistical Bias-Variance framework reveals relative noise levels in estimated time-attenuation-curves of 3-4% in tissue regions and below 1% in vessels when using optimized settings for regularization. Here, the effect of noise suppression depends on the interrelation between the number of iteration cycles and the constraints imposed by the temporal decomposition model.

For usage with slowly rotating imaging systems the presented model-based iterative dynamic reconstruction method is capable of recovering contrast time-attenuation-curves related to tissue perfusion. The proposed regularization framework is an effective means to limit the impact of projection noise which is a factor dominating estimation accuracy in tissue regions.

Based upon: C. Neukirchen, M. Giordano, and S. Wiesner, “An iterative method for tomographic x-ray perfusion estimation in a decomposition model-based approach”, *Medical Physics*, vol.37, no.12, pp. 6125-6141, 2010.

2.1 Introduction

Tomographic perfusion imaging requires tracking of dynamic contrast concentration in tissue and vessels after bolus injection to obtain contrast time-attenuation-curves (TACs). In perfusion CT which is a standard modality, e.g. for the assessment of stroke, the organ of interest is repeatedly scanned and reconstructed in a cine mode over 30-40 seconds in a typical protocol. Then, for neuro perfusion analysis, functional parameters like Cerebral Blood Flow (CBF), etc. are calculated (see e.g. [70, 122]).

Recently [8,35,124], interest came up to enable imaging of blood perfusion on interventional x-ray devices such as flat panel detector-based CT gantry systems [34] and C-arms, e.g. for outcome control during treatment. The specifications of these systems differ from modern CT scanners: slower angular rotation speed (e.g. 50^o/s for C-arms), lower detector frame rate (e.g. 30fps), and – in the case of C-arms – limited angular range (e.g. 220^o depending on the rotation mode). These restrictions make tomographic recovery of TACs challenging because the acquisition speed might be too slow to provide a sufficient amount of information for dynamic image reconstruction. Inconsistency of acquired projections due to fast temporal variations becomes a limiting issue, and simple reconstruction methods which assume simultaneously acquired projections tend to lose accuracy.

For perfusion CT, different types of dynamic reconstruction algorithms have been proposed: in a straightforward approach (see [70]), contiguous blocks of projections representing a 2π range are taken from the entire set of acquired projections. Standard FBP reconstruction is applied to each block to create an image corresponding to the central time frame within the current block. As an extension, smooth temporal window functions may be applied to compute a weighted average of projections in the considered time interval (see [108]). These approaches assume the rotational scanning is sufficiently fast such that projections contained in a window/block are temporally consistent, i.e., have been acquired quasi-simultaneously.
A second class of dynamic reconstruction methods aims at synthesizing missing projection data at any point in time from the projections acquired from identical viewing positions at different time points. In [49] a missing projection is computed by linear interpolation of projections acquired at the two closest points in time. In [33] a first order regression model over a flexible time interval is applied to synthesize the missing projection information. In [85] more prior knowledge about the perfusion processes is introduced to dynamic reconstruction: In brain perfusion the contrast TACs are temporally bandlimited, which holds similarly for the projection line integrals. Regular sampling of the bandlimited projection data caused by repeated rotations of the CT gantry is related to an ideal interpolator according to the sampling condition. Consequently, a polynomial approximation to the $sinc(t)$-based interpolation is used in [85] to compute the missing projections of slow rotational scanning.

The dynamic reconstruction method described here also follows the idea of complementing the limited amount of acquired information with prior knowledge about the perfusion curves. Such knowledge is implemented as a parametric spatio-temporal TAC representation similar to the one previously proposed for dynamic SPECT reconstruction [100]: it is assumed that the TACs can be formed by superposition of smooth temporal functions, which differs from the assertion of bandlimited contrast dynamics used in [85]. In addition, the proposed approach is flexible concerning the acquisition mode and is capable of handling various types of system trajectories. The sampling-based interpolation method [85] cannot be applied readily to non-continuous rotational scanning (which might be mandatory for C-arms with limited angular range); as noted in [84] one would have to cope with the effects of irregular sampling for this

case.

This Chapter is organized as follows: The structure of the parametric representation used to approximate the contrast TACs is explained in Sec. 2.2. An iterative optimization method that intrinsically regularizes the final solution is applied to find the optimal model parameters from the acquired projection data. The setup for a series of simulation experiments based on dynamic phantoms is detailed in Sec. 2.3. In Sec. 2.4 the effects of different types of acquisition modes and different modeling assumptions are compared and the sensitivity with respect to projection noise is evaluated. Sec. 2.5 discusses the experimental results and contains a brief summary.

2.2 Theory

Aim of the method is tomographic estimation of dynamic time-attenuation-curves (TACs) $\tilde{\boldsymbol{X}}_{\boldsymbol{d}}$ which are caused by the temporal variation of blood contrast concentration in vessels and tissue after bolus injection. The entire object attenuation $\tilde{\boldsymbol{X}}$ consists of the dynamic contrast $\tilde{\boldsymbol{X}}_{\boldsymbol{d}}$ plus the static anatomical contribution $\tilde{\boldsymbol{X}}_{\mathbf{s}}$. The object position and shape are assumed fixed, i.e. treatment of object motion or deformation is not detailed here.

The estimation of TACs is based on a set of attenuation line integrals $\tilde{\boldsymbol{p}}$ obtained from X-ray projections through the entire object $\tilde{\boldsymbol{X}}$. Using a slowly rotating imaging system, the line integrals $\tilde{\boldsymbol{p}}$ are acquired non-simultaneously (i.e. at different time points) from different viewing positions after contrast injection; hence, subsequent projection views correspond to different states of contrast concentration in the object. As in perfusion imaging the primary interest is in the pure contrast dynamics, in the actual approach the static object contribution to the line integrals is removed by $\tilde{\boldsymbol{p}}_{\boldsymbol{d}} = \tilde{\boldsymbol{p}} - \tilde{\boldsymbol{p}}_{\mathbf{s}}$. In this processing step, dynamic and static line integrals acquired at equivalent viewing positions must be subtracted pairwise. Typically, the static line integrals $\tilde{\boldsymbol{p}}_{\mathbf{s}}$ are acquired prior to contrast injection for all required viewing positions.

In the following, the estimation procedure is cast as an optimization problem based on the following elements:

System model A parametric representation $\boldsymbol{X}_{\boldsymbol{d}}(\boldsymbol{y})$ is used to describe the spatial and temporal characteristics of the TACs in the object. All model parameters are summarized in the parameter set $\boldsymbol{y}$.
The TAC representation $\boldsymbol{X}_{\boldsymbol{d}}(\boldsymbol{y})$ is projected forward according to the temporal and geometric properties of the rotational movement of the imaging system. This operation is formally described by the non-simultaneous projection $\mathcal{F}$, it yields the parametric line integrals $\boldsymbol{p}_{\boldsymbol{d}}(\boldsymbol{y}) = \mathcal{F}\boldsymbol{X}_{\boldsymbol{d}}(\boldsymbol{y})$.

Cost function The optimal set of parameters $\hat{\boldsymbol{y}}$ is obtained by minimizing the residual between the projected model and the acquired dynamic line integrals in a Least-Squares sense: $\hat{\boldsymbol{y}} = \text{argmin}_{\boldsymbol{y}} \,||\, \boldsymbol{p}_{\boldsymbol{d}}(\boldsymbol{y}) - \tilde{\boldsymbol{p}}_{\boldsymbol{d}} \,||^2$.

Optimization Numerical minimization of the residual is achieved by an iterative, gradient-based optimization method. A noise robust parameter estimation is facilitated by application of implicit regularization.

2.2.1 Linear spatio-temporal decomposition model

For $\boldsymbol{X_d}(\boldsymbol{y})$, which approximates the relevant TACs, a proper model structure is defined by balancing between the following requirements: i) It needs a sufficient degree of freedom in order to reflect all possible variations in the spatial and temporal properties of the TACs. ii) To facilitate a robust parameter estimation the flexibility/complexity has to be limited by introducing model constraints based on prior knowledge about the expected features of the TACs.

In the approach followed here, a spatio-temporal decomposition model is employed that makes use of a regular grid of totally R image voxels to describe the spatial structure of the TACs in the entire object. As a modeling constraint it is assumed that all TACs live in an N-dimensional temporal function subspace. This subspace is spanned by the set of N pre-defined basis functions $b_n(t)$ covering the time interval of dynamic acquisitions. Then, the TAC model in the r-th voxel is given as the superposition of basis functions: $x_{\mathbf{d}r}(t) = \sum_{n=1}^{N} y_{r,n}\, b_n(t)$. Here, the parameter $y_{r,n}$ denotes the weighting factor for the n-th basis function in the r-th image voxel.

In a time discrete description of the temporal dynamics using time steps $[1, \ldots, T]$ for T acquired dynamic projection views in total, the dynamic contrast is represented as the $R \times T$ matrix $\boldsymbol{X_d}$. The t-th column of $\boldsymbol{X_d}$ contains the dynamic attenuation of all image voxels at time step t; the r-th row contains the contrast TAC for the r-th image voxel. The time discrete version of the n-th temporal basis function $b_n(t)$ corresponds to a T-dimensional column vector $\boldsymbol{b}_n = (b_n(1) \cdots b_n(T))'$ with each component corresponding to a sample of the basis function. One obtains the $T \times N$ matrix $\boldsymbol{B}$ of sampled function values by adjoining all N vectors $\boldsymbol{b}_n$. Similarly, the weighting parameters $y_{r,n}$ may be arranged as a $R \times N$ matrix $\boldsymbol{Y}$. Then the decomposition model for the dynamic object can be written compactly[1]:

$$\boldsymbol{X_d} = \boldsymbol{Y} \cdot \boldsymbol{B}' \tag{2.1}$$

Typically, as a response to bolus injection, the dynamic TACs in tissue are related to positive, smooth curves with a rise-fall shape. When chosing the specific subspace constraint on the TAC model, prior knowledge on these shape characteristics should be taken into account. Hence, it is appropriate to select temporal basis functions which in a linear combination are expected to approximate these rise-fall-shape properties (see [100]). In this study two different families of basis functions are compared experimentally: i) Gaussian basis functions, ii) gamma-variate basis functions (these are typical for contrast concentration curves in blood [42]). For both cases, the basis functions are placed uniformly over the acquisition time interval (see Figure 2.1(a) and Figure 2.1(c)). To control the complexity of the decomposition model, the number N of different temporal basis functions contained in $\boldsymbol{B}$ is adjusted. One direct method for adjustment is to increase the spacing between the basis functions when lowering N. In a more systematic approach (see [74]) the complexity of the model can be limited by gradually reducing the linear dependencies across the original temporal basis functions: starting with a large set (e.g. $N = 25$) of original functions in $\boldsymbol{B}$ an orthogonal set of basis functions is generated by means of principal component analysis (PCA) [32]; i.e. the Eigenvector decomposition $\boldsymbol{V} \cdot \boldsymbol{\Sigma}^2 \cdot \boldsymbol{V}' = \boldsymbol{B} \cdot \boldsymbol{B}'$ yields the transformed functions in the columns of $\boldsymbol{V} \cdot \boldsymbol{\Sigma}$. Finally, a small set of those orthogonal functions is kept which are associated with the largest Eigenvalues. This method aims at retaining the maximum model flexibility for a given number of basis

[1] the symbol $'$ denotes matrix transpose

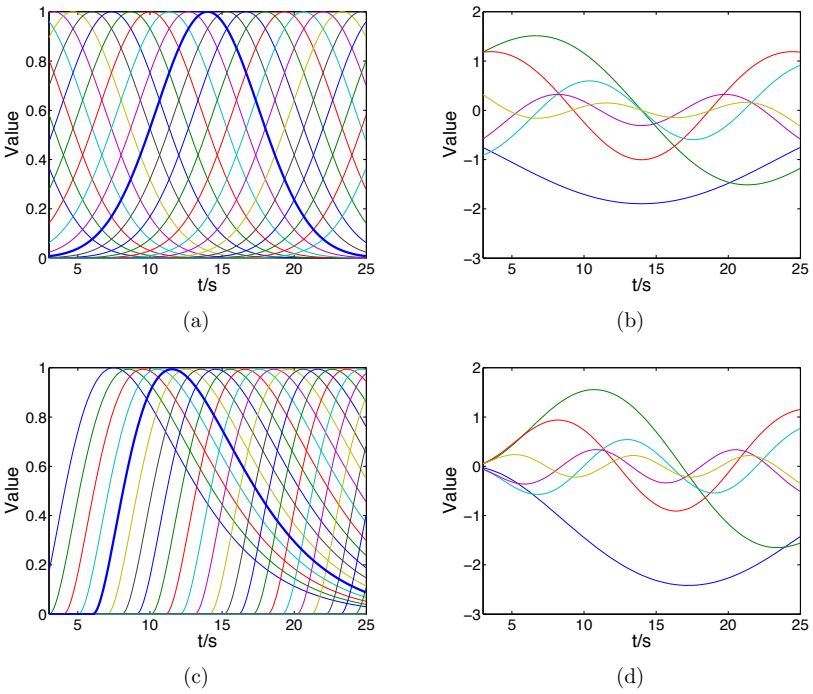

Figure 2.1. Temporal basis functions: (a) 25 Gaussian basis functions: $b_n(t) = exp(-\frac{(t-t_{Pn})^2}{2\sigma^2})$, variation parameter is peak time t_{Pn}; (b) 6 orthogonal functions via PCA reduction from (a); (c) 25 gamma-variate functions: $b_n(t) = exp(\beta)\left(\frac{(t-t_{0n})^2}{t_{Pn}}\right)^{\beta} exp(-\beta\frac{(t-t_{0n})^2}{t_{Pn}})$ for $t > t_{0n}$, variation parameters are t_{Pn}, and t_{0n}; (d) 6 orthogonal functions via PCA reduction from (c)

functions. In Figure 2.1(b) and Figure 2.1(d) the sets of 6 orthogonal functions derived via PCA from the original functions are depicted.

In an ideal scenario, the optimal set of basis functions – in a sense of least squares approximation error (see [39]) – can be obtained by application of the PCA-based reduction method to all TACs $\tilde{\boldsymbol{X}}_{\boldsymbol{d}}$ in the original dynamic sequence[2].

2.2.2 Non-simultaneous projection of the model

The non-simultaneous projection of the spatio-temporal model $\boldsymbol{X}_{\boldsymbol{d}}$ according to the temporal and geometric properties of the imaging system is described by the operation $\boldsymbol{p}_{\boldsymbol{d}} = \mathcal{F}\boldsymbol{X}_{\boldsymbol{d}}$. To generate a projection view at time step t such operation picks the volume image at this time instance (i.e. the t-th column of $\boldsymbol{X}_{\boldsymbol{d}}$) and computes line integrals for the corresponding viewing position α_t. Assuming a single projection view consists of L detector pixels, the associated L-dimensional projection vector $\boldsymbol{p}_{\boldsymbol{d}_{\alpha_t}}$ contains all line integrals acquired at time t. The entire

[2]In general, the original TACs $\tilde{\boldsymbol{X}}_{\boldsymbol{d}}$ are not known beforehand except for oracle experiements such as in Sec. 2.4.5.

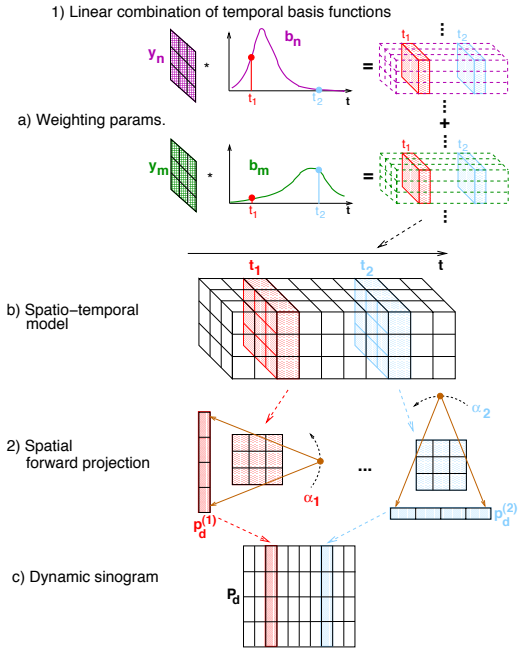

Figure 2.2. Operation example of non-simultaneous model-based forward projection: $\boldsymbol{y}_n$ and $\boldsymbol{y}_m$ represent the model parameters contained in the n-th and m-th columns of the weighting matrix $\boldsymbol{Y}$, respectively. The temporal model is composed from the related temporal basis functions in the vectors $\boldsymbol{b}_n$ and $\boldsymbol{b}_m$. The example shows spatial forward projections of the model for two different times t_1 and t_2 which are associated with the systems' viewing positions α_1 and α_2.

$(L \cdot T)$-dimensional projection column vector $\boldsymbol{p}$ consists of the stacked vectors $\boldsymbol{p_{d_{\alpha_t}}}$ for all T acquired projection views.

According to the structure of the decomposition model Eq. 2.1, the non-simultaneous projection operation $\boldsymbol{p_d} = \mathcal{F}(\boldsymbol{Y} \cdot \boldsymbol{B}')$ is implemented as a two-step procedure for each projection view. For this purpose, each R-dimensional column in the weighting parameter matrix $\boldsymbol{Y} = (\boldsymbol{y}_1 \cdots \boldsymbol{y}_N)$ is considered as a volumetric image of coefficients. For a time step t, all N images of coefficients are linearly combined by the temporal basis function samples $(b_{t,1}, \cdots, b_{t,N})$. Then, the resulting image is forward projected according to the corresponding viewing position α_t by the spatial projection operator $\mathcal{F}_{\alpha_t}$ which maps from the R-dimensional image space to the L-dimensional projection view. For the generation of the entire set of projections this can be formally written as (cf. [106]):

$$\begin{pmatrix} \boldsymbol{p_{d_{\alpha_1}}} \\ \vdots \\ \boldsymbol{p_{d_{\alpha_T}}} \end{pmatrix} = \begin{pmatrix} \mathcal{F}_{\alpha_1} b_{1,1} & \cdots & \mathcal{F}_{\alpha_1} b_{1,N} \\ \vdots & \ddots & \vdots \\ \mathcal{F}_{\alpha_T} b_{T,1} & \cdots & \mathcal{F}_{\alpha_T} b_{T,N} \end{pmatrix} \begin{pmatrix} \boldsymbol{y}_1 \\ \vdots \\ \boldsymbol{y}_N \end{pmatrix} \tag{2.2}$$

In x-ray tomography a first order approximation is typically used to describe the spatial projection operation. Then, the non-simultaneous forward projection in Eq. 2.2 is a linear operation:

$$\boldsymbol{p_d} = \boldsymbol{G} \cdot \boldsymbol{y} \tag{2.3}$$

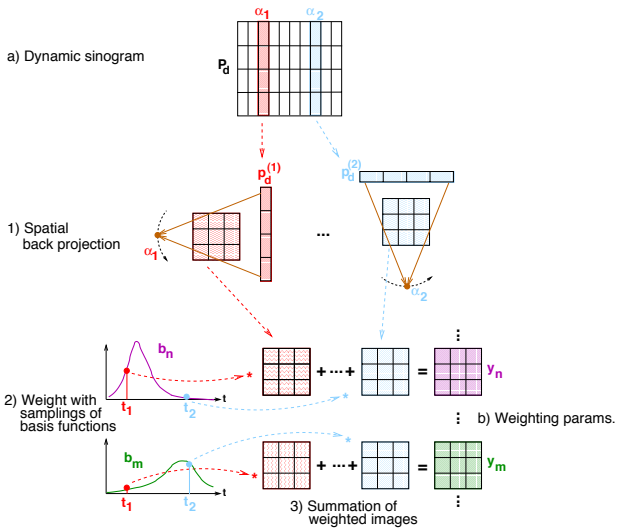

Figure 2.3. Operation example of non-simultaneous model-based back-projection: The line integrals in $\boldsymbol{p_d}^{(1)}$ and $\boldsymbol{p_d}^{(2)}$ are spatially backprojected according to the viewing positions α_1 and α_2, respectively. The model parameters in $\boldsymbol{y}_n$ and $\boldsymbol{y}_m$ (which are related to the temporal basis functions $\boldsymbol{b}_n$ and $\boldsymbol{b}_m$, respectively) are obtained from the weighted summation of the backprojections. The weights are taken from the associated temporal basis functions at the time points which correspond to the viewing positions, i.e. t_1 and t_2 in this example.

In practice the large system matrix $\boldsymbol{G}$ is never formed explicitly, but the non-simultaneous projection is realized as a mapping from the weighting parameters $\boldsymbol{y}$ to the line integrals $\boldsymbol{p_d}$ that is carried out in two steps for each acquired projection view (see Figure 2.2):

1) For the current acquisition time t, the model parameters in $\boldsymbol{y}$ are linearly combined with the values of the temporal basis functions in $\boldsymbol{B}$ at time t. This step results in a volumetric image of R voxels.

2) The generated image is geometrically forward projected by $\mathcal{F}_{\alpha_t}$ according to the current viewing position α_t. In the used implementation, the spatial projection from the regular voxel grid in image space to the grid of detector pixels is realized as the ray-driven method described in [58].

2.2.3 Iterative parameter optimization

Goal of the numerical parameter estimation method is to obtain the set of optimal weighting parameters $\hat{\boldsymbol{y}}$ by solving the linear Least-Squares problem

$$\hat{\boldsymbol{y}} = \underset{\boldsymbol{y}}{\operatorname{argmin}} \; ||\boldsymbol{G} \cdot \boldsymbol{y} - \tilde{\boldsymbol{p}}_{\boldsymbol{d}}||^2 \tag{2.4}$$

in a computationally efficient way.

Here, a gradient-based iterative procedure is introduced to solve the large scale problem in Eq. 2.4. Typically, the system matrix $\boldsymbol{G}$ is ill-conditioned, thus the direct solution $\hat{\boldsymbol{y}}$ is sensitive

to inconsistencies (e.g. projection noise) or even non-unique. Regularization methods [39] must be applied to yield a stabilized solution. As frequently practiced with iterative methods (e.g. [38, 39]), the regularizing effect is achieved by stopping iterations before noise tends to dominate the solution. The basic operation which updates the current estimate of the model's weighting parameter vector $\boldsymbol{y}^{(i)}$ at the i-th iteration step is an extended Landweber scheme (see [69]) which forms the basis of common algebraic reconstruction methods used in static tomographic image reconstruction (see e.g. [57, 126]):

$$\boldsymbol{y}^{(i+1)} \leftarrow \boldsymbol{y}^{(i)} + \lambda \boldsymbol{G}' \cdot \boldsymbol{D} \cdot (\tilde{\boldsymbol{p}}_{\boldsymbol{d}} - \boldsymbol{G} \cdot \boldsymbol{y}^{(i)}) \tag{2.5}$$

The relaxation constant λ controls the step size when updating the parameters $\boldsymbol{y}^{(i)}$ at each iteration. A diagonal matrix $\boldsymbol{D}$ is used for scaling each ray in the projection residual $\tilde{\boldsymbol{p}}_{\boldsymbol{d}} - \boldsymbol{G} \cdot \boldsymbol{y}^{(i)}$ to improve convergence speed. The procedure is initialized by setting all weighting parameters $\boldsymbol{y}^{(0)}$ to zero.

2.2.3.1 Model-based non-simultaneous back-projection

The matrix $\boldsymbol{G}'$ in Eq. 2.5 is the transpose to the system matrix:

$$\boldsymbol{G}' = \begin{pmatrix} b_{1,1}\,\mathcal{F}_{\alpha_1}' & \cdots & b_{T,1}\,\mathcal{F}_{\alpha_T}' \\ \vdots & \ddots & \vdots \\ b_{1,N}\,\mathcal{F}_{\alpha_1}' & \cdots & b_{T,N}\,\mathcal{F}_{\alpha_T}' \end{pmatrix} \tag{2.6}$$

Its operation can be interpreted as a model-based non-simultaneous back-projection which transforms from the space of line integrals to the domain of parameters $\boldsymbol{y}$. As shown in the example in Figure 2.3 it works symmetrically to the non-simultaneous forward projection, and can be carried out as a two-step procedure at time t:

1) The line integral data are geometrically back-projected into image space according to the current viewing position α_t. This results in a volumetric image of R voxels. In the implementation, a voxel-driven method is employed for mapping from the detector grid to the image grid.

2) For each temporal basis function in $\boldsymbol{B}$ a weighted copy of the generated image is created with the weighting factor equal to the basis function value at the current time t. For each individual basis function, the weighted images are accumulated separately over all viewing positions yielding the final parameters $\boldsymbol{y}$ of the spatio-temporal model.

2.2.3.2 Regularization

When using iterative methods for static tomographic reconstruction tasks it is common practice to regularize the resulting image by early stopping of iterations (see e.g. [45]). This is related to the properties of the iteration scheme in Eq. 2.5: In terms of singular vectors related to a Singular Value Decomposition (SVD) of the system matrix $\boldsymbol{G}$, the image components of the final image that are associated with large singular values exhibit faster convergence than those related to small singular values (see e.g. [38]). Typically, the large singular values of spatial projection operators are associated with smooth components in the image space (at least when using 'standard' spatial basis functions, such as image voxels) leading to suppression of image noise (i.e. high frequency components) in the early iteration steps.

Such semi-convergence property [39] of Eq. 2.5 is exploited for a noise-robust solution to the TAC estimation problem in Eq. 2.4. Hence, in addition to the constraints imposed on the solution by the choice of proper temporal basis functions, the number of iteration steps is adjusted in order to control noise levels and smoothness of the solution in the spatial and temporal domain. Even in the underdetermined case (i.e. with a total number $L \cdot T$ of projection rays smaller than the number $R \cdot N$ of weighting parameters) the early stopping of iterations will lead to a 'smooth' solution for $\boldsymbol{X_d}$ (c.f. [39]). However, as this favorable convergence property is related to the spectral properties of the model-based forward projection $\boldsymbol{G}$ it is strongly affected by the chosen structure of the decomposition model. Thus, as an extension to the design requirements for the decomposition model stated in Sec. 2.2.1, the temporal basis functions must be chosen sufficiently smooth (cf. Figure 2.1) to preserve the desired regularization properties of the iterative optimization method.

2.2.3.3 Acceleration of convergence

A common way to improve the speed of convergence of the extended Landweber scheme in Eq. 2.5 is to modify the spectral features of the system matrix (ideally without harming the regularization properties), e.g. by applying a proper scaling of the projection residuals by means of the diagonal matrix $\boldsymbol{D}$. Several methods for setting scaling factors have been suggested for iterative tomographic reconstruction methods. For the iterative parameter optimization pursued here the Component Averaging (CAV) scheme described in [9] is used to determine the scaling factors in $\boldsymbol{D}$: the k-th element in the diagonal of $\boldsymbol{D}$ is

$$d_{k,k} = \frac{1}{\sum_{l=1}^{R \cdot N} z_l \cdot g_{k,l}^2} \tag{2.7}$$

Here, $g_{k,l}$ is the element of the system matrix $\boldsymbol{G}$ at position (k, l), the quantity z_l denotes the number of non-zero elements in the l-th column of $\boldsymbol{G}$. In an implementation, the scaling factors according to Eq. 2.7 are computed on-the-fly during the non-simultaneous forward projection operation. Its practical usage aims at equalizing all projection residuals by compensating for i) variations in the intersection lengths of projection rays through the voxel grid for different detector pixels at different viewing positions, and ii) for variations of function values among the temporal basis functions (see Figure 2.1).

An additional acceleration of convergence is achieved by making use of an ordered subsets variant [50] of the original iteration scheme in Eq. 2.5. The set of acquired projections is partitioned into S different subsets which are processed subsequently in sub-iterations. A full iteration cycle is completed after processing all subsets once. For T acquired projection views in total, each subset contains the line integrals of $\frac{T}{S}$ views. The viewing positions within each subset are selected to yield an equi-temporal spacing of S time steps between projection acquisition times. The order of stepping through the subsets within an iteration cycle influences the rate of convergence (e.g. [87]). The common rationale for choosing a suitable accessing scheme is to order subsets such that they contain a maximum of independent information (in terms of angular viewing positions) with respect to the previously processed subsets. For the deployed implementation of the iteration scheme the subsets are ordered according to the golden ratio division of the scanning range as described in [65].

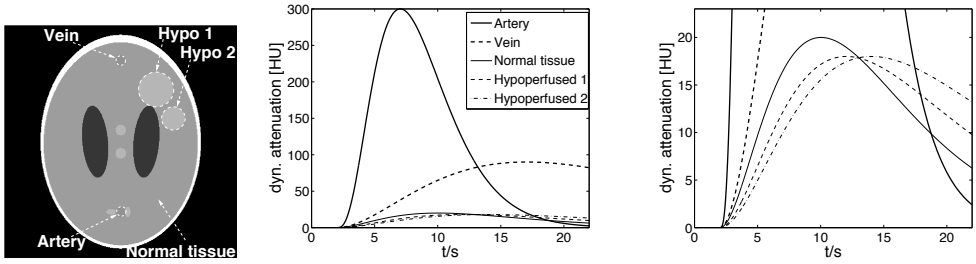

Figure 2.4. Synthetic dynamic head phantom: (a) static attenuation in a [0,100] HU window, showing the location of regions with additional dynamic attenuation, (b) dynamic time attenuation curves added to the five regions shown in (a), (c) is a zoom into (b)

2.3 Materials and methods

The feasibility of reconstructing dynamic contrast curves accurately using the proposed iterative method is evaluated in a simulation study.

2.3.1 Dynamic phantom data

The simulations are based on non-simultaneously acquired projections of two different types of dynamic software phantoms:

1. A synthetic head is derived from a Shepp-Logan-like phantom. It is based on 10 static ellipsoids representing the anatomic attenuation of the synthetic head shown in Figure 2.4. Time attenuation curves simulating the contrast dynamics in 5 different elliptical regions (representing artery, vein, normal tissue, and 2 different types of hypoperfused tissue) are added to the static phantom. These TACs resemble different instances of gamma-variate-functions (see [42]) and are parameterized to represent the dynamic X-ray attenuation of a typical brain perfusion CT contrast injection (see [64]). The simulated non-simultaneous acquisition of projections spans a time interval of 22 seconds.

2. A temporal sequence of 60 images (2-D slices of 512×512 pixel) of a human head that has been originally acquired with a neuro perfusion CT system over 30 seconds (i.e. an image slice has been reconstructed every 0.5 seconds after intra-venous injection of contrast). By making use of spline interpolation in the temporal domain, the total number of images in the sequence is increased to 1080 over the 30 seconds interval to finally match the target frame rate of the simulated non-simultaneous acquisitions.

For both phantoms the image slice size is 25cm x 25cm.

2.3.2 Acquisition modes

For the simulation experiments two different acquisition modes are applied to acquire dynamic projections of the phantoms (see Table 2.1):

Table 2.1. Parameters of non-simultaneous scanning modes

	Phantom 1	Phantom 2
Tot. dyn. scan time	22 seconds	30 seconds
Acq. Mode I) Multiple full rotations (360^o)		
rotation speed	49^o/s	54^o/s
tot. # rotations	3	4.5
proj. frame rate	32.7 fps	36.0 fps
tot. # acq. proj.	720	1080
Acq. Mode II) Repeated forward/backward sweeps (180^o)		
rotation speed	32.7^o/s	36.0^o/s
tot. # sweeps	4	6
proj. frame rate	32.7 fps	36.0 fps
tot. # acq. proj.	720	1080

Acq. Mode I
A continuously rotating scanning system. Simulated rotation speeds are adjusted such that 3 full (360^o) rotations are performed for acquisition of the first phantom, and 4.5 rotations for the second one, respectively. The detector frame rate is set to acquire 720 projections totally for the first phantom, and 1080 projections totally for the second one.

Acq. Mode II
A system that repeatedly sweeps along a 180° circular arc forward and backward in a toggled mode. For this acquisition mode the rotation speed is set to perform 2 forward and 2 backward sweeps for the first phantom, and 3 sweeps in each direction for the second one, respectively. The detector frame rates are identical to the first acquisition mode.

To assess the influence of projection noise, two different scenarios are considered in the simulation experiments: i) noise free projections; ii) simulated quantum noise in the projections, where the noise levels governed by the total (i.e. dynamic plus static) attenuation in the line integrals are due to a simulated X-ray flux of $2.1 \cdot 10^6$ direct photons per mm^2 on the detector in each projection view. A parallel beam geometry is assumed for all acquisition modes. The length of the detector row is 35.6 cm containing 429 pixel, the simulated detector pixel size is 0.83mm x 5.0mm.

2.3.3 Dynamic reconstruction

The total number and the shapes of the temporal functions contained in $\boldsymbol{B}$ may influence the accuracy and the computational complexity of the proposed TAC estimation method. Thus, a variety of different basis functions derived from the basic function families introduced in Sec. 2.2.1 are employed: Gaussian functions (Gs) or gamma-variate functions (GV) with a fixed width, equally distributed over the acquisition time interval (as depicted in Figure 2.1). Because the number of basis functions balances between robustness, computational complexity and modeling precision of the method, the total number N of functions is gradually reduced from 25 original functions. Both procedures introduced in Sec. 2.2.1 to reduce the number of functions are compared: i) direct reduction by increasing the spacing between the original

functions, ii) PCA based transformation and reduction using the ranking according to the Eigenvalues (see [74]). As a compact notation for the temporal model 'Gs-N' and 'GV-N' will be used to indicate a set of N temporal basis functions of the original Gaussian and gamma-variate type, respectively. Correspondingly, 'Gs-PCA-N' and 'GV-PCA-N' denote sets of N temporal basis functions which are derived via the PCA based reduction method from an original set of 25 Gaussian and 25 gamma-variate functions, respectively. None of the chosen temporal functions does exactly match any TAC contained in the dynamic phantoms

The spatial grid for dynamic reconstruction consists of a slice of 150x150 image voxels, voxel size is 1.66 mm (i.e. size of the reconstructed slice is 25cm x 25cm). To reduce the accumulation of spatial aliasing over iteration cycles (see e.g. [88]) a Hann low-pass filter is applied to the line integral residuals in each sub-iteration step.

The non-simultaneously acquired dynamic projections are preprocessed to remove the static anatomical information by subtracting the corresponding line intergral $\tilde{\boldsymbol{p}}_s$ from a non-contrasted acquisition sweep as outlined in Sec. 2.2. Non-contrasted line integral data are acquired from projections of the first time instance of both dynamic phantom sequences. In the noisy projections scenario, the same x-ray flux per view is assumed for the static acquisitions as for the dynamic ones.

For the subdivision into ordered subsets the acquired projections are partitioned into $S = 90$ sets; i.e. 8 projection views per subset are used for Phantom 1, 12 projection views for Phantom 2, respectively.

2.4 Results and discussion

A quantitative evaluation of TAC estimation accuracy is carried out for the synthetic dynamic head phantom (phantom 1) in 6 different spatially homogeneous regions of interest (ROIs) shown in Table 2.2. The ROIs are placed in the centers of the circular areas in Figure 2.4. For the CT perfusion data set (phantom 2) the accuracy is evaluated on a spatially global level.

The following evaluation metrics are used in each region: i) mean-squared-deviation between estimated TACs and true TACs (MSE), ii) spatial variation of TACs (Inhom), iii) decomposition of MSE into Bias and statistical Variance to assess propagation of projection noise.

For the mean-squared-error between the TACs in the estimated image sequence $\boldsymbol{X_d}$ and the true sequence $\tilde{\boldsymbol{X}}_{\boldsymbol{d}}$ the squared deviations are averaged over all voxels within a ROI and over all reconstructed time points[3]:

$$\mathrm{MSE}(\boldsymbol{X_d}\,,\,\tilde{\boldsymbol{X}}_{\boldsymbol{d}}) = \frac{1}{T\cdot|\mathrm{ROI}|}\sum_{t=1}^{T}\sum_{k\in\mathrm{ROI}}\left(x_{\mathbf{d}k,t}-\tilde{x}_{\mathbf{d}k,t}\right)^2 \tag{2.8}$$

The spatial variation in a given ROI is computed as the mean-squared-deviation between all estimated TACs for this region at a specific time point and the corresponding spatially averaged value. These squared deviations are averaged over all reconstructed time points to obtain the inhomogeneity of TACs:

$$\mathrm{Inhom}^2(\boldsymbol{X_d}) = \frac{1}{T\cdot|\mathrm{ROI}|}\sum_{t=1}^{T}\sum_{k\in\mathrm{ROI}}\left(x_{\mathbf{d}k,t}-\frac{1}{|\mathrm{ROI}|}\sum_{r\in\mathrm{ROI}}x_{\mathbf{d}r,t}\right)^2 \tag{2.9}$$

[3]the expression $k\in$ROI denotes the set of all voxels in the considered region;$|ROI|$ denotes the number of voxels in that region

Table 2.2. Regions of interests (ROIs) to evaluate the synthetic phantom

	Center position (cf. Figure 2.4 a)	# voxel in slice	$\tilde{\boldsymbol{X}}_{\boldsymbol{d}max}$	bar color
ROI 1	Artery	10	300 HU	
ROI 2	Vein	10	80 HU	
ROI 3	Hypoperfused 1	99	18 HU	
ROI 4	Hypoperfused 2	42	18 HU	
ROI 5	Normal tissue (horiz. mirror of ROI 3)	99	20 HU	
ROI 6	Normal tissue (horiz. mirror of ROI 4)	42	20 HU	

To assess the influence of projection noise, all parameter estimations are repeated $J = 25$ times with different instances of simulated quantum noise. An average estimated dynamic image sequence $\overline{\boldsymbol{X}_{\boldsymbol{d}}} = \frac{1}{J}\sum_{j=1}^{J} \boldsymbol{X}_{\boldsymbol{d}}{}^{(j)}$ can be obtained from the parameter estimates resulting from each simulated noise instance. According to [27] the statistical bias with respect to the true image sequence $\tilde{\boldsymbol{X}}_{\boldsymbol{d}}$ and the variance due to noise in the estimated dynamic image sequences can be computed as:

$$\text{Bias}^2 = \text{MSE}(\overline{\boldsymbol{X}_{\boldsymbol{d}}}\,,\, \tilde{\boldsymbol{X}}_{\boldsymbol{d}}) \tag{2.10}$$

$$\text{Variance} = \frac{1}{J}\sum_{j=1}^{J} \text{MSE}(\boldsymbol{X}_{\boldsymbol{d}}{}^{(j)}\,,\, \overline{\boldsymbol{X}_{\boldsymbol{d}}}) \tag{2.11}$$

Note that the average MSE over different noise instances is: $\frac{1}{J}\sum_{j=1}^{J} \text{MSE}(\boldsymbol{X}_{\boldsymbol{d}}{}^{(j)}\,,\, \tilde{\boldsymbol{X}}_{\boldsymbol{d}}) = \text{Bias}^2 + \text{Variance}$.

In the following, the TAC estimation accuracy is depicted as error bars for each ROI in the style of Figure 2.5; the relation to the individual ROIs can be identified by the color scheme shown in Table 2.2. For the noise-free cases, the square root of the mean-squared-error (i.e. RMSE) and the spatial inhomogeneity (i.e. Inhom) are presented as shown in Figure 2.5(a). For noisy projections, the errors are given in terms of the square root of the average MSE, Bias, and square root of the Variance (i.e. Std. Deviation) as depicted in Figure 2.5(b). To present the error bars of different ROIs on similar scales, all shown quantities (i.e. RMSE, Inhom, Bias, and Std. Dev.) are normalized by the maximum value of the true dynamic contrast attenuation $\tilde{\boldsymbol{X}}_{\boldsymbol{d}max}$ in each ROI (see Table 2.2).

2.4.1 Characterization of iterative parameter estimation method

2.4.1.1 Convergence

The convergence of the proposed iterative estimation method in the noisy projection data scenario is shown in Figure 2.6 for the setup Acq. Mode I, Gs-25. Figure 2.6(a) depicts the reduction of the projection residual $||\boldsymbol{G}\cdot\boldsymbol{y} - \tilde{\boldsymbol{p}}_{\boldsymbol{d}}||$ over the number of iteration cycles for different settings of the step size parameter λ. A fixed setting of $\lambda = 0.75$ which yields fast and stable convergence is used for the remainder of the experiments. The semi-convergence of the RMSE over iterations is demonstrated for a TAC in ROI 4 (i.e. a tissue region) in Figure 2.6(b). Here, the optimal regularization effect is achieved by stopping after 4 iteration cycles. Before this point the RMSE is dominated by the bias error, while in later iterations the growing variance leads to a further increase of the RMSE. As shown in Figure 2.6(c) the optimal number of

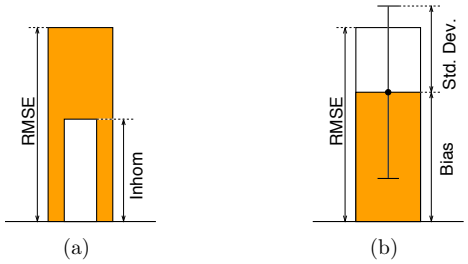

Figure 2.5. Error bar notation: (a) for the noise-free scenario the colored bar indicates RMSE, the inner white bar is spatial variation in terms of inhomogeneity, (b) for the noisy scenario the colored bar indicates Bias error, in combination with the upper white bar it is the RMSE, and the thin vertical bar corresponds to statistical Std. Deviation.

iteration cycles - in terms of minimization of the RMSE - differs from one region to another. In the tissue ROIs the optimal early stopping point occurs after 2–4 iteration cycles; for the vein (i.e. a region exhibiting much higher signal-to-noise levels) the optimum is reached beyond 20 iteration cycles. As there is no general optimal stopping rule which applies to all regions, in the following the number of iteration cycles is chosen heuristically as a reasonable tradeoff: For the noisy scenario the number of iteration cycles is set to 5. In the noise free case (i.e. the statistical variance equals zero) 20 iteration cycles are performed. Figure 2.6(d) demonstrates the approximation of the vein TAC over the first 5 iteration cycles.

2.4.1.2 Resolution

The resolution of the iterative estimation method is characterized by the spatial modulation transfer function (MTF) and by the temporal impulse responses shown in Figure 2.7. The spatial MTF is obtained from averaging the derivatives of profiles resulting from dynamic reconstruction of a horizontal and a vertical dynamic edge which follows the tissue TAC shown in Figure 2.4(b) for the setup Gs-25, Acq. Mode I. The number of iterations has a strong impact on spatial resolution, e.g. the resolution drops from 2.6lp/cm to 2.1lp/cm (in terms of the 50% MTF point) when decreasing the number of iteration cycles from 20 to 5 (see Figure 2.7(a)).

In general, the iterative dynamic reconstruction system is time-shift-variant – this property is mainly influenced by the choice of temporal basis functions. To assess temporal resolution, the responses to isolated temporal impulses in a spatially homogeneous image that occur at different points in time must be considered (e.g. Figure 2.7(b) shows the impulse responses at $t = \{5.2\text{s}, 14.0\text{s}, 22.8\text{s}\}$). In contrast to the Gaussian basis functions, the asymmetric shapes of the gamma-variate functions (cf. Figure 2.1(c)) yield sharp impulse responses in the early time ranges and smoother responses in the later phases, which facilitates a more accurate modeling of the fast raising edge in the early arterial TACs. In addition, the number of iteration cycles has an impact on temporal resolution: 5 iteration cycles (top of Figure 2.7(b)) lead to broader impulse responses than usage of 20 equivalent[4] iteration cycles (bottom of Figure 2.7(b)). These results demonstrate how the noise suppressing effect of stopping iterations early influences both the spatial and temporal resolution.

[4]To keep the amount of information contained in each subset balanced, for the impulse response simulations the number of subsets has been reduced to one while keeping the original number of subiteration steps.

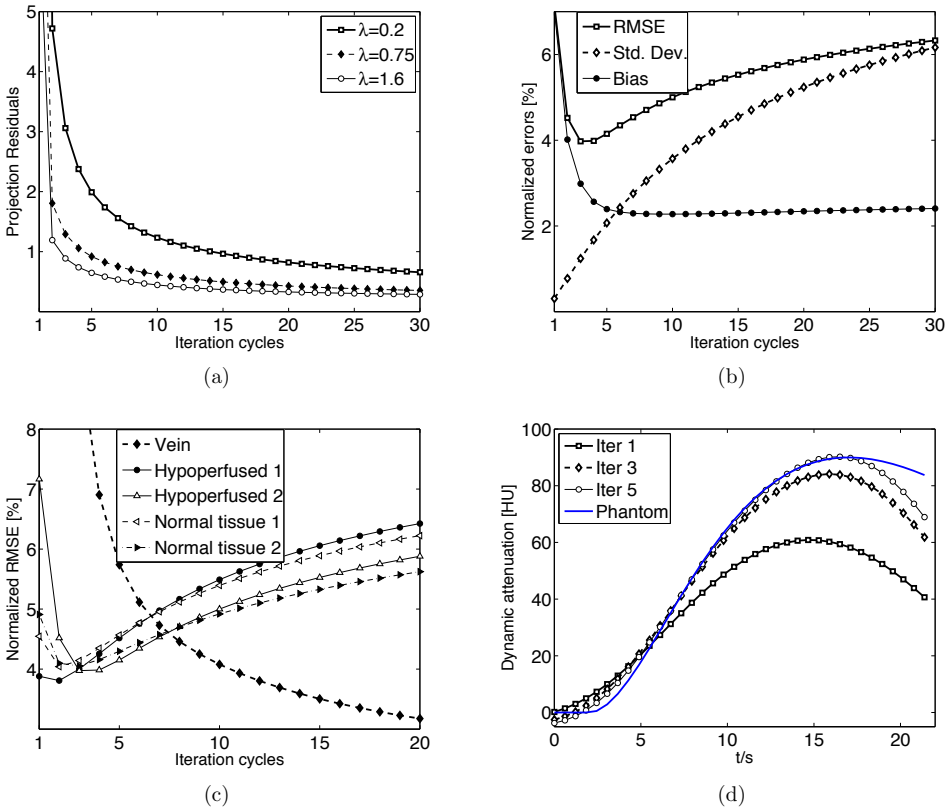

Figure 2.6. Convergence properties of the iterative method on noisy projections for a setup using 25 Gaussian basis functions and full rotational acquisitions (i.e. Gs-25, Acq. Mode I). (a) projection residuals over the number of iteration cycles for different λ; (b) normalized RMSE, normalized Bias and normalized Std. Deviation for ROI 4 over iteration cycles for $\lambda = 0.75$; (c) normalized RMSE for different ROIs over iteration cycles; (d) evolution of an estimated TAC in the vein for different numbers of iteration cycles

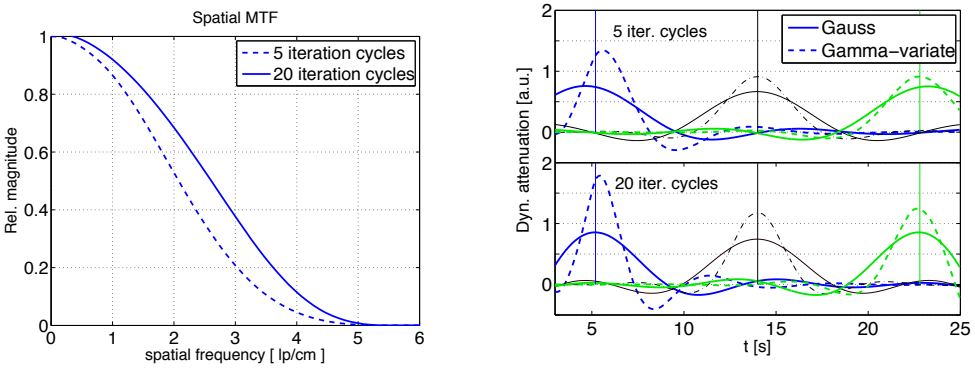

(a) Spatial modulation transfer functions (b) Temporal impulse responses

Figure 2.7. Spatial and temporal resolution of the iterative method for 5 and 20 iteration cycles. (a) spatial MTF derived from an edge that follows vein dynamics (cf. Figure 2.4(b)) for Gs-25, Acq. Mode I. (b) temporal responses of gamma-variate and Gaussian basis functions to impulses at three different time points (5.2s, 14.0s, and 22.8s) for Acq. Mode I with 5 and 20 equiv. iteration cycles (top and bottom figures, resp.).

2.4.2 Synthetic head phantom: Noise-free projections

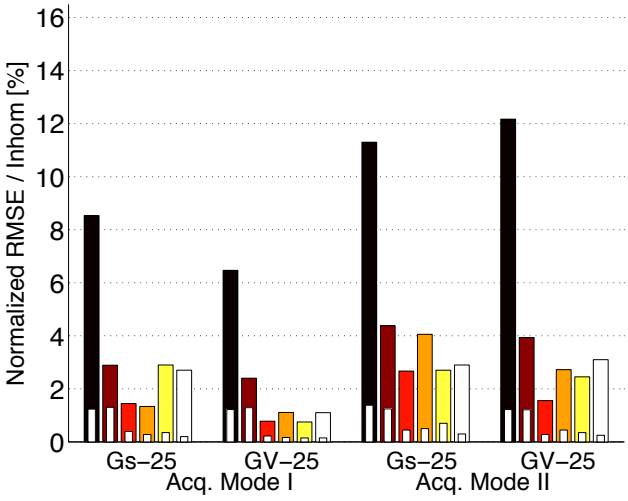

Figure 2.8. Normalized RMSE and inhomogeneity for noise-free projections of the synthetic head phantom using 25 Gaussian (Gs-25) and gamma-variate (GV-25) temporal basis functions after 20 iteration cycles. Acquisition modes are: multiple full rotations (Acq. Mode I), and repeated forw./backward (Acq. Mode II).

Figure 2.8 shows the results obtained with combinations of both acquisition modes and

both sets of original temporal basis functions (25 in each case). Comparing different scan trajectories in terms of RMSE, it is observed that multiple full rotations (Acq. Mode I) yield higher accuracy than the repeated forward/backward trajectory (Acq. Mode II) which suffers from the slower and irregular temporal coverage of the sweep range. In all scenarios depicted in Figure 2.8 the estimation of the artery TAC is less accurate (by a factor of ca. 4) than for the tissue regions. This effect points to the increased difficulties with estimating TACs that exhibit faster temporal dynamics. The gamma-variate temporal basis functions tend to perform better than Gaussian bases. This general trend applies to almost all ROIs and is attributed to the fact that the true TACs within the synthetic phantom better comply with the asymmetric shapes of gamma-variate basis functions.

Concerning spatial variability of estimated TACs (i.e. Inhom) the vessel ROIs 1 and 2 exhibit reduced homogeneity compared to the large tissue regions 3–6 which is mainly caused by the effect of the system MTF in small regions (cf. Figure 2.10). The degree of inhomogeneity in these regions levels off for different acquisition modes and different sets of basis functions. The spatial MTF effect leads to a significant contribution (ca. 50% for Acq. Mode I, ca. 30% for Acq. Mode II) of the spatial inhomogeneity to the entire RMSE in the vein region (ROI 2). For all other regions the impact of the MTF on the RMSE is small in comparison to the systematic deviations resulting from non-simultaneous acquisition and non-ideal temporal modeling.

Image maps and profiles of 3 cross-sections displaying the contrast peak characteristics in terms of *dynamic peak attenuation* and *peak time* are shown in Figure 2.9 and Figure 2.10, respectively, for the original phantom and for the estimated image sequences resulting from the usage of gamma-variate basis functions (i.e. GV-25). For the forward/backward acquisition mode (Acq. Mode II), artifacts due to the limited rotational speed and range of the simulated image acquisition system are visible: The artery – which is highly enhanced during a very short time period – and to a minor degree the vein are smeared out in source-detector direction at the system's turning points which coincide with the lowest effective angular speed. In comparison, the hypoperfused regions, which exhibit time attenuation curves of considerably lower and slower dynamics, do not suffer from such artifacts. These visual observations are consistent with the RMSE values reported in Figure 2.8: The error values obtained for ROI 1 (artery) with the forward/backward movement are considerably larger (exceeding 12% normalized RMSE) compared to Acquisition Mode I. Hence the streak artifact toward the outside of the artery also impairs the estimation accuracy inside the corresponding ROI. In all cases, the estimated images exhibit reduced sharpness – particularly visible around the edges of the hypoperfused regions – which is due to the MTF effect of the finite number of iteration cycles.

In a further series of experiments, the impact of a decreased temporal model complexity and flexibility on the estimation accuracy is investigated (cf. Sec. 2.3). The complexity is reduced by using 10 or 4 temporal basis functions in total. For reduction, both methods introduced in Sec. 2.2.1 are compared: direct reduction and PCA-based transformation.

Results obtained with Acquisition Mode I are summarized in Figure 2.11. A reduction of the number of basis functions down to 10 can be done safely by both methods (with and without PCA) without significant loss of accuracy. The direct reduction to 4 temporal functions leads to a drastic degradation of estimation accuracy for both function types; in particular for the Gs-4 function set the RMSE is increased by a factor beyond 10 for the tissue regions (not fully visible in Figure 2.11(a)). In such cases of a very restricted set of basis functions it is beneficial to apply the PCA transformation method prior to reduction in order to limit the loss of accuracy. Thus, given a small set of temporal functions the PCA-based reduction method leads to a less constrained temporal model for the TACs. However, for both scenarios (i.e.

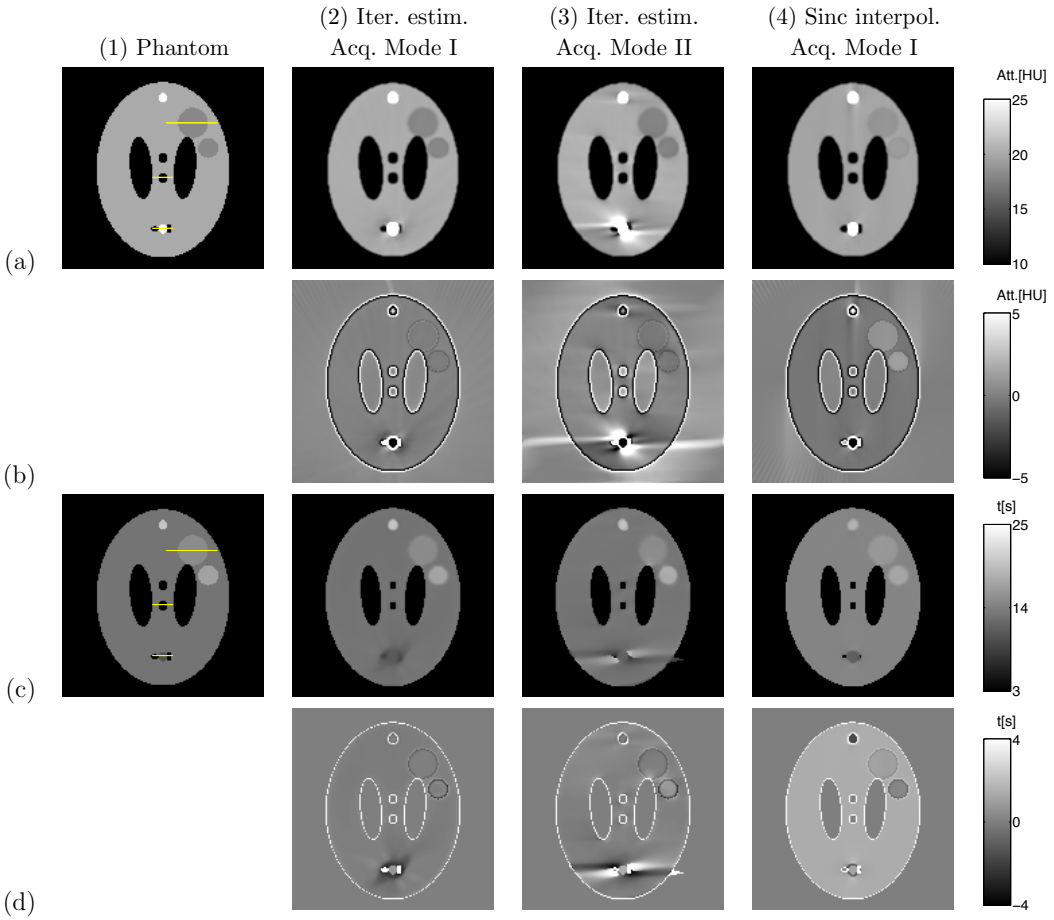

Figure 2.9. Estimated peak characteristics using noise-free projections of the synthetic head phantom. Columns are: (1) Phantom (with cross-sections used in Figure 2.10); (2) iter. estim. with Acq. Mode I; (3) iter. estim. with Acq. Mode II; (4) FBP using sinc interpolation with Acq. Mode I (discussed in Sec. 2.4.4). Iterative parameter estimation is based on 25 gamma-variate temporal basis functions (GV-25). Rows are: (a) peak attenuation; (b) difference of (a) to phantom data; (c) time of peak (only shown for voxels with $\max\{x_{\mathbf{d}}\} > 5$HU); (d) difference of (c) to phantom data.

Gs-PCA-4 and GV-PCA-4) the RMSE in the tissue regions is increased by a factor of more than 2 compared to the Gs-PCA-10 and GV-PCA-10 cases, respectively.

2.4.3 Synthetic head phantom: Noisy projections

Figure 2.12 lists the results in terms of RMSE, Bias, and Std. Dev. for noisy projection data obtained using both acquisition modes and the original sets of 25 Gaussian and gamma-variate basis functions, respectively. The early stopping (using 5 instead of 20 iteration cycles) leads

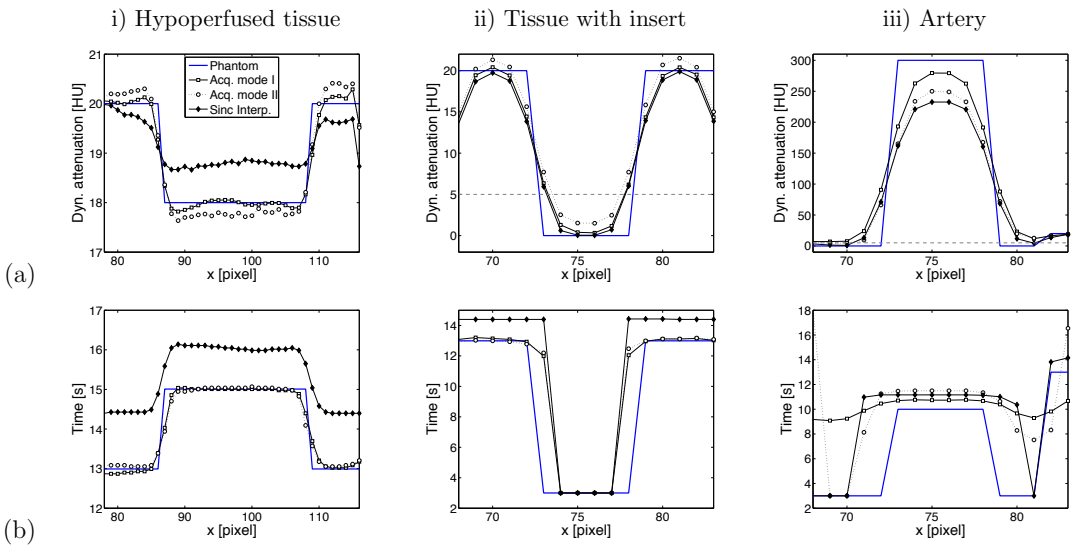

Figure 2.10. Profiles through 3 cross-sections of peak characteristics. Location of cross-sections in the phantom are indicated in Figure 2.9. Rows are: (a) peak attenuation; (b) time of peak (only effective for voxels with $\max\{x_{\mathbf{d}}\} > 5$HU, see dashed lines in Figure 2.10(a)).

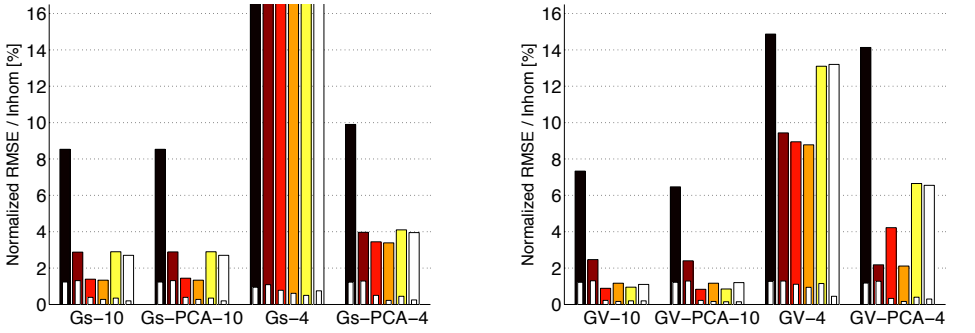

(a) Reduction from 25 Gaussian functions

(b) Reduction from 25 gamma-variate functions

Figure 2.11. Normalized RMSE and inhomogeneity for noise-free projections of the synthetic head phantom after 20 iteration cycles. Reduction to 10 and 4 temporal basis functions. Acquisition mode is multiple full rotations (Acq. Mode I).

to an increase of the bias error in all regions for all scenarios (cf. Figure 2.8). For Acquisition Mode II, which in the noise free case yields increased error levels (cf. Figure 2.8), the early-stopping-induced loss in terms of bias is less severe than for mode I. Concerning different basis functions, the bias error shows the same trend as observed in the noise-free case in that gamma-variate functions outperform Gaussian basis functions. The standard deviation due to noise has a strong influence on the TAC estimation accuracy in the tissue regions (ROIs 3-6). For the artery and the vein the impact of noise is negligible because the dynamic attenuation levels

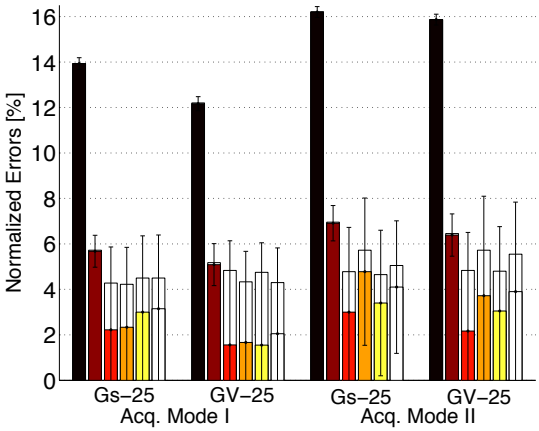

Figure 2.12. Normalized RMSE, Bias, and Std. Dev. for noisy projections of the synthetic head phantom after 5 iteration cycles. 25 Gaussian (Gs-25) and gamma-variate (GV-25) temporal basis functions. Acquisition modes are: multiple full rotations (Acq. Mode I), repeated forw./backward (Acq. Mode II).

of the TACs are much higher in these regions. When comparing different types of temporal basis functions, the gamma-variate functions are more sensitive to noise compared to Gaussian functions leading to an increase of the standard deviation in the tissue regions for all acquisition modes. As an overall result for the tissue regions there is no significant advantage in terms of RMSE when using gamma-variates instead of Gaussians with noisy projections. However, for the estimation of artery and vein TACs there is still a gain when using the temporal model based on gamma-variate functions.

For noisy projection data, Figure 2.13 shows the impact on estimation errors when reducing the original set of 25 gamma-variate functions down to 10 and 6 basis functions by using the direct method and the PCA transformation, respectively. As already observed for the noise-free simulations, the number of temporal basis functions can be safely reduced from 25 to 10 without significantly harming the bias error; this holds for all ROIs, for all acquisition modes and for both reduction methods (i.e. for GV-10 and GV-PCA-10). In the case of a further reduction to 6 basis functions (this is exemplified in Figure 2.13 for Acq. Mode I only) the bias errors are kept close to the original levels when using the PCA-based method. Contrary, usage of the more constrained temporal model GV-6 resulting from the increased spacing between the original gamma-variates leads to a increase of the bias in all regions.

Concerning Std. Dev. errors due to noise, usage of the PCA-based reduction method is inferior compared to the direct reduction of temporal basis functions for all acquisition modes (e.g. compare GV-PCA-10 vs. GV-10). Thus, the enhanced modeling flexibility gained by application of the PCA-based model reduction has an adverse effect on the noise robustness.

In Figure 2.14 this phenomenon affecting the TAC estimation accuracy and noise sensitivity is depicted over iteration cycles for the basis function sets GV-6 and GV-PCA-6 in ROI 4: the improved bias of the more flexible model GV-PCA-6 is overcompensated by its fast increasing standard deviation due to noise. At the optimal iteration stopping point (here: 3 cycles) this finally results in a negligible difference in RMSE between both function sets.

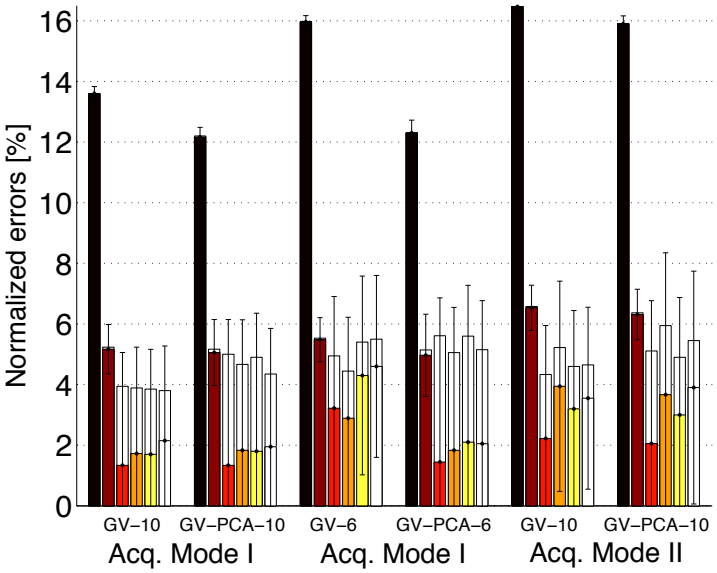

Figure 2.13. Normalized RMSE, Bias, and Std. Dev. for noisy projections of the synthetic head phantom after 5 iteration cycles. Reduction from 25 gamma-variate functions to 10 and 6 temporal basis functions. Acquisition modes are: multiple full rotations (Acq. Mode I), repeated forw./backward (Acq. Mode II).

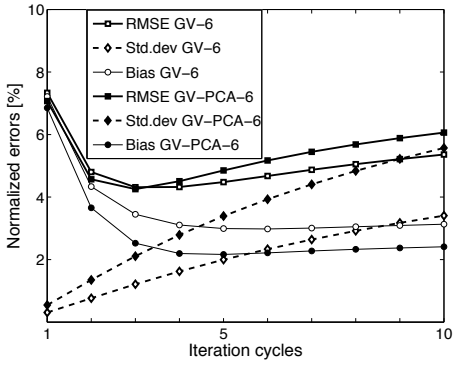

Figure 2.14. Convergence characteristics in ROI 4 for different temporal basis function sets: GV-6 vs. GV-PCA-6. Normalized RMSE, Bias, and Std. Dev. for noisy projections of the synthetic head phantom using multiple full rotations (Acq. Mode I).

According to the RMSE values depicted in Figure 2.13 (which have been obtained after 5 iteration cycles) for the tissue regions (ROIs 3-6) the RMSE performance using the directly reduced function sets is superior compared to the corresponding PCA-based models. Such enhanced noise robustness of the highly constrained model GV-10 even leads to an RMSE

improvement with respect to the original function set GV-25 for all acquisition modes (cf. Figure 2.12). However, for estimation of TACs in the vessel regions (which are less sensitive to noise) it is still beneficial to rely on the more flexible PCA-based model sets.

The peak dynamic contrast characteristics resulting from the TAC estimation using 25 gamma-variate basis functions in the presence of projection noise are displayed as images and cross-sections in Figure 2.15 and Figure 2.16, respectively. The visibility of the hypoperfused areas is reduced, but they can still be distinguished from the surrounding normal tissue. Artery and vein remain clearly visible, and also the characteristic streak artifacts along the system's turning point directions for Acquisition Mode II persist. In consistency with the results listed in Figure 2.12, the obtained images suffer from noise at similar levels irrespective of the acquisition mode.

2.4.4 Synthetic head phantom: Comparison with alternative dynamic reconstruction methods

For Acquisition Mode I the performance of the proposed iterative estimation method is compared with alternative dynamic reconstruction approaches. Two different analytic methods based on filtered backprojection (FBP) are considered for the fully rotational scan mode: i) the linearly interpolation method of [49], which linearly combines the projections of equivalent viewing positions from consecutive rotations; ii) the sinc-interpolation based on the ideal equi-temporal sampling approach proposed in [85], which assumes temporally bandlimited TACs that match the rotation speed. Given the slow system sampling rate of 0.14Hz (this corresponds to 7.3s full rotation time, see Acq. Mode I in Table 2.1), the 14.6s width of the sinc main lobe is broader than any of the impulse responses depicted in Figure 2.7 for the iterative estimation method. Hence, for the phantom TACs (shown in Figure 2.4(b)-(c)), in particular for their fast raising edges, such sampling condition is not ideally fulfilled and artifacts might occur due to temporal aliasing. The performance figures for the noise-free scenario and for noisy case are shown for both methods (which basically differ in the type of temporal interpolation kernel employed) in Figure 2.17. In the case of adding simulated projection noise a Hann low-pass filter (i.e. raised cosine, see [93]) is applied to the acquired projections with the cutoff set such that the statistical standard deviation errors in Figure 2.17(b) are on the same level as for the iterative method shown in Figure 2.12 for the scenario Acq. Mode I, GV-25.

For all scenarios and for all evaluated ROIs the ideal sampling-based method (that makes use of a temporal sinc-kernel) outperforms the linear interpolation approach (which confirms the findings in [85]) even though the sampling condition might be violated in some cases. However, in comparison to the proposed model-based iterative method (see Acq. Mode I in Figure 2.8 and Figure 2.12) the accuracy of both analytic reconstruction approaches is worse in the noise-free case as well as for noisy projections. Such gain in accurate TAC recovery can be attributed to the higher level of additional prior knowledge that is explicitly introduced to the iterative dynamic reconstruction method by making use of constrained temporal modeling.

Images and cross-sections of peak characteristics for the sinc-interpolation approach are shown in Figure 2.9 (last column) and in Figure 2.10 for noise-free projection data, and in Figure 2.15 (last column) and in Figure 2.16 for noisy data, respectively. Due to the limited temporal resolution of the sinc-kernel, the interpolated FBP method suffers from inaccurate approximation of the fast rising edges of the phantom TACs. Typically, this leads to the estimation of delayed contrast peaks, this effect becomes visible as an offset in the corresponding *time of peak* images.

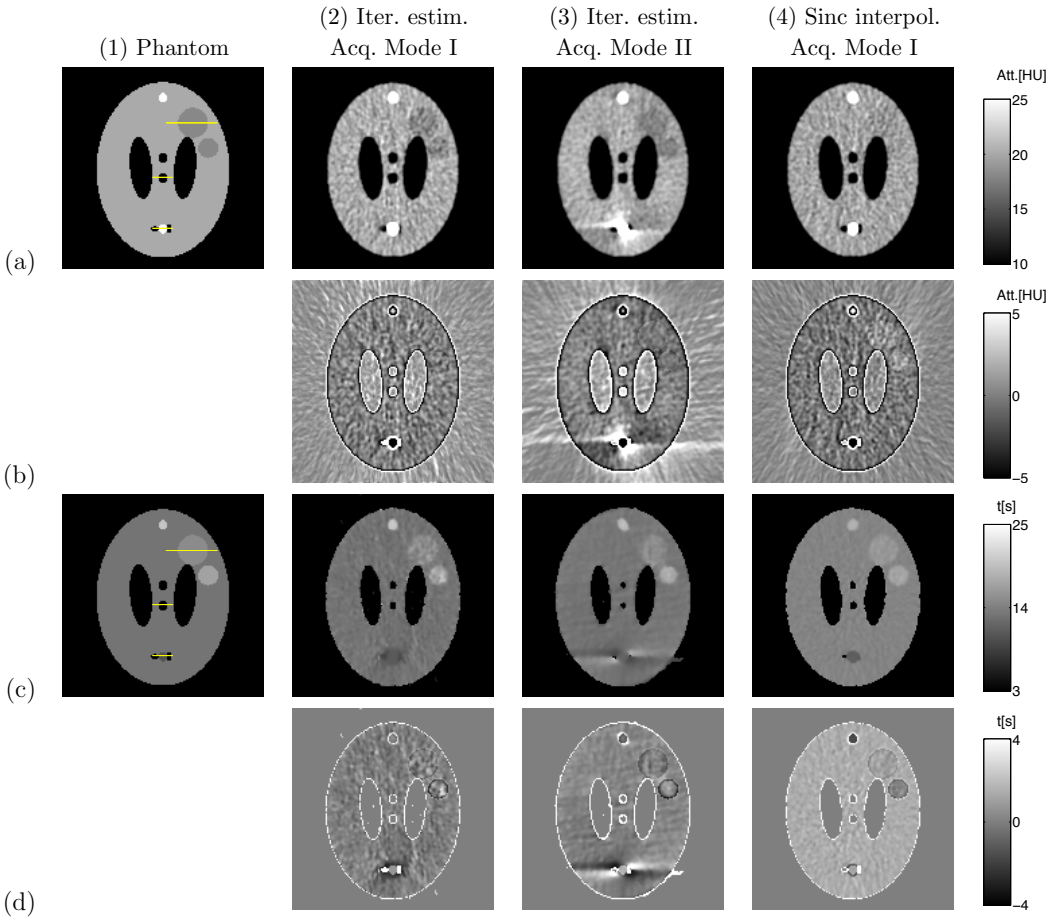

Figure 2.15. Estimated peak characteristics using noisy projections of the synthetic head phantom. Columns are: (1) Phantom (with cross-sections used in Figure 2.16); (2) iter. estim. with Acq. Mode I; (3) iter. estim. with Acq. Mode II; (4) FBP using sinc interpolation with Acq. Mode I (discussed in Sec. 2.4.4). Iterative parameter estimation is based on 25 gamma-variate temporal basis functions (GV-25). Rows are: (a) peak attenuation; (b) difference of (a) to phantom data; (c) time of peak (only shown for voxels with $\max\{x_{\mathbf{d}}\}$ >5HU); (d) difference of (c) to phantom data.

2.4.5 Neuro perfusion CT dataset

For an initial evaluation of the proposed iterative method on real neuro perfusion data, the image sequence originating from Perfusion-CT (cf. Sec. 2.3) is used as a dynamic phantom. Here, the quantitative assessment is based on the global RMSE (cf. Eq. 2.8) between the estimated and the true TACs within the entire image slice, including the air region surrounding the head (see Figure 2.18). All presented experiments concerning the neuro Perfusion-CT sequence involve noise-free projections.

The iterative dynamic reconstruction is applied to projections from both acquisition modes;

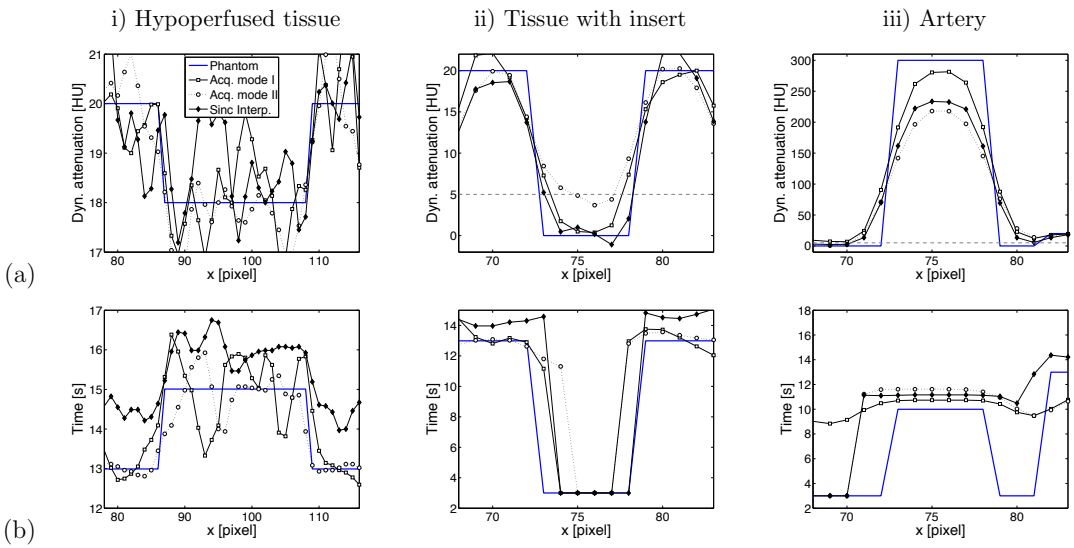

Figure 2.16. Profiles through 3 cross-sections of peak characteristics. Location of cross-sections in the phantom are indicated in Figure 2.15. Rows are: (a) peak attenuation; (b) time of peak (only effective for voxels with $\max\{x_{\mathbf{d}}\} > 5$HU, see dashed lines in Figure 2.16(a)).

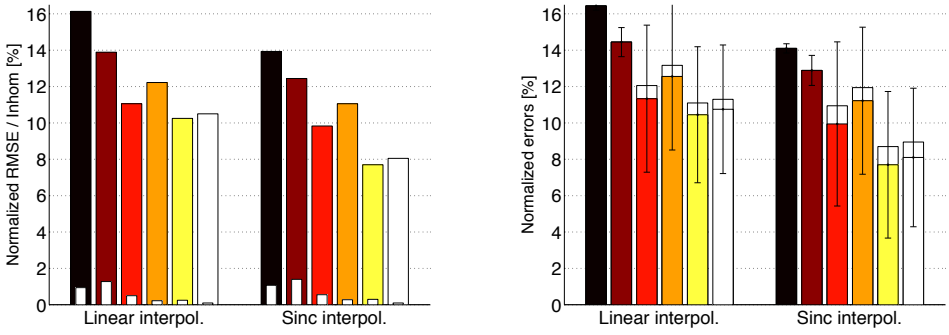

(a) Noise-free projection data

(b) Noisy projection data

Figure 2.17. Normalized RMSE, inhomogeneity, Bias, and Std. Dev. for (a) noise-free, and (b) noisy projections of the synthetic head phantom. Dynamic reconstruction using FBP-based interpolation methods: linear interpolation, and sinc interpolation. Acquisition mode is multiple full rotations (Acq. Mode I).

25 Gaussian (Gs-25) and gamma-variate (GV-25) temporal basis functions are employed. The obtained RMSE values are listed in Table 2.3. In addition, the global RMSE is given for the synthetic head phantom serving as a reference (corresponding to the ROI-specific figures shown in Figure 2.8). A comparison of acquisition modes reveals the same trend as for the synthetic head phantom: performance of Acq. Mode II is inferior compared to Mode I. The observed differences between the two investigated shapes of temporal basis functions, however, turn out

Table 2.3. Global RMSE for neuro perfusion CT sequence and for synthetic head phantom.

Basis functions	Perfusion CT sequence	Synthetic head phantom
	RMSE [HU]	
Acquisition Mode I: Multiple full rotations		
Gs-25	3.13	2.51
GV-25	3.14	2.40
TAC-PCA-25	3.10	-
Acquisition Mode II: Repeated forward/backward sweeps		
Gs-25	3.28	2.91
GV-25	3.30	2.90
TAC-PCA-25	3.20	-

to be negligible: In contrast to the synthetic head, the true time attenuation curves within the CT perfusion sequence do not have an exact gamma-variate shape and the usage of gamma-variate temporal basis functions does not yield an advantage over Gaussian functions. However, for the oracle scenario described in Sec. 2.2.1 an ideal set of 25 temporal basis functions (i.e. TAC-PCA-25) can be obtained by application of the PCA-based reduction method to the entire set of TACs in the neuro perfusion CT dataset. Based on such type of enriched prior knowledge the global RMSE is improved for both acquisition modes compared to the usage of the original sets of basis functions. This illustrates the benefit of including prior information to the temporal model.

On the basis of the dynamic reconstruction results, image maps of clinically relevant perfusion parameters — cerebral blood flow (CBF) (in ml/(100ml·min)), cerebral blood volume (CBV) (in %), and mean transit time (MTT) (in s) — are derived using the well-established slope method (see, e.g. [64]). The resulting images together with the peak time maps of the attenuation curves are shown in Figure 2.18 for the original dynamic CT data as well as for reconstructions using both scan modes and the gamma-variate basis functions (GV-25).

In the perfusion maps derived from the original CT data, an ischemic region in the left hemisphere is clearly recognizable by decreased CBF and CBV values and enhanced MTT and peak time. Like in the case of the synthetic head phantom, the images produced by the iterative model-based reconstruction exhibit a reduced spatial sharpness compared to the original, but the main features of the CBF and CBV images are well reproduced. In the MTT and peak time maps derived from the multiple full rotations (Acq. Mode I), the ischemic region is faithfully reconstructed as well. In the case of the repeated forward/backward sweeps (Acq. Mode II), however, the streak artifacts occurring at the trajectory's turning points already observed in the images of the synthetic head lead to a partial masking of the infarction area in the MTT and peak time realm.

2.5 Summary & Conclusion

Tomographic recovery of dynamic object contrast ideally requires availability of projections from all viewing positions at all time points simultaneously. For usage with slowly rotating systems which acquire projection data non-simultaneously, the proposed dynamic reconstruction method integrates prior knowledge by means of a parametric approximation of dynamic

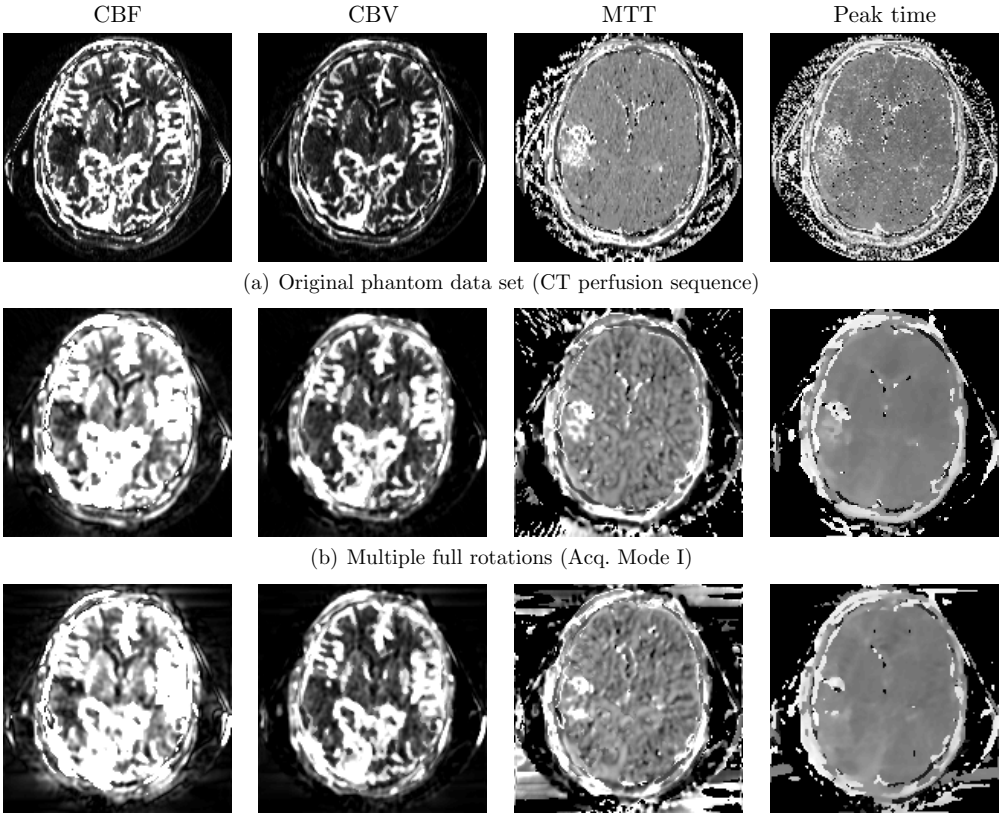

(a) Original phantom data set (CT perfusion sequence)

(b) Multiple full rotations (Acq. Mode I)

(c) Repeated forward/backward sweeps (Acq. Mode II)

Figure 2.18. Neuro perfusion CT dataset. Perfusion maps for different acquisition modes, temporal basis function set is GV-25: CBF in ml/(100ml·min) (range $[0, 120]$), CBV in % (range $[0, 20]$), MTT in s (range $[0, 10]$), and peak time in s (range $[0, 22]$)

contrast curves for compensating the lack of simultaneous acquisitions. In particular, a set of smooth basis functions is embedded as a temporal decomposition model in an iterative algebraic reconstruction method. Because the key operational steps are spatial forward- and back-projections as well as scalar products in image space, tomographic recovery of TACs is realized computationally efficient. In a series of simulation experiments this approach is capable of estimating TACs more accurately than alternative time-resolved reconstruction methods based on dynamic interpolation within FBP.

The amount of relevant information contained in the non-simultaneously acquired projections critically depends on the acquisition mode. The pursued simulation study compares two different acquisition modes that are compatible with interventional X-ray systems. Reconstruction of contrast curves is less accurate with projections from multiple repeated forward/backward sweeps (which applies e.g. to a C-arm system of limited angular range). This is primarily due to the system's slow and temporally irregular coverage of viewing positions along the sweep range. In particular the recovery of fast contrast dynamics – occurring in the

artery – is challenging and might result in streak artifacts directed toward the system's turning points in the reconstructed image space. The amount of relevant information contained in the projection data is improved by using acquisitions based on faster and continuous 360^o rotations (corresponding to a closed gantry system) that cover the scan range's viewing positions in a temporally regular way. Such mode yields an improved accuracy of estimated TACs and a reduction of image artefacts.

A second factor that influences performance of the proposed method refers to the properties of the temporal model in terms of flexibility and appropriateness. For an ideal noise-free scenario the study demonstrates that the larger the number of temporal basis functions, the lower the redundancy among them, and the better they potentially match the true contrast curves the more accurate are the estimated TACs. Here, the PCA-based model transformation is suitable to generate small models with optimal flexibility.

This situation changes when the acquired projections are affected by noise and regularization becomes crucial. Here, the level of effective noise suppression is determined by a complex interrelation between the number of iteration cycles and the constraints imposed by the predefined set of temporal basis functions. It turns out that very flexible temporal models, e.g. those obtained by PCA-based transformation, typically perform worse than more constrained models because of differences in noise sensitivity. In addition, simulation results reveal that for a fixed set of temporal basis functions the optimal number of iteration cycles – concerning regularization of noise – varies over different regions and is related to the local dynamic contrast-to-noise ratio: for instance, accurate estimation of contrast curves in vessel regions requires more iteration cycles than in tissue. In this study the number of iteration cycles is manually fixed according to experience. However, future investigations should automatically determine the optimal iteration stopping point; optimal early-stopping is still an active area of research in iterative image reconstruction [14]. In an optimal automated configuration, TACs at different spatial locations will be obtained after a different number of iteration steps. This might result in a more accurate estimation of contrast curves within vessels, which is typically required for the generation of quantitative physiological perfusion maps.

Chapter Three

Ray-based approach for skeletal muscle perfusion measurement on interventional x-ray systems

No great discovery was ever made without a bold guess.

— Isaac Newton (1642-1726)

Abstract — Periprocedural assessment of tissue perfusion by imaging methods could improve outcome control during treatment of peripheral vascular disease. Currently, endovascular revascularization treatments are assessed by planar angiography which only allows for qualitative inspection of blood flow in vessels. In this chapter, we present a method for periprocedural perfusion estimation based on temporal attenuation curves in skeletal muscles estimated using angiographic C-arm systems.

The proposed method tackles the loss of spatial depth information, which occurs in conventional angiography, by combining the acquired angiograms with two additional C-arm rotational scans. The area subject to contrast propagation is segmented from the two images, that are tomographically reconstructed from the rotational scans, and is then used to estimate the spatially averaged contrast attenuation along the X-ray directions. A segmentation method, which is tailored to the estimation procedure, is applied to limit inaccuracies in the estimation. The accuracy of the method in estimating tissue blood flow in muscular tissue is evaluated in a simulation study using experimental data from CT perfusion acquisitions.

Results show that perfusion estimation accuracy is limited, owing to spatial inhomogeneity of contrast in muscular tissue and to the presence of vessels along the X-ray directions. Nonetheless, the spatially averaged perfusion quantification allows for improved visual differentiation of normal and hypoperfused tissue in comparison with conventional planar angiography.

Periprocedural assessment of muscle perfusion through digital subtraction angiography is challenging due to lack of longitudinal information in the planar projections. By including additional 3D information on the anatomy, retrieved from rotational scans, the visualization and differentiation of normal and hypoperfused areas can be improved.

Based upon: M. Giordano, E. P. A. Vonken, M. Bertram, W. P. T. M. Mali, M. A. Viergever and C. Neukirchen, "Ray-Based Approach to Skeletal Muscle Perfusion Measurement on Interventional X-ray Systems", *Medical Physics*, vol.39, no.3, pp. 1190-1206, 2012.

3.1 Introduction

Peripheral arterial disease (PAD) [48] caused by obstruction of arterial blood flow, generally leads to tissue hypoperfusion and may cause gangrene in the later stages of the disease. Treatments of PAD, in recent years have shifted from open surgery toward percutaneous endovascularization procedures that include balloon angioplasty [67] and stenting. Outcome control of these procedures, which has the aim to assess the effective restoration of blood supply to the tissue, is currently limited to visual assessment of blood flow through the re-canalized vessels using X-ray angiography. For more effective treatment outcome control, quantitative assessment of tissue perfusion by enhanced imaging methods is highly desirable [113]. This can be achieved by MRI and CT skeletal muscle perfusion imaging which measure the blood flow at the micro vascular level [54].

CT perfusion (CTP) studies are based on contrast administration into the vasculature followed by continuous and fast rotations ($\sim$ 1-2 rot/s) of the CT gantry to capture the temporal evolution of contrast concentration in tissue. A temporal sequence of 3D tomographically reconstructed images is produced. The temporal evolution of contrast concentration in a voxel of the sequence is displayed as a temporal attenuation curve (TAC). However, CTP is not yet available in an interventional environment and thus requires the patient to be moved to the CT room which complicates the workflow.

C-arm X-ray imaging systems allow easy patient access to the surgeon during treatment. While in the past they have been used exclusively for planar imaging, in recent years they have been enabled with 3D imaging functionalities [36]. With the introduction of the flat detector technology and the continuous improvement of the contrast resolution [16, 55, 121, 125] CT-like soft tissue imaging has been made possible opening the possibility to enable perfusion imaging directly in the angioroom [1, 35].

The X-ray source and the detector of the C-arm however, have limited rotational capabilities in terms of speed and movement range: in a typical short scan acquisition, the C-arm performs a single sweep over 200° in 5-20s. Because of the slower rotation speed, the repeated tomographic reconstruction approach as used in diagnostic CTP tends to lose accuracy [108] and can not be applied for fully spatially resolved perfusion imaging. In Chapter 2, we investigated an acquisition protocol based on several forward/backward semi-rotations of the C-arm (multi-sweep) utilizing a temporal model to estimate the temporal evolution of contrast from the acquired dynamic projections. However, due to the slow rotational speed, the recovery of fast dynamics as the artery, which is crucial for accurate perfusion estimation, is challenging and might result in strong artifacts. In order to increase the temporal sampling of projections, Ganguly *et al.* [25] proposed to acquire several multi-sweep scans with multiple injections using different start times with respect to contrast injection and to interleave the acquired data. Their reconstruction method [19] is an adaptation of the method proposed by Montes *et al.* [85] to the C-arm. Results on animal data [19, 26] showed good agreement with CTP, with a slight tendency to underestimate the arterial TACs which caused overestimation of the perfusion.

In this chapter we present an approach which exploits the fast 2D acquisition frame rates of the C-arm in angiographic mode. When using the C-arm in angiographic mode, the X-ray source and detector remain at a fixed position during the dynamic acquisition of contrasted X-ray projections. These projections provide 2D blood flow information from one direction which may nevertheless provide valuable information in peripherals. In fact, perfusion in peripherals occurs mainly in muscle blocks [24] (see soleus, tibialis and gastrocnemius in Fig. 3.1). MR

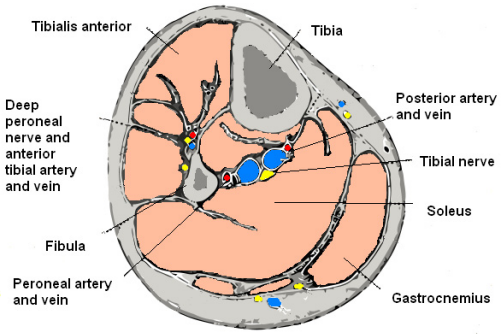

Figure 3.1. Cross-section of the lower leg and locations of the muscle blocks.

perfusion studies reported some degree of homogeneity within the single muscle blocks [113]. By assuming that contrast propagation is spatially homogeneous along the X-ray direction, a hypothesis which will be investigated in this chapter, the average contrast attenuation across the object from a single direction can be used for perfusion quantification.

Since all depth information is lost when projections are acquired at a fixed position [8], methods to make the 2D measurements quantitative need to be developed. Taguchi *et al.* [110] proposed to estimate region specific perfusion in the liver from projection angiograms by assuming homogeneous contrast uptake in each region. The region-related TACs are calculated by matching the estimated projections with the measured ones in a least squares sense. However, each region is assumed perfectly defined (e.g, from a pre-operative CT scan) and the accuracy in real cases has not yet been evaluated.

Schmitt *et al.* [103] proposed a method to determine the contrast agent propagation in vessels. First a 3D-RA acquisition is performed to reconstruct the morphology of the vessel in 3D and then angiography is acquired from a fixed view. The bolus propagation in the 3D vessel is obtained by mapping the gray values (i.e X-ray intensity) from the projections to the vessel tree. However the gray values in the 2D projections do not provide quantitative contrast concentration therefore the method is not quantitative.

Similarly to the method presented by Schmitt *et al.*, we propose to combine the temporal information acquired by angiography with the spatial information obtained by two 3D rotational scans to obtain quantitative perfusion. The spatial average of contrast density along the X-ray directions is estimated by normalizing the line integrals from the angiograms with the length of contrast material along the X-ray directions. The length of contrast material is determined by segmentation of the perfused territories in the reconstructed images. The resulting quantitative average perfusion can support the surgeon in decision making process during revascularization procedures.

Qualitative results with the proposed method were presented in [28]. In this chapter we introduce an additional procedure to estimate arterial contrast for perfusion quantification and carry out a quantitative evaluation of the accuracy on data simulated from CTP acquisitions.

3.2 Methods

The proposed method aims at measuring quantitative perfusion based on TACs in peripheral skeletal muscles. The TACs are derived from angiograms acquired at a fixed angular viewing position. The temporal information about the perfusion process, acquired via angiography, is combined with information on the spatial distribution of contrast, retrieved from two additional anatomical scans. The method is based on two steps which are depicted in the two large blocks of Fig. 3.2:

1. The anatomy is reconstructed via two rotational scans with injected contrast in semi-steady-state and without contrast, respectively. Subsequently, the organ area subject to blood perfusion is identified by 3D segmentation (upper block Fig. 3.2).

2. Temporal information is acquired through angiography, whereupon the averaged contrast induced attenuation is estimated by normalization (i.e., averaging) of the measured line integrals by the perfused organ extent (lower block Fig. 3.2).

The method provides a temporal sequence of 2D angiograms from a fixed viewing position which show contrast attenuation spatially averaged along the direction of the X-rays. From the angiograms tissue TACs and arterial TACs are derived and successively used to quantify the perfusion. The acquisition angle of the angiography is chosen during the procedure by the surgeon according to the vascular anatomy (e.g. minimizing overlap between tissue and bones).

3.2.1 Dynamic contrast estimation

Typically, in perfusion analysis, the temporal variation of contrast concentration in tissue and vessels, resulting from bolus injection into the vasculature, is analyzed. In X-ray imaging, the temporal evolution of contrast concentration causes a change in the X-ray attenuation of the object. Bones, air and other structures do not absorb contrast and thus exhibit a static attenuation over time. Therefore the attenuation in a dynamically contrasted object at a spatial location $\boldsymbol{x}$ consists of a static contribution $\mu_0(\boldsymbol{x})$ plus the contribution due to the dynamic propagation of contrast $\mu_d(\boldsymbol{x}, t)$

$$\mu(\boldsymbol{x}, t) = \mu_0(\boldsymbol{x}) + \mu_d(\boldsymbol{x}, t) \tag{3.1}$$

where t is the time variable.

The geometry of the projection acquisition is depicted in Fig. 3.3 and is described by the X-ray source position $\boldsymbol{\alpha}$ and by the detector pixel positions. For a given detector pixel at $\mathbf{v}$, where $\mathbf{v}$ is the position in the detector coordinate system (w, u), a ray path from the source to the detector pixel is described by the unit vector $\boldsymbol{\beta}(\mathbf{v}, \boldsymbol{\alpha})$. The location of a point on the ray path is indicated by $\boldsymbol{x}(r) = \boldsymbol{\alpha} + r\boldsymbol{\beta}$ with r varying between 0 and the source-to-detector pixel distance.

The proposed TAC estimation method is based on: a segmentation of the contrast enhanced tissue S, a segmentation of the artery A and an angiographic scan. The angiography consists of a set of line integrals [61] obtained from dynamic X-ray projections with the background (i.e. DSA mask [8]) removed in order to quantify pure contrast attenuation (step 4 in Fig. 3.2). The TAC estimation is performed separately for the tissue and for the artery.

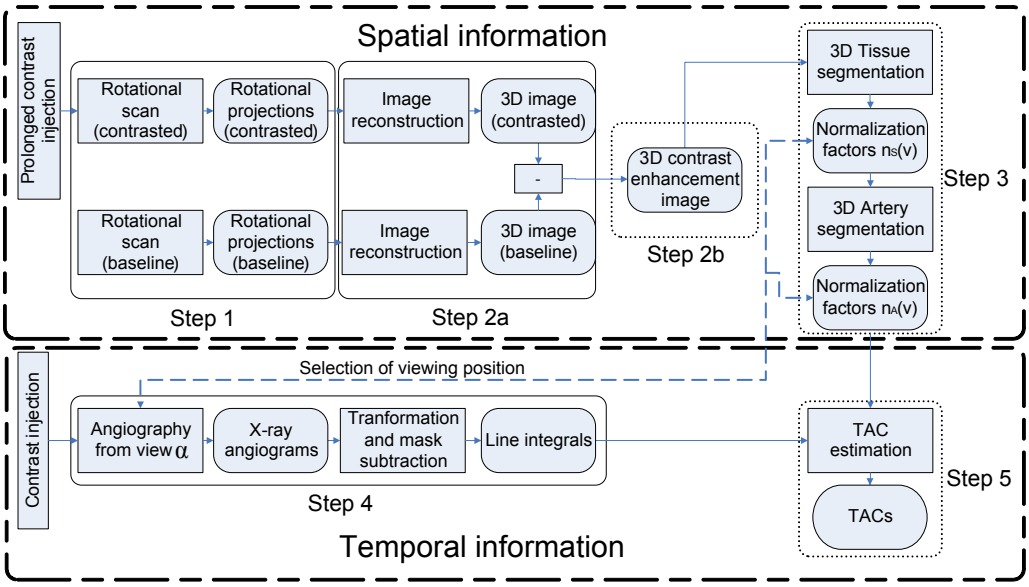

Figure 3.2. Workflow of the proposed method to estimate TACs in tissue. The upper block depicts the steps involved in the processing of the spatial information: rotational acquisition (Step 1); reconstruction of the 3D images and subtraction of the baseline image (Step 2a); contrast enhancement image (Step 2b); segmentation of tissue and artery and calculation of the normalization factors in tissue and artery (Step 3). The lower block depicts the steps involved in the processing of temporal information: angiography, transformation to line integrals and subtraction of the DSA mask (Step 4); estimation of the TACs through normalization of the line integrals (Step 5).

3.2.1.1 Tissue contrast estimation

The dynamic contrast estimation in tissue is based on a segmentation of the perfused tissue S and on the dynamic line integrals $\ell_d(\mathbf{v}, t)$ through the contrasted object which can be expressed as follows:

$$\ell_d(\mathbf{v}, t) = \int_{R \in S} \mu_d(\boldsymbol{x}(r), t) dr + \int_{R \notin S} \mu_d(\boldsymbol{x}(r), t) dr = \ell_d^{R \in S}(\mathbf{v}, t) + \ell_d^{R \notin S}(\mathbf{v}, t) \tag{3.2}$$

The terms $\ell_d^{R \in S}(\mathbf{v}, t)$ and $\ell_d^{R \notin S}(\mathbf{v}, t)$ stand for the line integral contributions inside and outside the segmented area S, respectively. R represents the range of r.

The dynamic contrast estimation in tissue is based on the following assumptions:

1. For each time point the contrast attenuation along all rays within the segmented area S is constant:

$$\int_{R \in S} \mu_d(\boldsymbol{x}(r), t) dr \simeq \mu_d(\mathbf{v}, t) \cdot n_S(\mathbf{v}) \quad \forall \mathbf{v} \tag{3.3}$$

$n_S(\mathbf{v}) = \int_{R \in S} dr$ is the length of the segmented area S along the ray determined by $\mathbf{v}$ (see Fig. 3.3) [51]. The segmented tissue area S is assumed perfused. $n_S(\mathbf{v})$ will be referred to as normalization factor. $\mu_d(\mathbf{v}, t)$ is the assumed attenuation along the ray $\mathbf{v}$ inside S.

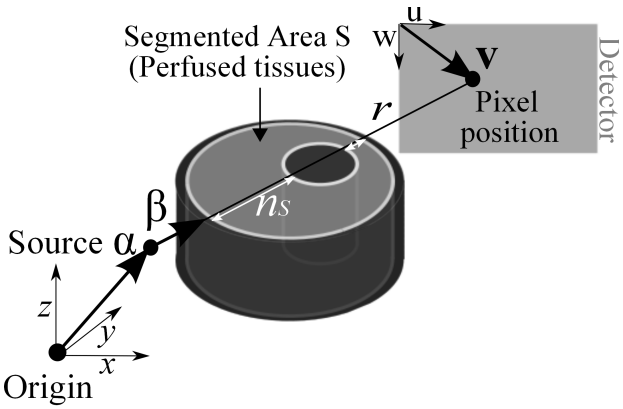

Figure 3.3. Sketch of the acquisition geometry and related notation. The semi-transparent cylinder represents a cross-sectional slab of the leg. The perfused tissue area S is depicted in grey. The white contours represent the borders of the segmented tissue area S. Dark grey areas depict the non-perfused areas (bone marrow and skin). The black line across the object is the ray path determined by the detector pixel position $\mathbf{v}$ (expressed in the detector coordinate system (w, u)) and the source position $\boldsymbol{\alpha}$ (expressed in the global coordinate system (x, y, z)). $\boldsymbol{\beta}$ indicates the ray direction. r is the position along the ray path. The white arrows depict the normalization factor $n_S(\mathbf{v})$ given by the length of the segmented area S along the ray path.

2. The line integral is dominated by the contribution inside the segmented area S

$$\ell_d^{R\in S}(\mathbf{v}, t) \gg \ell_d^{R\notin S}(\mathbf{v}, t) \tag{3.4}$$

By applying the above assumptions to the definition of line integral (Eq. 3.2) an estimate of the dynamic attenuation in tissue based on the measured line integrals is obtained (Step 5 in Fig. 3.2):

$$\hat{\mu}_d(\mathbf{v}, t) \simeq \frac{\ell_d(\mathbf{v}, t)}{n_S(\mathbf{v})} \tag{3.5}$$

$\hat{\mu}_d(\mathbf{v}, t)$ is the estimated average contrast attenuation in tissue for the ray $\mathbf{v}$. Since the acquired line integrals $\ell_d(\mathbf{v}, t)$ are known, the main parameters needed for the estimation are the normalization factors which are derived from the segmentation S.

3.2.1.2 Artery contrast estimation

The dynamic contrast estimation in the artery is based on a 3D segmentation of the artery A and on the dynamic line integrals $\ell_d(\mathbf{v}, t)$ through the artery. Let us define $V_{2D(Art)}$ as the 2D region on the detector plane corresponding to the rays that cross the artery (see Fig.3.4). The dynamic line integrals within $V_{2D(Art)}$ can be expressed, similarly as in Eq. 3.2, as the sum of the line integral contributions inside and outside the 3D segmented artery A: $\ell_d(\mathbf{v}, t) = \ell_d^{R\in A}(\mathbf{v}, t) + \ell_d^{R\notin A}(\mathbf{v}, t) \quad \forall \mathbf{v} \in V_{2D(Art)}$. The dynamic contrast estimation in the artery is based on the following assumptions:

1. For each time point the contrast attenuation along the rays in the artery A is constant:

$$\int_{R\in A} \mu_d(\boldsymbol{x}(r), t) dr \simeq \mu_d(\mathbf{v}, t) \cdot n_A(\mathbf{v}) \qquad \forall \mathbf{v} \in V_{2D(Art)} \tag{3.6}$$

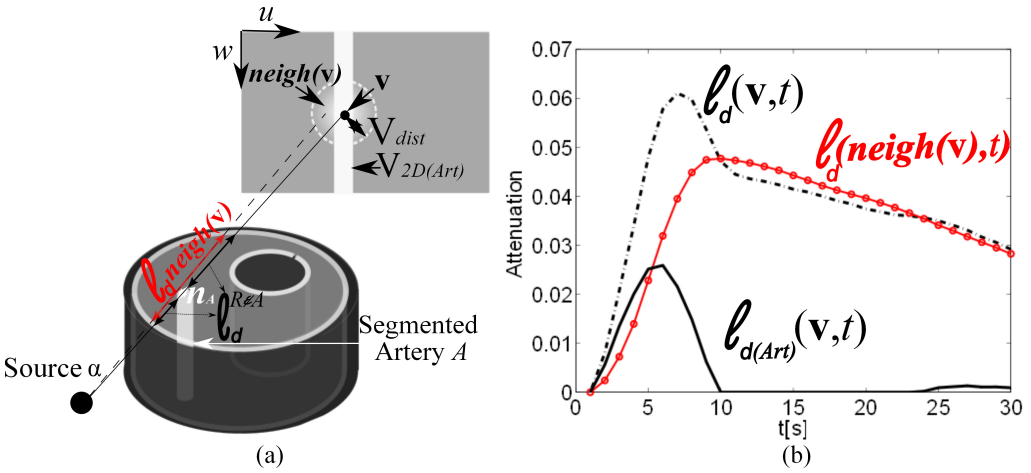

Figure 3.4. (a) A cross sectional slab of the leg illustrating the geometry for the estimation of arterial TACs. The dark grey and light grey areas depict contrasted tissue and non-contrasted tissue, respectively. The white cylinder depicts the 3D segmented artery A. Its projection on the detector plane is indicated by the white rectangular area $V_{2D(Art)}$. The solid line from the source α to the detector position $\mathbf{v}$ depicts a ray through the artery. n_A is the corresponding normalization factor given by the length of the artery along the ray path. The blurred area $neigh(\mathbf{v})$ on the detector depicts the neighborhood of $\mathbf{v}$. $\ell_d^{R\notin A}$ is the line integral contribution outside the segmented artery A and is indicated by the two black arrows. According to Eq.3.7 $\ell_d^{R\notin A}$ is approximated to the average line integral $\ell_d(neigh(\mathbf{v}))$ in the neighborhood $neigh(\mathbf{v})$. The average line integral $\ell_d(neigh(\mathbf{v}))$ is depicted for simplicity by a single red arrow. (b) The curves represent: the dynamic line integral through the artery $\ell_d(\mathbf{v},t)$ (dashed black curve), the average of the line integral in the neighborhood $\ell_d(neigh(\mathbf{v}),t)$ (red curve with circles) and the line integral contribution due to the arterial contrast $\ell_{d(Art)} = \ell_d(\mathbf{v},t) - \ell_d(neigh(\mathbf{v}),t)$ (solid black curve).

$n_A(\mathbf{v}) = \int_{R\in A} dr$ is the length of the segmented artery A (see Fig. 3.3) along the ray $\mathbf{v}$ (artery normalization factor).

2. The line integral contribution outside the artery can be approximated with the average of line integrals in the neighborhood:

$$\ell_d^{R\notin A}(\mathbf{v},t) \simeq \ell_d(neigh(\mathbf{v}),(t)) \forall \mathbf{v} \in V_{2D(Art)} \tag{3.7}$$

$\ell_d(neigh(\mathbf{v}),t)$ is the average of the line integrals in the 2D neighborhood of the artery (Fig.3.4(a)). The 2D neighborhood is defined as: $neigh(\mathbf{v}) : \forall \mathbf{v}' | \mathbf{v}' \notin V_{2D(Art)} \bigcap ||\mathbf{v} - \mathbf{v}'|| < V_{dist}$, where V_{dist} is a user defined distance (see Fig.3.4). The approximation in Eq. 3.7 is illustrated in Fig.3.4(a).

By applying the assumptions in Eq. 3.6 and Eq. 3.7 to the definition of line integrals for the artery, an estimation of the dynamic attenuation in the artery is obtained:

$$\hat{\mu}_{d(Art)}(\mathbf{v},t) \simeq \frac{\ell_d(\mathbf{v},t) - \ell_d(neigh(\mathbf{v}),t)}{n_A(\mathbf{v})} = \frac{\ell_{d(Art)}(\mathbf{v},t)}{n_A(\mathbf{v})} \tag{3.8}$$

$\ell_{d(Art)}$ is the line integral due to pure contrast attenuation in the artery (see curve in Fig. 3.4(b)). The estimation procedure in Eq.3.8 is mostly reliable within the time interval where venous flows is negligible. In fact, during the venous phase the contrast flowing in neighboring veins may cause erroneous estimation of arterial contrast. In addition, when the contrast in the neighborhood is higher than the arterial contrast (see Eq. 3.8), the estimated arterial contrast becomes negative. To limit this last issue, negative values in the arterial TACs $\hat{\mu}_{d(Art)}$ are clipped to zero.

As the estimated arterial input function is an approximation of the true, the slope method [80], which does not require the complete knowledge of the arterial input function but only its peak enhancement, is used for the calculation of the perfusion parameters.

The segmentation of tissue (S) and artery (A) will be detailed in Sec. 3.2.2 and 3.2.3, respectively.

3.2.2 Tissue Segmentation

The goal of the first segmentation step is to identify the perfused tissue area S in the organ of interest. The segmentation is carried out on a volumetric contrast distribution which is tomographically reconstructed after acquisition of two rotational scans. Rotational acquisitions consist of a set of rotational projections acquired while sweeping the C-arm around the object. Three dimensional images are reconstructed from the measured projections using the Feldkamp Davis Kress (FDK) reconstruction algorithm [17]. In the proposed algorithm two rotational scans are performed (Step 1 in Fig. 3.2): a baseline acquisition without contrast and an acquisition during injection of contrast. To ensure a semi-steady state distribution of contrast in the entire volume during the contrasted acquisition, a prolonged contrast injection has to be applied as described in [1] and [124]. In order to obtain the volumetric contrast distribution, the baseline image is subtracted from the contrasted image (Step 2a in Fig. 3.2) yielding a contrast enhancement image μ_{enh}. Air voxels in μ_{enh} are identified by applying a threshold (-950HU) to the baseline image and are subsequently discarded in μ_{enh}.

Two methods to segment the perfused area in the contrast enhancement image $\mu_{enh}(\boldsymbol{x})$ were investigated:

- Thresholding (S_{Thres}): this method estimates a segmented area $S_{Thres} \equiv \{\forall \boldsymbol{x} | T_{Low} < \mu_{enh}(\boldsymbol{x}) < T_{High}\}$ where T_{Low} and T_{High} define the range of attenuation in μ_{enh} corresponding to the perfused tissue. The thresholds T_{Low} and T_{High} are found by fitting a Gaussian mixture model [6] (GMM) to the histogram of μ_{enh}. The EM algorithm [119] is used to find the parameters of the Gaussians. The GMM aims at modeling the histogram of four different tissue types: non-perfused tissue (bone marrow, skin and fat), perfused tissue (mainly muscle), moderately contrasted vessels (veins and small arteries) and highly contrasted vessels (arteries). The thresholds T_{Low} and T_{High} are found by selecting the intersections of the perfused tissue gaussian distribution with the neighboring distributions.

- Minimum inconsistency (S_{MI}): this segmentation method is tailored to the estimation approach (Eq. 3.5). The method is based on the contrast enhancement image μ_{enh} and on the set of line integrals ℓ_{enh} computed through μ_{enh}. The average contrast attenuation along each ray is computed similarly as for the estimation of the TACs (Eq. 3.5): a segmented area S is assumed and the line integrals are normalized: $\ell_{enh}(\mathbf{v})/n_S(\mathbf{v})$.

The mean squared error between the estimated average contrast attenuation and the corresponding voxel values in μ_{enh} inside S is measured along the ray $\mathbf{v}$ as follows:

$$E^2_{enh}(\mathbf{v}, S) = \int_{R \in S} \left[\mu_{enh}(\boldsymbol{x}) - \frac{\ell_{enh}(\mathbf{v})}{n_S(\mathbf{v})} \right]^2 dr \tag{3.9}$$

The segmentation S_{MI} that minimizes E_{enh} for each ray $\mathbf{v}$ is then defined as:

$$S_{MI} \equiv \arg\min_S \{E_{enh}(\mathbf{v}, S)\} \qquad \forall \mathbf{v} \tag{3.10}$$

The minimization of Eq. 3.9 is carried out by means of simulated annealing [63] that allows finding global minima and avoids halting at local minima. The parameters of the annealing schedule are selected empirically by finding a compromise between accuracy of the result and speed of convergence. The initial state (i.e. initial segmentation) was set randomly.

3.2.3 Artery segmentation

The goal of the second segmentation step is to estimate the 3D spatial location of the artery A from the reconstructed contrast enhancement image μ_{enh}. Two methods are applied for the segmentation of the artery A:

- Thresholding (A_{Thres}): The segmentation is based on the 3D tissue segmentation S_{Thres} obtained by applying thresholding as described in Sec.3.2.2. From S_{Thres}, the 3D region corresponding to the arteries is selected. From this region, the feeding artery is selected manually while all other arteries are discarded.

- Minimum inconsistency (A_{MI}): Similarly to the tissue segmentation S_{MI} (see Sec.3.2.2) this segmentation is tailored to the estimation approach (Eq.3.8) and is based on the line integrals ℓ_{enh} computed through the contrast enhancement image μ_{enh}. The average contrast attenuation in the artery at the steady state is estimated by normalization with n_A: $(\ell_{enh}(\mathbf{v}) - \ell_{enh}(neigh(\mathbf{v})))/n_A$ ($neigh(\mathbf{v})$ is the neighborhood of $\mathbf{v}$ as defined in Sec.3.2.1.2) and is compared in a least squares sense to the corresponding voxel values of μ_{enh} in A:

$$E^2_{enh(Art)}(\mathbf{v}, A) = \int_{R \in A} \left[\mu_{enh}(\boldsymbol{x}) - \frac{\ell_{enh}(\mathbf{v}) - \ell_{enh}(neigh(\mathbf{v}))}{n_A(\mathbf{v})} \right]^2 dr \tag{3.11}$$

The segmentation A that minimizes $E_{enh(Art)}$ for all rays within $V_{2D(Art)}$ is defined as:

$$A_{MI} \equiv \arg\min_A \{E_{enh(Art)}(\mathbf{v}, A)\} \qquad \forall \mathbf{v} \in V_{2D(Art)} \tag{3.12}$$

Minimization in Eq.3.12 is carried out by simulated annealing as done in Sec.3.2.2.

Table 3.1. CTP data parameters

	CTP Case 1	CTP Case 2
Sequence length	40s	40s
Image rate	1 image/s	1 image/s
Image size (mm)	$(400 \times 400 \times 60) mm^3$	$(350 \times 350 \times 40)$ mm^3
Grid size	$(512 \times 512 \times 12)$voxels	$(512 \times 512 \times 64)$ voxels
Injection volume	15 ml (300 mg I/ml)	10 ml (300 mg I/ml)
Injection rate	1.5 ml/s	3 ml/s

Table 3.2. C-arm Simulated Acquisition Geometry

Detector grid	512×396 pixels
Detector surface	383×296 mm^2
Distance source detector	1190 mm
Distance source rot. axis	787 mm
Number of rotational projections	400/200°
Projection frame rate (angiography)	1 fps

3.3 Experiments

The TAC estimation accuracy is evaluated in a simulation study. CTP acquisitions of the lower calf (Sec.3.3.1.1), showing temporal contrast uptake, are used as input data for the simulations. The C-arm acquisitions, i.e. angiography and rotational scans, are simulated using a software environment as described in Sec. 3.3.1.2.

3.3.1 Simulations

3.3.1.1 Data preparation

CTP acquisitions consist of temporal sequences of 3D images showing the anatomy and the temporal contrast propagation. Two different patient cases were acquired, after contrast injection, on a 64-slice CT scanner. Intra-arterial injection of iodine solution was applied which yields higher contrast enhancement in comparison with intravenous injection. The contrast injection was administrated in the proximal superficial femoral artery. The image sequence specifications are listed in Tab. 3.1. In order to limit fluctuations in the TACs due to patient motion between consecutive time frames [79], the CTP sequences were registered using elastic registration [52]. Two patients were analyzed: one healthy patient (Case 1), and a patient affected by PAD (Case 2) who showed hypoperfusion in the gastrocnemius (Fig. 3.5(d)). Axial slices showing the maximum absolute attenuation of the CTP sequences are given in Fig. 3.5(a) and Fig. 3.5(d). For presentation of TACs, volumes of interest (VOIs) consisting of $3 \times 3 \times 3$ voxels were selected in the artery, tissue, hypoperfused tissue and veins (see small squares in Fig. 3.5(a) and Fig. 3.5(d)) in the central slice. The spatial average of the TACs inside the selected VOIs are shown in Fig. 3.5(b)-(c) and Fig. 3.5(e)-(f). The spatial average in the arterial VOI was used as arterial input function $\mu_{d(Art)}$ (Fig. 3.5(b)(e)) to compute the 3D perfusion map. The peripheral blood flow pbf was derived by applying the slope method [80]: $pbf(\mathbf{v}) = [\frac{d\mu_d(\mathbf{V},t)}{dt}]_{max} / [\mu_{d(Art)}(\mathbf{v},t)]_{max}$. The condition of no venous outflow before the time of maximum derivative in tissue TACs is well fulfilled in the CTP data (see Fig.3.5). For the

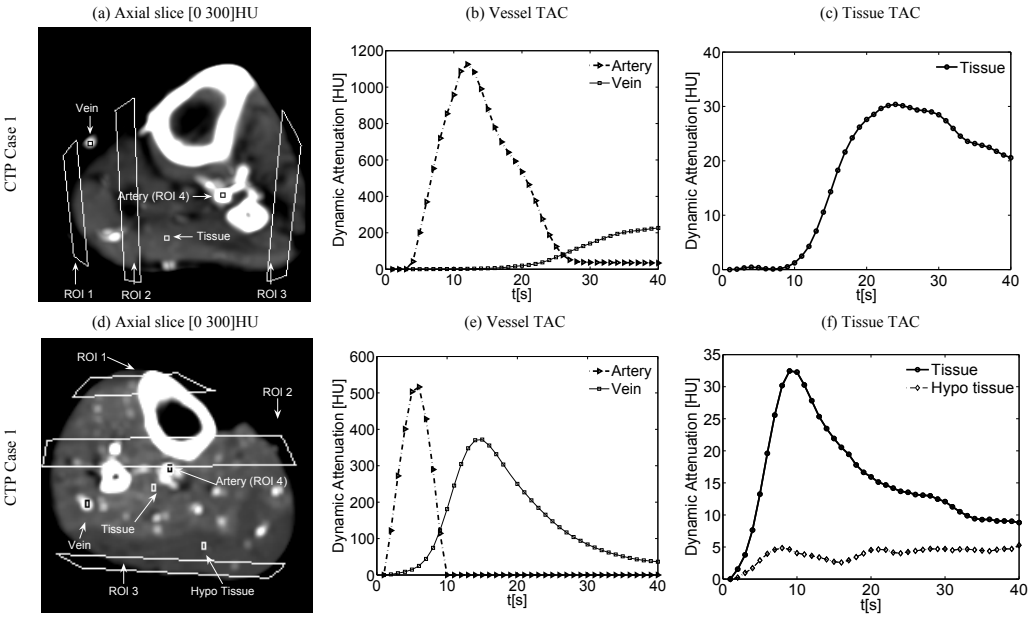

Figure 3.5. CTP sequence of a healthy patient (Case 1) (top row) and a patient affected by PAD (Case 2) (bottom row). (a)(d) Axial images (central slices) showing the maximum absolute attenuation and the location of selected VOIs (small boxes). The large rectangular shaped region depict the ROI used for the evaluation. The artery VOIs is also used for evaluation of the artery (ROI 4) and is the location of the arterial input function. (b)(e) TACs in vessels for the VOIs shown in (a)(d). (c)(f) TACs in tissue for the VOIs shown in (a)(d): the TAC in the hypoperfused tissue (f) exhibits reduced contrast attenuation in comparison with the TAC in normal tissue.

computation of perfusion, the passage of contrast agent from vascular to the interstitial space was assumed negligible [113].

The simulations of the C-arm rotational scans were based on phantoms created from the CTP sequence: to simulate the contrasted scan (i.e. the semi-steady state distribution of contrast), the temporal maximum of individual voxel attenuations in the CTP sequence was calculated; for the non contrasted scan, the first volume of the CTP sequence was selected. The C-arm rotational acquisitions were simulated by generating projections of these two phantoms as described in Sec. 3.3.1.2.

3.3.1.2 Simulation of C-arm acquisitions

As first step the angiographic acquisition was simulated using the complete CTP sequence. For each volume of the CTP sequence, a cone beam forward projection was generated producing a 2D temporal sequence of angiograms. Subsequently, the first frame of the sequence was subtracted from all the other frames to obtain the line integrals $\ell_d(\mathbf{v}, t)$. The C-arm acquisition geometry parameters are shown in Tab. 6.3. The acquisition angle $\boldsymbol{\alpha}$ was selected manually. Poisson noise was added to the projections ($5.5 \cdot 10^6 photons/mm^2$) equivalent to a X-ray tube setting of $3.25 mAs/frame$.

The frame rate used to simulate the angiography corresponds to that of the CTP data (i.e. 1 fps). Higher frame rates were not investigated as they would require time interpolation of the available data which would not add new information to the perfusion signal. Concerning timing requirements for sampling of fast dynamics, like in the artery, in [25] it was shown that even for intraarterial contrast injections, most of the spectral energy of the perfusion signal is contained between 0-0.15Hz. Therefore 1 fps can be assumed sufficient for accurate samplings. As for the benefit of using higher frame rates on image quality, this depends on the dose delivered to the patient. For a given dose, the signal-to-noise ratio obtained at higher frame rates by using data averaging is comparable to that obtained at lower frame rates [15].

The second step consisted of the simulation of the rotational C-arm acquisitions. For each of the two phantoms created from the CTP sequence (Sec. 3.3.1.1), a set of 400 cone beam projections was generated from equiangular views over a circular arc of 200°. Poisson noise was added to the projections ($2.1 \cdot 10^6$ photons/mm^2) corresponding to a total of 500 mAs for each rotational acquisition. The phantoms were assumed fixed, i.e. no motion during the acquisition was simulated. A short scan FDK algorithm [36] was used to reconstruct 3D images from the simulated projections. Noise in the rotational projections propagates through the reconstruction process to the reconstructed images and may influence the results of the segmentation. Therefore, a spatial low pass filter has been applied to the reconstructed images, viz. a 3D gaussian kernel with standard deviation $(5 \times 5 \times 5)$mm^3 and $(2 \times 2 \times 2)$mm^3 for Case 1 and Case 2, respectively.

The simulated forward projections were generated from the voxelized volumes by analytical forward projection utilizing the Philips-proprietary software RADONIS (Philips Research Hamburg) which allows to define the tube and the detector positions in order to match the real x-ray system configuration. Mono-energetic x-rays were assumed, therefore beam hardening was not modeled. Focal spot variation and limited detection efficiency were not simulated.

The object was assumed in the same position and orientation during the simulated rotational acquisitions and the simulated angiography. If object motion occurs between the rotational scan and the angiography a 3D/2D registration procedure [115, 116] must be applied.

As final steps, image segmentation was applied to the reconstructed images to obtain the normalization factors $n_S(\mathbf{v})$ and $n_A(\mathbf{v})$. Next, the TACs in tissue and in the artery were estimated according to Eq. 3.5 and Eq. 3.8 respectively. From the estimated TACs, the maps showing the 2D estimated peripheral blood flow $\widehat{pbf}(\mathbf{v})$ were derived by the slope method. The arterial input function was determined taking the spatial average of the 2D TACs over the arterial 2D ROI. This 2D ROI was obtained by projection of the 3D arterial VOI selected in the CTP data (Sec.3.3.1.1).

3.3.2 Evaluation

The accuracy of the proposed method is typically affected by two main sources of error: i) spatial inhomogeneity of the contrast attenuation along the ray paths ii) residual contrast attenuation outside the segmented area S (Fig. 3.6). These are influenced by the choice of the segmented area S (see segment in Fig. 3.6) and A. In the first part of the evaluation (Sec. 3.3.2.1), the estimation accuracy and the sources of inaccuracy are analyzed for a reference segmentation. In the second part (Sec. 3.3.2.2), the influence of the segmentation method on the estimation accuracy is assessed by comparing the results obtained from the two segmentation methods proposed in Sec. 3.2.2 and 3.2.3. The accuracy is assessed both on the estimated

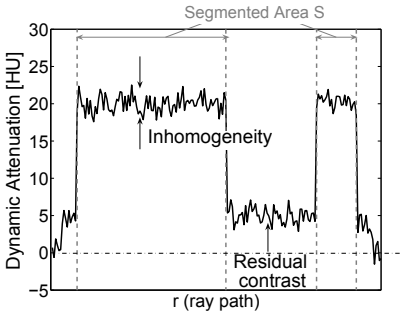

Figure 3.6. Attenuation profile (black line) at a given time point along the ray path shown in Fig. 3.3 and segmented area S (gray arrows) along the same ray path. Sources of inaccuracy for the estimation method: inhomogeneity of contrast attenuation in S along the ray path (double black arrow) and residual contrast (single black arrow).

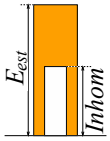

Figure 3.7. Error bar notation: the colored bar indicates the relative E_{est} (relative estimation error) and the inner white bar is the relative $Inhom$ (relative inhomogeneity) along the ray in the segmented area S. Both quantities are defined in Sec. 3.3.2.1.

TACS and on the estimated perfusion values.

3.3.2.1 Estimation accuracy

To qualitatively assess the correspondence between estimated 2D TACs and true 3D TACs, the spatial average of the estimated 2D TACs $\hat{\mu}_d^{ROI}(t) = \frac{\sum_{\mathbf{V}\in ROI}\hat{\mu}_d(\mathbf{V},t)}{|ROI|}$ (where $|ROI|$ is the number of pixels in the ROI) over a region of interest (ROI) in the projection domain, is compared to a reference 3D TAC $\bar{\mu}_{d(S)}^{ROI}(t)$. The reference $\bar{\mu}_{d(S)}^{ROI}(t)$ is calculated from the true 3D TACs by computing the spatial averaged of the 3D TACs over the ray $\mathbf{v}$ in S:

$$\bar{\mu}_{d(S)}(\mathbf{v},t) = \frac{1}{\int_{R\in S} dr}\int_{R\in S}\mu_d(\boldsymbol{x},t)dr \tag{3.13}$$

and then averaging $\bar{\mu}_{d(S)}(\mathbf{v},t)$ over the ROI: $\bar{\mu}_{d(S)}^{ROI}(t) = \frac{\sum_{\mathbf{V}\in ROI}\bar{\mu}_{d(S)}(\mathbf{V},t)}{|ROI|}$. Qualitative correspondence between the estimated 2D peripheral blood flow $\widehat{pbf}$ and the 3D blood flow pbf is assessed visually and by comparing the average of the estimated $\widehat{pbf}$ over a 2D ROI in projection domain and the average pbf over the corresponding 3D ROI.

To quantitatively assess the TACs estimation accuracy and to investigate the sources of error, a comparison between the true 3D TACs and the estimated 2D TACs is performed. For a given segmentation S, the comparison is based on the mean squared error between the true 3D TACs $\mu_d(\boldsymbol{x},t)$ and a TAC estimate $c(\boldsymbol{x},t)$ along a given ray $\mathbf{v}$ inside S. First it is useful to define the squared error at a time point t:

$$E_{\mu}^{2}(\mathbf{v}, c, S, t) = \frac{1}{\int_{R\in S} dr} \int_{R\in S} \left[\mu_d(\boldsymbol{x}, t) - c(\boldsymbol{x}, t)\right]^2 dr \tag{3.14}$$

Then the mean squared error is:

$$E^{2}(\mathbf{v}, c, S) = \frac{1}{T} \int_{T} E_{\mu}^{2}(\mathbf{v}, c, S, t) dt \tag{3.15}$$

The estimation error for the proposed method (Eq. 3.5) is as follows:

$$E_{est}^{2}(\mathbf{v}, S) = E^{2}(\mathbf{v}, \frac{\ell_d}{n_S}, S) \tag{3.16}$$

The segmentation yielding the minimum estimation error is found by solving the optimization problem:

$$S^{*} \equiv arg\min_{S}\{E_{est}(\mathbf{v}, S)\} \quad \forall \mathbf{v} \tag{3.17}$$

S^{*} will be referred to as Reference segmentation throughout the chapter, and the corresponding error $E_{est}(\mathbf{v}, S^{*})$ is the minimum estimation error which describes the accuracy limit of the proposed estimation method. Similarly, a Reference segmentation A^{*} is also defined for the artery as:

$$A^{*} \equiv arg\min_{A}\{E_{est}(\mathbf{v}, A)\} \quad \forall \mathbf{v} \in V_{2D(Art)} \tag{3.18}$$

The minimization of Eq. 3.17 and Eq. 3.18 is carried out by simulated annealing in the same fashion as in Sec. 3.2.2.

Next the potential sources of inaccuracy (Fig. 3.6) are investigated. The inhomogeneity is assessed by measuring the contrast variation inside the segmented area S along a ray path. The contrast variation is calculated as the mean squared difference between the true TACs along $\mathbf{v}$ in S and $\bar{\mu}_{d(S)}(\mathbf{v}, t)$. First the squared difference at time t is defined:

$$Inhom_{\mu}(\mathbf{v}, S, t) = E_{\mu}(\mathbf{v}, \bar{\mu}_{d(S)}, S, t) \tag{3.19}$$

Then the mean squared difference is:

$$Inhom(\mathbf{v}, S) = E(\mathbf{v}, \bar{\mu}_{d(S)}, S) \tag{3.20}$$

The relative contribution of the inhomogeneity to the estimation error is quantified as a proportion of E_{est}. The average $Inhom$ and the average E_{est} are depicted by error bars in the style used in Fig. 3.7 for the three ROIs defined in Figs. 3.11 and 3.12. The difference between the squared estimation error E_{est} and the squared $Inhom$ yields the squared error due to the residual contrast outside S: $(\frac{\ell_d^{R\notin S}}{n_S})^2 = E_{est}^2 - Inhom^2$ (note that these quantities are averaged over time). Hence the differences between E_{est} and $Inhom$ in the bars (Fig. 3.7) represent the error due to the residual contrast. Patients were subject to different injection protocols and thus may exhibit different contrast levels. Therefore $Inhom$ and E_{est} were normalized by the average of the temporal peaks of the voxels along the ray in the segmented area thus yielding relative $Inhom$ and relative E_{est}. For a comprehensive analysis, the comparison of $Inhom$ and E_{est} is performed for all segmentation methods: S^{*}, S_{MI} and S_{Thres}.

In addition, the cause of inhomogeneity in the segmented area S is investigated. The time course of the inhomogeneity averaged over a ROI $Inhom_{\mu}^{ROI}(t) = \frac{\sum_{\mathbf{v}\in ROI} Inhom_{\mu}(\mathbf{v},S,t)}{|ROI|}$ was calculated and its relation with the perfusion signal in tissue $\bar{\mu}_{d(S)}^{ROI}(t)$ was analyzed.

The analysis of the sources of inaccuracy is performed similarly for the estimation of peripheral blood flow $\widehat{pbf}$. The error definitions are given for errors between the 2D peripheral blood flow estimates and the true 3D blood flow. The error measure is defined similar as in Eq. 3.14 for single quantities (i.e. non temporal):

$$E_f^2(\mathbf{v}, c, S) = \frac{1}{\int_{R\in S} dr} \int_{R\in S} [pbf(\boldsymbol{x}) - c(\boldsymbol{x})]^2 \, dr \tag{3.21}$$

The error on the estimated blood flow is then:

$$E_{pbf}^2(\mathbf{v}, S) = E_f^2(\mathbf{v}, \widehat{pbf}, S) \tag{3.22}$$

Next, the mean blood flow along a ray is defined as:

$$\overline{pbf}(\mathbf{v}) = \frac{1}{\int_{R\in S} dr} \int_{R\in S} pbf(\boldsymbol{x}) dr \tag{3.23}$$

The inhomogeneity of the blood flow along the ray is then defined as:

$$Inhom_{pbf}(\mathbf{v}, S) = E_f(\mathbf{v}, \overline{pbf}, S) \tag{3.24}$$

Similarly to the analysis for the TACs error, the average $Inhom_{pbf}$ and the average E_{pbf} were calculated and depicted by error bars in the style used in Fig. 3.7 for the ROIs 1 2 and 3. For visualization purposes, $Inhom_{pbf}$ and E_{pbf} were normalized by the mean blood flow $\overline{pbf}(\mathbf{v})$ along the ray.

3.3.2.2 Validation of the method

The second aspect of the evaluation is focused on the systematic errors in the estimation due to spatial segmentation inaccuracies. The performance of the two proposed segmentation methods S_{MI} and S_{Thres} is compared in terms of TACs and pbf estimation error. For quantitative comparisons the average relative E_{est} and the average relative E_{pbf} over the ROIs is calculated and shown as error bars.

3.4 Results

Figure 3.8 shows axial slices of the reconstructed contrast enhancement images. In Fig. 3.9 the segmented tissue areas S and the arteries A for all segmentation methods are shown: Reference, Thresholding and Minimum inconsistency. The segmented areas S and A obtained by the Reference segmentation and the Minimum inconsistency are influenced by the choice of the angular viewing position which is indicated by the arrows in Fig. 3.9. Such dependency allows for a TAC estimation which is optimized for the chosen viewing position. This dependency can be perceived by inspecting the non segmented areas in Fig. 3.9(b) and Fig. 3.9(d) which are oriented along the ray direction. In contrast, Thresholding relies exclusively on the voxel attenuation and does not depend on the viewing position, in fact no streaks are visible in the related segmented images (Figs. 3.9(e)-(f)). The artery segmentation A also varied according

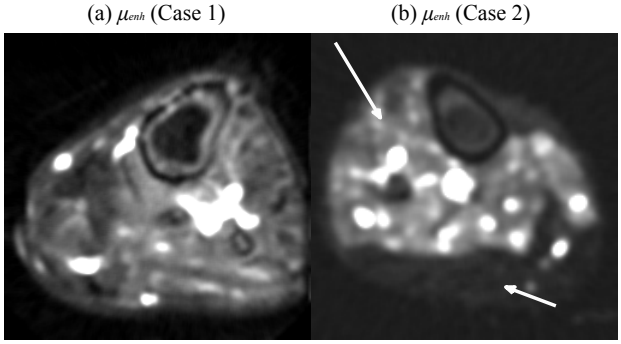

Figure 3.8. Axial slices of the reconstructed contrast enhancement images μ_{enh} (range: [0 80]HU) used as input image for the segmentation. The arrows in (b) point at a normal perfused area (upper arrow) and at the hypoperfused area (bottom arrow).

to the segmentation method applied. Increased size of the artery was experienced when using the Thresholding in comparison to the Reference segmentation.

The parametric maps displaying the estimated dynamic peak attenuation (i.e. temporal peak of $\hat{\mu}_d$) and obtained by applying the different segmentation methods (S^*, S_{MI}, S_{Thres}) are shown in Fig. 3.10. The hypoperfused area and the normal perfused area in Case 2 are visualized on the right-hand part and on the left-hand part of the peak attenuation map (see arrows in Fig. 3.10(b)). In Figs. 3.10(g)-(l) the peak intensity of the line integrals (i.e. temporal peak of $\ell_d(\mathbf{v}, t)$) and the time to peak are shown.

Figure 3.11 and Fig. 3.12 show the estimation error $E_{est}(\mathbf{v}, S)$ and the inhomogeneity $Inhom(\mathbf{v}, S)$ obtained by applying different segmentation methods. ROI positions are depicted in Fig. 3.11(a) and Fig. 3.12(a). The corresponding ROI in the 3D volume are shown in Fig. 3.5(a) and Fig. 3.5(d). The average relative errors and the average relative inhomogeneities in the 2D ROIs are shown in Fig. 3.13 for both cases.

Figure 3.14 shows the estimated 2D TAC $\hat{\mu}_d^{ROI}(t)$ and the reference 3D TAC $\bar{\mu}_{d(S)}^{ROI}(t)$ for Case 1 in the tissue ROI 2. The bias in the estimation can be attributed to the residual contrast outside the segmented area S. In the same figure, the time course of the inhomogeneity $Inhom_t(\mathbf{v}, S, t)$ is shown by the error bar. The inhomogeneity increases correspondingly with the perfusion signal onset and reaches a maximum (7-8HU) approximately at the peak of the perfusion signal ($\sim 22s$).

The estimated arterial input function averaged over the 2D ROI 4 is shown in Fig. 3.15 for different segmentations (A^*, A_{MI}, A_{Thres}). In the same figure the true arterial input function calculated from the CTP data is shown. A trend in underestimating the arterial input function was observed for almost all scenarios. Additionally, at later stages of the perfusion the estimated artery TACs for Case 2 (Fig. 3.15(b)) are overestimated which can be attributed to the contrast flowing into a neighboring vein.

Figure 3.16 depicts the peripheral blood flow maps pbf calculated for the original CTP data and the 2D estimated blood flow $\hat{pbf}$ obtained for different segmentation methods.

The locations of the 2D ROIs and the corresponding 3D ROIs in the volume are indicated by the white rectangles. Average estimated blood flow in the 2D ROIs and in the corresponding 3D ROIs are reported in Tab.3.3. The average blood flow in the 3D CTP data is computed for each segmentation method in the volume intersected by the backprojecion of the 2D ROI

Table 3.3. Average of the estimated 2D blood flow $\hat{pbf}$ and 3D blood flow pbf (plus standard deviation) in CTP data [ml/100ml/min]. The average in 3D is computed for each segmentation method in the intersection between the backprojected 2D ROI and the corresponding segmented area S.

		Case 1			Case 2		
Segmentation	Data	ROI 1	ROI 2	ROI 3	ROI 1	ROI 2	ROI 3
Reference	CTP (3D)	$15 \pm (6)$	$16 \pm (6)$	$20 \pm (7)$	$27 \pm (15)$	$88 \pm (28)$	$9 \pm (4)$
-	2D estimation	14	15	27	36	96	10
Min. inconsistency	CTP (3D)	$17 \pm (5)$	$16 \pm (6)$	$21 \pm (10)$	$26 \pm (16)$	$66 \pm (40)$	$9 \pm (5)$
-	2D estimation	15	16	26	26	80	8
Thresholding	CTP (3D)	$19 \pm (5)$	$19 \pm (8)$	$22 \pm (11)$	$27 \pm (19)$	$55 \pm (30)$	$9 \pm (7)$
-	2D estimation	43	45	51	25	104	8

(rectangle in Fig. 3.16) and the corresponding segmented area S, therefore average blood flow values in 3D differs slightly over the different segmentation methods (Tab.3.3).

For most scenarios the estimated blood flow is close to the average blood flow in the 3D volume. In general, overestimation is experienced for the thresholding segmentation (last row in Tab.3.3), which can be attributed to the underestimated arterial input function. The blood flow in Case 2 in the hypoperfused area (ROI 3) is notably lower (9 ml/100ml/min) as compared to the blood flow in healthy muscles (27 ml/100ml/min) (ROI 1). The estimated 2D blood flow maps allows to differentiate these two areas both visually (Fig. 3.16(d)) and quantitatively.

Maps showing the errors E_{pbf} between the estimated 2D blood flow and the corresponding 3D blood flow and the inhomogeneity $Inhom_{pbf}$ in S are shown in Figs.3.17 and 3.18. The average relative E_{pbf} and average relative $Inhom_{pbf}$ in the three tissue ROIs are shown in Fig. 3.19.

3.5 Discussion

Results show that accuracy of the estimated TACs in arteries and tissue is in the range of $12 - 19\%$ and $22 - 28\%$ relative error for Case 1 and 2, respectively.

For TACs in tissue, the inaccuracies are caused mainly by the inhomogeneity of the contrast attenuation: for tissue ROIs 1, 2 and 3, more than 80% of the error is due to inhomogeneities (Fig. 3.13). The temporal inhomogeneity in Fig. 3.14 shows that these inhomogeneities increase with the transit of contrast in tissue. Since the noise variance in CTP data has been shown to be almost independent of contrast concentration [84], one could postulate, in accordance with previous findings in MR perfusion [24], that the inhomogeneities are characteristic of the way contrast propagates in the muscular tissue.

This situation changes for rays intersecting also vessels (veins and small arteries) for which the estimation errors are mainly due to the residual contrast. Typically the vessels are not included in the segmented area S (Fig.3.9) thus they contribute to the residual contrast (see Fig. 3.6). The error caused by the residual contrast in vessels can be perceived from the large differences between the error $E_{est}(\mathbf{v}, S)$ and the inhomogeneity $Inhom(\mathbf{v}, S)$, which are particularly evident in Case 1 when comparing Fig. 3.11(a) with Fig. 3.11(b).

The estimation of TACs in the artery is mainly affected by inhomogeneities within the segmented artery. These inhomogeneities are attributed to the partial volume effect in the CTP data, and therefore, they are merely due to the simulation. Other inaccuracies in the arterial

TACs are due to the contrast flowing in overlapping veins which cause overestimation of the TACs at later stages (Fig.3.15). However, since the perfusion values are only based on the peak enhancement in the artery, this effect does not have an impact on the calculation of perfusion. The estimated peak attenuation is close to the original peak for almost all scenarios: arterial peaks estimated by the Reference segmentation and Minimum inconsistency segmentation were within 10% of the original peaks, while peaks estimated by Thresholding segmentation were underestimated due to the overestimated size of the segmented artery.

Consistently with the results for TACs, the accuracy of the estimated blood flow depends on the anatomical structures intersected by the rays. For rays crossing tissue (ROIs 1, 2 and 3), the accuracy is in the order of 25-50% and $40-70\%$ relative error for Case 1 and 2, respectively (Fig.3.17 and Fig.3.18). Large part of the error is due to spatial inhomogeneity of the perfusion in tissue. The measured spatial inhomogeneity levels are in line with previous MR studies on peripheral perfusion [24]. Higher perfusion errors are experienced for rays crossing vessels (veins and arteries) in comparison to rays crossing tissue (Fig.3.17 and 3.18). These errors are mainly due to the residual perfusion outside the segmented area S, which can be perceived, similarly as for the TACs, from the large differences between the perfusion error E_{pbf} and the inhomogeneity $Inhom_{pbf}$ (Fig.3.17 and Fig.3.18).

TACs and blood flow estimation accuracy highly depends on the segmentation method applied (see Fig. 3.13). The segmentation based on the Minimum inconsistency provided a more accurate estimation of the TACs in comparison to the segmentation based on thresholding. The better performance of the Minimum inconsistency method can be attributed to the fact that it better fits to the estimation procedure (cf. Eq. 3.5 and Eq. 3.9) and thus allows to minimize inhomogeneity and additional contrast more effectively. Despite the fact that the Minimum inconsistency segmentation is based only on a single instance of the data, i.e. the contrast enhancement image, the obtained segmented areas S and A are similar to those of the Reference segmentation thus leading to comparable errors both on the estimated TACs and on the estimated blood flow (Fig. 3.13 and Fig. 3.19). However, some segmentation errors for the Minimum inconsistency segmentation were observed for Case 2 around the bone area, in the hypoperfused area and in vessels (cf. Fig. 3.9(b) and Fig. 3.9(d)) These errors are attributed partially to the lack of temporal data in the reconstructed images and partially to the post filtering of the reconstructed images which introduces loss of resolution in the images. The influence of these segmentation errors on the estimation accuracy was however negligible (Fig. 3.13(b)).

The reduced performance of the thresholding segmentation has a large impact on the estimation accuracy. Concerning tissue segmentation, in Case 1 a large tissue area exhibiting reduced contrast attenuation is excluded from the segmented area (see Fig. 3.9(e)). This results in overestimation of the TACs which caused higher error levels in comparison with the other segmentation methods. In Case 2 (Fig. 3.9(f)) all perfused and non perfused tissue (bone marrow, fat and skin) were included in the segmented area S resulting in high inhomogeneity and increased estimation error in comparison with the Minimum inconsistency method (Fig. 3.13(b)).

Concerning the segmentation of the artery, when using thresholding the artery was oversized in comparison to the Reference segmentation, causing underestimation of the arterial input function (see Fig. 3.15). The segmentation by Minimum inconsistency (Sec. 3.2.3) allowed to achieve a more precise segmentation improving the estimation of the arterial input function.

The impact of beam hardening on the accuracy of the method was assessed by additional simulations which are not documented here for brevity. Typically, the line integrals measured

with energy integrating detectors assumes a linear relation between the line integral and the object thickness. In the reality this relation is not linear due to the polychromatic nature of x-rays. The non-linearity results in an error on the line integral which depends on the composition of the materials and on their thickness. The simulations showed that the error due to beam hardening for simple leg phantoms consisting of tissue, bone and typical contrast concentrations, is negligible in comparison with the other error sources.

Despite the high spatial inhomogeneity measured in skeletal muscle perfusion, average quantification of blood flow in ROIs were close to the average blood flow in the original CTP data for most scenarios (see Tab. 3.3). The average perfusion quantification improves visual differentiation between hypoperfused areas and normally perfused areas (Fig. 3.10(b) and 3.16(b)). This differentiation is challenging by using conventional DSA due to the dependence of the line integrals on the object thickness (Fig. 3.10). Therefore the proposed approach represents a possible improvement over conventional DSA.

3.6 Summary and Conclusion

We have presented a method for quantitative spatially averaged perfusion estimation in skeletal muscles using interventional X-ray C-arm systems. The method is based on angiography acquired from a fixed angular viewing position. The lack of spatial depth information in angiography is tackled by acquiring two additional rotational scans from which the area subject to contrast propagation is segmented. The method relies on the assumption that the contrast absorption is spatially homogenous within the segmented area and along the direction of the acquired X-ray.

Results on data simulated from CTP acquisitions in the lower calf showed that the accuracy of the method is limited by spatial inhomogeneity of the perfusion which is characteristic in muscular tissues. Nonetheless, we have shown that average perfusion quantification, as provided with the proposed method, can improve detection of lesions in comparison to conventional DSA. Therefore, the proposed method represents a step toward quantitative periprocedural perfusion assessment. Future investigations will focus on the improvement of the estimation accuracy by relaxing the assumptions on the homogeneity of the contrast attenuation.

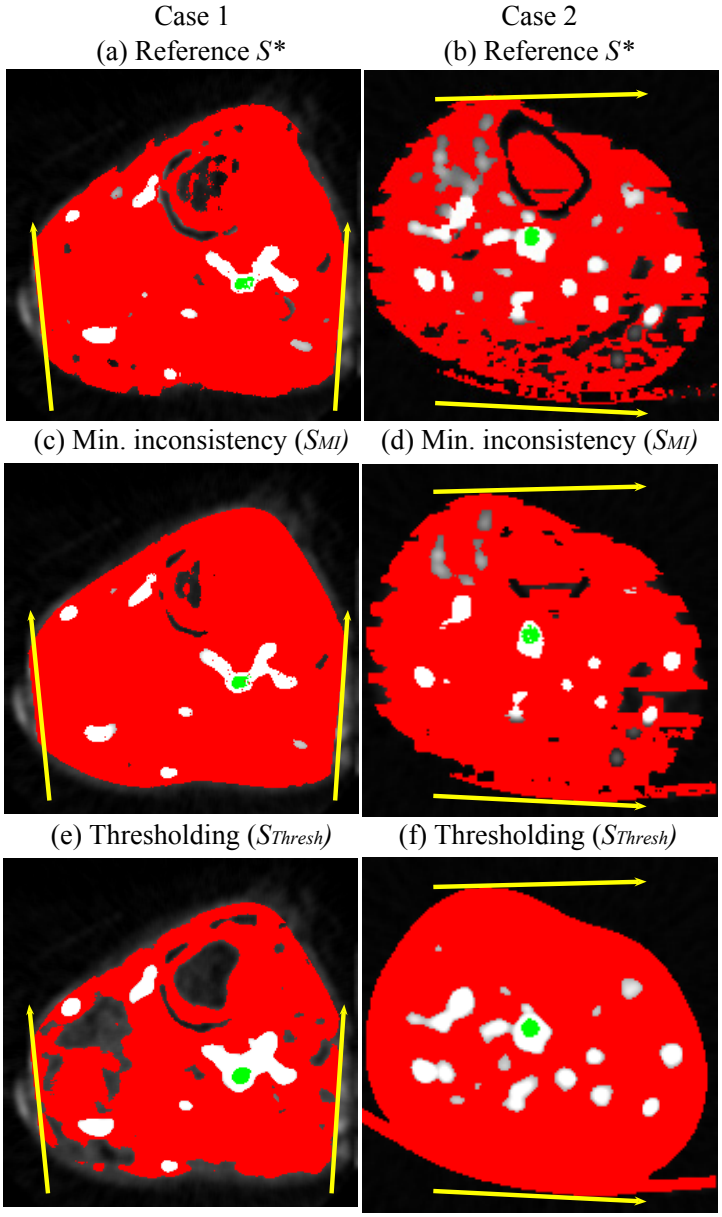

Figure 3.9. Segmentation of the contrast enhancement image μ_{enh} for Case 1 (left column) and Case 2 (right column). (a)(b) Reference segmentation (S^*): the red area overlaid on the contrast enhancement image depicts the segmented area S, the green area depicts the segmented artery A. (c)(d) Segmented areas (S_{MI}) obtained using the Minimum inconsistency segmentation. (e)(f) Segmented areas (S_{Thres}) obtained using segmentation based on thresholding. The yellow arrows in indicate the directions of X-rays to generate the angiograms.

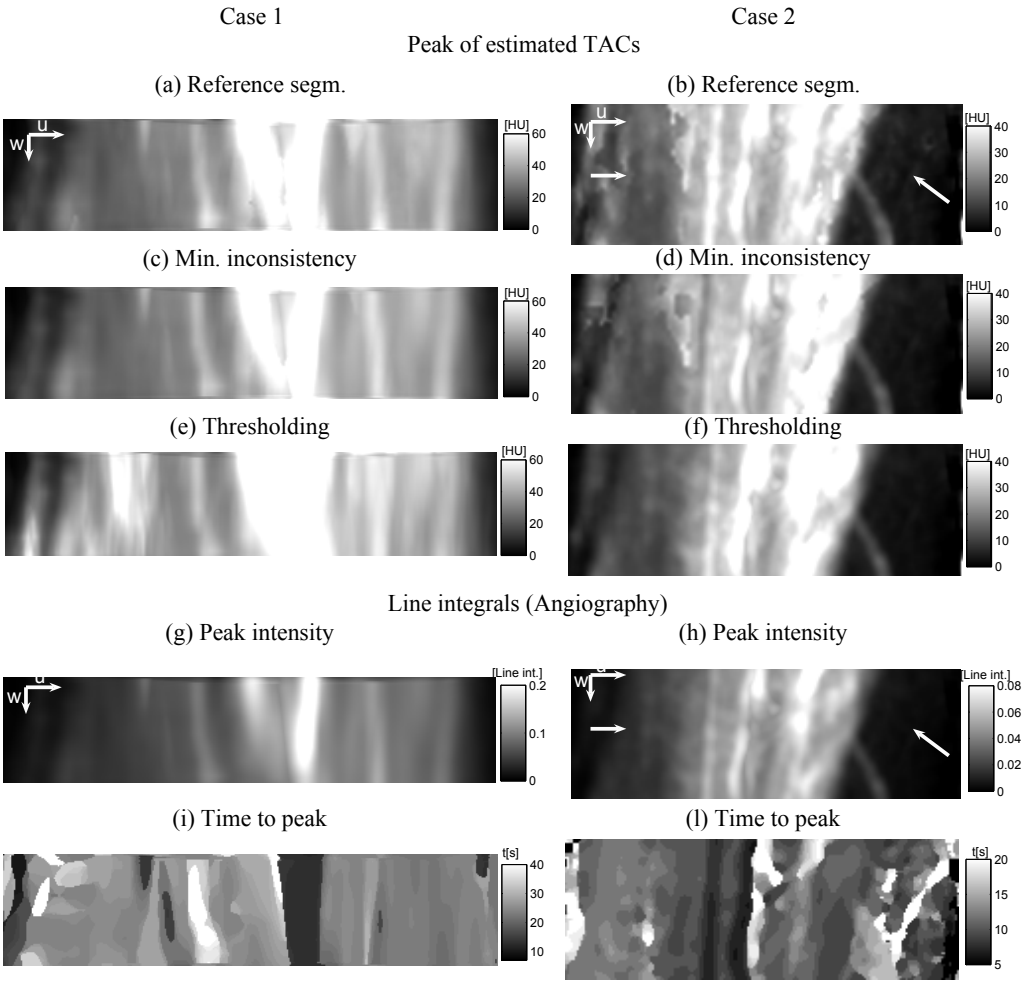

Figure 3.10. Peak attenuation maps of the estimated TACs obtained with the proposed estimation method for Case 1 (left column) and Case 2 (right column). The maps show results obtained by applying different segmentation methods. The maps are shown in projection space, i.e. on the detector plane. The orientation of the detector axis (u and w in Fig. 3.3) is shown on the upper left of (a) and (b). The viewing directions used to generate the angiograms are depicted in Fig. 3.9. (a)(b) Peak attenuation map obtained using the Reference segmentation. (c)(d) Peak attenuation map obtained applying the Minimum Inconsistency method. (e)(f) Peak attenuation map obtained applying thresholding. (g)(h) Peak intensity of the line integrals (standard DSA). (i)(l) Time to peak of the line integrals.

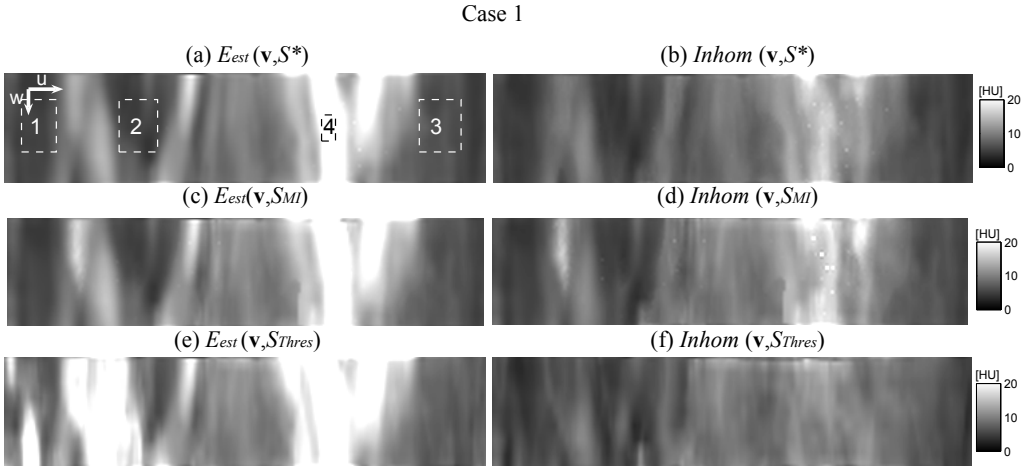

Figure 3.11. Case 1: Estimation error E_{est} and Inhomogeneity $Inhom$ for the TACs estimated with proposed approach obtained by applying different segmentation methods (S^*, S_{MI}, S_{Thres}). (a) Locations of four ROIs used for quantitative analysis.

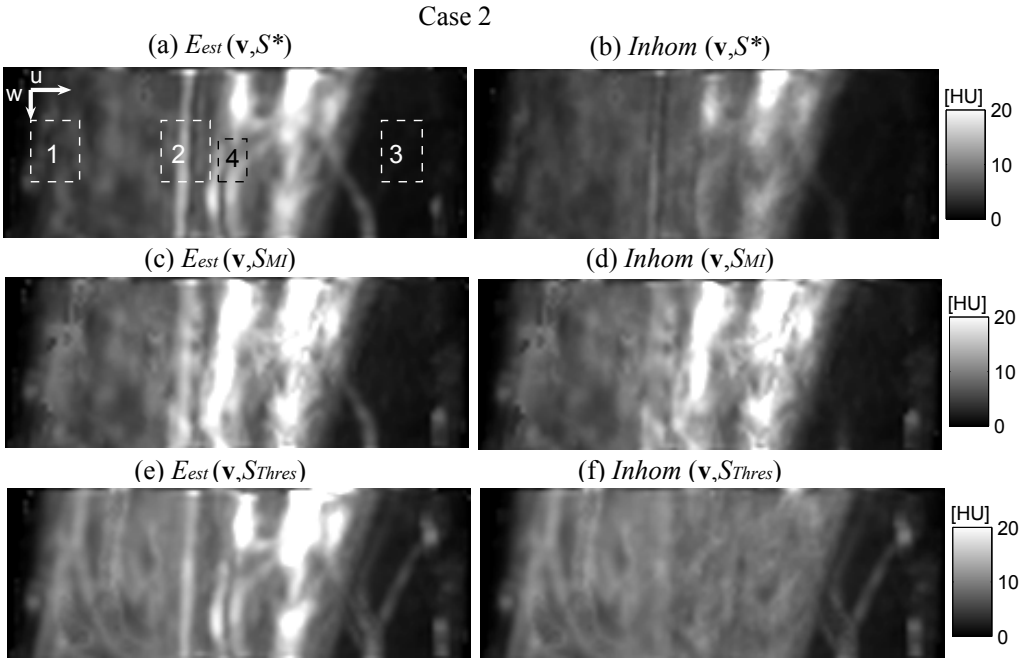

Figure 3.12. Case 2: Estimation error E_{est} and Inhomogeneity $Inhom$ for the TACs estimated with the proposed approach obtained by applying different segmentation methods (S^*, S_{MI}, S_{Thres}). (a) Locations of four ROIs used for quantitative analysis.

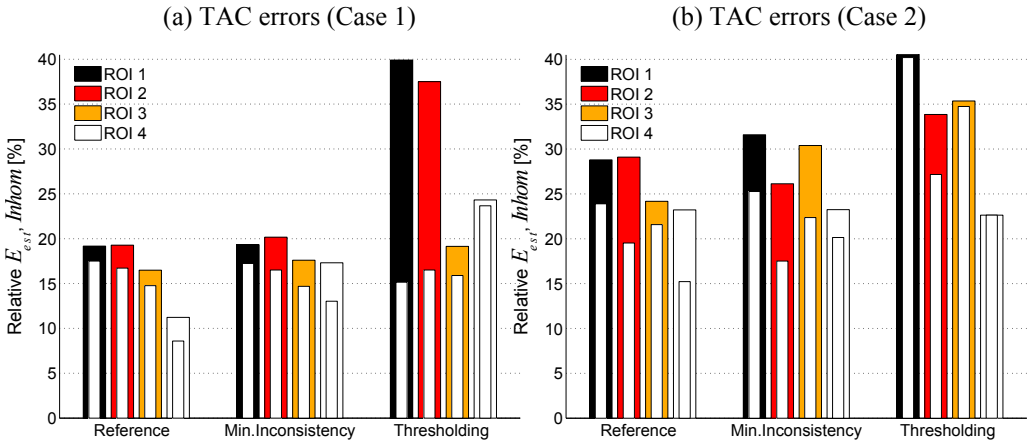

Figure 3.13. Average relative errors and average relative inhomogeneities for the proposed approach obtained by applying different segmentation methods (S^*, S_{MI}, S_{Thres}). The errors and inhomogeneities are measured over the four ROIs shown in Fig. 3.11(a). (a) Case 1 (b) Case 2

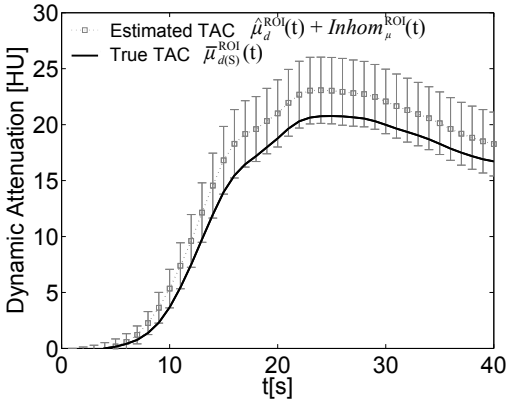

Figure 3.14. Average true TAC $\bar{\mu}_{d(S)}^{ROI}$ for ROI 2 in Fig. 3.11(a) and average estimated TAC $\hat{\mu}_d^{ROI}(t)$ plus average inhomogeneity $Inhom_t^{ROI}(t)$ (error bar). The inhomogeneity increases in correspondence with the onset of the TACs.

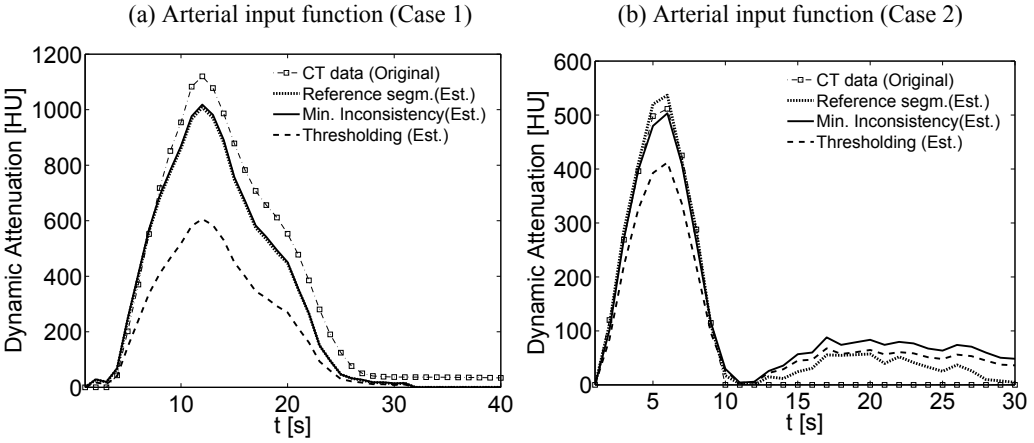

Figure 3.15. Estimated arterial input function and true arterial input function. The estimation is shown for different segmentation methods (A^*, A_{MI}, A_{Thres}) for Case 1 (a) and Case 2 (b)

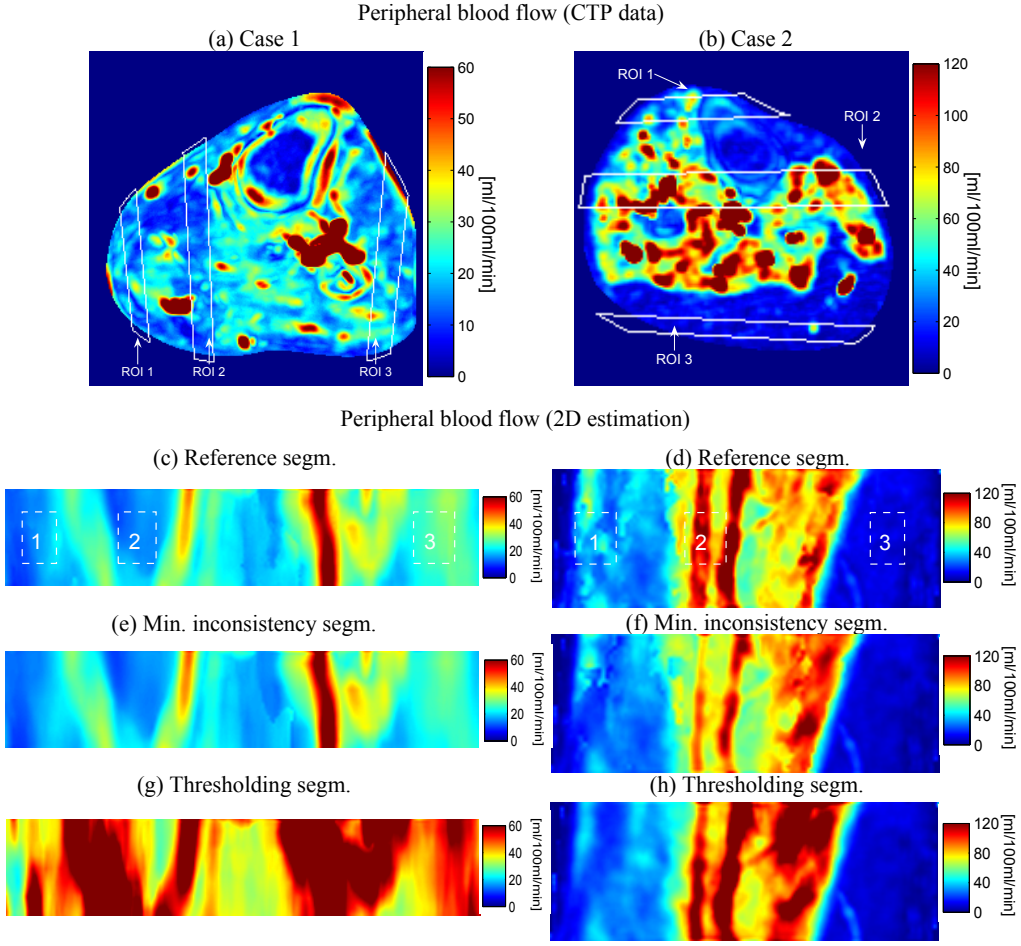

Figure 3.16. Perfusion maps showing peripheral blood flow. (a)(b) Peripheral blood flow in the original CTP data for Case 1 (a) and Case (2). The location of the ROIs used for evaluation is depicted by the rectangles. (c)-(h) Estimated 2D peripheral blood flow for different segmentation methods. (c)(d)

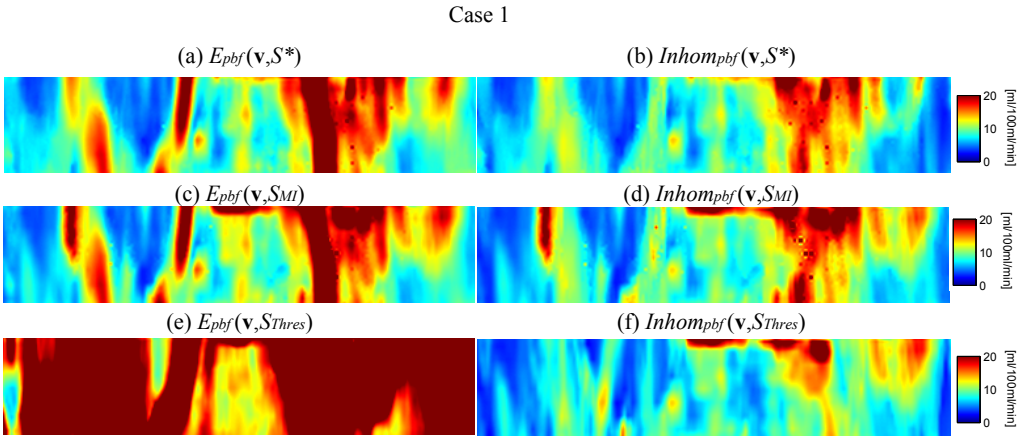

Figure 3.17. Case 1: Perfusion estimation error E_{pbf} and Inhomogeneity $Inhom_{pbf}$ for the estimated 2D blood flow obtained by applying different segmentation methods (S^*, S_{MI}, S_{Thres}).

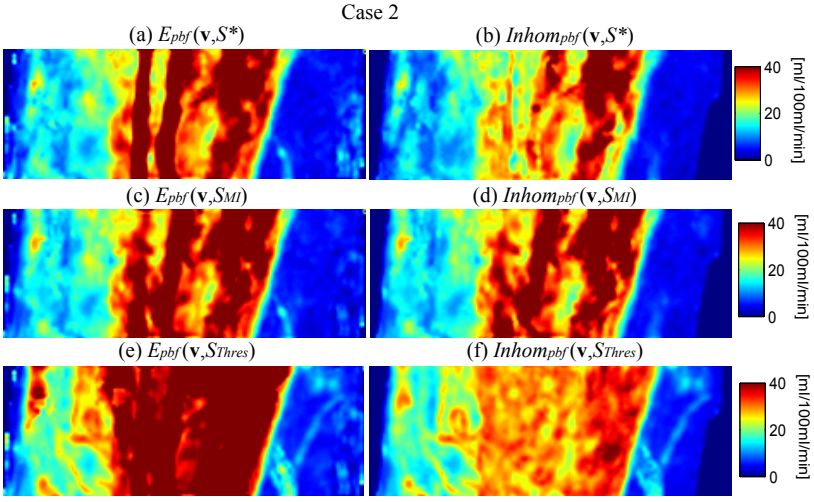

Figure 3.18. Case 2: Perfusion estimation error E_{pbf} and Inhomogeneity $Inhom_{pbf}$ for the estimated 2D blood flow obtained by applying different segmentation methods (S^*, S_{MI}, S_{Thres}).

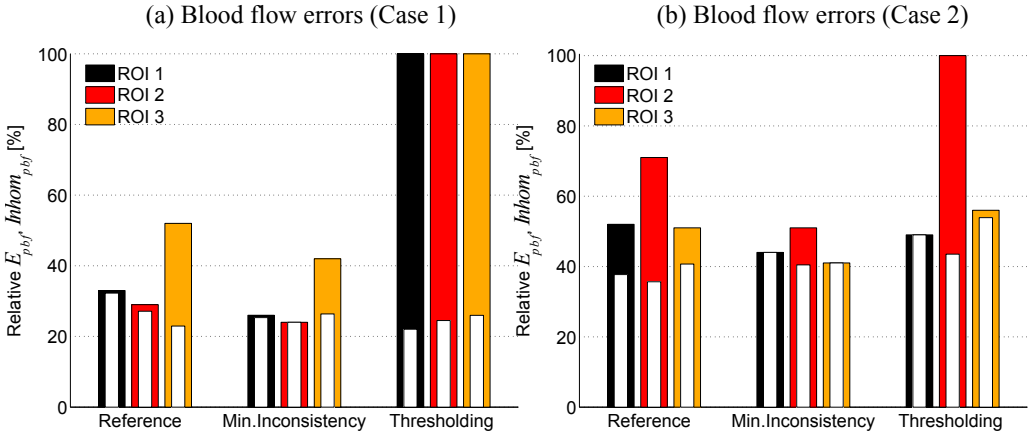

Figure 3.19. Average relative E_{pbf} and average relative $Inhom_{pbf}$ for the proposed approach obtained by applying different segmentation methods (S^*, S_{MI}, S_{Thres}). The errors and inhomogeneities are measured over the three tissue ROIs shown in Fig. 3.16.

Chapter Four

Spatially regularized region-based perfusion estimation in peripherals using angiographic C-arm systems

It is not knowledge, but the act of learning, not possession but the act of getting there, which grants the greatest enjoyment.

— Carl Friedrich Gauss (1777-1855)

Abstract — The outcome assessment of endovascular revascularization procedures in the lower limbs currently is carried out by X-ray digital subtraction angiography (DSA). Due to the two-dimensional nature of this technique, only visual assessment of arterial blood flow is possible and no tissue blood flow information (i.e. perfusion) is available to assess the effective restoration of blood supply to the tissue. In this chapter we propose a method for interventional perfusion estimation in peripherals using C-arms which is based on DSA and two additional 3D images reconstructed from rotational scans. The method assumes spatial homogeneity of contrast within multiple regions identified by segmentation of the reconstructed 3D images. A dedicated segmentation method, which relies on local contrast homogeneity and connectivity of anatomical structures, is introduced. Region-based perfusion is obtained by mapping the 2D blood flow information from DSA to the 3D segments by solving an inverse problem. Instability of the solution, due to the spatial overlap of the regions, is addressed by applying spatial and temporal regularization.
The method was evaluated on data simulated from CT perfusion scans of the lower limb. Blood flow values estimated with the optimal number of segmented regions exhibited errors of 1 ± 4 and 2 ± 11 ml/100ml/min for the two analyzed cases, respectively. This level of accuracy showed to be sufficient to differentiate hypoperfused and normally perfused areas. The use of spatial and temporal regularization proved to be an effective way to limit inaccuracies due to instability in the solution of the inverse problem. Results in general proved the feasibility of C-arm interventional perfusion imaging by combination of temporal information derived from DSA and spatial information derived from 3D reconstructions.

Based upon: M. Giordano, E. P. A. Vonken, M. Bertram, W. P. T. M. Mali, M. A. Viergever and C. Neukirchen, "Spatially regularized region-based perfusion estimation in peripherals using angiographic C-arm systems", *Physics in Medicine and Biology*, vol.57, no.22, pp. 7239–7259, 2012.

4.1 Introduction

Peripheral arterial disease (PAD) is a major health care concern causing obstruction of blood flow in the arteries of the legs [48]. Among the major risk factors associated with PAD are diabetes and advanced age. Particularly in diabetic patients, PAD can cause limb ischaemia and lead to amputation in the most severe cases. Treatment of PAD in recent years has shifted from open surgery toward percutaneous endovascularization procedures [120] that include balloon angioplasty and stenting. Today, outcome of such minimally invasive interventions is assessed by visual inspection of the blood flow in the recanalized vessels using DSA. In DSA a time sequence of planar projections is acquired from a fixed viewing position during bolus injection. After acquisition, the "pre-bolus" image is subtracted from all the contrasted images, so as to mask out bones and soft tissue and to visualize the filling of contrast in vessels. DSA however, provides only qualitative visualization of blood flow. In fact, owing to the overlap of the anatomical structures along the ray paths, all contrast information in tissue along the longitudinal direction is lost. If the contrast concentration in tissue (i.e. perfusion) could be measured during revascularization, this would provide important information about the effective restoration of blood flow supply to the tissue.

Skeletal muscle perfusion nowdays can be assessed by CT perfusion (CTP) [71]. CTP is based on a short bolus injection followed by multiple fast rotations ($\sim$ 2 rot/s) of the CT gantry, which aim at capturing the temporal dynamics of contrast in the object. A temporal sequence of 3D images is reconstructed by using standard reconstruction techniques. The temporal contrast concentration in a region of interest (ROI) or in a voxel is quantified as a time attenuation curve (TAC) from which perfusion parameters [80] (blood flow, blood volume and mean transit time) are extracted. However, CTP is not available in an interventional environment and requires the patient to be moved to the CT-room which complicates the workflow.

C-arm X-ray systems, that allow for easy patient access during intervention, have been used in the past exclusively for planar and 3D imaging [36]. In recent years, the improvement of the contrast resolution due to the introduction of flat detector technology [16, 55], in combination with the use of high (intraarterial) contrast, has opened to the possibility of perfusion imaging directly in the angioroom. The capabilities of these systems are inferior to that of modern CT scanners: lower angular rotational speed ($\sim$ 50 deg/s) and limited angular range (220°). These limitations make the recovery of TACs challenging because the temporal sampling rate is too low for dynamic reconstruction [108]. In Chapter 2 we proposed to estimate TACs from multiple consecutive forward/backward short scans (i.e. multi-sweep) by applying an iterative reconstruction method which exploits prior knowledge on the contrast dynamics. However, the slow rotational speed makes the recovery of fast arterial dynamics, which are crucial for accurate perfusion estimation, challenging and prone to strong artifacts. To increase the temporal sampling of projections, Ganguly *et. al.* [25] proposed to acquire several multi-sweep acquisitions with multiple injections using different start times with respect to contrast injection and to interleave the acquired data. Results obtained with this method were promising [21, 26], however the complex acquisition protocol limits the applicability in a clinical environment.

In this chapter we propose a 3D perfusion estimation method that makes use of standard C-arm acquisitions. We exploit the fast acquisition frame rate of the C-arm used in angiographic mode and combine it with 3D images reconstructed from rotational scans. This method extends the method presented in Chapter 3 where we estimated 2D perfusion. In Chapter 3, the average contrast density along the x-ray directions was obtained by normalizing the line

integrals by the length of contrast material along the x-ray directions. The length of contrast material was determined by a single volumetric segmentation from 3D reconstructions assuming global contrast homogeneity. Results showed that the accuracy is limited owing to contrast inhomogeneity along the ray directions. In the method proposed here, we relax the assumption on global homogeneity by assuming a set of multiple 3D regions related to local contrast homogeneity. Perfusion homogeneity in peripherals was investigated earlier in MR perfusion studies [24], which showed that perfusion is associated with distinct muscle groups and exhibits some degree of homogeneity within the single groups. Therefore, if the muscle groups are modeled using a sufficient number of segmented regions, the perfusion within the regions can be assumed homogeneous.

The key idea for our estimation method is that if TACs exhibit local similarity in 3D regions, they can be estimated by mapping the dynamic information from the 2D angiograms to the 3D regions by inversion of regions' projections. This method requires (i) a 3D segmentation of the object in regions which share the same contrast dynamics ii) solution of the inverse problem to map the 2D angiograms to the 3D regions. The computational effort with respect to the method presented in Chapter 3 is higher, yet the proposed method provides 3D perfusion information which has a higher clinical value.

A similar approach was proposed by Taguchi *et. al.* [109] for liver perfusion. They assume a segmentation of the liver in homogeneous regions and estimate region-specific TACs from projection angiograms by solving a least square problem. However, in their simulations on idealized phantoms, the regions are assumed perfectly defined and no method to derive the regions is proposed. In the method presented here, we introduce a segmentation method to derive the regions from 3D reconstructions. This segmentation method exploits contrast homogeneity and connectivity of the anatomical regions to limit segmentation errors originating from the lack of temporal data in the reconstructions. The mapping procedure from the 2D angiograms to the 3D regions resembles an ill-posed problem due to the overlap of the regions in projection space [30]. We address instability in the inversion operation by temporal and spatial regularization of the solution, whereas in Taguchi's work [110] only temporal regularization was applied.

The major contributions presented in this chapter are: (i) a dedicated 3D segmentation method to derive regions with homogeneous contrast dynamics from 3D images reconstructed from rotational scans; (ii) a procedure to map 2D angiograms to 3D regions which addresses instability in the inversion operation by temporal and spatial regularization. Qualitative results obtained with a first implementation of this method were presented in [29,30]. In this chapter we introduce spatial regularization in the mapping procedure and carry out a quantitative evaluation of the accuracy and of the error sources (i.e. contrast inhomogeneity, segmentation errors and estimation errors). The evaluation is carried out on data simulated from CTP scans.

4.2 Methods

The proposed method estimates tissue perfusion from a temporal series of angiograms acquired at a fixed viewing position. It relies on two additional 3D images reconstructed from rotational scans. The main idea is to map the blood flow information from the 2D projections to the 3D reconstructed object by exploiting knowledge of the perfused anatomy. This knowledge consists of a segmentation of the anatomy into regions of homogeneous contrast characteristics. The method consists of two main steps which are illustrated in Fig. 4.1:

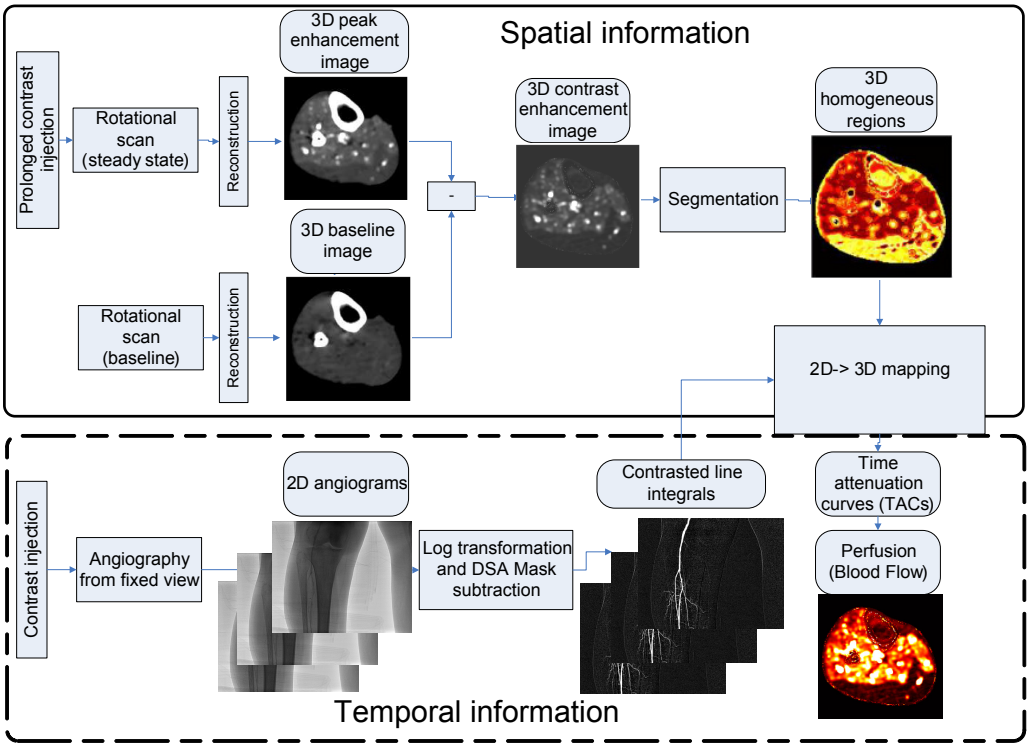

Figure 4.1. Workflow of the perfusion estimation method.

1. Two 3D rotational scans, one without contrast and one with contrast in steady state, are acquired to reconstruct the morphology of the perfused territories. 3D segmentation is applied to identify regions exhibiting similar contrast properties (upper block in Fig. 4.1).

2. After a short bolus injection, angiography is acquired from a fixed angular view (lower block in Fig. 4.1). Then the regional contrast dynamics in the 3D object are estimated by mapping the 2D projections to the 3D segmented object via solving the inverse problem.

The information generated is a dynamic 3D object consisting of regions with spatially constant contrast attenuation from which perfusion parameters are derived.

4.2.1 Model for TAC representation

The aim of the method is the estimation of TACs $\mu(\boldsymbol{x}, t)$ caused by the time-variation of contrast concentration in tissue and vessels after bolus injection. The total attenuation $\mu_d(\boldsymbol{x}, t)$ at time t and position $\boldsymbol{x}$ consists of the static contribution $\mu_0(\boldsymbol{x})$, due to the structures that do not absorb contrast (bones, fat), plus a contribution due to contrast propagation $\mu(\boldsymbol{x}, t)$: $\mu_d(\boldsymbol{x}, t) = \mu(\boldsymbol{x}, t) + \mu_0(\boldsymbol{x})$. Here it is assumed that no object motion or deformation occurs.

The proposed method relies on the assumption that within 3D regions, multiple TACs can be approximated by a single characteristic TAC:

$$\mu(\boldsymbol{x}, t) \simeq \bar{\mu}_{k(\boldsymbol{x})}(t) \tag{4.1}$$

The index $k(\boldsymbol{x})$ indicates the region at location $\boldsymbol{x}$. Each region S_c is defined as: $S_c \equiv \forall \boldsymbol{x} : k(\boldsymbol{x}) = c$ with $c \in 1 \ldots N_R$ (N_R is the total number of regions). $\bar{\mu}_c(t)$ denotes the characteristic TAC of the c-th region. The regions are identified by segmentation of 3D images reconstructed from rotational scans. The segmentation method is described in Sec. 4.2.2. The estimation of the characteristic TACs from the angiograms is detailed in Sec. 4.2.3.

4.2.2 Segmentation

The aim of the segmentation of reconstructed images is to identify 3D regions having similar TACs. The 3D images are reconstructed from projections obtained by rotational scans. The Feldkamp Davis Kress (FDK) algorithm [17] is used to reconstruct the images from the set of projections. Two rotational scans are performed (Fig. 4.1): a baseline scan without injected contrast, from which a baseline image μ_0 is reconstructed; a steady state contrast scan, from which a peak enhancement image μ_s is reconstructed. Prior to the steady state scan, a prolonged contrast injection [124] is performed to ensure maximal and stable contrast in the vasculature and in tissues throughout the scan. The attenuation in the peak enhancement image is assumed to approximate the temporal maximum of the TAC: $\mu_s(\boldsymbol{x}) \simeq \max_t\{\mu_d(\boldsymbol{x}, t)\}$. The attenuation in the baseline image is assumed to approximate the first (i.e. non-contrasted) time-frame of the TAC: $\mu_0(\boldsymbol{x}) \simeq \mu_d(\boldsymbol{x}, 0)$. After 3D reconstruction, the baseline image is subtracted from the peak enhancement image to yield the contrast enhancement image $\mu_{enh}(\boldsymbol{x}) = \mu_s(\boldsymbol{x}) - \mu_0(\boldsymbol{x})$. This image resembles the volumetric contrast density.

The segmentation is based on the local similarity of volumetric contrast density in μ_{enh}. To segment regions with similar TACs, it is assumed that areas with similar volumetric contrast density exhibit similar TACs. The k-means clustering [73] is applied to group the voxels in regions with maximum similarity. Connectivity of the segmented regions [111] is enforced by taking into account the voxels' intensity in the neighborhood: to each image voxel at position $\boldsymbol{x}$, a feature vector $\boldsymbol{f}(\boldsymbol{x})$ is assigned which consists of the intensity at $\boldsymbol{x}$ and in the 26-connected-neighborhood [41], i.e. $\boldsymbol{f}(\boldsymbol{x}) = [\mu_{enh}(\boldsymbol{x}), \mu_{enh}(\boldsymbol{x} + \Delta_1), \ldots, \mu_{enh}(\boldsymbol{x} + \Delta_{26})]$ (the Δ_i's are the displacements between $\boldsymbol{x}$ and the i-th connected neighbor). In the following we will denote the i-th component of the feature vector as $f_{(i)}(\boldsymbol{x}), i = 1, \ldots, \eta$ (η is the number of feature components, in this case $\eta = 27$).

The k-means algorithm is applied to minimize the sum of squared differences between the voxels' features $\boldsymbol{f}(\boldsymbol{x})$ and their associated cluster centroids $\boldsymbol{z}_{k(\boldsymbol{x})}$ (i.e. the mean feature in the region):

$$\arg\min_{k(\boldsymbol{x})}\{\sum_{\boldsymbol{x}} ||\boldsymbol{f}(\boldsymbol{x}) - \boldsymbol{z}_{k(\boldsymbol{x})}||^2\} \tag{4.2}$$

In the remainder of the article we will refer to the argument in equation 4.2 as the objective function I.

The solution provided by k-means depends on the number of clusters and on the choice of initial centroids [56]. In the proposed segmentation method we allow a variable number of clusters (i.e. regions) by cluster splitting. This allows to achieve segmentations that are less dependent on the initial settings. The key idea is to derive the initialization of the centroids from segmentations with lower number of clusters by splitting the most inhomogeneous clusters.

Table 4.1. Segmentation parameters

Parameter	meaning	value (determination)
N_{init}	initial number of clusters	10 (input parameter)
N	number of clusters at the current iteration	- (variable of the algorithm)
N_R	target number of clusters	50-300 (input parameter)
N_{empty}	number of empty clusters	- (automatic)
N_{split}	number of clusters to be splitted	$0.1 * N$ (automatic)
$iter$	number of current iteration	(variable of the algorithm)
$iter_{Split}$	number of k-means subiteration	2 (experimental)
γ	fraction of the cluster standard variation	0.1 (experimental)
I_{old}	old value of the objective function	(variable of the algorithm)
I	current value of the objective function	(variable of the algorithm)

The proposed segmentation method has similarities with the ISODATA algorithm [5], [78]. A schematic representation of the algorithm is provided in Fig. 4.2. In table 4.1 all segmentation parameters and the way they are determined is reported. To initialize the algorithm, the user points at N_{init} seed locations $[\boldsymbol{x}_1, \boldsymbol{x}_2, ..., \boldsymbol{x}_{N_{init}}]$ in μ_{enh} corresponding to anatomical structures that are wished to be segmented (e.g. artery, veins, tissue, hypoperfused tissue). The features associated with the selected seeds are used to initialize the centroids: $\boldsymbol{z}_1 = \boldsymbol{f}(\boldsymbol{x}_1), \boldsymbol{z}_2 = \boldsymbol{f}(\boldsymbol{x}_2), ..., \boldsymbol{z}_{N_{init}} = \boldsymbol{f}(\boldsymbol{x}_{N_{init}})$. Successively, the segmentation starts to iterate. Each iteration consists of a number $iter_{Split}$ of k-means subiterations and one cluster splitting subiteration (Fig. 4.2). This succession ensures a consistent improvement of the objective function and of the clusters homogeneity. In case clusters become empty after a subiteration, their respective centroids are discarded.

At each splitting iteration, the clusters to be split are chosen according to a score P_c which takes into account cluster inhomogeneity and size. The N_{split} clusters with the highest score are split. The score P_c is based on three criteria:

- $\bar{\sigma}_c$: the cluster standard deviation averaged over all components. This criteria asseses the absolute cluster inhomogeneity. $\bar{\sigma}_c$ is based on the components of the cluster standard deviation: $\sigma_c = [\sigma_{c_{(1)}}, \sigma_{c_{(2)}}, \ldots, \sigma_{c_{(\eta)}}]$ where the i-th component $\sigma_{c_{(i)}}$ is defined as:

$$\sigma_{c_{(i)}} = \sqrt{\frac{1}{|S_c|} \sum_{\boldsymbol{x} \in S_c} (f_{(i)}(\boldsymbol{x}) - \boldsymbol{z}_{c_{(i)}})^2} \tag{4.3}$$

  $\boldsymbol{z}_{c_{(i)}}$ is the i-th component of the c-th centroid, $|S_c|$ is the number of voxels in the c-th cluster. The cluster standard deviation averaged over all components is defined as:

$$\bar{\sigma}_c = \sqrt{\frac{\sum_{i=1}^{\eta} \sigma_{c_{(i)}}^2}{\eta}} \tag{4.4}$$

- $\zeta_c = \bar{\sigma}_c / \max_{(i)}\{\boldsymbol{z}_{c_{(i)}}\}$: the cluster standard deviation normalized by the largest cluster component. This criteria assesses the relative cluster inhomogeneity. $\max_{(i)}\{\boldsymbol{z}_{c_{(i)}}\}$ is the largest component of the c-th centroid.

- $|S_c|$: the cluster size.

These criteria are combined to give the total score as follows:

$$P_c = \frac{\bar{\sigma}_c - \bar{\sigma}_{min}}{\bar{\sigma}_{max} - \bar{\sigma}_{min}} + \frac{\zeta_c - \zeta_{min}}{\zeta_{max} - \zeta_{min}} + \frac{|S_c|_c - |S_c|_{min}}{|S_c|_{max} - |S_c|_{min}} \tag{4.5}$$

$\bar{\sigma}_{max}$ and $\bar{\sigma}_{min}$, and similarly ζ_{max}, ζ_{min}, $|S_c|_{max}$ and $|S_c|_{min}$, indicate the highest and the lowest quantities over all clusters and are used to normalize each criterion between 0 and 1 and P_c between 0 and 3.

After selection of the clusters to be split, cluster splitting is performed by replacing the original centroid $\boldsymbol{z}_c$ with two centroids centered at $\boldsymbol{z}_c$ plus/minus a fraction γ of the clusters standard deviation, e.g. $\boldsymbol{z}_c^+ = \boldsymbol{z}_c + \gamma\sigma_c$ and $\boldsymbol{z}_c^- = \boldsymbol{z}_c - \gamma\sigma_c$. After the split, the objective function is recalculated, and if the new configuration improves the objective function w.r.t. to the previous configuration, the new N_{split} centroids are accepted, otherwise the previous configuration is restored (Fig. 4.2). The execution of the algorithm terminates when the target number of clusters N_R is reached and further iterations do not improve the objective function.

4.2.3 TACs estimation

The TAC estimation is based on a temporal series of 2D angiograms acquired from a fixed viewing position after short bolus injection. A temporal series of 2D line integrals $\boldsymbol{\ell}_d^*(t)$ is obtained from the angiograms by applying the log transform [61]. As the primary interest is to measure pure contrast dynamics, the static object contribution is removed by subtracting the first non-contrasted time frame $\boldsymbol{\ell}_0^*$ (i.e. DSA mask): $\boldsymbol{\ell}^*(t) = \boldsymbol{\ell}_d^*(t) - \boldsymbol{\ell}_0^*$. (see Fig. 4.1).

The system geometry to acquire angiography is described by the X-ray source position $\boldsymbol{\alpha}$ and a detector pixel position $\boldsymbol{v}$. A ray path from the source to a detector pixel is described by the unit vector $\boldsymbol{\phi}(\boldsymbol{v}, \boldsymbol{\alpha})$. The position on a ray is indicated by $\boldsymbol{x}(r) = \boldsymbol{\alpha} + r\boldsymbol{\phi}$ with r varying between 0 and the source-to-detector pixel distance R.

The TAC estimation relies on an inversion operation which maps the 2D line integrals to the regions of the 3D object. This operation is the inverse of a forward projection operation that is defined by considering the TAC representation model in Eq. 4.1. Dynamic line integrals through the contrasted object are modeled as a combination of the characteristic TACs in the voxels on the considered ray:

$$\ell(\boldsymbol{v}, t) = \int_0^R \mu(\boldsymbol{x}(r), t)dr \simeq \sum_{c=1}^{N_R} \bar{\mu}_c(t) \int_0^R \delta_{c,k(\boldsymbol{x}(r))}dr \tag{4.6}$$

The expression $\delta_{c,k(\boldsymbol{x})}$ equals one when a voxel at position $\boldsymbol{x}$ is assigned to the c-th segmented region. $\int_\infty \delta_{c,k(x(r))}dr$ resembles the intersection of a ray with the c-th region. Equation (4.6) can be rewritten in matrix notation for all detector pixels:

$$\boldsymbol{\ell}(t) = \boldsymbol{W} \cdot \bar{\boldsymbol{\mu}}(t) \tag{4.7}$$

$\boldsymbol{W}$ is a $J \times N_R$ projection operator which maps from the N_R-dimensional space of image segments to the J-dimensional projection domain (J denotes the number of detector pixels). The columns of $\boldsymbol{W}$ consist of the intersection lengths of the regions with the ray paths [51]. Therefore $\boldsymbol{W}$ depends on the spatial configuration of the regions and on the viewing position $\boldsymbol{\alpha}$. $\bar{\boldsymbol{\mu}}(t)$ is an N_R-dimensional vector containing the values of the characteristic TACs for the segmented regions at time t. The J-dimensional vector $\boldsymbol{\ell}(t)$ contains the modeled line integrals at time t.

To obtain an estimate $\hat{\boldsymbol{\mu}}(t)$ of the characteristic TACs, the difference between the modeled line integrals $\boldsymbol{\ell}(t)$ and the acquired line integrals $\boldsymbol{\ell}^*(t)$ is minimized in a least squares sense. The minimization is performed for each time point independently:

$$\hat{\boldsymbol{\mu}}(t) = \arg\min_{\hat{\boldsymbol{\mu}}(t)} ||\boldsymbol{\ell}^*(t) - \boldsymbol{\ell}(t)||^2 \qquad \forall t \tag{4.8}$$

Typically, the projection matrix $\boldsymbol{W}$ is ill-conditioned. This is mainly due to the overlap of regions in projection space which can cause the column of $\boldsymbol{W}$ to become linearly dependent. As a consequence the solution to (4.8) is sensitive to inconsistencies [39] caused by quantum noise in $\boldsymbol{\ell}^*(t)$ and by the mismatch between $\boldsymbol{\ell}^*(t)$ and $\boldsymbol{\ell}(t)$. These inconsistencies typically lead to oscillations in $\hat{\boldsymbol{\mu}}(t)$ [110]. In our approach, spatial and temporal regularization is applied to obtain a stabilized solution of (4.8). Spatial regularization is achieved via truncated singular value decomposition [40] (tSVD). In tSVD the regularizing effect is realized by retaining a selected number i_{Reg} of the largest singular values of $\boldsymbol{W}$ and discarding the remaining smaller singular values. In the projector operator $\boldsymbol{W}$, the small singular values are commonly associated with high spatial frequency components in projection space, typically corresponding to fine regions like arteries and veins. However, since accurate TAC estimation in arteries is crucial for perfusion estimation, it is favorable to preserve these structures, which are also characterized by a high signal to noise ratio, and to smooth less enhanced structures characterized by lower signal to noise ratio [30]. To achieve this goal, the projection operator $\boldsymbol{W}$ is modified by multiplication with a diagonal scaling matrix: $\boldsymbol{W}_D = \boldsymbol{W} \cdot \boldsymbol{D}$. In the matrix $\boldsymbol{D}$, the c-th elements on the diagonal are set to:

$$d_{c,c} = \frac{1/|S_c| \sum\limits_{\boldsymbol{x} \in S_c} \mu_{enh}(\boldsymbol{x})}{\sum\limits_{j=1}^{J} w_{j,c}} \tag{4.9}$$

$w_{j,c}$ is the intersection length of the j-th ray through the c-th segmented region. The numerator in the right hand side of (4.9) consists of the averaged contrast enhancement in the reconstructed images and aims at weighting the projected regions in $\boldsymbol{W}$ according to their expected signal-to-noise ratio. The denominator compensates for the different sizes of the projected regions, thus making their contribution independent of the region size. The choice of the number of retained singular values i_{Reg} is addressed in Sec. 4.4.2.

The regularized solution to the least squares problem in equation 4.8 is given by:

$$\hat{\boldsymbol{\mu}}(t) = \boldsymbol{D} \cdot \boldsymbol{W}_D^+ \cdot \boldsymbol{\ell}^*(t) \tag{4.10}$$

$\boldsymbol{W}_D^+$ is the regularized inverse of $\boldsymbol{W}_D$.

Temporal regularization is achieved by smoothing the estimated TACs $\hat{\boldsymbol{\mu}}(t)$ in the time domain by Gaussian filtering. The filter parameters were determined experimentally as a tradeoff between noise reduction and smoothing of the TACs. In our experiments, good results were obtained using a gaussian kernel of length 5s with standard deviation of 3s. By carrying out the regularization separately in the temporal and in the spatial domain, a better control on the desired characteristics of the estimated TACs can be achieved.

Table 4.2. CTP data parameters

	CTP Case 1	CTP Case 2
Sequence length	40s	40s
Image rate	1 image/s	1 image/s
Image size (mm)	$(200 \times 200 \times 60)\text{mm}^3$	$(350 \times 350 \times 40)$ mm^3
Grid size	$(512 \times 512 \times 12)$voxels	$(512 \times 512 \times 64)$ voxels
Injection volume	15 ml (300 mg I/ml)	10 ml (300 mg I/ml)
Injection rate	1.5 ml/s	3 ml/s

Table 4.3. C-arm simulated acquisition geometry

Detector grid	512×396 pixels
Detector surface	383×296 mm^2
Distance source detector	1190 mm
Distance source rot. axis	787 mm
Number of rotational projections / range	400/200°
Projection frame rate (angiography)	1 fps

4.3 Experiments

The accuracy of the perfusion estimation method is evaluated in a simulation study on data simulated from CTP scans of the lower leg. The CTP datasets were used as input data to simulate the perfusion process. C-arm acquisitions, i.e. angiography and rotational scans, are simulated via software by generating synthetic projections of the CTP volumetric data (see Sec. 4.3.1.2).

4.3.1 Simulations

4.3.1.1 Data Preparation

Two CTP scans were acquired on a 64-slice CT scanner on two patients affected by arterial occlusions and undergoing peripheral revascularization. CTP scans consist of 3D temporal sequences acquired after a short bolus injection. An intraarterial injection of iodinated contrast agent was administrated in the proximal superficial femoral artery outside the reconstructed field of view. The injection protocols and the imaging specifications for both CTP acquisitions are listed in table 4.2. The institutional review board of the University Medical Center Utrecht approved our retrospective study and informed consent was waved.

Axial slices showing the temporal maximum of voxels' attenuation of the CTP data are shown in Fig. 4.3. The patients (Case 1 and Case 2) present comparable leg diameter ($\sim$ 100mm) and similar amount of fat. Case 1 presents spatially homogeneous contrast enhancement and regular anatomy, while Case 2 shows hypoperfusion in the gastrocnemius muscle (lower region in Fig. 4.3(b)) and presence of collateral vasculature. To limit motion artifacts occurring between consecutive time frames, each image frame was registered to the first time frame using elastic image registration [52].

Perfusion maps showing the peripheral blood flow pbf were derived from the CTP TACs by applying the well established slope method [80]. For both CTP datasets the condition of no venous outflow before the time of maximum derivative is well fulfilled. The arterial

input function (AIF), which is required to normalize the tissue contrast attenuation against variations in the injection protocol, was calculated by taking the spatial average in a volume of interest (VOI) of the feeding artery (Artery VOI in Fig. 4.3).

The simulations of the C-arm rotational scans were based on digital phantoms created from the CTP sequence. To simulate the contrast distribution during the steady state scan, the temporal maximum of individual voxel attenuation in the CTP sequence was used (steady state phantom); for the baseline scan, the first volume of the CTP sequence was used (baseline phantom).

4.3.1.2 C-arm Simulation

In the first step of the simulations, the angiographic acquisition was simulated. For each volume of the CTP sequence, a cone beam forward projection was generated, resulting in a temporal sequence of 2D angiograms. Subsequently, the first frame of the 2D sequence was subtracted from all frames to obtain the contrasted line integrals $\boldsymbol{\ell}^*(t)$. The acquisition angle $\boldsymbol{\alpha}$ was selected manually. Poisson noise was added to the projections ($5.5 \cdot 10^6$ photons/mm^2) equivalent to a X-ray exposure of 3.25 mAs/frame.

The second step consisted of the simulation of rotational C-arm acquisitions. For each of the two phantoms created from the CTP sequence (i.e. the steady state phantom and the baseline phantom described in Sec. 4.3.1.1), a set of 400 cone beam projections was generated from equiangular views over a circular arc of 200°. Poisson noise was added to the projections ($2.1 \cdot 10^6$ photons/mm^2) corresponding to a total x-ray exposure of 500 mAs for each scan. The C-arm acquisition geometry parameters are shown in table 4.3. The short scan FDK algorithm [36] was used to reconstruct 3D images from the simulated projections. In order to reduce noise in the reconstructed images while preserving the edges, we applied a 3D bilateral filter [114] with spatial-domain standard deviation $(1.5 \times 1.5 \times 1.5)$mm^3, kernel size $(3 \times 3 \times 3)$mm^3 and intensity-domain standard deviation of 0.05 normalized units. The filter parameters were determined experimentally as a tradeoff between noise reduction and preservation of low contrasted structures.

The simulated forward projections were generated utilizing the Philips-proprietary software package Radonis (Philips Research Europe, Hamburg, Germany). Mono-energetic x-rays were assumed, therefore the effects of beam hardening were not taken into account but were analyzed in separate experiments which are discussed in Sec. 4.4.3. The phantoms were assumed in the same position for both angiographic and rotational scans. In the case of real image acquisitions, 3D/2D registration [75] can be applied to align the 3D images to the 2D angiograms.

Given the simulated C-arm data, the estimated TACs were obtained by: applying image segmentation to the 3D reconstructed images, calculating the projection matrix $\boldsymbol{W}$ from the segmented regions, and estimating TACs from angiography according to Eq. (4.10). The estimated peripheral blood flow $\hat{pbf}$ was calculated from the estimated TACs by the slope method.

In terms of computation time, the current Matlab implementation, which is not optimized for speed, takes 3-8 minutes (depending on the number of segmented regions). The most time consuming tasks are the k-means subiterations in the segmentation algorithm that require handling of large memory blocks.

4.3.2 Evaluation

A quantitative assessment of the TAC estimation accuracy and of the blood flow estimation accuracy is carried out in the six VOIs shown in Fig. 4.3 (note that the VOIs are selected manually and do not correspond to segmented regions). Additionally, the error sources contributing to the TAC estimation error are investigated. Three error sources affect the TAC estimation error with each source being connected with a processing step of the algorithm: i) errors introduced by the inversion operation in the estimation procedure ii) errors due to the segmentation of reconstructed images iii) errors due to the modeling assumptions on TAC homogeneity (Eq. 4.1).

Three evaluation metrics are defined to assess the contribution of each error source to the TAC estimation error: the TAC estimation error, the segmentation error, the modeling error. The evaluation metrics are evaluated at different points of the processing chain. Each metric contains the contribution of one or more error sources (Fig. 4.4). The metrics are assessed by comparison of the CTP TACs with the estimated TACs, and with intermediate results obtained from the segmentation. Their definition is based on the mean squared difference between the true TACs $\mu(\boldsymbol{x}, t)$ in the CTP phantom and a given TAC estimate $g(\boldsymbol{x}, t)$:

$$e^2(g, VOI) = \frac{1}{T|VOI|} \int_{\boldsymbol{x} \in VOI} \sum_t [\mu(\boldsymbol{x}, t) - g(\boldsymbol{x}, t)]^2 d\boldsymbol{x} \tag{4.11}$$

The metrics are averaged over all voxels within a VOI and over the time points ($|VOI| = \int_{\boldsymbol{x} \in VOI} d\boldsymbol{x}$ denotes the VOI size). The evaluation metrics are defined as follows:

- **TAC estimation error** $e(\hat{\mu}_{k(\boldsymbol{x})}, VOI)$: is defined as the mean square difference between the CTP TACs and the estimated TACs $\hat{\mu}_{k(\boldsymbol{x})}$ where $k(\boldsymbol{x})$ is the region index at location $\boldsymbol{x}$ for the segmentation of reconstructed images. This metric includes the contribution of all sources i) ii) and iii).

- **Segmentation error** $e(\bar{\mu}_{k(\boldsymbol{x})}, VOI)$: is defined by considering the average CTP TACs in the segmented regions. This metric is defined as the mean square difference between the CTP TACs in the selected VOI and the average CTP TACs $\bar{\mu}_{k(\boldsymbol{x})}$ computed in the segmented regions $k(\boldsymbol{x})$. This metric includes the contribution of sources ii) and iii).

- **Modeling error on the Reference segmentation** $e(\bar{\mu}_{k_{Ref}(\boldsymbol{x})}, VOI)$: this metric coincides with source iii) and evaluates the validity of the modeling assumptions on TAC homogeneity (Eq. 4.1). It is defined by considering a Reference segmentation $k_{Ref}(\boldsymbol{x})$. The Reference segmentation represents the optimum segmentation in terms of homogeneity. The Reference segmentation is obtained by applying the segmentation algorithm directly to the CTP TACs (i.e. by taking the feature vector $\boldsymbol{f}(\boldsymbol{x})$ equal to the CTP TACs $\mu(\boldsymbol{x}, t)$), which corresponds in fact to minimizing TACs inhomogeneity in the segmented regions.

  Given the Reference segmentation $k_{Ref}(\boldsymbol{x})$, $e(\bar{\mu}_{k_{Ref}(\boldsymbol{x})}, VOI)$ is defined as the mean square difference between CTP TACs and the average CTP TACs $\bar{\mu}_{k_{Ref}(\boldsymbol{x})}$ in the segmented regions $k_{Ref}(\boldsymbol{x})$. Note that the Reference segmentation $k_{Ref}(\boldsymbol{x})$ is introduced for two reasons: to assess the validity of the homogeneity assumptions and to provide a reference for the evaluation of the segmentation (see Sec. 4.4.1). In the experiments $k_{Ref}(\boldsymbol{x})$ is never used for the estimation of TACs from the angiograms.

The relative contribution of each error source to the TAC estimation error is quantified as a proportion to the TAC estimation error as follows (Fig. 4.4):

- contribution of source i) by $(e(\hat{\mu}_{k(\boldsymbol{x})}, VOI) - e(\bar{\mu}_{k(\boldsymbol{x})}, VOI))/e(\hat{\mu}_{k(\boldsymbol{x})}, VOI)$.
- contribution of source ii) by $(e(\bar{\mu}_{k(\boldsymbol{x})}, VOI) - e(\bar{\mu}_{k_{Ref}}(\boldsymbol{x}), VOI))/e(\hat{\mu}_{k(\boldsymbol{x})}, VOI)$.
- contribution of source iii) by $e(\bar{\mu}_{k_{Ref}}(\boldsymbol{x}), VOI))/e(\hat{\mu}_{k(\boldsymbol{x})}, VOI)$.

To compensate for different contrast levels in the VOIs, the evaluation metrics are normalized by the mean peak attenuation over the TACs in the VOI. The global TAC estimation error, i.e. the TAC estimation error $e(\hat{\mu}_{k(\boldsymbol{x})}, VOI)$ with VOI extended to the entire volumetric image, is assessed for different numbers of segmented regions to analyze the dependency of the accuracy on the numbers of segmented regions.

The error analysis for the estimated blood flow $\hat{pbf}$ consists of a qualitative and quantitative comparison of $\hat{pbf}$ with the true blood flow pbf. The qualitative comparison is performed by visual comparison of the blood flow maps. The quantitative comparison is performed by using the Bland-Altman plot [7] which measures the agreement between $\hat{pbf}$ and pbf based on the difference $Diff_{pbf} = \hat{pbf} - pbf$ against the mean $((\hat{pbf} + pbf)/2)$. The Bland-Altman analysis was performed for Case 1 within the VOIs Tissue 1, Tissue 2 and Tissue 3 (Fig. 4.3(a)), and for Case 2 within the VOIs Tissue 1, Tissue 2 and Hypo tissue (Fig. 4.3(b)). The impact of the number of segmented regions is also assessed in the analysis.

4.4 Results and discussion

4.4.1 Segmentation of reconstructed images

In Fig. 4.5 the results of the segmentation for Case 1 are shown. Figures 4.5(e)-(g) show the segmentation $k(\boldsymbol{x})$ of the reconstructed images obtained with the proposed segmentation method. Figure 4.5(a) and 4.5(b)-(d) show the time-to-peak (TTP) of the CTP phantom and the Reference segmentation $k_{Ref}(\boldsymbol{x})$, respectively. These figures are used for evaluation of $k(\boldsymbol{x})$.

To clearly visualize the segmented regions, we associated each region with the average time-to-peak (TTP) of the CTP TACs over the region: for each segmented region we fetched the corresponding TACs in the CTP phantom and we calculated the average TTP, then we associated a color to the region according to the average TTP. The correct segmentation is then assessed by the color similarity between the segmented regions and the CTP phantom. Typically, arterial exhibit early TTP and are given in dark red, tissue regions have intermediate TTP and are given in orange, veins have late TTP and are given in yellow. In the TTP image (Fig. 4.5(a)) two arteries (circles A1 and A2) and 2 veins (circles V1 and V2) can be identified by the early and late TTP, respectively.

In Fig. 4.5(b)-(d) and 4.5(e)-(g), the solid circles around arteries and veins indicate correct segmentation (i.e. similar in color and shape to the TTP of the CTP phantom), while the dashed circles indicate erroneous segmentation due to mixed regions. Mixed regions, containing both arteries and veins, can be observed in the segmentation with 50 regions shown in Fig. 4.5(f). Here the vein regions in V2 extend over the arterial regions in A2 and therefore they exhibit earlier TTP than in the CTP phantom (cf. V2 Fig. 4.5(f) with V2 in Fig. 4.5(a)). A similar effect occurs between the artery A1 and the vein V1. These errors are caused by the lack of temporal information in the reconstructed images. Because of this effect, arteries and

veins that exhibit similar contrast density in the reconstructed images are joined in the same segmented regions. The use of more segmented regions and of the neighborhood information, as shown in Fig. 4.5(g), allows a finer segmentation of the vessel borders which improves the separation of arteries and veins. Here in fact the average TTP in V1 and V2 is closer to that in the CTP phantom, however in V2 some mixed regions from tissue (yellow areas) and artery borders (orange areas) are still present.

4.4.2 Regularized estimation of TACs

For accurate and robust estimation of TACs, the number of retained singular values i_{Reg} (Sec. 4.2.3) for spatial regularization is selected based on analysis of the TAC estimation error. In Fig. 4.6(a) the global estimation error $e(\hat{\mu}_{k(\boldsymbol{x})}, VOI)$ is plotted against the number of retained singular values i_{Reg} for a segmentation with 300 regions. In Fig. 4.6(b) the TAC estimation error $e(\hat{\mu}_{k(\boldsymbol{x})}, VOI)$ in 6 VOIs is plotted against i_{Reg}. The optimal i_{Reg}, in terms of minimal $e(\hat{\mu}_{k(\boldsymbol{x})}, VOI)$, differs from one VOI to the other. In low enhanced structures as tissue (i.e. regions with low signal-to-noise levels), the TAC estimation benefits from stronger regularization which attenuates noise in the TACs; here the optimal i_{Reg} occurs between 40 and 100 retained singular values. For strongly enhanced regions such as arteries and veins (i.e. regions with high signal-to-noise levels), the estimation error is constant between 300 and 150 retained singular values and then increases for lower number of retained singular values due to attenuation of the TAC amplitude. Consequently, the number of retained singular values i_{Reg} is chosen as a tradeoff by selecting the one which minimizes the global estimation error. In Fig. 4.6(a), the optimal i_{Reg} occurs at 60 retained singular values.

4.4.3 TACs and Blood flow estimation error

Figure 4.7 shows the TAC evaluation metrics assessed in the individual VOIs for a segmentation with 300 regions. Figure 4.8 shows the global TAC estimation error against different numbers of segmented regions. Figure 4.9 shows the estimated AIF for different numbers of regions along with the true AIF derived from the CTP data.

The results show that TAC estimation accuracy varies between VOIs (see Fig. 4.7) and depends to some extent on the number of segmented regions (Fig. 4.8). For most VOIs TAC accuracy was in the range $10 - 25\%$. Concerning the accuracy of arterial TACs, which is crucial for perfusion estimation, the minimum estimation error was obtained at 300 and 150 regions for Case 1 and Case 2, respectively. For these settings, the error on the arterial peak, which influences directly the estimated blood flow, was below 10%. Given these results we can state that, as concerning estimation of arterial TACs, the proposed method is potentially more accurate than methods based on multiple slow C-arm rotations, which require temporal interpolation of TACs [19] or temporal modeling, like the method proposed in Chapter 2. In fact, the high temporal resolution achievable by angiography leads to more accurate estimation of fast dynamics.

As for the influence of the number of segmented regions on TACs accuracy, the global TAC estimation error (Fig. 4.8) exhibits a minimum between 50 and 100 regions and has a slight tendency to increase towards higher numbers of regions. The increase is attributed to the inversion of the projector operator $\boldsymbol{W}$, which becomes more unstable for larger numbers of regions due to higher overlap of the regions in the projection domain [30].

The analysis of the error sources shows that errors due to the inversion operation (i.e. source i)) have the highest contribution (around 50%) to the TAC estimation error, while segmentation errors and modeling errors have a lower contribution ($5-30\%$). This can be observed from the large difference between the error plot in Fig. 4.7(a) and 4.7(b) and between 4.7(d) and 4.7(e). The low contribution of the modeling errors to the TAC estimation error shows that inhomogeneity is not a limiting factor for the estimation accuracy. The modeling errors were less than 8% relative to the mean TAC peak (Fig. 4.7(c) and 4.7(f)), which demonstrates that the assumption on contrast homogeneity holds for the examined CTP data.

Beam hardening artifacts, due to the non linear relation between measured line integrals and object thickness [61], may influence the TAC accuracy in two ways: i) by generating artifacts in the reconstructed 3D images impacting the segmentation, ii) by causing quantitative errors in the measured 2D angiograms. While the first source of error is partially compensated in the system with a correction algorithm [46], the second is not compensated and can cause approximation errors in the 2D line integrals resulting in additional estimation errors in Eq. 4.8. These approximation errors were quantified through additional simulations on geometrical phantoms which are not documented here for brevity (see Chapter 6). The simulations showed that for typical leg thicknesses and typical contrast concentrations used in perfusion analysis, relative errors are negligible in comparison with the other error sources.

Perfusion maps obtained for different numbers of segmented regions are shown in Figs. 4.10 and 4.11, for Case 1 and Case 2, respectively. Here also the Bland-Altman plots of the corresponding blood flow estimations are shown. In the Bland-Altman plots, the mean difference $\overline{Diff}_{pbf}$ is depicted by the black horizontal line. The mean difference plus-minus twice the standard deviation (SD) of the difference $\overline{Diff}_{pbf} \pm 2\sigma_{Diff_{pbf}}$ is depicted by the horizontal green line. The Bland-Altman plots are characterized by linear-like distributions, each line representing samples belonging to the same segmented region: in fact, in each region the estimated blood flow is constant and therefore the difference $Diff_{pbf}$ is linear with pbf. In Fig. 4.10(d) and 4.11(d) $\overline{Diff}_{pbf}$ and SD are plotted for different numbers of segmented regions.

Visual comparison between the estimated blood flow maps and the true maps shows good agreement and correct separation of hypoperfused and normally perfused areas (see Fig. 4.10(c) and 4.11(c)). The estimated blood flow maps are characterized by a spatial averaging effect which is caused by the homogeneity assumption in the segmented regions. This averaging effect is particularly noticeable in the case of fewer segmented regions (Fig. 4.10(b)). By using more segmented regions, more details of the perfusion patterns are recovered and vessels are better identified; however, higher noise levels are observed due to instability in the inversion of the projection operator.

As for the quantitative accuracy of the estimated blood flow, for the estimation with optimal number of segmented regions, the Bland-Altman analysis showed a mean difference of 1 ± 4 ml/100ml/min and 2 ± 11 ml/100ml/min for Case 1 and Case 2, respectively. True CTP blood flow values were in the range $7-20$ ml/100ml/min and $5-80$ ml/100ml/min. The level of accuracy was sufficient for correct identification of hypoperfused areas with low signal-to-noise ratio, which proved to be challenging in previous studies [30]. The improved accuracy is attributed to the use of temporal and spatial regularization in the solution of the inverse problem. A slight tendency to underestimate low perfused areas and overestimate high perfused areas can be observed from the Bland-Altman plots (Fig. 4.10(f) and 4.11(f)). This can be attributed to the type of regularization which tends to attenuate low enhanced regions, thus emphasizing high enhanced regions to balance the total attenuation. As for the influence of the number of segmented regions, the optimal blood flow accuracy was measured at 100 and

50 segmented regions for Case 1 and 2, respectively. The increase of the number of regions up to 300 did not improve the accuracy as $\overline{Diff}_{pbf}$ and SD remain almost constant with a slight tendency to increase (Fig. 4.10(d) and 4.11(d)). The increase of $\overline{Diff}_{pbf}$ and SD can be attributed to the higher complexity at higher number of regions.

4.5 Summary and Conclusion

In this chapter we have introduced a method for periprocedural perfusion estimation in peripherals using angiographic C-arm systems. The method relies on planar angiography acquired from a fixed viewing angle, and on two 3D images reconstructed from rotational scans. The method assumes homogeneous contrast propagation within 3D regions segmented from the reconstructed images. A dedicated segmentation method, which exploits local contrast homogeneity and connectivity of the anatomical regions, is applied to tackle the lack of temporal information in the 3D reconstructed images. The perfusion is estimated by mapping the 2D blood flow acquired with angiography to the 3D segments via inversion of the projection operator. Instability of the inversion operation is addressed by applying spatial and temporal regularization.

Simulation experiments on CTP data show that the estimated perfusion maps are characterized by a spatial averaging effect which tends to smooth fine structures. However, the level of spatial detail of the estimated blood flow is sufficient for quantitative perfusion estimation in the legs, since here, the perfusion is associated with large muscle compartments exhibiting quasi homogeneous contrast enhancement. Inaccuracies in the estimation of blood flow originate mainly from errors due to the inversion operation. The combined use of spatial and temporal regularization proved to be an effective way to limit these inaccuracies. In general, the accuracy of the proposed method is sufficient for quantitative differentiation of healthy and hypoperfused tissues.

In conclusion, our simulation study proved the feasibility of C-arm interventional perfusion imaging by combination of planar DSA and 3D reconstructions. The method can be potentially used for outcome assessment of revascularization procedures by comparing post-interventional perfusion measurements to pre-interventional perfusion measurements. In future studies, the clinical validation on C-arm data needs to be carried out. In particular, the validation against gold standard modalities (e.g. CTP or MR perfusion) needs to be carried out to assess the effective accuracy of the estimated perfusion maps.

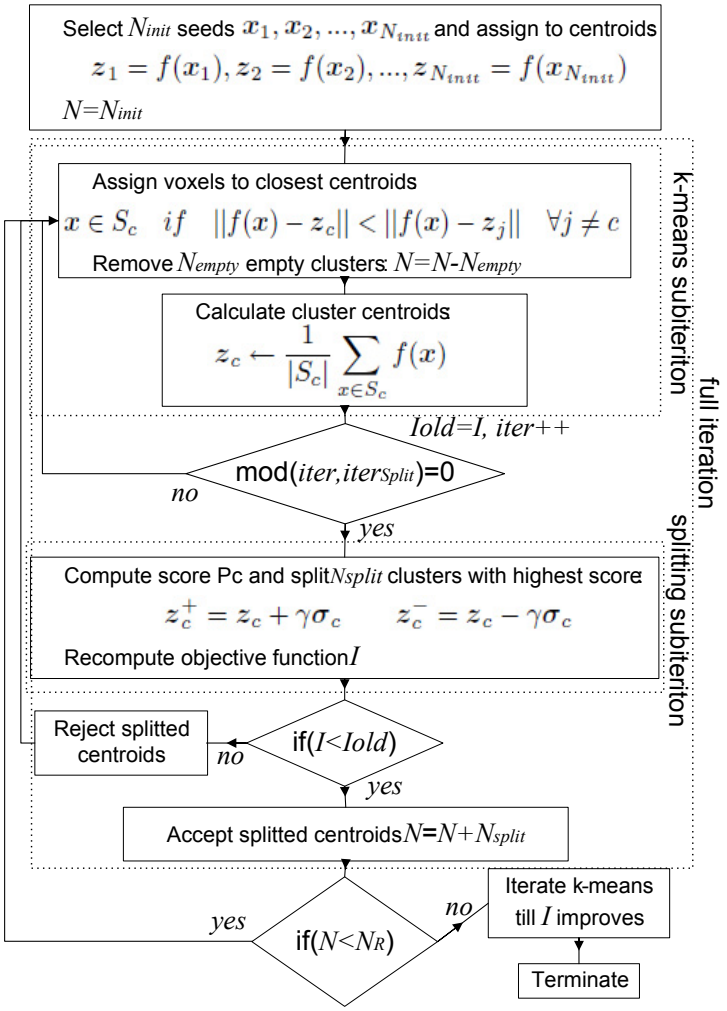

Figure 4.2. Workflow of the segmentation algorithm. Cluster centroids are initialized with seeds selected by the user. Each segmentation iteration consists of a number of $iter_{Split}$ k-means subiterations and a cluster splitting subiteration. The mechanism to alternate k-means and splitting is represented by the modulo operation *mod*. After splitting, the objective function is recalculated and the new centroids are accepted only if the objective function has improved with respect to the old value before the splitting.

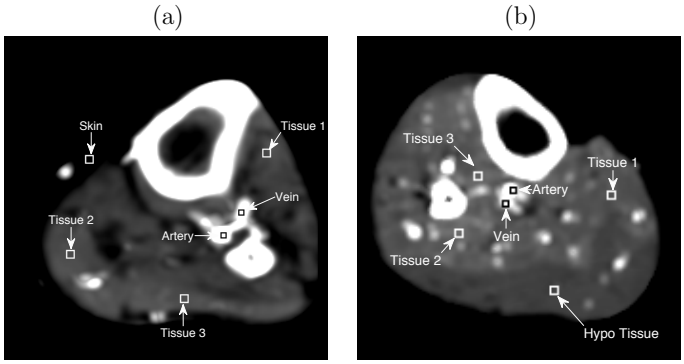

Figure 4.3. CTP data: temporal maximum of voxels' attenuation in the central axial slice, range=[0 300]HU (a) Case 1. The rectangles depict the location of the 6 VOIs used for evaluation: Artery, Vein, Tissue 1, Tissue 2, Tissue 3 and Skin (b) Case 2. The rectangles depict the location of 6 VOIs used for evaluation: Artery, Vein, Tissue 1, Tissue 2, Tissue 3 and Hypo perfused tissue.

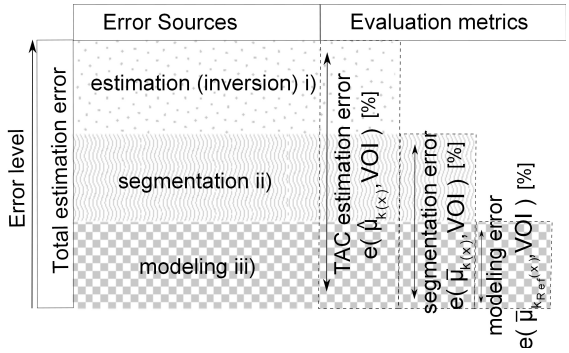

Figure 4.4. Error sources and their relation with the evaluation metrics. The y axis indicate the error level. The error sources are represented as pattern boxes along the x axis. The evaluation metrics: the TAC estimation error $e(\hat{\mu}_{k(\boldsymbol{x})}, VOI)$, the segmentation error $e(\bar{\mu}_{k(\boldsymbol{x})}, VOI)$ and the modeling error $e(\bar{\mu}_{k_{Ref}(\boldsymbol{x})}, VOI)$ assess the contribution of one or more error sources. The TAC estimation error includes the contribution of all sources i), ii) and iii), the segmentation error includes the contribution of ii) and iii), the modeling error $e(\bar{\mu}_{k_{Ref}(\boldsymbol{x})}, VOI)$ coincides with source iii).

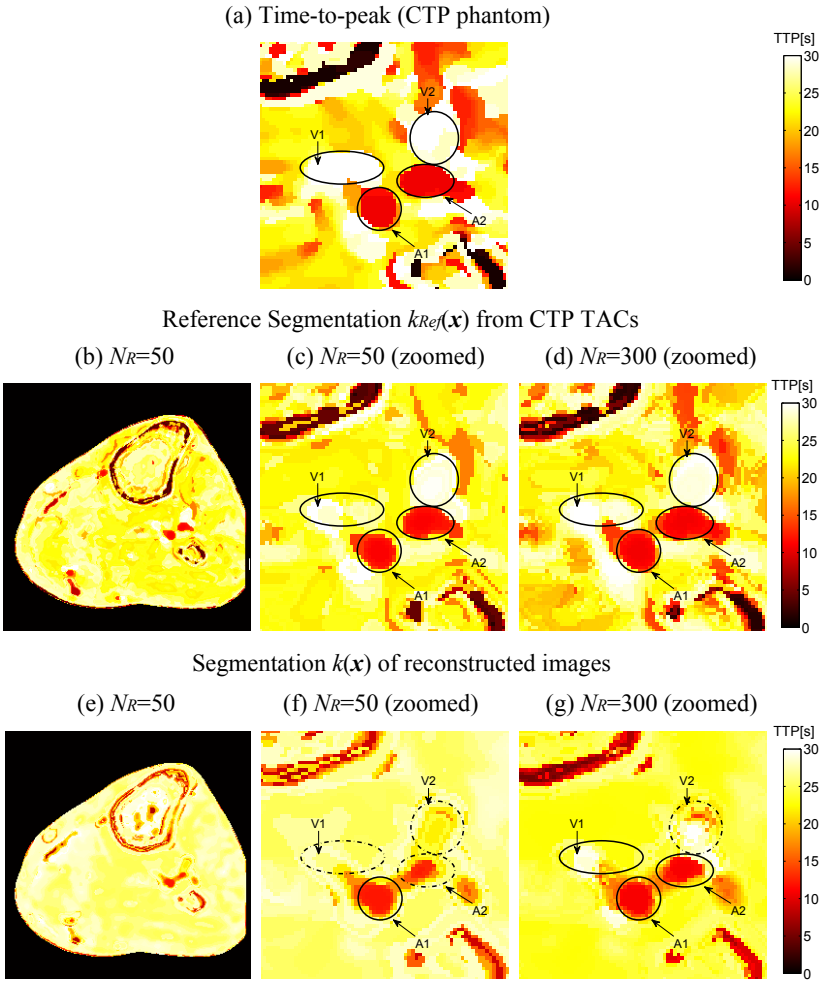

Figure 4.5. Segmentation in the central axial slice for Case 1. The segmented regions are colored according to the average time-to-peak of the corresponding CTP TACs. (a) Time-to-peak of the TACs in the CTP phantom (b)-(d) Reference segmentation $k_{Ref}(\boldsymbol{x})$ with 50 (b)(c) and 300 (d) segmented regions. The solid line circles in (a), (c) and (d) indicate correct (i.e. similar in color and shape to the CTP phantom) segmentation of arteries (A1 and A2) and veins (V1 and V2). (e)-(g) Segmentation $k(\boldsymbol{x})$ of reconstructed images for 50 (e)(f) and 300 (g) segmented regions. The dashed line circles in (f) and (g) indicate erroneous segmentation of vessels due to mixed regions containing both arteries and veins.

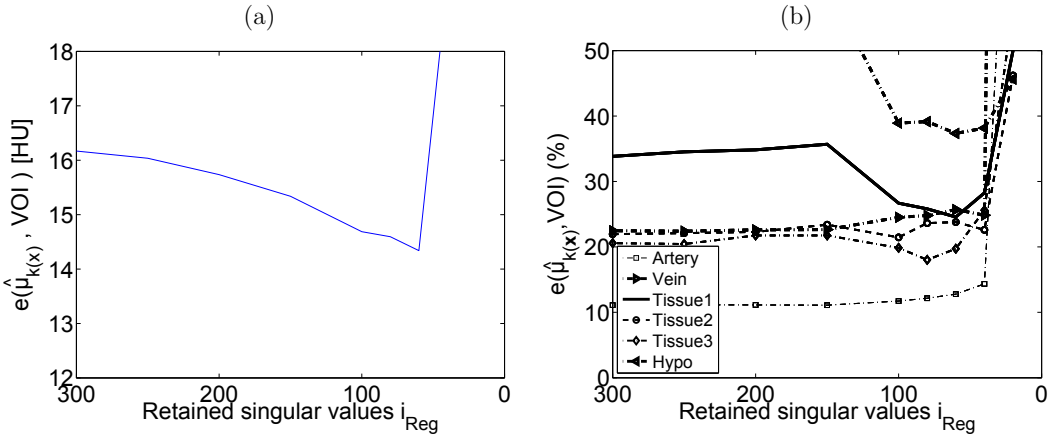

Figure 4.6. TAC estimation error against the number of retained singular values i_{Reg} for a segmentation $k(\boldsymbol{x})$ with 300 regions. (a) Global TAC estimation error. (b) TAC estimation error $e(\hat{\mu}_{k(\boldsymbol{x})}, VOI)$ computed in 6 VOIs.

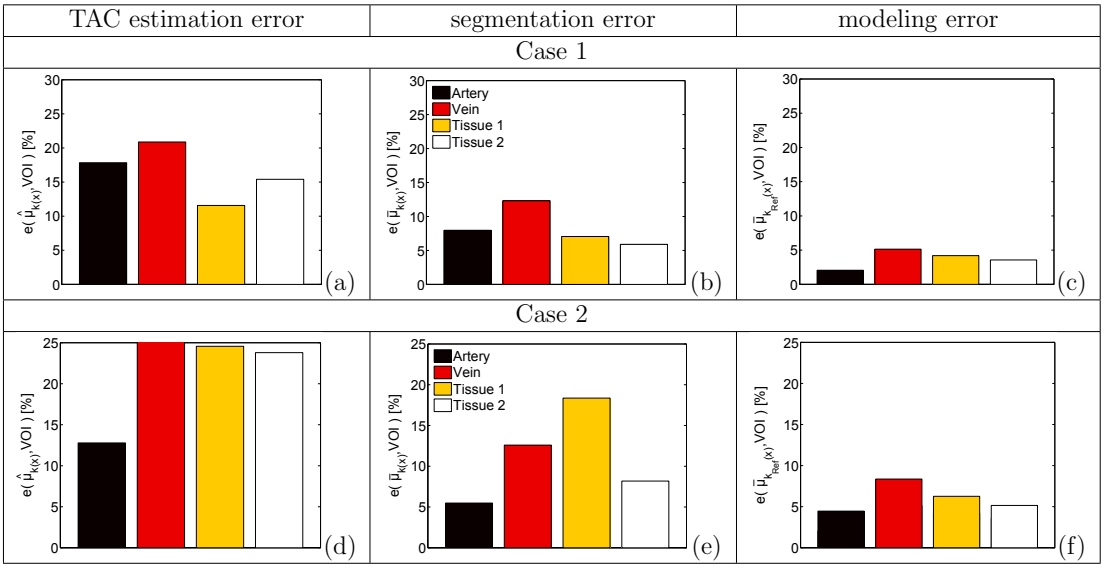

Figure 4.7. TAC error evaluation for an estimation with 300 segmented regions. The errors are assessed in 4 VOIs: Artery, Vein, Tissue 1 and Tissue 2. (a)(d) TAC estimation error $e(\hat{\mu}_{k(\boldsymbol{x})}, VOI)$. (b)(e) Segmentation error $e(\bar{\mu}_{k(\boldsymbol{x})}, VOI)$. (c)(f) Modeling error $e(\bar{\mu}_{k_{Ref}(\boldsymbol{x})}, VOI)$.

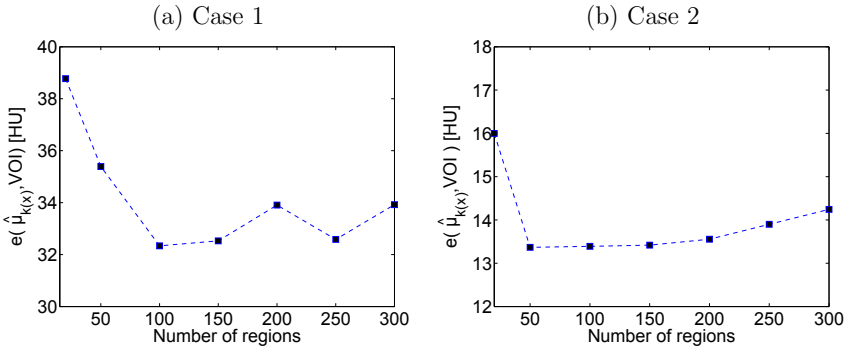

Figure 4.8. Global TAC estimation error against the number of segmented regions for Case 1 (a) and Case 2 (b)

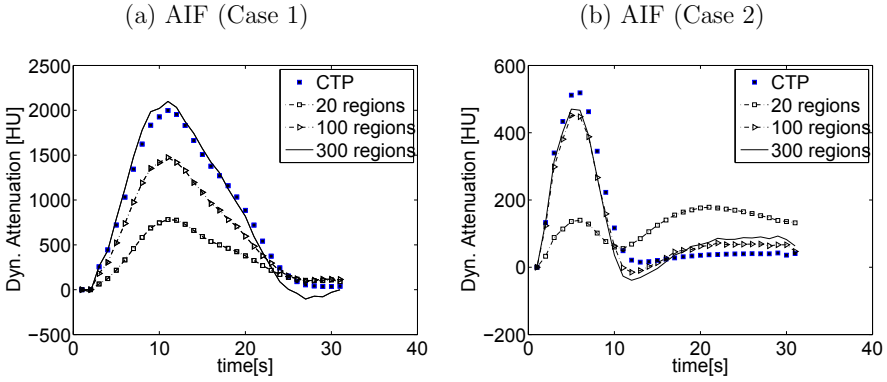

Figure 4.9. Estimated AIF for different numbers of segmented regions and true AIF computed from the CTP phantom. (a) Case 1, (b) Case 2.

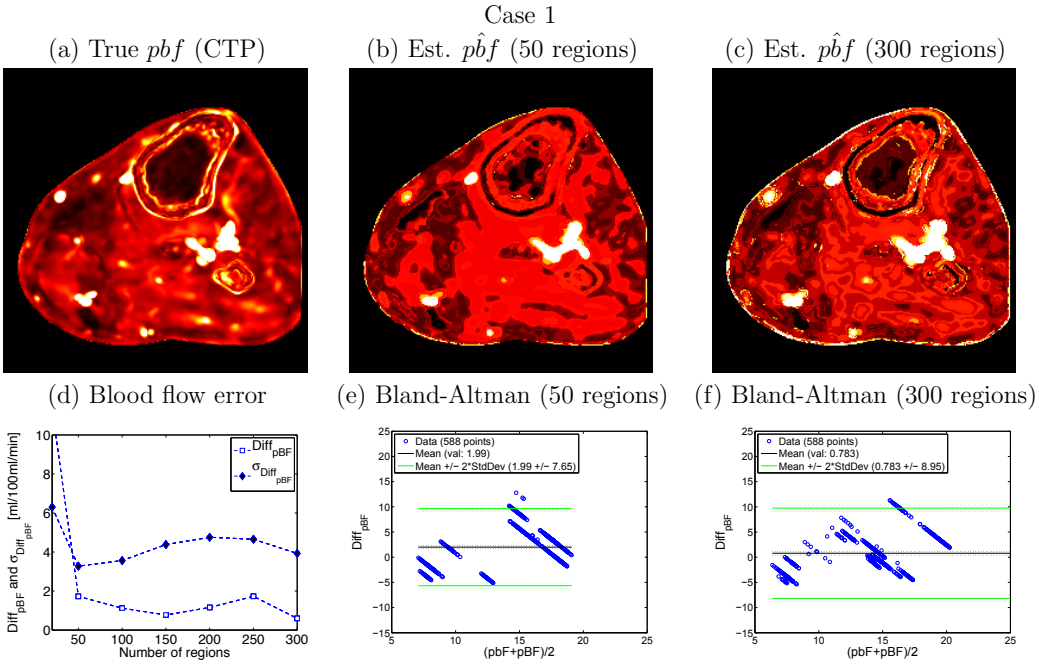

Figure 4.10. Estimated peripheral blood flow maps and Bland Altman analysis for Case 1. (a) True blood flow map computed from the original CTP TACs in the central axial slice, range=[0 50] ml/100ml/min. (b)(c) Estimated blood flow map for 50 (b) and 300 (c) segmented regions, range=[0 50] ml/100ml/min. (e)(f) Bland Altman plots related to the estimated blood flow with 50 (e) and 300 (f) segmented regions. The black and the green horizontal lines indicate the mean difference $\overline{Diff}_{pbf}$ and plus-minus twice the standard deviation of the difference $\pm 2\sigma_{Diff_{pbf}}$. $\overline{Diff}_{pbf}$ and $\sigma_{Diff_{pbf}}$ are calculated over the complete set of voxels related to 3 tissue VOIs. (d) Mean difference $\overline{Diff}_{pbf}$ and standard deviation of the difference $\sigma_{Diff_{pbf}}$ against the number of segmented regions.

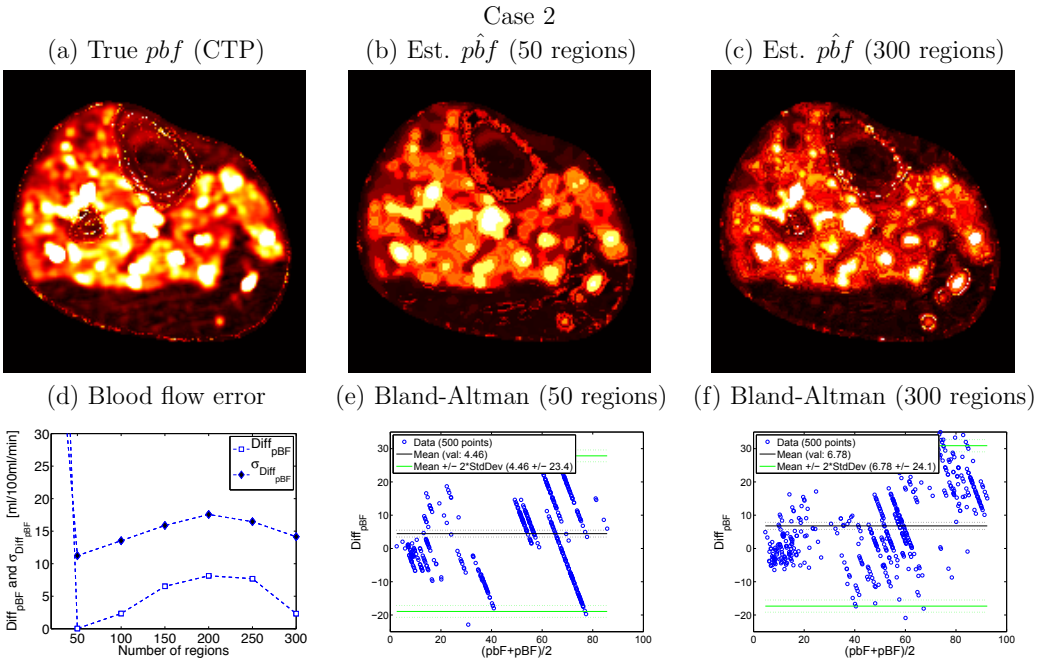

Figure 4.11. Estimated peripheral blood flow maps and Bland Altman analysis for Case 2. (a) True blood flow map, range=[0 100] ml/100ml/min. (b)(c) Estimated blood flow map for 50 (b) and 300 (c) segmented regions, range=[0 100] ml/100ml/min. (e)(f) Bland Altman plots.

Chapter Five

Feasibility evaluation of region-based perfusion estimation in peripherals using C-arm systems

Men love to wonder, and that is the seed of science.

— Ralph Waldo Emerson (1803-1882)

Abstract — In this chapter we evaluate the feasibility of perfusion estimation in peripherals using C-arms. The estimation is based on a method which combines a temporal angiographic sequence with two 3D images reconstructed from rotational scans. The method provides quantitative perfusion spatially averaged over multiple 3D regions. The practical issues relative to the implementation of the method in a clinical environment are tackled. In particular we define the injection protocol to acquire the contrast rotational scan and a strategy to register the 3D reconstructed images to the 2D angiograms. The method is evaluated on patient data acquired with a C-arm during the revascularization procedure. Several aspects are considered in the evaluation: consistency of the estimated contrast curves, contrast resolution and visual correspondence with MRA acquisitions.

Results showed a good consistency of the estimated curves with the measurements and a good capability to separate venous contrast enhancement from tissue contrast enhancement which is challenging from standard angiography. The contrast resolution was sufficient to differentiate low perfused regions, like fat tissues and hypoperfused tissues, from perfused muscle regions and arteries. When trying to obtain higher tissue contrast enhancement by increasing the volume of injected contrast (35 ml), image artifacts were experienced in the reconstructed image which makes the modeling of perfused regions more challenging. The optimal volume of injected contrast must be therefore defined such as to optimize the balance between contrast enhancement and artifacts in the reconstructed images. The image quality and contrast resolution in the MRA images was not sufficient for a comprehensive evaluation of the perfusion maps. The correspondence with the estimated perfusion maps in fact could only be confirmed for one of the two analyzed cases. This suggests that in future studies, for a more comprehensive evaluation of the perfusion estimation method, different imaging modalities (e.g. CTP, MR perfusion or PET) should be used.

Based upon: M. Giordano, E. P. A. Vonken, M. Bertram, W. P. T. M. Mali, M. A. Viergever and C. Neukirchen, "Feasibility evaluation of region-based perfusion estimation in peripherals using C-arm systems", *submitted*.

5.1 Introduction

Recently the treatment of peripheral arterial disease (PAD) has shifted from from open surgery toward percutaneous endovascularization procedures like balloon angioplasty and stenting [120]. These procedures have the aim to restore the blood flow to the diseased tissue by unblocking the obstructed artery with the support of catheters, balloons and stents. The angiosome model has been recently introduced to help the interventional radiologist in the selection of the vessel to be targeted for revascularization. According to the angiosome model [112] three-dimensional tissue blocks are fed by specific arteries named 'angiosomes'. By targeting the vessels feeding the diseased tissue area it has been showed that a better better blood re-perfusion of the diseased muscular territory can be achieved [2]. If perfusion in the diseased tissue area could be measured before and after the procedure, the surgeon could evaluate directly after treatment the technical success of the procedure. Currently revascularization procedures are assessed by X-ray digital subtraction angiography (DSA) [11] consisting of a temporal series of projection images acquired after short bolus injection. However, due to the projective nature of DSA, only qualitative information on the arterial blood flow is available, and no quantitative information on tissue perfusion can be assessed.

In order to measure tissue perfusion, like in CT perfusion (CTP) [71], dynamic contrast information in tissue and vessels is required. Dynamic contrast is measured as a time-attenuation-curve (TACs) related to a voxel or a region of interest. In CTP the temporal evolution of contrast is captured by fast and continuos rotations of the CT gantry during bolus injection.

Recently, several methods [18,84] have been proposed to estimate perfusion with slowly rotating C-arm angiographic systems which can be used in an interventional environment. C-arm systems have inferior capabilities in comparison to CT with respect to rotational range and speed. This makes the estimation of TACs challenging as less spatial and temporal information is available. In the method proposed in Chapter 2 and in that proposed by Ganguly *et al.* [25], multiple consecutive forward/backward short scans are performed and temporal models are fit to the acquired projection data in order to derive the TACs. However, the complex acquisition protocol makes the implementation of these methods in a clinical environment difficult. Another class of perfusion estimation methods is that based on the combination of DSA and 3D images which was first introduced by Taguchi [109] and developed further by us in Chapter 3 and 4. These methods are based on scanning protocols which can be realized on current C-arm systems. In the method proposed in Chapter 3 we assume a segmentation of the perfused territories which is derived from images reconstructed from C-arm scans. The 2D perfusion in the imaging plane is estimated by normalizing the line integrals in the DSA by the length of contrast material along the ray directions. The length of contrast material was determined from the segmentation assuming global contrast homogeneity. Results on data simulated from CTP acquisition showed that the accuracy of the estimated perfusion is limited due to spatial inhomogeneity of contrast. In Chapter 4 we relaxed the assumption on homogeneity by assuming a set of multiple segmented 3D regions sharing similar contrast dynamics. The key idea of this second approach is to map the 2D blood flow from the DSA to the 3D regions by inversion of regions' projections thus obtaining 3D region-based perfusion information. The segmented regions are identified from the reconstructed 3D images by applying a dedicated segmentation algorithm which exploits local contrast similarity. The mapping of blood flow from the DSA to the 3D regions is an ill-posed problem due to the overlap of the regions in the projection domain. This makes the resulting TACs prone to numerical oscillations [30]. To tackle instability, we apply temporal and spatial regularization (see Chapter 4). Results

obtained on data simulated from CTP acquisitions show that such method provides perfusion maps with a level of detail sufficient to detect all relevant perfusion patterns and hypoperfused areas.

In this chapter we evaluate the feasibility of the 3D region-based estimation method on clinical data acquired with a C-arm during revascularization procedures. In particular we evaluated: i) the correlation of the estimated TACs with the corresponding time intensity curves (TICs) in DSA ii) the correspondence of the estimated perfusion maps with maps obtained with MRA of the same patients iii) the capability to detect low contrast details as hypoperfused regions. Additionally some practical aspects like the injection protocol (Sec. 5.2) and the registration of the reconstructed 3D images to the DSA (Sec. 5.3.1) are discussed. In Section 5.3.2 and 5.3.3 we shortly describe the segmentation and the TAC estimation procedure, however for a detailed description of the method we refer to Chapter 4.

5.2 Image acquisition workflow

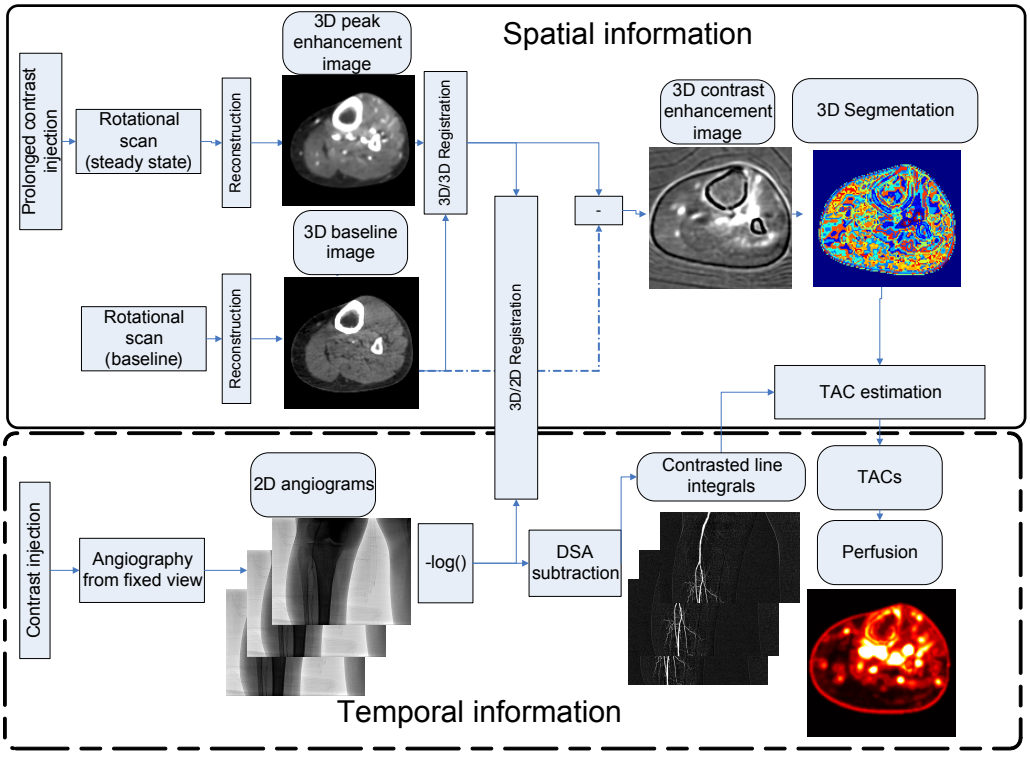

Figure 5.1. Image acquisition workflow.

We acquired X-ray images with a C-arm during treatment of patients affected by arterial occlusions and processed the images 'offline' with the region-based perfusion estimation method. The images were acquired on two patients (Case 1 and Case 2) which were treated by angioplasty with the aim to restore blood flow to the muscle of the lower leg. The images

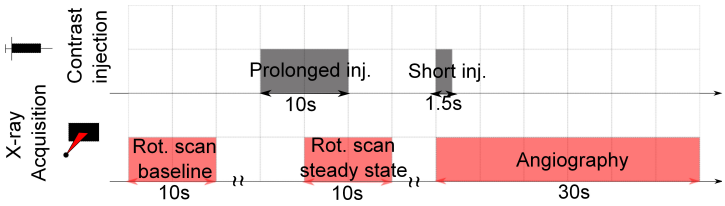

Figure 5.2. Injection protocol for the measurement of perfusion.

were acquired with an Allura Xper FD20 system (Philips Healthcare, Best, The Netherlands) immediately after treatment.

The acquired data for each patient consist of two sets of images. The first set contains 3D spatial information on the perfused anatomy and consists of two 3D images reconstructed from as many rotational scans, one baseline scan, from which a baseline image $\mu_0(\boldsymbol{x})$ is reconstructed, and one steady state scan acquired with a prolonged contrast injection, from which a peak contrast enhancement image $\mu_s(\boldsymbol{x})$ is reconstructed. The second set of images contains temporal contrast information and consists of planar (i.e. 2D) angiography acquired after short bolus injection from a fixed viewing position. After the acquisition, the two sets of images are processed to calculate the perfusion (i.e. tissue blood flow). The method is based on a segmentation of the reconstructed images in homogeneous regions and a mapping procedure which maps the 2D blood flow information from the angiography to the 3D segmented regions. A complete workflow of the method is shown in Fig. 5.1.

Each rotational scan consists of 626 projections acquired during a rotation of the C-arm around the patient at a frame rate of 60 frames/s. For the rotational steady state scan, a prolonged contrast injection of a iodine solution (Visipaque, 270 mg iodine/ml diluted with saline, GE Healthcare, Princeton, New Jersey) of the duration of 10s was administrated in the superficial femoral artery. The injection rate was 3.5 ml/s for Case 1 and 2.5 ml/s for Case 2. The prolonged injection ensures stable and maximum contrast enhancement in vessels and tissue throughout the scan [124]. The acquisition was started with a delay of 5s with the respect to the beginning of the contrast injection to ensure fully opacification in the vasculature. The injection protocol including rotational acquisitions and angiography is illustrated in Fig. 5.2. After acquisition of the rotational scan, a cone beam reconstruction algorithm [36] was used to reconstruct 3D images from the acquired projections. The 3D reconstructed images are isotropic and consist of $(256 \times 256 \times 198)$voxels encompassing a $(252 \times 252 \times 194)\text{mm}^3$ field of view.

The angiographic scan was acquired from a fixed viewing position which was selected to have a clear visualization of the arterial flow. The angiographic scan consists of a temporal series of projections acquired at a frame rate of 1 frame/s after a short undiluted bolus injection (270 mg iodine/ml). The temporal series covers a time interval of 30 s and shows the contrast propagation in arteries, tissue and veins on the imaging plane. The projection images consist of images of (792×1024)pixels encompassing a $(296 \times 383)\text{mm}^2$ field of view. The measured angiograms are transferred to the workstation and later combined with the 3D data for the estimation of perfusion. Prior to TAC estimation, the reconstructed 3D images are registered to the 2D angiograms [75] to ensure correct mapping of 3D volumes into the 2D angiograms (Sec. 5.3.1).

5.3 Data processing

In the following we introduce the processing steps necessary for the estimation of perfusion from the acquired data: 3D/2D registration, segmentation and TAC estimation. For a complete description of the method please refer to Chapter 4.

5.3.1 3D/2D registration

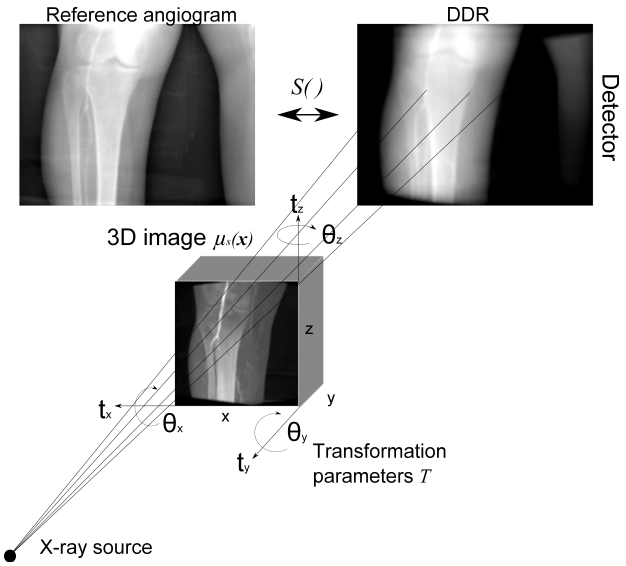

Figure 5.3. Illustration of the 3D/2D registration method. A 3D rigid transformation T is applied to the peak enhancement image $\mu_s(\boldsymbol{x})$. Then the 3D image is projected to the imaging plane generating a DDR. The DDR is compared to the reference angiogram according to the metric $S()$ and the process is repeated until convergence.

The first processing step consists of applying a 3D/2D registration to register the reconstructed 3D volumes to the temporal sequence of angiograms. By applying 3D/2D registration, a motion-free backprojection of the angio data into the volumetric segments can be performed to estimate the TACs (Sec.5.3.3).

The 3D/2D registration algorithm aims at finding a geometrical 3D transformation T of the 3D volume such that its projection, called digitally reconstructed radiograph (DDR), matches the angiographic data [95]. To maximize the similarity between the DDR and the angiography, the 3D/2D registration is applied on the 3D peak enhancement image μ_s and on a reference angiogram selected from the angiographic sequence (see Fig. 5.3). The reference angiogram is selected as the one showing the maximum contrast intensity in the artery similarly as in [104]. Motion in the angiography between consecutive time frames is assumed negligible.

For the registration algorithm we used a 3D rigid-body transformation $T = (\theta_x, \theta_y, \theta_z, t_x, t_y, t_z)$ [95] where $(\theta_x, \theta_y, \theta_z)$ are the 3 rotation parameters and (t_x, t_y, t_z) are the translation parameters. The optimal transformation parameters $\dot{T}$ are estimated by iteratively maximizing

(minimizing) a similarity (dissimilarity) metric $S()$ calculated between the current DRR and the reference angiogram:

$$\dot{T} = \arg\min_{T}\{S(\ell_{ref}, F(T(\mu_s(\boldsymbol{x}))))\} \tag{5.1}$$

F indicates the forward projection operator which projects voxels into the imaging plane. Three different similarity (dissimilarity) metrics were compared in the evaluation: the sum of squares difference (SSD) [117], the normalized cross correlation (NCC) [96] and the normalized mutual information (NMI) [97]. After running the registration algorithm with all three different metrics, the transformation yielding the best alignment was selected while all the other transformations were discarded. The quality of the registration was judged visually by assessing the alignment in the main artery (Sec. 5.4.1) and at the bifurcations. The minimization in Eq. 5.1 was carried out by the Levenberg-Marquardt algorithm [99]. The registration was initialized assuming no motion between the rotational and the angiographic scans (i.e. all rigid-body parameters equal to zero) which for both cases was not far from the optimal transformation.

5.3.2 Segmentation

A segmentation algorithm is applied to the reconstructed 3D images to identify 3D regions with similar contrast characteristics. Note that the segmentation can be applied before or after 3D/2D registration. In order to enhance contrast differences, the segmentation algorithm is applied to the contrast enhancement image $\mu_{enh}(\boldsymbol{x})$ obtained by subtraction of the baseline image $\mu_0(\boldsymbol{x})$ from the peak enhancement image $\mu_s(\boldsymbol{x})$: $\mu_{enh}(\boldsymbol{x}) = \mu_s(\boldsymbol{x}) - \mu_0(\boldsymbol{x})$. This image provides the volumetric blood volume fraction [80] in the object. Prior to subtraction, the baseline image $\mu_0(\boldsymbol{x})$ is registered to the peak enhancement image $\mu_s(\boldsymbol{x})$ by 3D rigid registration to compensate for motion between the baseline and the contrast enhancement scan [124].

The segmentation algorithm works on the assumption that areas with similar blood volume exhibit similar contrast dynamics. Voxels with similar intensity (i.e. blood volume) in $\mu_{enh}(\boldsymbol{x})$ are segmented in regions so as to to maximize regions homogeneity and connectivity. A modified k-means algorithm [78] is applied to determine the regions. A detailed description of the segmentation algorithm is provided in Chapter 4.

5.3.3 TAC estimation

The TAC estimation method aims at estimating the TACs $\mu(t, \boldsymbol{x})$ (t is the time index and $\boldsymbol{x}$ is the spatial location) from the acquired angiograms. The estimation relies on the segmented 3D regions (Sec. 5.3.2) and on a set of contrasted line integrals. The contrasted line integrals $\ell^*(t, v)$ are derived from the angiograms by applying the log operation to the measured x-ray intensities, and then by subtracting the DSA mask (i.e. the first non contrasted time frame) (see Fig. 5.1).

The TAC estimation procedure assumes that within the 3D segmented regions the TACs are spatially homogeneous and can be approximated by a characteristic TAC: $\mu(\boldsymbol{x}, t) \simeq \bar{\mu}_{k(\boldsymbol{x})}(t)$ where $k(\boldsymbol{x})$ is the region index at $\boldsymbol{x}$. A set of modeled contrasted line integrals $\boldsymbol{\ell}(t)$ is obtained as linear combination of the characteristic TACs and the forward projection operator $\boldsymbol{W}$:

$$\boldsymbol{\ell}(t) = \boldsymbol{W} \cdot \bar{\boldsymbol{\mu}}(t) \tag{5.2}$$

$\boldsymbol{W}$ is the forward projection operator and maps the image segments into the projection domain. To estimate the TACs $\hat{\boldsymbol{\mu}}(t)$, the least square difference between the modeled line integrals $\boldsymbol{\ell}(t)$ and the acquired line integrals $\boldsymbol{\ell}^*(t)$ is minimized:

$$\hat{\boldsymbol{\mu}}(t) = \arg\min_{\hat{\boldsymbol{\mu}}(t)} ||\boldsymbol{\ell}^*(t) - \boldsymbol{\ell}(t)||^2 \qquad \forall t \tag{5.3}$$

The solution to this least square problem is found by inversion of the projection operator $\boldsymbol{W}$:$\hat{\boldsymbol{\mu}}(t) = \boldsymbol{W}^+ \cdot \boldsymbol{\ell}^*(t)$. Instability of the solution of the inverse problem is tackled by applying spatial and temporal regularization (see Chapter 4). Successively to TACs estimation, the blood flow is calculated by the well established slope method [80]. Since the estimated blood flow is constant within the 3D segmented regions, the blood flow values may present sharp edges between the regions (see Chapter 4). To smooth the edges between regions we filtered the blood flow maps with a 3D gaussian filter with kernel size $(3 \times 3 \times 3)\text{mm}^3$ and standard deviation $(1.5 \times 1.5 \times 1.5)\text{mm}^3$.

5.4 Results

In the following section we present the results obtained with the perfusion estimation method. In Sec. 5.4.1 we assess the results of the 3D/2D registration. In Sec. 5.4.2 we evaluate the consistency of the 3D estimated TACs with the corresponding TICs in DSA. In Sec. 5.4.3 we assess the correspondence of the estimated perfusion maps with maps obtained from MRA acquisitions and then we assess the contrast resolution of the estimated maps.

5.4.1 Visual evaluation of 3D/2D registration

We evaluated the 3D/2D registration algorithm by assessing the alignment of the DDRs and the reference angiogram ℓ_{ref} for different similarity metrics. Since there is not a 'gold-standard' transformation available, the registration was evaluated visually by assessing the alignment of the enhanced vessels.

Figure 5.4(a) and 5.4(b) show the DDR and the reference angiogram. To better visualize enhanced vessels in the DDR, prior to forward projection the baseline image is subtracted from the peak enhancement image; similarly, in the reference angiogram the vessels were enhanced by subtracting the DSA mask.

The difference between the DDR and the reference angiogram (cf. Fig. 5.4(a) and 5.4(b)) are attributed to: i) the different x-ray energy spectra in angiographic and rotational mode [95] ii) different injection protocols iii) different position of the catheter during the contrast injection. Figure 5.4(c)-(e) show a chessboard mix of the DDR and of the reference angiogram for registrations obtained with different similarity measures. In general all alignments look more precise for the main artery (upper branch) and less precise in the smaller bifurcations mainly due to differences in the small contrasted vessels. The SSD provided slightly better alignment in the main artery (see arrows in Fig. 5.4) in comparison to NCC and NMI. Therefore the transformation obtained with SSD was used in the estimation of the TACs. The misalignment in the main artery obtained with SSD was less than 1 mm. This can be assumed sufficient for accurate mapping of the 3D segmented regions to the angiograms.

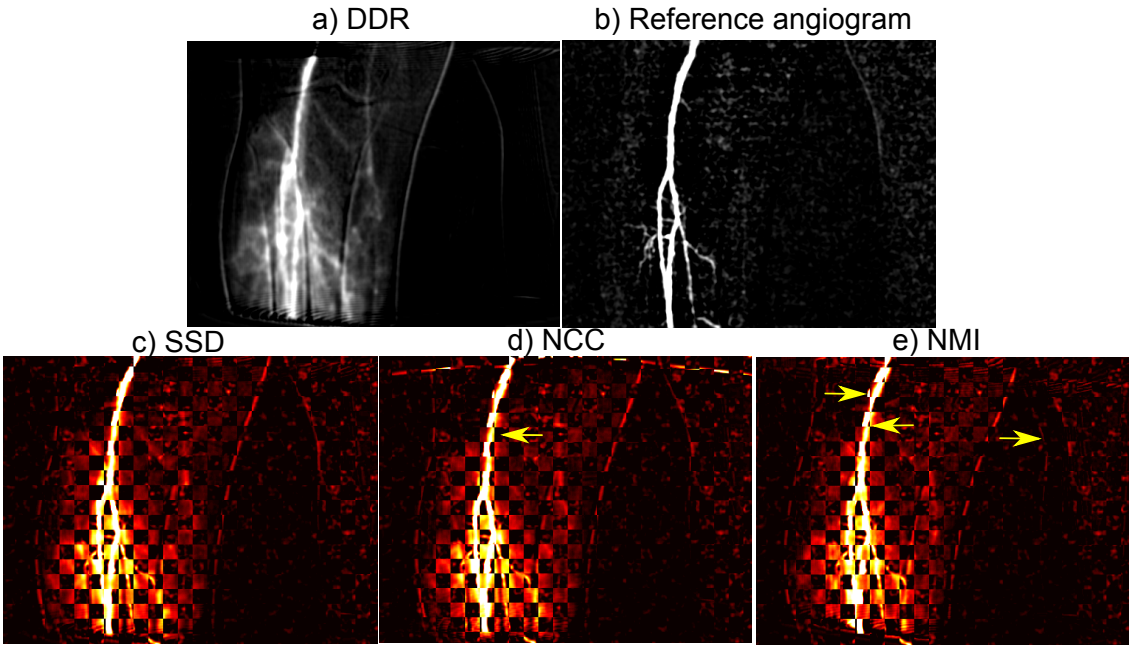

Figure 5.4. Results for the 3D/2D registration of the peak enhancement image to the angiographic sequence (case 2). (a) DDR generated from the registered 3D peak enhancement image (b) Reference angiogram taken at 15s. (c)-(e) Chessboard visualization of the DDR and the reference angiogram for different registration metrics: sum of squares difference (SSD), the normalized cross correlation (NCC) and the normalized mutual information (NMI)

5.4.2 TAC consistency with DSA

In this section we evaluated the consistency of the TACs estimated from the C-arm CT data (CCT TACs) with the TICs measured in DSA (DSA TICs). The consistency is evaluated by visual assessment of the correlation between the CCT TACs and the DSA TICs. The DSA TICs are obtained by sampling the contrasted line integrals $\ell^*(t)$ over time within a 2D region of interest (ROI) in the imaging plane.

In Fig. 5.5(a)-(b) we show the contrasted line integrals $\ell^*(t)$ in the imaging plane for Case 1. Figure 5.5(a) shows the line integrals at 9s while Fig. 5.5(b) shows the time-to-peak (TTP) of the line integrals (i.e. TTP of the DSA TICS). Typically arteries have a TTP of around 10-15s (blue-green), perfused tissue around 20s (yellow) and veins higher than 25s (red). Because of the overlap with tissue, veins are more difficult to spot in the TTP images. One example of vein can be identified in Fig. 5.5(b) on the lower right.

To analyze the correlation between CCT TACs and DSA TICs, we computed the spatially averaged CCT TACs over a volume of interest (VOI), and compared it with the spatially averaged DSA TICs in the corresponding 2D ROI on the imaging plane. The corresponding 2D ROI was obtained by projection of the VOI into the imaging plane. Three VOIs with size $(3 \times 3 \times 3)$voxels were selected in the artery, perfused tissue and vein. The locations of the 2D ROIs are indicated by the arrows in Fig. 5.5(b) and 5.6(b). In Fig. 5.5(c)-(d) we show the DSA TICs calculated in the 2D ROIs for Case 1. In Fig. 5.5(e)-(f) we show the CCT TACs

calculated in the VOIs. In Fig. 5.6 we show the same set of images and curves for Case 2.

The CCT TACs show a good correlation with the DSA TICs which can be observed by the similar shape of the curve and same TTP (cf. 5.5(c) with 5.5(e) and 5.5(d) with (f)). Especially in arteries the shape and the TTP of the CCT TACs was very similar to that of the DSA TICs. In tissue, due to the overlap with vein regions in the projection domain, the DSA TICs are contaminated with venous contrast enhancement (see the late peak in Fig. 5.6(d)). In the CCT TACs, it was possible to separate the tissue and vein contrast enhancement (see the CCT TACs in Fig.5.6(f)).

5.4.3 Comparison with MRA

We evaluated the blood flow maps obtained with the perfusion estimation method by visual comparison with blood flow maps obtained from contrast enhanced MR angiographic (MRA) acquisitions of the same patients. Typically, MRA acquisitions are acquired to inspect the arterial viability and the presence of stenosis in patients with suspected PAD. The MRA images also show the contrast enhancement in the surrounding tissues which allows to inspect, to some extent, also the tissue blood flow. The MRA acquisitions consist of time sequences of T1-weighted images acquired on a 1.5T scanner during injection of gadolinium. The acquisition parameters were as follows: gradient echo sequence with $TE = 2.12$ ms and $TR = 4.30$ ms, time resolution 2s, flip angle=20 deg, resolution on the coronal plane $(0.9 \times 0.9)\text{mm}^2$, slice thickness 2.2 mm. The reconstructed data consisted of a time sequence of 3D images showing the anatomy plus the temporal contrast propagation. The relative difference with respect to the first non contrasted image $c(t) = c_d(t) - c_0$ (where $c_d(t)$ is the total signal while c_0 is the first time frame) is used to quantify the contrast time intensity curve.

In Fig. 5.7(a) we show the MRA peak enhancement image computed as $\max_t(c_d(t))$. This image shows the anatomy plus the contrast enhancement in tissue and vessels. Herein the different anatomical regions are visible: fat-bone marrow (medium bright), tissue (dark) and contrasted vessels (bright). In Fig. 5.7(b) we show the peak enhancement image $\mu_s(\boldsymbol{x})$ reconstructed from the CCT data. The axial slice was selected so as to show the same slice for both CCT and MRA images.

In Fig. 5.7(c) we show the MRA contrast enhancement image computed on the subtracted curves as $\max_t(c(t))$. This image shows mainly the areas subject to contrast propagation. In Fig. 5.7(d) we show the contrast enhancement image $\mu_{enh}(\boldsymbol{x})$ computed from the CCT data.

From the time intensity curves $c(t)$, a relative blood flow map was computed by the slope method (Fig. 5.7(e) and Fig. 5.8(e)). In Fig. 5.7(f) and Fig. 5.8(f) we show the blood flow map estimated from the CCT data for Case 1 and 2, respectively. In Case 1 the blood flow in tissue areas was rather homogeneous while in Case 2 the perfusion was restricted to a single muscle area while a large hypoperfused area was identified (see Fig. 5.8(f)). The hypoperfused area is attributed to the presence of stenosis in the related feeding artery. The hypoperfused area, which was clearly identified with CCT, could only be partially identified with MRA due to the high level of artifacts (see dark area on the left side of Fig. 5.8(e). For Case 1, on the contrary, we observed a good correspondence of the contrast patterns between CCT and MRA.

Next we analyzed the capability of the two modalities to visualize contrast difference between perfused tissue and fatty tissue like skin and bone marrow. This capability is assessed by inspecting the difference in blood flow values and contrast enhancement between perfused tissue and the fatty tissue. In general fatty tissues are expected to absorb less contrast than muscular tissue. For Case 1, even though the contrast differences were small, both techniques

were capable to differentiate perfused tissues from fatty tissues (see Fig. 5.7(e) and 5.7(f)). The contrast enhancement image from CCT exhibited a streak artifact. This is attributed to the higher contrast concentration used which caused photons starvation in the acquired projections. Despite this artifact, contrast differences in the skin and bone marrow could still be detected.

For case 2, the images obtained with MRA exhibited high noise levels and artifacts which made difficult the differentiation of fatty tissues. Some contrast differences however could be observed (Fig. 5.8(e)) but were not sufficient to clearly spot the fatty tissue areas. On the contrary, the perfused maps estimated from the CCT data showed a higher contrast resolution which allowed the differentiation of perfused tissue and fatty tissue (see Fig. 5.8(f)).

In general the results prove the practical feasibility of perfusion imaging in an interventional environment by combination of DSA and 3D reconstructions. The proposed method provides 3D perfusion information allowing for easier detection of hypoperfused areas which is challenging from standard angiography. The 3D visualization of perfusion increases the amount of information available to the surgeon for treatment assessment.

5.5 Summary and Conclusion

In this chapter we evaluated the feasibility of perfusion imaging in peripherals with C-arm interventional systems. The method we applied is based on the combination of dynamic contrast information derived from DSA and spatial information derived from 3D images reconstructed from rotational scans. The perfusion is obtained by mapping the 2D blood flow from the DSA to the 3D reconstructed images.

The evaluation was performed on C-arm data (i.e. angiography plus rotational scans) acquired on patients during their revascularization procedures and was focused on three aspects: correlation of the estimated 3D TACs with the measured 2D DSA TICs, correspondence of the estimated perfusion maps with perfusion maps obtained from MRA scans, capability to detect low contrast details in fatty tissues.

Our evaluation study showed a good correlation of the 3D TACs and 2D DSA TICs. Additionally, with the 3D TACs it was possible to separate venous and tissue TACs. This was not possible with DSA due to the overlap of different anatomical structures in the projection domain.

The comparison of the CCT perfusion maps with MRA maps could be performed only for one of the cases, for which a discrete correspondence was found. For the second case the image quality of the MRA images was to low to perform the comparison. For future studies, we suggest to use different modalities for validation of perfusion measurements like CT perfusion, PET or dedicated perfusion MR scans [113].

Despite the low perfusion values in peripherals (the measured perfusion values were in the range 1-15 ml/100ml/min), the contrast resolution and image quality of perfusion maps was sufficient to differentiate perfused tissue from fat and hypoperfused tissue. In future studies, the use of pharmacological agents to induce higher blood flow in tissue muscles like adenosine could be investigated [44].

Particular care must be taken to avoid image artifacts which might be induced by high contrast concentrations in vessels. These artifacts in fact might deteriorate the segmentation step, which is crucial for perfusion estimation, and thus obstruct the visualization of perfusion. Based on our results, for artifact-free images, we recommend the use of no more than 25 ml

diluted contrast volume for the peak enhancement image.

In general the results prove the practical feasibility of perfusion imaging in an interventional environment by combination of DSA and 3D reconstructions. With the current framework, in order to assess perfusion differences during procedures, the radiologist would have to perform four rotational scans, (two before and two after the procedure) and two angiographic scans (one before and after the procedure). This however would mean a high amount of contrast and high radiation delivered to the patient. In future studies, alternatives to lower the number of scans required should be investigated. For instance the possibility to use the same segmentation for the estimation before and after the procedure should be investigated. Furthermore, anatomical models containing information on the angiosomes could be used to reduce the amount of anatomical information required and thus avoid the need for multiple rotational scans.

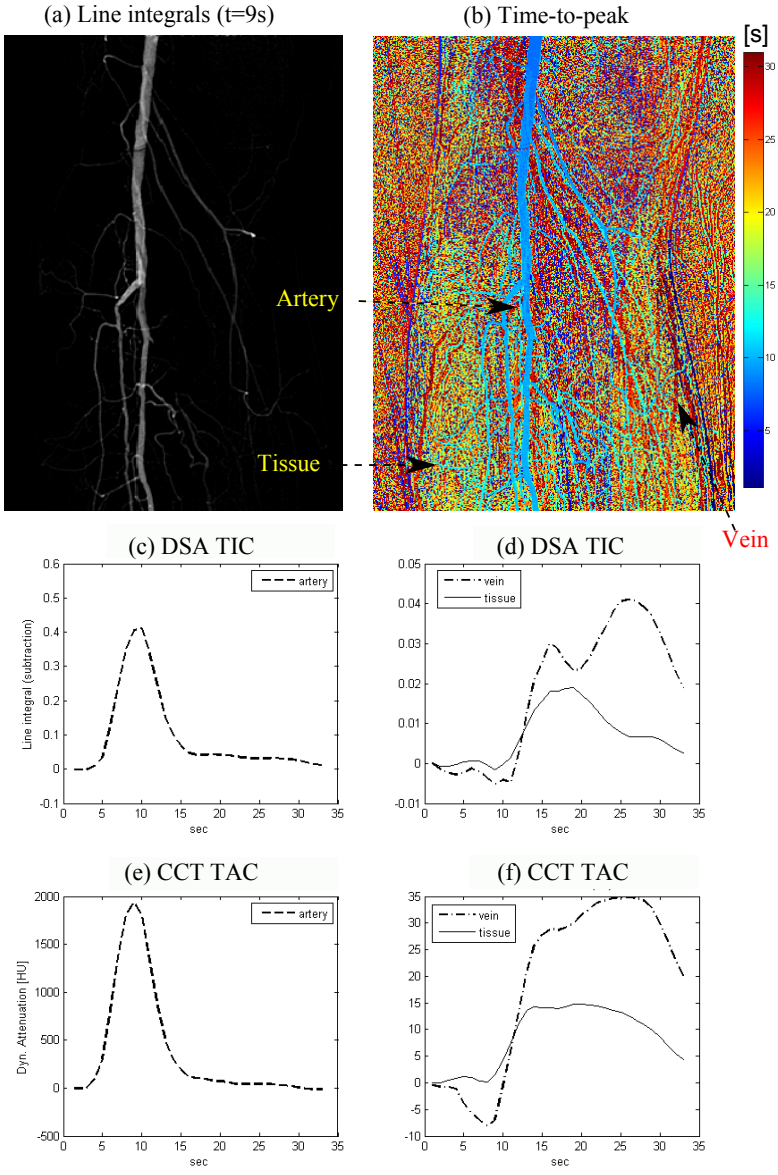

Figure 5.5. TAC consistency analysis for case 1: (a) Contrasted line integrals $\ell^*(t)$ calculated from the angiograms at time t=9s, (b) Time-to-peak of the contrasted line integrals, (c) Arterial DSA TIC calculated from $\ell^*(t)$, (d) Tissue and venous DSA TIC, (e) Arterial CCT TAC estimated with our proposed method, (f) Tissue and venous CCT TAC.

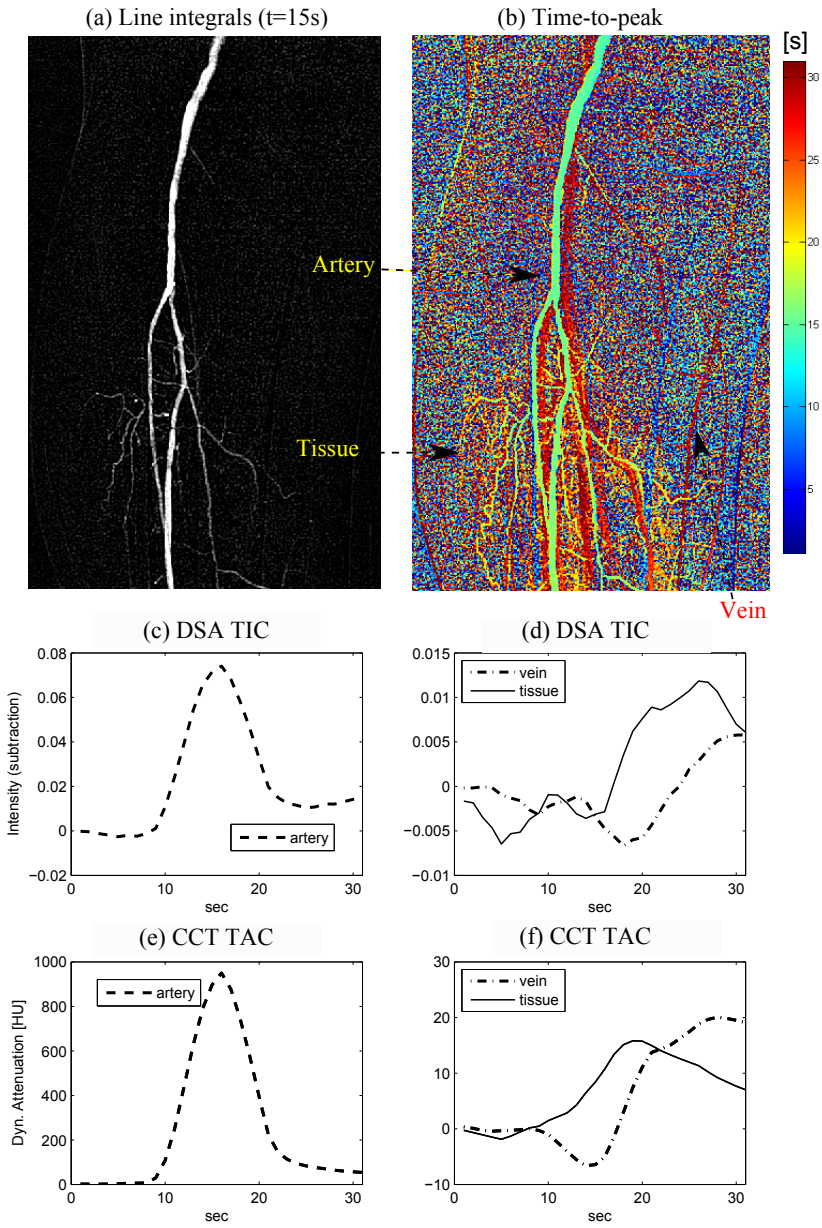

Figure 5.6. TAC consistency analysis for case 2.

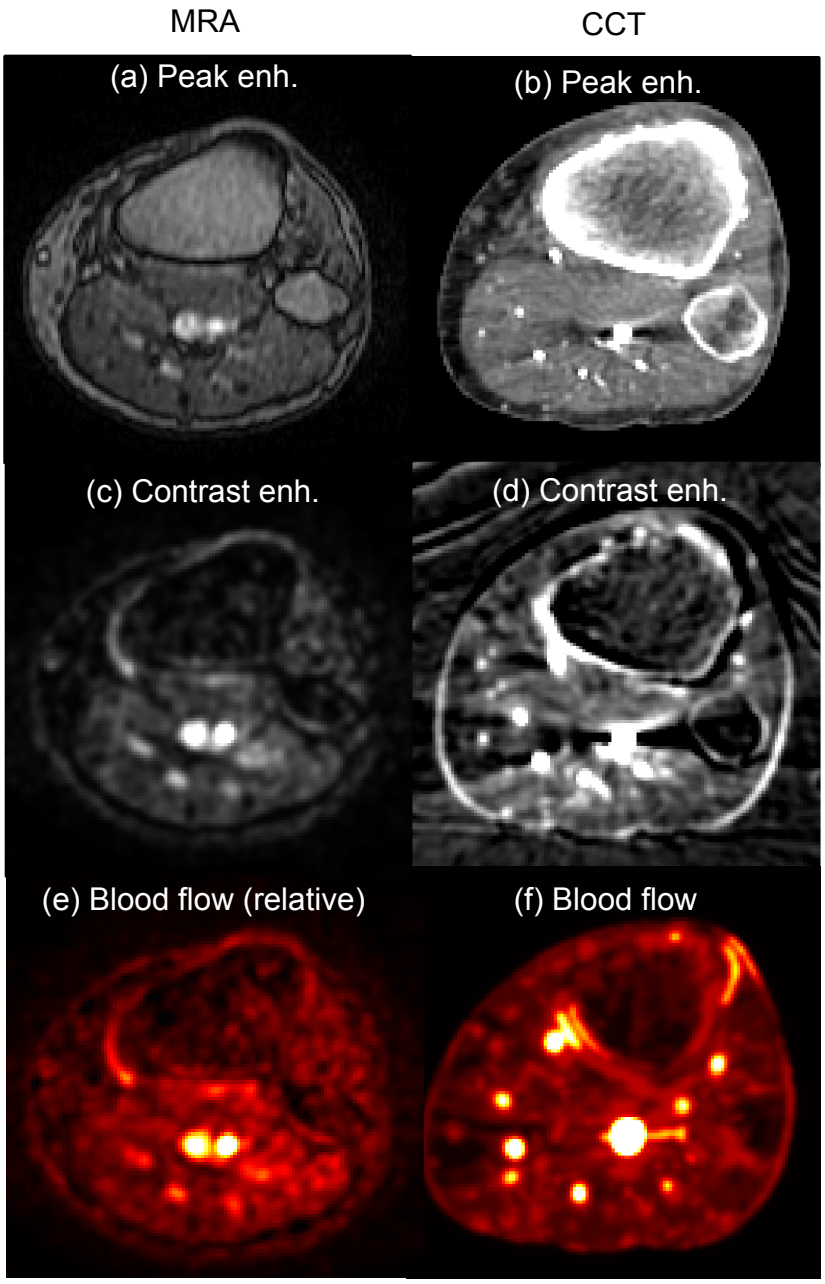

Figure 5.7. Comparison of blood flow maps estimated with our method from CCT data and maps obtained from MRA data for case 1: (a) Time-peak enhancement of the MR sequence (b) Peak enhancement image μ_s reconstructed from the rotational CCT data, range [-100 400]HU. (c) Time-peak enhancement of the MRA sequence with background subtraction (relative units) (d) Contrast enhancement image μ_{enh} obtained from the reconstructed CCT data, range [-10 100]HU. (e) Blood flow map of the MRA sequence (relative units) (f) Blood flow map estimated from CCT data with our proposed method, range [0 100]ml/100 ml/min.

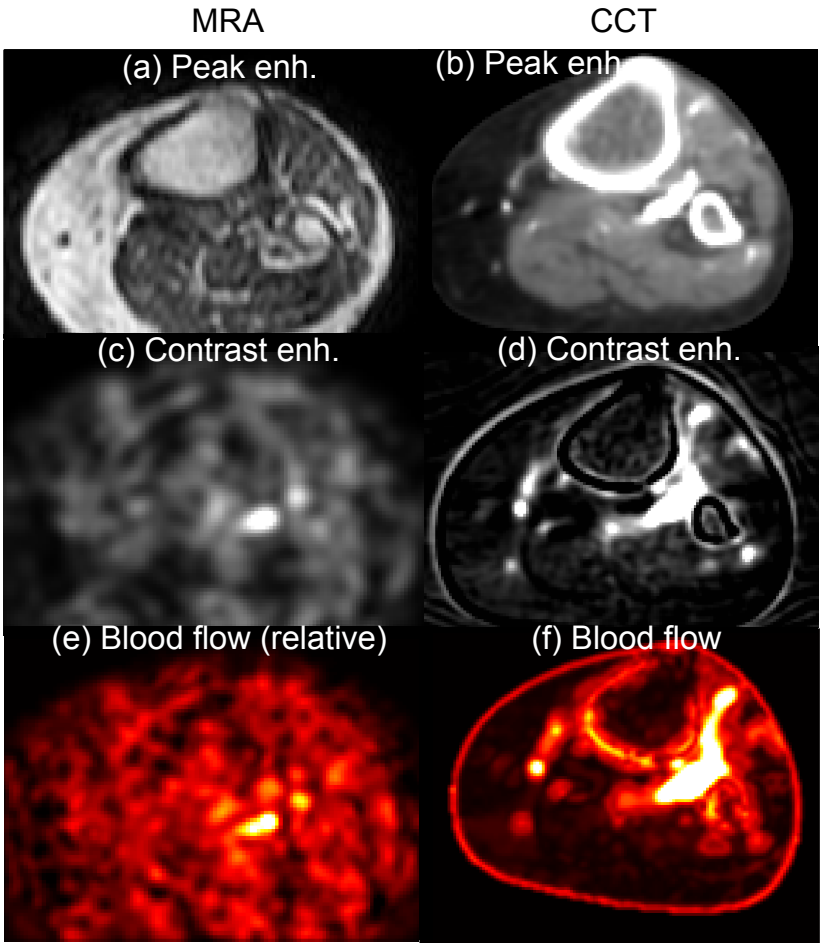

Figure 5.8. Comparison of blood flow maps estimated with our method from CCT data and maps obtained from MRA data for case 2. See caption of figure 5.7. (f) Blood flow map estimated from CCT data with our proposed method, range [0 40]ml/100 ml/min.

Chapter Six

Effects of beam hardening on the measurement of contrast enhancement by digital subtraction angiography

An expert is a person who has made all the mistakes that can be made in a very narrow field.

— Niels Bohr (1885-1962)

Abstract — In this chapter we evaluate the effects of beam hardening on the measurement of contrast enhancement by planar X-ray digital subtraction angiography. Contrast enhancement measurements using common X-ray energy integrating detectors assume a monochromatic x-ray beam. This assumption allows to define a linear relation between the measured attenuation and the contrast concentration in the object. However, due to the polychromatic nature of x-rays, in reality this relation is not linear and the so called beam hardening effect occurs.
A simulation study is carried out to assess the influence of different factors on the beam hardening error: body materials (tissue, bone), contrast material concentration and monochromatic energy to model the monochromatic x-ray.
The results show that the major factor influencing the error is the variation of the monochromatic beam energy from the optimal effective energy. These variations result in an offset which, for typical leg geometries and contrast concentrations, is in the order of 5% for each variation of 1 keV. The offset however does not influence the computation of perfusion since this is based on the normalization of tissue contrast enhancement by the arterial contrast enhancement which experience similar offsets.
Other factors like the iodine concentration and the body thickness, which can modify the spectra of the x-ray signal, have shown to have only a limited impact on the beam hardening error.
This study suggests that beam hardening is not a limiting issue for quantification of contrast enhancement by DSA. However to optimize accuracy, a calibration procedure which accounts for local variations of the effective energy of the x-ray beam would be beneficial.

Based upon: M. Giordano, K. J. Engel, E. P. A. Vonken, M. A. Viergever, C. Neukirchen, "Effects of beam hardening on the measurement of contrast enhancement by digital subtraction angiography", *submitted*.

6.1 Introduction

Quantitative perfusion imaging has been recently proposed as a tool for treatment outcome of complex minimally invasive procedures like stroke treatment [18] and peripheral revascularization [120]. In peripheral revascularization procedures, quantitative perfusion information is relevant to establish the effective restoration of blood flow from the reopened artery towards the diseased tissue. In the current workflow only qualitative information on the arterial blood flow is available by using X-ray digital subtraction angiography (DSA). DSA is based on a time sequence of projection images acquired during injection of a short bolus where the first pre-contrast image is subtracted from all images to retain only information about the contrast enhancement in vessels. Due to the projective nature of this technique, only qualitative information on the blood flow can be retrieved as the depth information is lost in the projection process. Videodensitometry has been proposed to measure quantitative blood flow by DSA [107]. Molloi *et al.* [81] proposed to measure quantitative coronary blood flow by calibration of the DSA values: a system iodine calibration slope is calculated from acquisitions on phantoms with iodine inserts of known concentration. This calibration slope is used to convert the DSA values in the coronary artery into blood flow values. Furthermore in order to remove the attenuation of the surrounding tissue, the author applies a similar method to tissue subtracted images obtained from dual-energy DSA acquisitions [82]. These techniques are suitable to measure blood flow in small structure like arteries. However, to estimate blood flow in tissue, the tissue thickness must be taken into account as it modulates the DSA signal. In Chapter 3 we proposed a method for average tissue perfusion measurement by dividing the DSA values by the thickness of the perfused tissue retrieved from 3D images reconstructed from C-arm rotational scans. In Chapter 4 we extended this method for 3D region-based perfusion by using a 3D segmentation of the perfused tissue.

All the methods mentioned so far are based on the contrast enhancement information contained in the DSA. Measurements of contrast enhancement using common energy integrating detectors assume a linear relation between the measured contrast and the contrast agent concentration in the object. Nevertheless, due to the polychromatic nature of x-rays and the energy dependency of the materials attenuation, the relation between the measured contrast attenuation and the contrast density is not linear and the so called 'beam hardening' effect occurs. The non linearity is due to the fact that as the x-ray beam traverses the body, lower-energy photons are absorbed stronger than high energy photons resulting in the beam getting 'harder', i.e. richer in high energy photons. Consequently, a discrepancy occurs between the measured attenuation, which is not linear with the contrast density, and the expected attenuation which assumes linearity. Fieselmann *et al.* [20] measured the linearity between the reconstructed attenuation values and the effective contrast concentration in a cylindrical phantom using a C-arm. His experiments showed that the linearity is well preserved for typical iodine concentrations used in brain perfusion. Some methods were proposed to analyze and correct for beam hardening artifacts in 3D reconstructed images induced by the presence of contrast [59, 90]. However to our knowledge the effects beam hardening induced on the measurement of contrast enhancement in planar DSA images was not addressed. In this study we aim at assessing the effects of different factors, like body materials and theoretical assumptions, on the measurement of contrast enhancement by DSA. The focus is on DSA acquisitions in peripherals aimed at quantifying tissue perfusion. The analysis is carried out by simulation on 1D and 2D software phantoms.

6.2 Method

In this study we evaluate the effect of beam hardening on the measurement of contrast enhancement by X-ray based DSA. The contrast enhancement in DSA is quantified as line integrals derived from the x-ray measurements by the log transformation [61]. The beam hardening is due to assumptions made on the spectral characteristics of the detected x-rays. Most common detectors used in x-ray imaging operate in integrating mode [61] that means that the measured signal is proportional to the photons' energy integrated over the whole spectrum. X-rays are therefore assumed monochromatic. Under this assumption the relation between the measured line integrals and the object attenuation is linear. However, due to the polychromatic nature of x-rays the real measurements are in general not linear with the object attenuation and a discrepancy occurs between the ideal line integrals (we will refer to these as 'monochromatic line integrals'), which assume a monochromatic x-ray spectrum, and the measured line integrals (we will refer to these as 'polychromatic line integrals') which are based on a polychromatic x-ray spectrum.

Our evaluation aims at assessing the error between monochromatic and polychromatic line integrals measured for an object where a contrast agent is injected. The line integrals are assumed after removal of the non contrasted structures (i.e. DSA Mask).

In order to define the error, the definition of polychromatic and monochromatic line integrals is given for a generic object constituted by M different materials. The object is assumed having two different states, a pre-contrast state and a post-contrast state where the additional attenuation due to the contrast agent is considered. The line integrals are defined as the total contrasted line integral $p_{C(poly)}$ related to the post-contrast state, minus the line integral $p_{0(poly)}$ related to the pre-contrast state. The definition of polychromatic line integrals p_{poly} is as follows:

$$\begin{aligned} p_{poly} &= p_{C(poly)} - p_{0(poly)} \\ &= -ln\frac{I_C}{I_0} \\ &= -ln\frac{\int_0^{E_{max}} E \cdot S_{in}(E) \cdot e^{-\sum_{j=1}^{M} \mu'_j(E) T'_j} dE}{\int_0^{E_{max}} E \cdot S_{in}(E) e^{-\sum_{j=1}^{M} \mu_j(E) T_j} dE} \end{aligned} \tag{6.1}$$

I_C and I_0 are the measured x-ray intensities for the post-contrast and pre-contrast state, respectively. The numerator in the last term quantifies the object attenuation in the post-contrast state while the denominator quantifies the object attenuation in the pre-contrast state. E_{max} is the maximum energy of the x-ray beam. $S_{in}(E)$ is the x-ray spectrum at the input of the object. The $\mu'_j(E)$'s are the attenuation coefficients of the j-th material for the post-contrast state while the $\mu_j(E)$'s are the ones for the pre-contrast state. T'_j and T_j are the projected mass densities [59] of the j-th material for the post-contrast and the pre-contrast state, respectively. The projected mass density is defined as the line integral of the mass density ρ_j along the ray L: $T_j = \int_L \rho_j(x, y, z)ds$.

Next we define the monochromatic line integrals. If we assume that the beam is monochromatic, i.e. the energy content reduces to an energy E_{mono}, the line integral in Eq. 6.1 reduces to a linear combination of the attenuation coefficients:

$$p_{mono} = p_{C(mono)} - p_{0(mono)} = \sum_{j=1}^{M} \mu_j(E_{mono})[T'_j - T_j] \tag{6.2}$$

$p_{C(mono)}$ and $p_{0(mono)}$ are the monochromatic line integrals for the post-contrast and pre-contrast state, respectively.

Typically, for simple objects consisting of a single material, E_{mono} is assumed to correspond to the 'effective energy' (i.e. $E_{mono} = E_{eff}$) of the scanner. The 'effective energy' is the energy at which the given material exhibits the same attenuation coefficient as is measured by the scanner [61, 76]:

$$p_{mono}(E_{mono} = E_{eff}) \sim p_{poly} \tag{6.3}$$

Since we consider objects consisting of different materials with different spectral properties, the effective energy of the scanner depends on the object and system definition. In our study we estimate the effective energy by minimizing the discrepancy between the monochromatic line integrals and the polychromatic line integrals. The estimation of the effective energy will be discussed more in detail Sec. 6.3.1.

Finally we provide the definition of the error used to assess the influence of beam hardening on the measurement of line integrals. This is defined as the difference between polychromatic line integrals and the monochromatic line integrals:

$$\varepsilon_{BH} = p_{mono} - p_{poly} \tag{6.4}$$

This error definition and the definition of the relative error $\mathcal{E}_{BH} = \varepsilon_{BH}/p_{poly}$ will be used throughout the chapter.

6.2.1 Multi material object representation

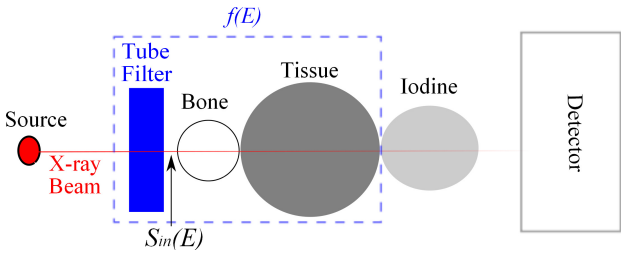

Figure 6.1. Schematic representation of the multi material object constituted of bone, tissue and iodine. $f(E)$ includes the tube filter, tissue and bone absorption and acts as a filter on the incoming x-ray beam.

In order to calculate line integrals we introduce a representation for a generic multi material objects. This representation assumes a specific order of the materials so as to simplify the calculation of line integrals and better characterize the influence of each material. The generic multi material object is constituted by tissue (including skin and bone marrow), bones and a iodine concentration which simulates the contrast in tissue and arteries.

To simulate the perfusion process, the object is defined in two states:

- (pre-contrast state): in this state the object is composed of tissue and bones.
- (post-contrast state): in this state the object is composed of tissue, bones and a iodine concentration. Here, in comparison with the pre-contrast state, the x-rays experience the additional attenuation due to the presence of the iodine concentration.

The calculation of the line integrals assumes a specific order of the materials (see Fig. 6.1): first the beam enters bone, then tissue and then the iodine concentration. Note that the values of the line integrals are independent from the order of the materials.

In the simulations, the attenuation in tissue, skin and bone marrow is approximated with that of water while the attenuation of bone is approximated with that of calcium.

6.2.2 Calculation of line integrals

In the following we provide the specific formulas for the calculation of polychromatic and monochromatic line integrals through the generic multi material object defined in Sec. 6.2.1.

For the polycromatic case the line integrals are calculated as follows:

$$p_{poly} = -ln\frac{\int_E E \cdot S_{in}(E) \cdot e^{(-\mu_W(E)T_W - \mu_B(E)T_B - \mu_I(E)T_I)}dE}{\int_E E \cdot S_{in}(E) \cdot e^{(-\mu_W(E)T_W - \mu_B(E)T_B)}dE} \tag{6.5}$$

$S_{in}(E)$ is the x-ray spectra at the input of the object (Fig. 6.1). $\mu_W(E)$, $\mu_B(E)$, and $\mu_I(E)$ are the attenuation coefficients of water, calcium, and iodine, respectively. T_W, T_B and T_I are the projected mass densities of water, bone and iodine, respectively. T_W includes the projected mass density of tissue (T_T) and that of skin and bone marrow (T_S): $T_W = T_T + T_S$.

If we include the attenuation of water and bone in one single term $f(E)$, Eq. 6.5 can be rewritten in a more compact form as:

$$p_{poly} = -ln\frac{\int_E f(E)e^{(-\mu_I(E)T_I)}dE}{\int_E f(E)dE} \tag{6.6}$$

The term $f(E) = S_{in}(E) \cdot E \cdot e^{(-\mu_W(E)T_W - \mu_B(E)T_B)}$ is the x-ray spectra after crossing T_W thickness of water and T_B thickness of bone (Fig. 6.1). This term can be interpreted as a filter which filters out low energy photons from the x-ray beam.

For the calculation of the monochromatic line integrals, the linear combination of the attenuation coefficients computed at the effective energy E_{eff} is considered. The effective energy is estimated as the one that minimizes the beam hardening error for line integrals calculated through a test phantom. The selection of the effective energy is detailed in Sec.6.3.1.

6.3 Evaluation

In the evaluation we analyze the influence of different factors on the beam hardening error: i) influence of the monochromatic energy E_{mono} selected to model the monochromatic line integrals ii) influence of different amounts of water, calcium and iodine. The evaluation consists in three parts. In the first part we select the effective energy needed for the calculation of the monochromatic line integrals. In the second part we perform a qualitative analysis of the influence of different amounts of water, calcium and iodine on the beam hardening error. In the third part we perform a quantitative analysis of the beam hardening error for a leg phantom

Table 6.1. Attenuation in the 1D object

Composition	attenuation	
	pre-contrast	post-contrast
Water, Calcium and Iodine	$\mu_W(E)T_W + \mu_B(E)T_B$	$\mu_W(E)T_W + \mu_B(E)T_B + \mu_I(E)T_I\lambda_w$

with typical iodine concentrations; here in addition, the influence of the monochromatic energy is assessed.

6.3.1 Selection of effective energy

The effective energy is selected as the monochromatic energy E_{mono} which minimizes the beam hardening error between monochromatic and polychromatic line integrals. Since the effective energy can vary according to the composition of the object crossed by the x-rays, in order to account for all different combinations of materials we estimated the effective energy from the leg phantom described in Sec. 6.3.3. The effective energy is estimated by minimization of the average error $\bar{\mathcal{E}}_{BH}$:

$$E_{eff} = \arg \min_{E_{mono}} \{\bar{\mathcal{E}}_{BH}\} \tag{6.7}$$

$\bar{\mathcal{E}}_{BH}$ is equal to the relative error $\mathcal{E}_{BH} = (p_{mono}(E_{mono}) - p_{poly})/(p_{poly})$ spatially averaged over all non-zero pixels in the projection image. The effective energy E_{eff} is used throughout this chapter for the calculation of the monochromatic line integrals by substituting $E_{mono} = E_{eff}$ in Eq. 6.2.

6.3.2 Qualitative evaluation

Here we assess qualitatively the influence of body materials and different iodine concentrations on the beam hardening error for a simple 1D object. During the pre-contrast state the object consists of water and calcium. During the post-contrast state, the object consists of the same materials as in the pre-contrast state plus an additional iodine concentration. The concentration of iodine is assumed to be a part λ_W of pure iodine. In the following λ_W is referred to as the iodine concentration factor. The composition and the attenuation of the 1D object during the pre-contrast and the post-contrast state is described in table 6.1.

In the qualitative evaluation we evaluated: i) for a projected water mass density of 5 and 12 g/cm^2, the relative error $\mathcal{E}_{BH}$ versus the projected mass density of iodine, ii) for a fixed projected mass density of iodine of 30 mg/cm^2, the relative error $\mathcal{E}_{BH}$ versus the projected mass of water with and without bone attenuation.

6.3.3 Quantitative leg phantom evaluation

In the third part of the evaluation we assess the beam hardening error $\mathcal{E}_{BH}$ for line integrals calculated across a leg phantom. An axial view of the leg phantom is presented in Fig. 6.2. Six regions were simulated: Bones, Bone marrow, Tissue, Skin, Artery and Vein. The phantom diameter was 100 mm and the diameter of the artery and of the vein was 5 mm. The composition of the regions and their attenuation during the pre-contrast and the post-contrast state is described in table 6.2. During the post-contrast state, an additional attenuation term

(a) pre-contrast image (b) post-contrast image

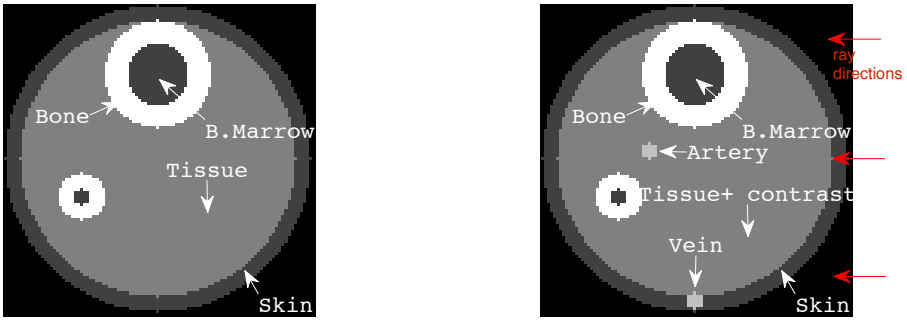

Figure 6.2. Multi material 3D leg phantom: (a) in the pre-contrast state the object consists of bone (white rings), tissue (clear grey), bone marrow (dark grey) and skin (dark grey). (b) In the post-contrast state the object consists of contrast enhanced tissue (clear grey), the contrast enhanced artery (bright grey), bone and bone marrow.

Table 6.2. Attenuation in the leg phantom

Region	composition	attenuation	
		pre-contrast	post-contrast
Bone	Calcium	$\mu_B(E)T_B$	$\mu_B(E)T_B$
Tissue/Artery	Water, Iodine	$\mu_W(E)T_T$	$\mu_W(E)T_T + \mu_I(E)T_I\lambda_W$
Skin/Bone marrow	Water	$\mu_W(E)T_S$	$\mu_W(E)T_S$

Table 6.3. Acquisition Geometry

Detector grid	512×396 pixels
Detector surface	383×296 mm^2
Distance source detector	1190 mm
Distance source rot. axis	787 mm

representing iodine, is introduced in tissues, artery and vein region. The iodine concentration factor λ_W was chosen to be $\lambda_W = 3.3 \cdot 10^{-3}$ for a iodine density in tissue of 1.6 mg/cm^3, and $\lambda_W = 4 \cdot 10^{-2}$ for a iodine density in the artery of 65.0 mg/cm^3. These values were selected to have iodine concentrations around 2-3 times higher than those reported in [107] for brain perfusion. By selecting such high concentrations of iodine we can evaluate the error in a 'worst case scenario'. The profile of the projected masses for the different leg phantom materials are illustrated in Figure 6.3.

The simulation of the angiographic acquisition was based on cone beam forward projections of the phantom's regions. The projected mass densities of the regions were obtained by applying the Joseph algorithm [58] assuming homogeneous densities in the regions. A cone beam geometry (see table 6.3) was used to generate the projected mass densities. The angular view selected for the forward projection is indicated by the arrows in Fig. 6.2.

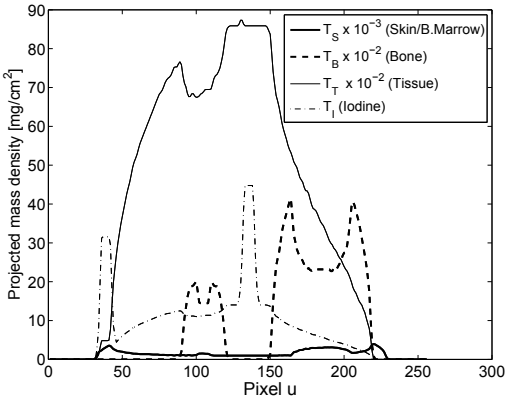

Figure 6.3. Profile of the projected mass density for the leg phantom.

The line integrals were obtained from the projected mass densities of the regions according to Eq. 6.1 and Eq. 6.2. A 2D map of the error $\mathcal{E}_{BH}$ was calculated in the projection domain. In particular we analyzed the error homogeneity and the areas most affected by beam hardening. Additionally, the influence of the choice of the monochromatic energy E_{mono} was assessed by calculating the error map for different E_{mono}'s.

6.3.4 Simulation Settings

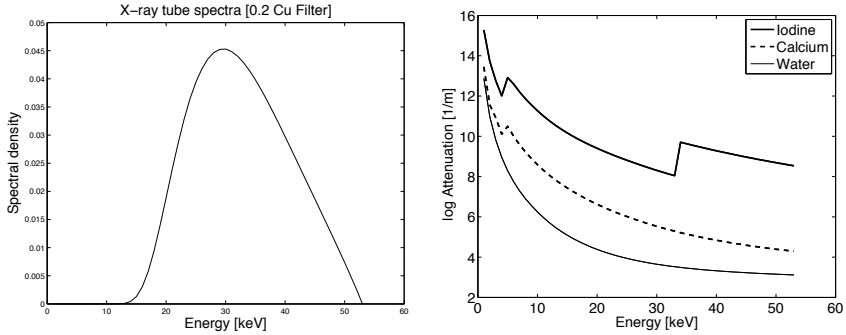

Figure 6.4. (a) X-ray tube spectra after filtration with 0.2 mm Cu filter. (b) Energy dependent attenuation coefficient of water, calcium and iodine.

The input spectra $S_{in}(E)$ of the x-rays was calculated using in-house software assuming a C-arm system with an X-ray tube operating at 53 kVp and a 0.2 mm Cupper filter (Fig. 6.4(a)). The attenuation coefficients of water, calcium and iodine were taken from available databases and are shown in Fig. 6.4(b). The mass density assumed for water calcium and iodine was 1 g/cm^3, 1.5 g/cm^3 and 4.9 g/cm^3 respectively. For the leg phantom, the effective concentration in the artery and in the tissue was obtained by multiplying the mass density by the respective concentration factor λ_W (see Sec. 6.3.2).

6.4 Results/Discussion

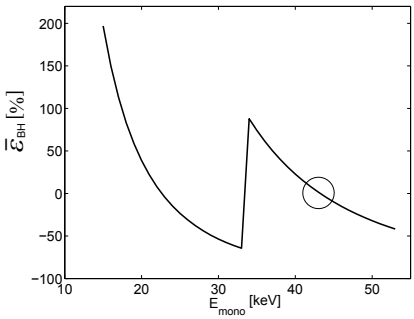

Figure 6.5. Selection of the effective energy E_{eff} for the calculation of the monochromatic line integrals. The spatial average error $\bar{\mathcal{E}}_{BH}$ refers to line integrals calculated through the leg phantom. The effective energy is found at 43 keV.

In Fig. 6.5 we show the selection of the effective energy. Here he spatial average error $\bar{\mathcal{E}}_{BH}$ versus E_{mono} is shown. A large dependency of the error from the effective energy can be observed: in the range of energies 30-40 keV the error varies from -50% to 80%. The minimum error was found for $E_{mono} = 43$ keV. Typically, the minimum error is obtained when the energy content of the monochromatic and the polychromatic x-ray beam are most similar. If we consider the polychromatic beam, its mean energy is approximately 30 keV before entering the object (see Fig. 6.4) and increases as the beam crosses the phantom due to the absorbtion of low energy photons in tissue and bone. In general we can assume that at the output of the object the mean energy is close to the effective energy E_{eff}.

The trend of the error in Fig. 6.5 resembles very closely the shape of the k-edge of the iodine attenuation coefficient (see Fig.6.4(b)). This can be explained by comparing the attenuation experienced by the monochromatic x-ray beam at E_{mono} and the attenuation experienced by the polychromatic beam at the mean energy ($\sim$ 43keV). Monochromatic x-ray beams at energies above the k-edge (33 keV $< E_{mono} <$ 44 keV) experience higher attenuation in iodine in comparison with the polychromatic beam at the mean energy (see the iodine attenuation coefficient for (33 keV $< E_{mono} <$ 44 keV) in Fig.6.4(b)) and therefore the error is positive. Monochromatic x-ray beams at energies just below the k-edge (23 keV $< E_{mono} <$ 33 keV)experience lower iodine attenuation in comparison with the polychromatic beam at the mean energy (see the iodine attenuation coefficient for (23 keV $< E_{mono} <$ 33 keV) in Fig.6.4) and therefore the error becomes negative.

In Fig. 6.6 we show the error $\mathcal{E}_{BH}$ for the 1D simulation: figure 6.6(a) shows the error $\mathcal{E}_{BH}$ against the projected mass density of iodine. The beam was assumed pre-hardened by 5 g/cm^2 (solid line) and 12 g/cm^2 (dashed line) of water. In Fig. 6.6(b) we show the polychromatic line integral p_{poly} and the monochromatic line integral p_{mono} against the projected mass density of water for a beam pre-hardened by 30 mg/cm^2 of iodine. The solid line refers to a beam with an additional 'pre-hardening' of 2 g/cm^2 projected mass density of bone while the dashed line refers to a beam without bone 'pre-hardening'. In Fig. 6.6(c) we show the error corresponding to p_{poly} and p_{mono} shown in Fig. 6.6(b).

The results in Fig. 6.6(a) show that the relative error due to beam hardening is proportional to the projected mass density of iodine. For perfusion estimation methods based on line

integrals in 2D projections, like the ones proposed in Chapter 3 and 4, this dependency can affect the accuracy of the blood flow values. The calculation of blood flow values in fact is based on the contrast enhancement in tissue and in the feeding artery which refer to different contrast densities. However, the level of error for iodine projected mass densities up to 60 mg/cm^2, which can be considered rather high concentrations, was below 10%, and therefore the influence of the iodine concentration on the error can be considered minimal.

The results illustrated in Fig. 6.6(c) shows that the influence of water and bones on the the error is minimal: the range of error $\mathcal{E}_{BH}$ for the quantities of bone and water considered was $\pm 5\%$. The influence is caused by the dependency of the the polychromatic line integral on the projected mass density of water and bones (note that in the monochromatic case the iodine contrast enhancement does not depend on the projected mass density of water and bone, see Fig. 6.6(c)). These materials in fact determine the amount of 'pre-hardening' of the polychromatic signal spectrum. The dependency of the polychromatic line integral on the amount of water and bones can be observed in Fig. 6.6(b): if the bone is not included (dashed line) p_{poly} increases with the projected water mass density, while if bone is included p_{poly} decreases with the projected water mass density. This can be explained by considering the mean energy of the polychromatic x-ray beam. Let us consider the case when the bone is not present (dashed curve in Fig. 6.6(b)): for small quantities of water the 'pre-hardening of low energy photons is moderate so that the mean energy of p_{poly} is around 30 keV where the iodine attenuation is rather low (see the iodine attenuation coefficient in Fig. 6.4(b). By increasing the quantity of water, low energy photons are more strongly attenuated increasing the mean energy of the beam over the k-edge of iodine which results in higher iodine attenuation (see the iodine attenuation coefficient above the k-edge in Fig. 6.4(b)). If we consider the case when the bone is present, low energy photons are attenuated even for small quantities of water resulting in a mean energy of the polychromatic beam just above the k-edge. By increasing the amount of water the mean energy of the polychromatic beam increases even further which results in a decrease of the iodine attenuation (see iodine attenuation coefficient for $E \geq 40$ keV in Fig. 6.4(b)).

Figure 6.7 shows the 2D map of $\mathcal{E}_{BH}$ obtained for the leg phantom. The location of the regions is indicated within the map. Figure 6.7(b) shows the profile of the 2D map along the central row for different energies E_{mono}. The location of the profile is indicated in Fig. 6.7(a) by the white dashed line. As it can be seen, for E_{mono} different from the effective energy ($E_{eff} = 43$ keV) an offset in the error is experienced (Fig. 6.7(b)): for differences of 1 keV the offset is around 5%. This result is in accordance with the result obtained in Fig. 6.5 and confirms the strong dependency of the error from the selected effective energy. As concerning results obtained at the effective energy, the relative error is below 8%. The error is rather homogeneous in tissue and less homogeneous in bones and contrasted vessels where peaks in the order of $6-8\%$ are experienced. In bones these peaks are due to the higher 'pre-hardening' which modifies the mean energy of the polychromatic x-ray beam while in the vessels they are attributed to the higher contrast density.

Additionally, in accordance with the results of Fig. 6.6(c) (dashed line) the errors in vessels are higher at the border of the object, where the projected mass of water is lower, and lower toward the center of the object where the projected mass of water is higher (see Fig. 6.7(a) and (b)). For the bones the effect is the opposite, here in fact errors at the borders are lower than in the center of the object (Fig. 6.7(a) and (b)).

6.5 Conclusion

In this chapter we evaluated the impact of beam hardening on the measurement of contrast enhancement by DSA. This is especially relevant for perfusion estimation methods based on planar angiographic acquisitions. The evaluation was based on the discrepancy between 'expected' line integrals, which assume a monochromatic x-ray beam, and 'measured' line integrals, which assume a polychromatic x-ray beam. The focus of the evaluation was on the influence of body materials, contrast concentrations, and monochromatic energy used to model the expected monochromatic line integrals.

In general results showed that the highest factor influencing the beam hardening is the choice of the monochromatic energy. Variations of this energy from the optimal monochromatic energy (i.e. the effective energy) result in large offset of the contrast enhancement measurements. The offset however does not influence the computation of perfusion values due to the normalization of tissue contrast enhancement by the arterial contrast enhancement.

Other factors like the iodine concentration and the body materials have less influence on the measurement of contrast enhancement. The errors are proportional to the iodine concentration. However, for the concentrations we considered ($\sim$65 mg/cm^3), the errors were below 8%. In the reality we can expect even lower concentrations in arteries and therefore these errors can be assumed negligible. The presence of bone along the x-rays has shown to cause errors in the range $6 - 8\%$. The different thickness of the body along the x-rays causes different 'pre-hardening' of the x-ray signal which can result in inhomogeneities of the contrast enhancement measurement. Nevertheless, for typical leg geometries these inhomogeneities cause relative errors below 2% and therefore they are negligible.

In conclusion our analysis shows that the beam hardening is not an issue for the measurement of contrast enhancement by DSA. Our study suggests that a more precise modeling of the effective energy could improve the accuracy of contrast enhancement. For instance one approach could be to consider the pre-contrast image as water-attenuation only (bone can be considered as water of higher density). Knowing the original spectrum and the water attenuation, for each image pixel one could calculate the 'equivalent water thickness' and from that the 'pixelwise' effective energy. This more precise local effective energy could be used to reduce the beam hardening error and thus to achieve a more accurate perfusion quantification.

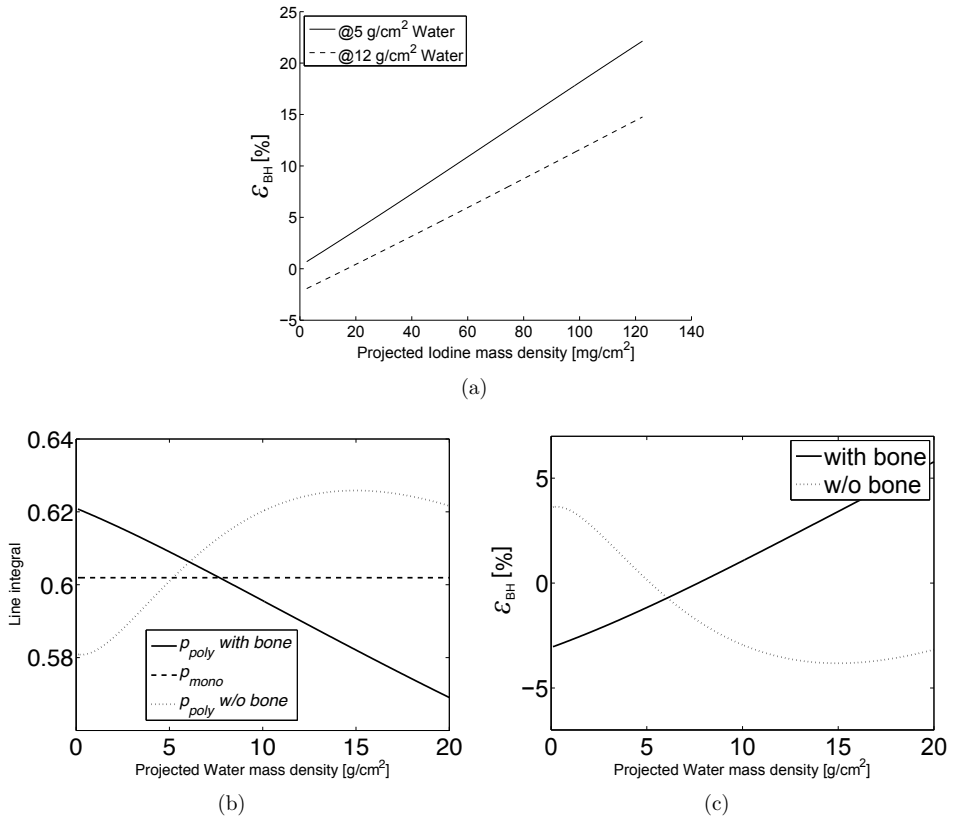

Figure 6.6. Beam hardening error $\mathcal{E}_{BH}$ for the 1D simulation (a) $\mathcal{E}_{BH}$ against the projected mass density of iodine. The beam was assumed pre-hardened by 5 g/cm^2 (solid line) and 12 mg/cm^2 (dashed line) of water. (b) Line integral versus the projected mass water density. The beam is assumed 'pre-hardened' by 30 mg/cm^2 of iodine. (c) Beam hardening error $\mathcal{E}_{BH}$ against the projected mass density of water for the same settings as in figure (b).

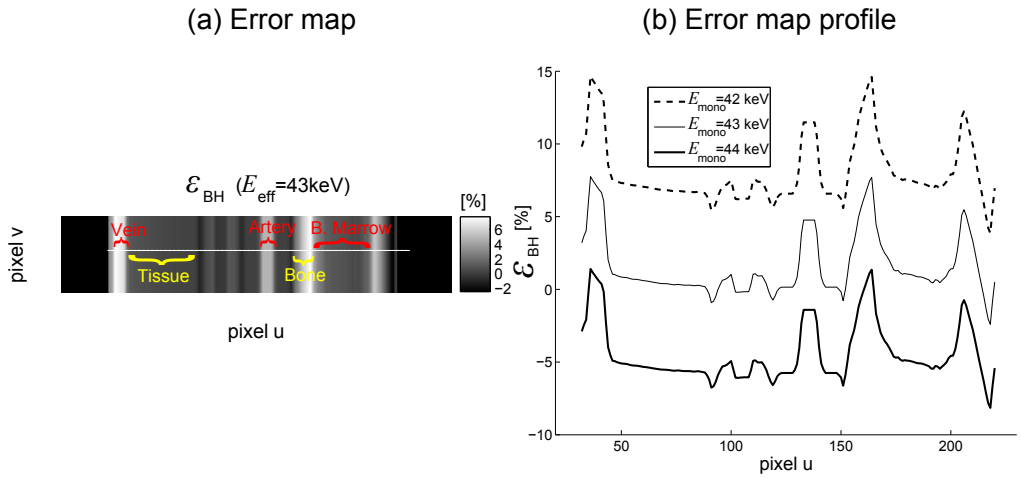

Figure 6.7. Error map related to the line integrals calculated for the 3D leg phantom. (a) 2D map of the relative error $\mathcal{E}_{BH}$ calculated at the effective energy $E_{eff} = 43$ keV. (b) Profile of the 2D map for different monochromatic energies E_{mono}.

Chapter Seven

Summary

Considerate la vostra semenza: fatti non foste a viver come bruti, ma per seguir virtute e canoscenza. (Consider well the seed that gave you birth: you were not made to live as brutes, but to follow virtue and knowledge)

— Dante Alighieri (1265–1321)

In peripheral revascularization procedures a target vessel is treated in order to restore the blood flow toward the tissue. Currently, treatment assessment is carried out by angiography, which allows only for a qualitative inspection of the blood flow in the arteries. Periprocedural assessment of tissue perfusion would be a valuable tool to assess the effective restoration of blood flow toward the tissue and thus to evaluate the technical success of the revascularization procedure. Perfusion quantification however requires the knowledge of the dynamic contrast evolution in the 3D object which is only available on tomographic modalities as CT, PET and MR.

This thesis investigates different possibilities to measure quantitative perfusion with interventional C-arm systems. The current use of C-arm systems is merely for 2D angiographic acquisitions, however recent developments have enabled 3D imaging also on these systems. Nevertheless, the dynamic 3D performance of C-arms in terms of angular speed and range are limited in comparison to CT, which makes perfusion imaging a challenging task.

Other researchers [18] have investigated the possibility to measure perfusion by applying dynamic reconstruction algorithms on data acquired over multiple rotations of the C-arm. Even though this approach has shown promising results, it requires the delivery of a large amount of contrast and radiation dose to the patient. Additionally, it requires a complex acquisition protocol that is currently not available on commercial systems.

In this thesis we propose a set of methods based on angiography and 3D images which can be realized on commercially available C-arm systems. To tackle the lack of temporal and spatial information in the acquired data, prior knowledge about the contrast distribution is integrated in the perfusion estimation procedure. The thesis focuses on the technical implementation of the methods and on their evaluation on simulated and clinical data.

Chapter 1: In this chapter, after providing an introduction on interventional radiology, we discuss the workflow for the treatment of patients affected by peripheral arterial disease. In addition we present the angiosome theory recently introduced to guide the vascular surgeon in the selection of the vessel to target for revascularization. Recent studies showed that by targeting the angiosome which supplies the diseased area, a better blood re-perfusion and thus a better healing of the diseased area can be achieved. To verify the effective re-perfusion in the diseased area, methods to quantify the perfusion during the procedure need to be developed.

In the rest of the chapter we introduce the basic principles of CT perfusion imaging and discuss the challenges involved in the measurement of perfusion with interventional C-arm systems.

Chapter 2: In this chapter we introduce an iterative tomographic perfusion estimation method which aims at 3D spatially resolved perfusion estimation. The method is based on projection data acquired over several multisweeps of the C-arm. The main concept is to exploit prior knowledge on the contrast dynamics which is integrated in a dynamic reconstruction algorithm as a parametric model. The model is based on a set of smooth basis functions which aim at approximating the contrast dynamics. The issue of projection noise propagating to the reconstructed images is tackled by regularization, realized by early stopping of the iteration cycles, and by the use of smooth basis functions in the model.

Results obtained in a simulation study on phantom data showed that the time attenuation curves (TACs) reconstructed from multisweep acquisitions are less accurate than TACs reconstructed from full continuous C-arm rotations. This is due to the irregular sampling of projections at the turning points that, especially for fast dynamics like in the arteries, results in streak artifacts. The analysis of noise propagation revealed that the effective noise suppression depends on a complex interrelation between the number of iteration cycles and the constraints imposed by the parametric model. This suggests that for an optimized estimation, TAC estimated in different regions should be obtained after a different number of iteration cycles.

Chapter 3: In this chapter we propose a method for 2D spatially averaged perfusion estimation in the lower leg. This method is based on a temporal angiographic sequence acquired from a fixed angle and two 3D images reconstructed from C-arm rotational scans. The temporal information derived from the angiography is combined with the spatial information derived from the 3D images to obtain perfusion information spatially averaged along the direction of the x-rays. The main assumption is that perfusion is spatially homogeneous within a single volumetric region and along the orientation of the x-rays. The average perfusion along the ray directions is obtained by normalizing the projection line integrals in the angiography by the length of contrast derived from a segmentation of the 3D images. Results obtained on data simulated from CTP acquisitions showed that the estimation accuracy is limited due to contrast inhomogeneity in the segmented region. Nonetheless, the quantification of spatially averaged perfusion allows for improved visualization and detection of hypoperfused regions in comparison with standard angiography.

Chapter 4: In this chapter we extend the method presented in **Chapter 3** to obtain 3D region-based perfusion. Based on the results of **Chapter 3**, here we relax the assumption on homogeneity by assuming contrast homogeneity within multiple 3D segmented regions. By increasing the number of regions, the spatial homogeneity of contrast in the regions can be increased thus allowing better modeling of the spatial distribution of contrast concentration. To identify the regions from the reconstructed 3D images, we introduce a dedicated 3D segmentation method which relies on local contrast homogeneity. The region-based TACs are estimated by mapping the 2D blood flow information from the DSA to the 3D segments. Instability in the mapping procedure is addressed by spatial and temporal regularization.

Results on data simulated from CTP scans showed that the spatial resolution of the perfusion maps depends on the selected number of segmented regions: the higher the number of regions the higher the spatial resolution. The higher resolution however, is obtained at the cost of increased noise and irregularities in the estimation. Spatial regularization showed to be an effective way to limit the irregularities. For the two analyzed cases, the TAC estimation accuracy with respect to the ground truth CTP data was in the range of $10 - 25\%$ relative

error, which showed to be sufficient to detect the most relevant perfusion patterns and to differentiate hypoperfused from normally perfused regions.

Chapter 5: In this chapter we evaluate the clinical feasibility of perfusion estimation using C-arm systems. In particular we evaluate the method proposed in **Chapter 4** on C-arm data acquired on patients during their revascularization procedure. The practical issues related to the implementation of the method in a clinical environment are discussed. The injection protocol to acquire the 3D rotational scans is designed such as to optimize the balance between contrast enhancement and image reconstruction artifacts. A 3D/2D registration algorithm is applied to register the 3D images to the angiographic sequence.

Results showed that the 3D estimated TACs can provide a better separation of contrast dynamics in tissue and veins which often overlap in DSA images. Furthermore the method was capable to distinguish lower enhanced areas like fat tissue and hypoperfused tissue from normally perfused are like muscular tissue. The comparison of the estimated perfusion maps with preprocedural MRA perfusion maps was challenging due to the poor image quality of the MRA images. This suggests that in future, different modalities (e.g. MR perfusion, CTP or PET) should be used to evaluate quantitatively the estimated perfusion maps. In conclusion the results proved the clinical feasibility of perfusion estimation with C-arms by combination of 2D angiography and 3D images.

Chapter 6: In this chapter we assess the effect of beam hardening on the measurement of contrast enhancement by DSA. This is especially relevant for the perfusion estimation methods proposed in **Chapter 3** and **Chapter 4**, which rely on the contrast enhancement measured by DSA. Contrast enhancement measurements performed with common energy integrating detectors assume a monochromatic x-ray beam. However, because of the polychromatic nature of x-rays, a non-linearity, referred to as 'beam hardening', occurs in the measurements.

A simulation study, carried out on software phantoms, showed that the major factor influencing the contrast enhancement measurements is the choice of the monochromatic energy used to model the measurements. Deviations from the ideal monochromatic energy result in offsets in the measurements in the order of 5% for each keV. The offset however does not represent an issue for the computation of perfusion since perfusion is obtained by normalization of the tissue TACs by the arterial TACs. In conclusion, the results in this chapter showed that the effects of beam hardening on the measurement of contrast enhancement by DSA are negligible.

In this thesis we have presented a set of novel methods to estimate quantitative perfusion from angiographic images. These methods are designed to support the vascular radiologist in the outcome assessment of endovascular reascularization procedures. The main advantage of the proposed methods lies in the simple acquisition protocols that can be implemented on most commercially available C-arm systems. The spatial resolution achieved is slightly inferior to that of fully 3D spatially resolved estimation methods due to the assumption on perfusion homogeneity. However, the results have shown that in legs, where perfusion occurs in large three-dimensional muscle blocks, the resolution achieved is sufficient to differentiate lesions from healthy tissues and to visualize the most relevant details of the vasculature.

The proposed methods were first evaluated on phantom data to assess the theoretical estimation accuracy (**Chapter 3** and **4**). Then, a qualitative evaluation was performed on C-arm data acquired on patients during the revascularization procedure (**Chapter 5**). In this evaluation we proved the feasibility of the method by a practical point of view. However, in the evaluation we also observed a number of limitations that still need to be addressed.

First, a comprehensive evaluation needs to be performed to assess the quantitative accuracy

of the method. In our evaluation on C-arm data we used MRA data as reference but the poor image quality did not allow a comprehensive evaluation. In future studies, other modalities like CT perfusion, MR perfusion or PET could be used.

Another limitation emphasized by our study is the low tissue contrast enhancement in the reconstructed 3D images. This issue can have impact on the segmentation step and result in incorrect modeling of the perfused regions. One way to tackle this issue is to increase the injected volume of contrast and/or the contrast concentration. However, as we have experienced in the evaluation on C-arm data, this may result in image artifacts in the arteries. Alternatives should be found to increase the contrast enhancement in tissues while keeping the contrast enhancement in arteries at a reasonable level. One option could be the use of pharmacological agents, like adenosine, to induce higher blood flow in tissue muscles [44].

Another limitation of our method is the high amount of contrast and radiation dose delivered to the patient. Although the amount of injected contrast and the radiation dose is lower than with other proposed methods [18], for clinical usage they should be further reduced. Currently, in order to measure perfusion before and after the treatment, two angiographic scans and two rotational steady state scans (plus a rotational baseline scan without contrast) are required. The two rotational steady state scans are required to obtain the segmentation of the perfused regions before and after the treatment. These rotational scans require the injection of a large volume of contrast which is often harmful for the patient. Ways to reduce the number of rotational scans should be found. For instance, anatomical image models, containing information on the angiosomes, could be used to enhance the knowledge on the perfused anatomy.

In conclusion, in this thesis we have proposed a set of methods for perfusion quantification in peripherals using interventional C-arm systems. We have shown that by adding anatomical information derived from 3D images, quantification of tissue perfusion from angiographic images can be achieved. Based on the contributions made in this thesis, direct and quantitative assessment of peripheral revascularization procedures could be made available in the future and could be used as a tool to optimize revascularization procedures.

Bibliography

If I have seen further than others, it is by standing upon the shoulders of giants.

— Isaac Newton (1642-1726)

[1] A.S. Ahmed, M. Zellerhoff, C.M. Strother, K.A. Pulfer, T. Redel, Y. Deuerling-Zheng, K. Royalty, D. Consigny, D.B. Niemann, "C-Arm CT Measurement of Cerebral Blood Volume: An Experimental Study in Canines", *American Journal of Neuroradiology*, vol. 30, pp. 917–922, 2009.

[2] V.A. Alexandrescu, G. Hubermont, Y. Philips, B. Guillaumie, C. Ngongang, P. Vandenbossche, K. Azdad, G. Ledent, J. Horion, "Selective primary angioplasty following an angiosome model of reperfusion in the treatment of Wagner 1-4 diabetic foot lesions: practice in a multidisciplinary diabetic limb service", *Journal of Endovascular Therapy*, vol. 15, no. 5, pp. 580–593, 2008.

[3] V. Alexandrescu, M. Söderström, M. Venermo, "Angiosome theory: fact or fiction?", *Scandinavian journal of surgery: SJS: official organ for the Finnish Surgical Society and the Scandinavian Surgical Society*, vol. 101, no. 2, p. 125, 2012.

[4] L. Axel, "Cerebral blood flow determination by rapid-sequence computed tomography: theoretical analysis.", *Radiology*, vol. 137, no. 3, pp. 679–686, 1980.

[5] G. H. Ball & D. J. Hall, "Isodata, a novel method of data analysis and classification", *Tech. Rep. Stanford University, Stanford, CA*, 1965.

[6] C. M. Bishop, *Neural Networks for Pattern Recognition*, first ed., Oxford University Press, 1995.

[7] J. M. Bland & D. G. Altman, "Statistical methods for assessing agreement between two methods of clinical measurement", *The Lancet*, vol. 327, no. 8476, pp. 307 – 310, 1986.

[8] H. Bogunovic & S. Loncari, "Estimating perfusion using X-ray angiography", in *Proc. (IEEE) Intern. Symp. Imag. Sig. Proc. Anal. (ISPA)*, pp. 147–150, 2005.

[9] Y. Censor & T. Elfving, "Block-iterative algorithms with diagonally scaled oblique projections for the linear feasibility problem", *SIAM Journal on Matrix Analysis and Applications*, vol. 24, pp. 40–58, 2002.

[10] B. G. Ziedses des Plantes, "Subtraktion. Eine Rontgenographische Methode zur Separaten Abbildung Bestimmter Teile des Objekts", *Fortschritte auf dem Gebiete der Rntgenstrahlen*, vol. 52, pp. 69–79, 1935.

[11] L. WexlerD.R. Enzmann S.J. Riederer G.S. Keyes W.F. Collins W.R. Brody D.F. Guthaner, "Evaluation of peripheral vascular disease using digital subtraction angiography", *Radiology*, vol. 147, no. 2, pp. 393–8, 1983.

[12] C. T. Dotter, "Cardiac catheterization and angiographic technics of the future. Background and current status of clinical catheter angiography.", *Cesk. Radiol.*, vol. 19, no. 4, pp. 217–36, 1965.

[13] C. T. Dotter & M. P. Judkins, "Transluminal treatment of arteriosclerotic obstruction. Description of a new technic and a preliminary report of its application.", *Circulation*, vol. 30, pp. 654–670, 1964.

[14] T. Elfving & T. Nikazad, "Stopping rules for Landweber-type iteration", *Inverse Problems*, vol. 23, pp. 1417–1432, 2007.

[15] D. R. Enzmann, W. T. Djang, S. J. Riederer W. F. Collins A. Hall, G. S. Keyes, W. R. Brody, "Low-dose, high-frame-rate versus regular-dose, low-frame-rate digital subtraction angiography", *Radiology*, vol. 146, pp. 669–676, March 1983.

[16] R. Fahrig, A. Ganguly, J. D. Starman, N. K. Strobel, "C-arm CT with XRIIs and digital flat panels: a review", in *Proc. SPIE*, vol. 5535, p. 400, 2004.

[17] L. A. Feldkamp, L. C. Davis, J. W. Kress, "Practical cone-beam algorithm", *J. Opt. Soc. Am. A*, vol. 1, no. 6, pp. 612–619, 1984.

[18] A. Fieselmann, *Interventional Perfusion Imaging Using C-arm Computed Tomography: Algorithms and Clinical Evaluation*, Ph.D. thesis, Universitt Erlangen-Nrnberg, Germany, 2011.

[19] A. Fieselmann, A. Ganguly, Y. D.-Zheng, M. Zellerhoff, J. Boese, J. Hornegger, R. Fahrig, "A Dynamic Reconstruction Approach for Cerebral Blood Flow Quantification With an Interventional C-arm CT", in *Biomedical Imaging: From Nano to Macro, 2010 IEEE International Symposium on*, pp. 53–56, 2010.

[20] A. Fieselmann, A. Ganguly, Y. Deuerling-Zheng, J. Boese, R. Fahrig, J. Hornegger, "Using a C-arm CT for interventional perfusion imaging: a phantom study to measure linearity between iodine concentration and Hounsfield values", in *Medizinische Physik 2010, Freiburg i. Br., Germany*, 2010.

[21] A. Fieselmann, A. Ganguly, Y. Deuerling-Zheng, M. Zellerhoff, C. Rohkohl, J. Boese, J. Hornegger, R. Fahrig, "Interventional 4-D C-arm CT Perfusion Imaging Using Interleaved Scanning and Partial Reconstruction Interpolation", *IEEE Transactions on Medical Imaging*, vol. 31, no. 4, pp. 892–906, 2011.

[22] A. Fieselmann, M. Kowarschik, A. Ganguly, J. Hornegger, R. Fahrig, "Deconvolution-based CT and MR brain perfusion measurement: theoretical model revisited and practical implementation details", *Journal of Biomedical Imaging*, vol. 2011, p. 14, 2011.

[23] R. Fontaine, M. Kim, R. Kieny, "Die chirurgische Behandlung der peripheren Durchblutungsstörungen", *Helv Chir Acta*, vol. 21, no. 5-6, pp. 499–533, 1954.

[24] L. R. Frank, E. C. Wong, L. J. Haseler, R. B. Buxton, "Dynamic imaging of perfusion in human skeletal muscle during exercise with arterial spin labeling", *Magn. Reson. Med.*, vol. 42, pp. 258–267, 1999.

[25] A. Ganguly, A. Fieselmann, J. Boese, C. Rohkohl, J. Hornegger, R. Fahrig., "Evaluating the feasibility of C-arm CT for brain perfusion imaging: an in vitro study", in *Proc. SPIE*, vol. 7625, 2010.

[26] A. Ganguly, A. Fieselmann, M. Marks, J. Rosenberg, J. Boese, Y. Deuerling-Zheng, M. Straka, G. Zaharchuk, R. Bammer, R. Fahrig, "Cerebral CT Perfusion Using an Interventional C-Arm Imaging System: Cerebral Blood Flow Measurements", *American Journal of Neuroradiology*, vol. 32, no. 8, pp. 1525–1531, 2011.

[27] S. Geman, E. Bienenstock, R. Doursat, "Neural Networks and the Bias/Variance Dilemma", *Neural Comp.*, vol. 4, no. 1, pp. 1–58, 1992.

[28] M. Giordano, C. Neukirchen, M. Bertram, W. Mali, M. A. Viergever, E.-J. Vonken, "Perfusion estimation in the peripheral vasculature using C-arm X-ray systems", in *Proc. (IEEE) Nuclear Science Symposium and Medical Imaging Conference (NSS/MIC)*, pp. 3017–3020, 2009.

[29] M. Giordano, C. Neukirchen, M. Bertram, W. Mali, M. A. Viergever, E.-J. Vonken, "A framework for estimating region-related perfusion in the peripheral vasculature using interventional X-ray systems", in *Proc. CARS 2010*, p. S55, 2010.

[30] M. Giordano, E.-J. Vonken, M. Bertram, W. Mali, M. A. Viergever, C. Neukirchen, "Region Based Perfusion Estimation in Peripherals Using C-arm Systems: a Simulation Study", in *Proc. (IEEE) Nuclear Science Symposium and Medical Imaging Conference*, 2011.

[31] O. Glasser, *Wilhelm Conrad Rntgen und die Geschichte der Rntgenstrahlen; 3rd ed.*, Springer, Berlin, 1995.

[32] G. H. Golub & C. F. Van Loan, *Matrix Computations*, second ed., Johns Hopkins Press, Baltimore, MD, USA, 1989.

[33] P. Grangeat, A. Koenig, T. Rodet, S.Bonnet, "Theoretical framework for a dynamic cone-beam reconstruction algorithm based on a dynamic particle model", *Phys. Med. Biol.*, vol. 47, pp. 2611–2625, 2002.

[34] M. Grasruck, R. Gupta, B. Reichardt, Ch. Suess, B. Schmidt, K. Stierstorfer, S. Popescu, T. Brady, T. Flohr, "Combination of CT scanning and fluoroscopy imaging on a flat panel CT scanner", in *Proc. SPIE Med. Img. Conf.*, 2006.

[35] M. Grasruck, R. Gupta, B. Reichhardt, E. Klotz, B. T. Schmidt, T. Flohr, "Perfusion analysis using a wide coverage flat-panel volume CT: feasibility study", in *Proc. SPIE Med. Img. Conf.*, 2007.

[36] M. Grass, R. Koppe, E. Klotz, R. Proksa, MH. Kuhn, H. Aerts, "3D reconstruction of high contrast objects using C-arm image intensifier projection data", *Comput. Med. Imaging Graph.*, vol. 23, no. 6, pp. 311–321, 1999.

[37] A. Grüntzig & H. Hopff, "Percutaneous recanalization after chronic arterial occlusion with a new dilator-catheter (modification of the Dotter technique)(author's transl)].", *Deutsche medizinische Wochenschrift (1946)*, vol. 99, no. 49, p. 2502, 1974.

[38] M. Hanke & P.C. Hansen, "Regularization methods for Large-Scale problems", *Surv. Math. Ind.*, no. 3, pp. 253–315, 1993.

[39] P. C. Hansen, *Rank-Deficient and Discrete Ill-Posed Problems: Numerical Aspects of Linear Inversion*, SIAM, Philadelphia, PA, USA, 1998.

[40] P. C. Hansen, "Regularization Tools Version 4.0 for Matlab 7.3", *Numerical Algorithms*, vol. 46, pp. 189–194, 2007.

[41] R. M. Haralick & L. G. Shapiro, *Computer and Robot Vision, Volume I*, Addison-Wesley, 1992.

[42] M. D. Harpen & M. L. Lecklitner, "Derivation of gamma variate indicator dilution function from simple convective dispersion model of blood flow", *Med. Phys.*, vol. 11, no. 5, pp. 690–692, 1984.

[43] E. Haschek & O. Th. Lindenthal, "Ein Beitrag zur praktischen Verwertung der Photographie nach Rntgen", *Wiener Klinische Wochenschrift*, vol. 9, no. 4, pp. 63–64, 1896.

[44] I. Heinonen, J. Kemppainen, K. Kaskinoro, J.E. Peltonen, R. Borra, M.M. Lindroos, V. Oikonen, P. Nuutila, J. Knuuti, Y. Hellsten, others, "Comparison of exogenous adenosine and voluntary exercise on human skeletal muscle perfusion and perfusion heterogeneity", *Journal of Applied Physiology*, vol. 108, no. 2, pp. 378–386, 2010.

[45] T. J. Herbert, "Statistical stopping criteria for iterative maximum likelihood reconstruction of emission images", *Phys. Med. Biol.*, vol. 35, pp. 1221–1232, 1990.

[46] G. T. Herman, "Correction for beam hardening in computed tomography", *Phys. Med. Biol.*, vol. 24, no. 1, pp. 81–106, 1979.

[47] A.T. Hirsch, Z.J. Haskal, N.R. Hertzer, C.W. Bakal, M.A. Creager, J.L. Halperin, L.F. Hiratzka, W.R.C. Murphy, J.W. Olin, J.B. Puschett, others, "ACC/AHA 2005 Guidelines for the Management of Patients With Peripheral Arterial Disease (Lower Extremity, Renal, Mesenteric, and Abdominal Aortic): A Collaborative Report from the American Association for Vascular Surgery/Society for Vascular Surgery,? Society for Cardiovascular Angiography and Interventions, Society for Vascular Medicine and Biology, Society of Interventional Radiology, and the ACC/AHA Task Force on Practice Guidelines (Writing Committee to Develop Guidelines for the Management of Patients With Peripheral Arterial Disease)", *Journal of the American College of Cardiology*, vol. 47, no. 6, pp. e1–e192, 2006.

[48] A. T. Hirsch, M. H. Criqui, D. Treat-Jacobson, J. G. Regensteiner, M. A. Creager, J. W. Olin, S. H. Krook, D. B. Hunninghake, A. J. Comerota, M. E. Walsh, M. M. McDermott, W. R. Hiatt, "Peripheral Arterial Disease Detection, Awareness, and Treatment in Primary Care", *JAMA: J. Am. Med. Assoc.*, vol. 286, no. 11, pp. 1317–1324, 2001.

[49] J. Hsieh, Y. Wei, G. Wang, "Fractional scan algorithms for low-dose perfusion CT", *Med. Phys.*, vol. 31, no. 4, pp. 1254–1257, 2004.

[50] H. M. Hudson & R. S. Larkin, "Accelerated image reconstruction using ordered subsets of projection data", *IEEE Transactions on Medical Imaging*, vol. 13, no. 4, pp. 601–609, 1994.

[51] R. H. Huesman, B. W. Reutter, G. L. Zeng, G. T. Gullberg, "Kinetic parameter estimation from SPECT cone-beam projection measurements", *Phys. Med. Biol.*, vol. 43, no. 4, pp. 973–982, 1998.

[52] L. Ibanez, W. Schroeder, L. Ng, J. Cates, the InsightSoftware Consortium, R. Hamming, "The ITK Software Guide", *Kitware, Inc. (ISBN 1-930934-10-6)*, 2003.

[53] H. Ilkka, S. Bengt, K. Jukka, H.T. Sipilä, O. Vesa, N. Pirjo, K. Juhani, K. Kari, H. Ylva, "Skeletal muscle blood flow and oxygen uptake at rest and during exercise in humans: a pet study with nitric oxide and cyclooxygenase inhibition", *American Journal of Physiology-Heart and Circulatory Physiology*, vol. 300, no. 4, pp. H1510–H1517, 2011.

[54] D. C. Isbell, F. H. Epstein, X. Zhong, J. M. DiMaria, S. S. Berr, C. H. Meyer, W. J. Rogers, N. L. Harthun, K. D. Hagspiel, A. Weltman, C. M. Kramer, "Calf Muscle Perfusion at Peak Exercise in Peripheral Arterial Disease: Measurement by First-Pass Contrast-Enhanced Magnetic Resonance Imaging", *Journal of Magnetic Resonance Imaging*, vol. 25, pp. 1013–1020, 2007.

[55] D. A. Jaffray & J. H. Siewerdsen, "Cone-beam computed tomography with a flat-panel imager: Initial performance characterization", *Medical Physics*, vol. 27, p. 1311, 2000.

[56] A. K. Jain, M. N. Murty, P. J. Flynn, "Data clustering: a review", *ACM Comput. Surv.*, vol. 31, pp. 264–323, September 1999.

[57] M. Jiang & G. Wang, "Convergence studies on iterative algorithms for image reconstruction".

[58] Peter M. Joseph, "An Improved Algorithm for Reprojecting Rays through Pixel Images", *IEEE Transactions on Medical Imaging*, vol. 1, no. 3, pp. 192 –196, nov. 1982.

[59] P. M. Joseph & C. Ruth, "A method for simultaneous correction of spectrum hardening artifacts in CT images containing both bone and iodine", *Medical Physics*, vol. 24, no. 10, pp. 1629–1634, 1997.

[60] P. Dawson K.A. Miles & M.P. Hayball, *Functional Computed Tomography*, Oxford ISIS Medical Media, 1997.

[61] A. C. Kak & M. Slaney, *Principles of Computerized Tomographic Imaging*, first ed., IEEE Press, 1988.

[62] W. Kalender & Y. Kyriakou, "Flat-detector computed tomography (FD-CT)", *European Radiology*, vol. 17, no. 11, pp. 2767–2779, 2007.

[63] S. Kirkpatrick, "Optimization by simulated annealing: Quantitative studies", *Journal of Statistical Physics*, vol. 34, no. 5-6, pp. 975–986, 1984.

[64] E. Klotz & M. Koenig, "Perfusion measuments of the brain: using dynamic CT for the qunatitative assessemnt of cerebral ischemia in acute stroke", *Eur. Radiol.*, vol. 30, no. 3, pp. 170–184, 1999.

[65] T. Koehler, "A projection access scheme for iterative reconstruction based on the golden section", in *Proc. (IEEE) Nucl. Sci. Symp. and Med. Imag. Conf. (NSS-MIC)*, vol. 6, pp. 3961–3965, 2004.

[66] M. Koenig, E. Klotz, B. Luka, D.J. Venderink, J.F. Spittler, L. Heuser, "Perfusion CT of the brain: diagnostic approach for early detection of ischemic stroke.", *Radiology*, vol. 209, no. 1, pp. 85–93, 1998.

[67] V. M. Krepel, G. J. van Andel, W. F. van Erp, P. J. Breslau, "Percutaneous transluminal angioplasty of the femoropopliteal artery: initial and long-term results", *Radiology*, vol. 156, pp. 325–328, 1985.

[68] RA Kruger, CA Mistretta, J. Lancaster, TL Houk, M. Goodsitt, CG Shaw, SJ Riederer, J. Hicks, J. Sackett, AB Crummy, others, "A digital video image processor for real-time x-ray subtraction imaging", *Optical Engineering*, vol. 17, no. 6, pp. 176652–176652, 1978.

[69] L. Landweber, "An iteration formula for fredholm integral equation of the first kind", *Amer. J. Math.*, vol. 73, pp. 615–624, 1951.

[70] T. Y. Lee, "CT perfusion: principles, applications and problems", in *Proc. SPIE*, vol. 5535, pp. 77–88, 2004.

[71] P. F. Ludman, M. Volterrani, A. L. Clark, P.A. Poole-Wilson, S. Rees, A.J. Coats, "Skeletal muscle blood flow in heart failure measured by ultrafast computed tomography: validation by comparison with plethysmography.", *Cardiovasc Res.*, vol. 27, p. 11091115, 1993.

[72] Koenig M., "Brain perfusion CT in acute stroke: current status", *European journal of radiology*, vol. 45, pp. S11–S22, 2003.

[73] J. B. MacQueen, "Some Methods for classification and Analysis of Multivariate Observations", in *Proceedings of 5th Berkeley Symposium on Mathematical Statistics and Probability, University of California Press*, 1967.

[74] J. S. Maltz, "Direct recovery of regional tracer kinetics from temporally inconsistent dynamic ECT projections using dimension-reduced time-activity basis", *Phys. Med. Biol.*, vol. 45, no. 11, pp. 3413–3429, 2000.

[75] P. Markelj, D. Tomaevic, B. Likar, F. Pernu, "A review of 3D/2D registration methods for image-guided interventions", *Medical Image Analysis*, vol. 16, no. 3, pp. 642 – 661, 2012.

[76] E. C. McCullough, "Photon attenuation in computed tomography", *Medical Physics*, vol. 2, no. 6, pp. 307–320, 1975.

[77] P. Meier & K.L. Zierler, "On the theory of the indicator-dilution method for measurement of blood flow and volume", *Journal of applied physiology*, vol. 6, no. 12, pp. 731–744, 1954.

[78] N. Memarsadeghi, D. M. Mount, N. S. Netanyahu, J. Le Moigne, "A Fast Implementation of the ISODATA Clustering Algorithm", *International Journal of Computational Geometry and Applications*, vol. 17, pp. 71–103, 2007),.

[79] A.M. Mendrik, E.P. A Vonken, B. van Ginneken, E.J. Smit, A. Waaijer, G. Bertolini, M.A. Viergever, M. Prokop, "Automatic Segmentation of Intracranial Arteries and Veins in Four-dimensional Cerebral CT Perfusion Scans", *Med. Phys*, vol. 37, no. 6, pp. 2956–2966, 2010.

[80] K. A. Miles & M. R. Griffiths, "Perfusion CT: a worthwhile enhancement?", *British Journal of Radiology*, vol. 76, pp. 220–231, 2003.

[81] S. Molloi, G. Bednarz, J. Tang, Z. Yifang, M. Tarun, "Absolute volumetric coronary blood flow measurement with digital subtraction angiography", *The International Journal of Cardiac Imaging*, vol. 14, pp. 137–145, 1998.

[82] S. Molloi, Y.-J. Qian, Atila Ersahin, "Absolute volumetric blood flow measurements using dual-energy digital subtraction angiography", *Medical Physics*, vol. 20, no. 1, pp. 85–91, 1993.

[83] E. Moniz, "L'angiographie cerebrale", in *Paris. Masson*, 1931.

[84] P. Montes, *Dynamic cone-beam reconstruction for perfusion computed tomography*, Ph.D. thesis, Univ. of Heidelberg, Germany, Dec. 2006.

[85] P. Montes & G. Lauritsch, "A temporal interpolation approach for dynamic reconstruction in perfusion CT", *Med. Phys.*, vol. 34, no. 7, pp. 3077–3092, 2007.

[86] P. Montes & G. Lauritsch, "Low-Noise Dynamic Reconstruction for X-Ray Tomographic Perfusion Studies Using Low Sampling Rates", *International Journal of Biomedical Imaging*, vol. 2009, 2009.

[87] K. Mueller, R. Yagel, J. F. Cornhill, "The weighted distance scheme: A globally optimizing projection ordering method for the algebraic reconstructionmethod (ART)", *IEEE Transactions on Medical Imaging*, vol. 16, no. 2, pp. 223–230, 1997.

[88] K. Mueller, R. Yagel, J. J. Wheller, "Anti-aliased three-dimensional cone-beam reconstruction of low-contrast objects with algebraic methods", *IEEE Transactions on Medical Imaging*, vol. 18, no. 6, pp. 519–537, 1999.

[89] N.A. Mullani, K.L. Gould, others, "First-pass measurements of regional blood flow with external detectors.", *Journal of nuclear medicine: official publication, Society of Nuclear Medicine*, vol. 24, no. 7, p. 577, 1983.

[90] O. Nalcioglu & R. Y. Lou, "Post-reconstruction method for beam hardening in computerised tomography", *Physics in Medicine and Biology*, vol. 24, no. 2, p. 330, 1979.

[91] C. Neukirchen, "An extended temporal interpolation approach for dynamic object reconstruction", in *Proc. 11th Fully 3D*, pp. 379–82, 2011.

[92] L. Norgren, WR Hiatt, JA Dormandy, MR Nehler, KA Harris, FGR Fowkes, others, "Inter-society consensus for the management of peripheral arterial disease (TASC II)", *Journal of Vascular Surgery*, vol. 45, no. 1, p. 5, 2007.

[93] A.V. Oppenheim & R.W. Schafer, *Discrete-Time Signal Processing*, Prentice-Hall, Englewood Cliffs, NJ, USA, 1989.

[94] M.M. Payne, "Charles Theodore Dotter: the father of intervention", *Texas Heart Institute Journal*, vol. 28, no. 1, p. 28, 2001.

[95] G.P. Penney, P.G. Batchelor, D.L.G. Hill, D.J. Hawkes, J. Weese, "Validation of a two-to three-dimensional registration algorithm for aligning preoperative CT images and intraoperative fluoroscopy images", *Medical physics*, vol. 28, p. 1024, 2001.

[96] G.P. Penney, J. Weese, J.A. Little, P. Desmedt, D.L.G. Hill, others, "A comparison of similarity measures for use in 2-D-3-D medical image registration", *Medical Imaging, IEEE Transactions on*, vol. 17, no. 4, pp. 586–595, 1998.

[97] J.P.W. Pluim, J.B.A. Maintz, M.A. Viergever, "Mutual-information-based registration of medical images: a survey", *Medical Imaging, IEEE Transactions on*, vol. 22, no. 8, pp. 986–1004, 2003.

[98] F. Pomposelli, "Arterial imaging in patients with lower extremity ischemia and diabetes mellitus", *Journal of Vascular Surgery*, vol. 52, no. 3, pp. 81S–91S, 2010.

[99] W. H. Press, S. A. Teukolsky, W. T. Vetterling, B. P. Flannery, *Numerical Recipes in C: The Art of Scientific Computing*, 2nd ed., Cambridge University Press, New York, NY, USA, 1992.

[100] B. W. Reutter, G. T. Gullberg, R. H. Huesman, "Direct least-squares estimation of spatiotemporal distributions from dynamic SPECT projections using a spatial segmentation and temporal B-splines", *IEEE Transactions on Medical Imaging*, vol. 19, no. 5, pp. 434–450, 2000.

[101] W. C. Rntgen, "ber eine neue Art von Strahlen", in *Sitzungsberichte der Wrzburger Physik.-Medic.-Gesellschaft*, pp. 132–141, 1895.

[102] J. Rosch, F.S. Keller, J.A. Kaufman, "The birth, early years, and future of interventional radiology", *Journal of vascular and interventional radiology*, vol. 14, no. 7, pp. 841–854, 2003.

[103] H. Schmitt, M. Grass, V. Rasche, O. Schramm, S. Haehnel, K. Sartor, "An Xray-based method for the determination of the contrast agent propagation in 3-D vessel structures", *IEEE Trans. Med. Imag*, vol. 23, no. 3, pp. 251–262, 2002.

[104] H. Schmitt, M. Grass, R. Suurmond, T. Koehler, V. Rasche, S. Haehnel, S. Heiland, "Reconstruction of blood propagation in three-dimensional rotational X-ray angiography (3D-RA)", *Comput. Med. Imaging Graph.*, vol. 29, no. 7, pp. 507–520, 2005.

[105] S. I. Seldinger, "Catheter replacement of the needle in percutaneous arteriography; a new technique", *Acta radiologica*, vol. 39, no. 5, pp. 368–376, 1953.

[106] S. Serowy, O. Gurvit, M. Skalej, G. Rose, "A Jacobi-like Solution to the Model Based Tomographic X-Ray Perfsuion Imaging", in *Proc. (IEEE) Nucl. Sci. Symp. and Med. Imag. Conf. (NSS-MIC)*, pp. 3085–3088, 2007.

[107] S. D. Shpilfoygel, R. A. Close, D. J. Valentino, G. R. Duckwiler, "X-ray videodensitometric methods for blood flow and velocity measurement: A critical review of literature", *Medical Physics*, vol. 27, no. 9, 2000.

[108] K. Taguchi, "Temporal resolution and the evaluation of candidate algorithms for four-dimensional CT", *Med. Phys.*, vol. 30, no. 4, pp. 640–650, 2003.

[109] K. Taguchi & J.-F.H. Geschwind, "Toward Region-of-Interest (ROI)-based 4D perfusion using angiography system", in *Proc. IEEE Nuclear Science Symposium and Medical Imaging Conference*, pp. 4238–4240, 2008.

[110] K. Taguchi & J.-F.H. Geschwind, "Perfusion from angiogram and a priori (PAP) with temporal regularization", in *Proc. SPIE*, vol. 7258, 2009.

[111] H. Tang, J-L. Dillenseger, X.D. Bao, L. M. Luo, "A vectorial image soft segmentation method based on neighborhood weighted Gaussian mixture model", *Comput. Med. Imaging Graph.*, vol. 33, no. 9, pp. 644–650, 2009.

[112] G.I. Taylor & JH Palmer, "The vascular territories (angiosomes) of the body: Experimental study and clinical applications", *British journal of plastic surgery*, vol. 40, no. 2, pp. 113–141, 1987.

[113] R. B. Thompson, R. J. Aviles, A. Z. Faranesh, V. K. Raman, V. Wright, R. S. Balaban, E. R. McVeigh, R. J. Lederman, "Measurement of Skeletal Muscle Perfusion During Postischemic Reactive Hyperemia Using Contrast-Enhanced MRI With a Step-Input Function", *Magn. Reson. Med.*, vol. 54, no. 2, pp. 289–298, 2005.

[114] C. Tomasi & R. Manduchi, "Bilateral Filtering for Gray and Color Images", in *Proc. 6th Int. Conf. on Computer Vision*, pp. 839–46, 1998.

[115] D. Tomazevic, B. Likar, T. Slivnik, F. Pernus, "3-D/2-D registration of CT and MR to X-ray images", *IEEE Trans. Med. Imag*, vol. 22, no. 11, pp. 1407–1416, 2003.

[116] M.J. van der Bom, L.W. Bartels, M.J. Gounis, R. Homan, J. Timmer, M.A. Viergever, J.P.W. Pluim, "Robust initialization of 2D-3D image registration using the projectionslice theorem and phase correlation", *Med. Phys.*, vol. 37, no. 4, pp. 1884–1892, 2010.

[117] L. Van Tran & J. Sklansky, "Flexible mask subtraction for digital angiography", *Medical Imaging, IEEE Transactions on*, vol. 11, no. 3, pp. 407–415, 1992.

[118] M.A. Weber, M. Krix, S. Delorme, "Quantitative evaluation of muscle perfusion with CEUS and with MR", *European radiology*, vol. 17, no. 10, pp. 2663–2674, 2007.

[119] W.M. Wells, W.L. Grimson, R. Kikinis, F.A. Jolesz, "Adaptive segmentation of MRI data", *IEEE Trans. Med. Imag*, vol. 15, no. 4, pp. 429–442, 1996.

[120] C. J. White & Gray W. A., "Endovascular Therapies for Peripheral Arterial Disease An Evidence-Based Review", *Circulation*, vol. 116, pp. 2203–2215, 2007.

[121] J. Wiegert, M. Bertram, D. Schaefer, N. Conrads, N. Noordhoek, K. Jong, T. Aach, G. Rose, "Soft-tissue contrast resolution within the head of human cadaver by means of flat-detector-based cone-beam CT", in *Proc. SPIE*, vol. 5368, 2004.

[122] M. Wintermark, P. Maeder, J. P. Thiran, P. Schnyder, R. Meuli, "Quantitative assessment of regional cerebral blood flow by perfusion CT studies at low injection rates: a critical review of the underlying theoretical models", *Eur. Radiol.*, vol. 11, no. 7, pp. 1220–1230, 2001.

[123] E. Zeitler, W. Schoop, I. Schmidtkte, "Mechanische bchandlung von beckenarterienstenosen mit der perkutanen kathetertechnik", *Verh Dtsch Kreislaufforsch*, vol. 37, pp. 402–407, 1971.

[124] M. Zellerhoff, Y. Deuerling-Zheng, C. M. Strother, A. Ahmed, K. Pulfer, T. Redel, K. Royality, J. Grinde, D. Consigny, "Measurement of cerebral blood volume using angiographic c-arm systems", in *Proc. SPIE*, vol. 7262, 2009.

[125] M. Zellerhoff, B. Scholz, E.-P. Ruehrnschopf, T. Brunner, "Low contrast 3D reconstruction from C-arm data", in *Medical Imaging 2005: Physics of Medical Imaging. Edited by Flynn, Michael J. Proceedings of the SPIE*, vol. 5745, pp. 646–655, 2005.

[126] G. L. Zeng & G. T. Gullberg, "Unmatched projector/backprojector pairs in an iterative reconstruction algorithm", *IEEE Transactions on Medical Imaging*, vol. 19, no. 5, pp. 548–555, 2000.

Samenvatting

There are things known and there are things unknown, and in between are the doors of perception.

— Aldous Huxley (1894-1963)

In perifere revascularisatie procedures wordt een doelvat behandeld om de bloedtoevoer naar het weefsel te herstellen. Momenteel wordt het resultaat tijdens de behandeling gevalueerd door middel van angiografie waardoor slechts een kwalitatieve indruk van de bloedstroom wordt verkregen in de grote vaten. Periprocedurele beoordeling van de perfusie van het weefsel zou een waardevol instrument zijn om de effectiviteit en dus het technische succes van de revascularisatie procedure te beoordelen. Perfusie kwantificering vereist echter kennis van de contrastdynamiek in 3D wat op dit moment alleen beschikbaar is via tomografische modaliteiten zoals CT, PET en MR.

Dit proefschrift onderzoekt verschillende methodes om kwantitatieve perfusie te meten op de interventionele C-boog-systemen zelf. Het huidige gebruik van C-boog systemen beperkt zich tot 2D angiografische acquisities, echter, recente ontwikkelingen maken ook 3D beeldvorming op deze systemen mogelijk. Toch zijn de 3D-prestaties van C-bogen in termen van hoeksnelheid en het afbeeldingsbereik beperkt in vergelijking met CT, waardoor perfusie beeldvorming een uitdaging is.

In dit proefschrift presenteren we een set van perfusietechnieken op basis van 2D en 3D angiografiebeelden zoals die gemaakt kunnen worden op huidige klinische C-boog-systemen.

Om de beperkte temporele en ruimtelijke informatie in de beelden te compenseren, is voorkennis over de fysiologische contrast verdeling gentegreerd in de perfusiemeting. Dit proefschrift richt zich op de technische implementatie van deze methodieken en op evaluatie middels simulaties en op klinische data.

Hoofdstuk 1: In dit hoofdstuk wordt, na een korte inleiding over interventionele radiologie, de workflow besproken voor de behandeling van patinten met perifeer arterieel vaatlijden. Daarnaast wordt het angiosoom model besproken, die de interventionalist kan helpen bij de keuze van het te revasculeren vat. Recente studies tonen aan dat door het verbeteren van de perfusie specifiek in het aangedane angiosoom, een betere genezing optreedt. Om de effectiviteit van de perfusieverbetering tijdens de procedure te evalueren, worden de methoden om kwantitatieve perfusie te meten ontwikkeld. In de rest van het hoofdstuk worden de basisprincipes van CT perfusie beeldvorming besproken. Tenslotte worden de uitdagingen bij de meting van perfusie met interventionele C-boog-systemen bediscussieerd.

Hoofdstuk 2: In dit hoofdstuk introduceren we een iteratieve tomografische methode die gericht is op een 3D perfusie schatting. De methode is gebaseerd op projectiegegevens over meerdere rotaties van de C-boog. Het belangrijkste concept is om voorkennis te benutten van

de contrast dynamiek en dat die wordt gentegreerd in het dynamische reconstructiealgoritme voor een parametrisch model. Het model is gebaseerd op een set van gladde basisfuncties die de contrast dynamiek benadert. De ruis in de projectiebeelden wordt beperkt door regularisatie middels op tijd stoppen van de iteraties in combinatie met de gladde basisfuncties van het model.

Uit de resultaten van een fantoomstudie blijkt dat de tijdattenuatiecurves (TAC's) zoals gereconstrueerd uit multisweep opnames minder nauwkeurig zijn dan de TAC's gereconstrueerd op basis van continue volledige rotaties. Dit komt door de veranderde dichtheid van de meetpunten bij de omkeerpunten wat met name in situaties van snelle dynamiek zoals in slagaders, resulteert in streepartefacten. Uit analyse van ruispropagatie in de berekeningen bleek dat de effectieve ruisonderdrukking afhankelijk is van een complexe wisselwerking tussen het aantal iteraties en de beperkingen die worden opgelegd door het parametrisch model. Dit suggereert dat een optimale schatting van de TACs in verschillende gebieden wordt verkregen na een verschillend aantal iteraties.

Hoofdstuk 3: In dit hoofdstuk wordt een methode voorgesteld voor een 2D perfusie schatting in het onderbeen. Deze methode is gebaseerd op de tijdserie van een angio gemaakt onder een vaste hoek in combinatie met twee 3D beelden gereconstrueerd uit C-boog rotatiescans. De temporele informatie uit de angiografie wordt gecombineerd met de ruimtelijke informatie uit de 3D-beelden om de perfusie te schatten. Uitgangspunt is dat de perfusie homogeen is zowel binnen het doelvolume als langs de richting van de x-stralen. De gemiddelde perfusie langs de straal richtingen wordt verkregen door het normaliseren van de integralen langs de projecties in de angiografie met de corresponderende lengte van contrast afgeleid uit een segmentatie van de 3D beelden.

Resultaten op data gesimuleerd uit CTP acquisities tonen aan dat de nauwkeurigheid beperkt wordt door de contrast inhomogeniteit in het gesegmenteerde gebied. Desalniettemin, de kwantificatie van de gemiddelde perfusie zorgt voor een verbeterde visualisatie en faciliteert de opsporing van gebieden met verminderde perfusie ten opzichte van standaard angiografie.

Hoofdstuk 4: In dit hoofdstuk hebben we de methode uit hoofdstuk 3 uitgebreid. De vooronderstelling van homogeniteit in het doelgebied wordt afgezwakt en vervangen door veronderstelde homogeniteit binnen meerdere 3D gesegmenteerde deelgebieden. Door een groter aantal regio's, wordt de spatiele homogeniteit van contrast in iedere regio verhoogd, waardoor een betere modellering van de TAC mogelijk is. Om de deelgebieden in de gereconstrueerde 3D-beelden te bepalen, introduceren we een segmentatie methode gebaseerd op connectiviteit. De regio-gebaseerde TAC's worden geschat door het projecteren van de 2D bloedstroom informatie van de DSA op de 3D-segmenten. Instabiliteit in de oplossing van de projectie procedure wordt geregeld door zowel spatiele als temporele regularisatie.

Uit resultaten van simulaties op CTP scans, bleek dat de ruimtelijke resolutie van de perfusie beelden afhankelijk is van het gekozen aantal gesegmenteerde deelgebieden: hoe hoger het aantal gebieden hoe hoger de spatiele resolutie. Echter, de hogere resolutie gaat ten koste van meer ruis en onregelmatigheden in de schatting. Ruimtelijke regularisatie bleek een effectieve manier om deze onregelmatigheden te controleren. Voor de twee onderzochte voorbeelden, bleek de nauwkeurigheid van de TAC in vergelijking met de CTP waardes, in de grootteorde van $10-25\%$ relatieve fout, voldoende om de belangrijkste perfusie patronen te detecteren en om te differentiren tussen hypoperfusie en normale perfusie.

Hoofdstuk 5: In dit hoofdstuk evalueren we de klinische haalbaarheid van de perfusie meting met C-boog-systemen. In het bijzonder evalueren we de methode van hoofdstuk 4 op C-boog gegevens verkregen bij patinten tijdens de revascularisatie procedure. De praktische

kwesties in verband met de uitvoering van de methode in een klinische omgeving worden besproken. Het injectie-protocol om de 3D-rotatie-scans te maken is ontworpen, waarbij gepoogd is de balans tussen de hoeveelheid contrast aankleuring en beeldartefacten te optimaliseren. Een 3D/2D registratie algoritme werd toegepast om de 3D-beelden op de angiografische sequentie registreren.

De resultaten laten zien dat de berekende 3D TAC een betere scheiding kan laten zien van contrast dynamiek in weefsel en bloedvaten, dan DSA waarbij deze gebieden vaak overlappen. Verder is de methode in staat om gebieden met lagere perfusie zoals vetweefsel en ischemisch weefsel van normaal doorbloed spierweefsel te onderscheiden. Streepartefacten door een te hoge jodiumconcentratie in slagaders werden verminderd door het gebruik van eenvoudige nabewerking technieken. De vergelijking van de perfusie beelden met standaard verkregen preprocedurele MRAs werd bemoeilijkt doordat de beeldkwaliteit van MRA beelden in weefsel duidelijk lager was dan van de C-boog beelden. In de toekomst zullen andere modaliteiten (bv MR perfusie, CTP of PET) gebruikt moeten gaan worden om de perfusie kwantitatief te evalueren en de methodes te valideren. Concluderend, blijkt de klinische haalbaarheid aangetoond van perfusie metingen met C-boog beelden door middel van de combinatie van 2D angiografie en 3D-beelden.

Hoofdstuk 6: In dit hoofdstuk evalueren we het effect van de beam hardening op de meting van de contrast aankleuring bij DSA. Dit is met name relevant voor de perfusie schattingsmethoden voorgesteld in hoofdstuk 3 en hoofdstuk 4, die berusten op de contrast passage zoals gemeten in DSA beelden. Contrastmetingen uitgevoerd met de gebruikelijke energie integrerende rntgendetectoren gaan uit van een monochromatische bundel. Vanwege de aard van polychromatische rntgenstraling ontstaat een niet-lineariteit in de metingen, genaamd beam hardening. Simulaties uitgevoerd met software fantomen tonen aan dat de belangrijkste factor in de meting de keuze is van de monochromatische energie in het meetmodel. Afwijkingen van de ideale monochromatische energie lijden tot offsets in de metingen in de orde van 5% per keV. De offset vormt echter geen probleem voor de berekening van de perfusie, omdat deze wordt verkregen via normalisatie van de weefsel TACs op de arterile TAC's. Kortom, de resultaten van dit hoofdstuk tonen aan dat het effect van beam hardening op de meting van de contrastpassage bij DSA verwaarloosbaar is.

In dit proefschrift hebben we een aantal nieuwe methodes gepresenteerd om kwantitatieve perfusie metingen te doen op basis van angiografische beelden. Deze methoden zijn ontwikkeld om de interventionalist te ondersteunen door tijdens de procedure de resultaten van endovasculaire revascularizatie te evalueren. Het belangrijkste voordeel van de voorgestelde methodes ligt in de eenvoudige acquisitieprotocollen die kunnen worden uitgevoerd op de meeste commercieel beschikbare C-boog systemen. De spatiele resolutie die wordt bereikt met de voorgestelde methoden is iets minder dan die van volledig 3D meetmethodes door de aanname van homogeniteit in perfusiegebieden. Echter, het blijkt dat in geval van interventies van beenvaten, waarbij de perfusie varieert in relatief grote driedimensionale spier-blokken, de resolutie voldoende is om laesies te onderscheiden van gezonde weefsels en om de meest relevante informatie over het vaatstelsel visualiseren.

De voorgestelde methoden werden eerst gevalueerd op fantoom data om de theoretisch haalbare nauwkeurigheid (hoofdstukken 3 en 4) te onderzoeken. Vervolgens werd een kwalitatieve evaluatie uitgevoerd op C-boog data verkregen van patinten tijdens de revascularisatieprocedure (hoofdstuk 5). In deze evaluatie hebben we de haalbaarheid aangetoond van de methode vanuit een praktisch oogpunt. Echter, een aantal beperkingen van de werkwijze moten nog worden aangepakt.

In verder onderzoek zal eerst een grondige evaluatie moeten worden uitgevoerd om de kwantitatieve nauwkeurigheid van de methode te bepalen. In onze evaluatie van C-boog data gebruikten we Standaard MRA data als referentie, maar de beperkte beeldkwaliteit van deze datasets in weefsel bleken onvoldoende voor een uitgebreide evaluatie. In toekomstige studies, zullen andere modaliteiten, zoals CT perfusie, MR perfusie of PET gebruikt moeten worden.

Een andere moeiljkheid die in onze studie naar voren komt, is de beperkte contrast aankleuring in de 3D-beelden. Dit probleem kan invloed hebben op de segmentatie stap en zou kunnnen resulteren in onjuiste modellering van de perfusie regio's. Er zal een oplossing gevonden moeten worden om de contrast aankleuring in de weefsels te verhogen, terwijl de artefacten als gevolg van overmatige contrastaankleuring in de slagaders vermeden worden. Een mogelijkheid zou het het gebruik van farmacologische middelen zijn, zoals adenosine, om een hogere perfusie in spier weefsel te induceren [44].

Een andere beperking van onze methode is het grote contrastvolume en de hoge stralingsdosis voor de patint. Hoewel de hoeveelheid ingespoten contrast en de stralingsdosis lager zijn dan bij andere voorgestelde methodes [18], zullen zij voor algemeen klinisch gebruik verder verlaagd moeten worden. Momenteel worden, om perfusie te meten zowel vr als na de behandeling, twee angiografische scans en twee 3D rotatie opnames gemaakt. De 3D is vereist zowel zonder contrast injectie als met het contrast in de pseudo steady state. Vooral de pseudo steady state 3D rotatie opname vereist de injectie van een ruime hoeveelheid contrast. Ook zullen manieren gevonden moeten worden om het aantal vereiste rotatie scans te verminderen. Bijvoorbeeld zouden anatomisch modellen met informatie over de angiosomen gebruikt kunnen worden.

Samenvattend hebben wij in dit proefschrift een set van methodes gepresenteerd voor perfusie kwantificatie in perifere weefsels met behulp van interventionele C-boog-systemen. We hebben aangetoond dat door toevoeging van anatomische informatie uit 3D-beelden, kwantificatie van weefselperfusie op basis van angiografische beelden kan worden bereikt. Gebaseerd op de methodes uit dit proefschrift kan in de toekomst periprocedurele en kwantitatieve informatie ter beschikking worden gesteld voor de beoordeling van een perifere revascularisatie procedure. Daarnaast zou dit kunnen worden gebruikt als een instrument om revascularisatie procedures te optimaliseren.

Acknowledgements

Every human heart beat is a universe of possibilities.

— Gregory David Roberts

Accomplishing this PhD has been the most challenging but also rewarding experience I went through in my life. During my PhD many have been the difficulties, however, behind every obstacle, there was always a reward that motivated me to keep hard and continue focusing on my final goal. Now that I finally achieved this goal, I would like to thank all the people that helped me, inspired me and motivated me, and without whom I would have not made it.

Before mentioning all the people that contributed to this thesis, I would like to point out the international character of my work. During my PhD in fact, I had the opportunity to experience the working culture of two countries: Germany, the Netherlands and Italy. In Germany (Aachen), where my PhD project was initiated, I spent 4 years working at Philips Research Aachen. Here, besides learning all the secrets of X-ray imaging, I also experienced the german culture. In the Netherlands (Utrecht), where I spent the last year of my PhD, I experienced the life as a PhD student of the Image Science Institute (ISI). As a consequence of this international experience, many are the people that I encountered and that I would like to thank.

The first person, without whom probably I would not have made it, is Prof. Max Viergever. He supported me and helped me from the first day to the last moments of this Ph.D. I am deeply indebted towards Max, and I hope that the scientific contributions contained in this thesis may pay back my debt. Hardly in my life I have encountered such competent and professional person such Max. Besides being one of the world's recognized experts in image processing, his organizational and managing skills are remarkable. Even though his heavy responsibilities as director of the ISI, Max always found time to revise my results and to give suggestions on how to improve the methods. Max, it has been an honor to join the ISI group under your supervision, I wish you and the ISI a lot of success for the future.

One thing that I learned during my PhD is that if you want to solve medical imaging problems you need good ideas. Dr. Christoph Neukirchen, who was my supervisor at Philips Research Aachen, is one always keen to generate new, good and simple ideas, to solve complicated problems. Most of the things I learned on X-ray imaging, I owe them to Christoph. Thanks to his patience and dedication, we managed to solve complicated medical imaging problems by providing easy and robust solutions. Christoph is one of most brilliant and skilled scientist I ever met and I wish him a lot of success for the future challenges. Christoph, working with you has been an honor and I will hardly forget the afternoons spent together solving medical imaging problems.

Another person who was fundamental in achieving this PhD is Dr. Evert-Jan Vonken of the Department of Radiology of UMC Utrecht. I hardly met such competent and friendly doctor as Evert-Jan. He has both technical and medical knowledge, and this combination was crucial to understand the implications of our techniques by a clinical point of view. Besides his skills, Evert-Jan was always available to help me with anything, from technical things to practical aspects (like the translation into dutch of the summary of this thesis). I am very grateful to Evert-Jan and I am glad that he was my academic supervisor. Evert-Jan, thank you again for what you have done in supporting me during these years.

Another important person to whom I am grateful is Dr. Matthias Bertram, department head of the X-ray Imaging Systems group at Philips Research Eindhoven. Matthias not only gave me the opportunity to start this PhD under a Marie Curie grant, but allowed me also to continue the PhD under the support of Philips Research. Matthias, I remember as it was yesterday when I entered your office for the first time and you explained me the topic of the PhD. Your encouragements at the beginning were crucial to trigger my curiosity in the field of medical imaging. Also, the evenings you organized to welcome me and the other students in the group, made us feel less far from home. Thank you again for having given me the opportunity to do a PhD in medical imaging. I wish you too a lot of success for the future.

This thesis could not have been possible without the support and supervision of Prof. Mali to whom I address my sincere gratitude. His supervision at the beginning of the project was crucial to define the aim of this thesis.

Next to my supervisors, I would like to thank all the scientists who have made a direct or indirect contribution to this thesis. I would like to thank all the XIS group of Philips Research Aachen (now transferred to Eindhoven). In particular Dr. Engel-Klaus Juergen, who reviewed the last chapter on beam hardening. Klaus Juergen, thank you again for having introduced me to the world of spectral x-rays and related aspects. Dr. Alfonso Isola who helped me with the image registration required to register the CTP sequences used in Chapter 3 and 4. Alfonso, thank you for the nice discussions on italian politics and italian football and for your help and friendship during the last period of my PhD. Dr. Jens Wiegert with whom I had numerous discussions on CT imaging, medical imaging in general and spanish culture. Dr. Bernd Menser for the support on the calculation of the spatial modulation transfer function in Chapter 2. Dr. Steffen Wiesner for the support in Chapter 2.

I would like to thank the friends and colleagues working in the 'hardware group' of the XIS, with whom I shared many lunches and entertaining evenings: Tobias, Annand, Chaitanya and Mezbah. Thank you guys for the good time spent together. I wish you good luck for the future challenges. My thanks also go to the other Marie Curie students with whom I shared the experience of being a PhD student in Germany: Qi Sun and Colas Schretter. Special thanks go to the colleagues of Philips Research Hamburg Dirk Shaffer, Michael Grass, Eberhard Hansis, Irina Waechter-Stehle and Ewald Roessl, for the interesting discussions during the meetings and the scientific conferences.

During my period in Aachen, I had the chance to meet many extraordinary people, who became my friends and with whom I shared many amusing evenings and events: Sylvain, Ramon, Christopher, Meaza. Even if we are not living in the same city anymore, I will always keep with me the memory of your true friendship and support during these years. My gratitude goes also to Jennifer, for having supported me in the difficult moments and for the advices in the first articles.

During my period in Utrecht I had the chance to get to know the PhD students and researchers of the ISI. These are extraordinary and dedicated people, with whom I shared an

important moment of my PhD. Among these, I would like to mention the people of the AMOR meetings for the interesting discussions on image registration: Josien, Floris, Paul, Yolanda and Marijn. I would also like to thank all the PhD students of the E building, with whom I shared many coffee breaks, in particular Mie kee Lam for having introduced me to the PhD life in Utrecht. Special thanks also go to the friends of the 'Cambridgelaan' residence and to all those I met in Utrecht and with whom I enjoyed some good moments during the fabulous 'dutch' summer. A special acknowledgement to Alessia for her support during the transition phase from Utrecht to Maastricht.

I would also like to thank all my friends that supported me from Italy and Belgium, and with whom I spent some nice moments during the holidays: Fabrizio, Daniele, Pietro, Wouter, Liesbeth, Gabriele, Silvia and Massimo. Thank you for the good moments we spent together, I hope we will have many more in future.

A very important person who supported me during many years of my PhD, and without whom I would have not made it is Sara. Thank you Sara for all your support and for giving me courage for so many years. I wish you good luck for your PhD and a lot of success for the future.

I would also like to thank my new colleagues from Pie Medical Imaging and in particular René Guillaume and Boudewijn Verstraelen who gave me the opportunity to continue working in medical imaging in the Netherlands.

Last but not least, I would like to thank my family for the continuous support since I was born. Dear parents, Rosa and Antonio, and dear brothers, Giancarlo and Gennaro, thank you for always believing in me, and for comforting me in the difficult moments of my life. I feel very lucky having you as my family. I hope that this thesis will make you proud of me and will give you at least a fragment of the happiness you deserve.

Marco Giordano
Maastricht, January 2013

Publications

Publications in International Journals:

- C. Neukirchen, **M. Giordano**, S. Wiesner, "An iterative method for tomographic x-ray perfusion estimation in a decomposition model-based approach", *Medical Physics*, vol. 37, no. 12, pp. 6125-6141, December 2010.
- **M. Giordano**, E. P. A. Vonken, M. Bertram, W. P. T. M. Mali, M. A. Viergever, C. Neukirchen, "Ray-based approach to skeletal muscle perfusion measurement on interventional x-ray systems", *Medical Physics*, vol. 39, no. 3, pp. 1190-1206, March 2012.
- **M. Giordano**, E. P. A. Vonken, M. Bertram, W. P. T. M. Mali, M. A. Viergever, C. Neukirchen, "Spatially regularized region-based perfusion estimation in peripherals using angiographic C-arm systems", *Physics in Medicine and Biology*, vol. 57, no. 22, pp. 7239–7259, November 2012.
- **M. Giordano**, E. P. A. Vonken, M. Bertram, W. P. T. M. Mali, M. A. Viergever, C. Neukirchen, "Feasibility evaluation of region-based perfusion estimation in peripherals using C-arm systems", *submitted*.
- **M. Giordano**, K. J. Engel, E. P. A. Vonken, M. A. Viergever, C. Neukirchen, "Effects of beam hardening on the measurement of contrast enhancement by digital subtraction angiography", *submitted*.

Publications in International Conference Proceedings:

- **M. Giordano**, C. Neukirchen, M. Bertram, W. P. T. M. Mali, M. A. Viergever, E. P. A. Vonken, "Perfusion estimation in the peripheral vasculature using C-arm x-ray systems", in *2009 IEEE Nuclear Science Symposium Conference Record (NSS/MIC 2009, Orlando, FL, USA)*, pp. 3017–3020, 2009.
- **M. Giordano**, C. Neukirchen, M. Bertram, W. P. T. M. Mali, M. A. Viergever, E. P. A. Vonken, "A framework for estimating region-related perfusion in the peripheral vasculature using interventional x-ray systems", in *International Journal of Computer Assisted Radiology and Surgery* (CARS 2010, Genève, Switzerland), vol. 5, S55.
- **M. Giordano**, E. P. A. Vonken, M. Bertram, W. P. T. M. Mali, M. A. Viergever, C. Neukirchen, "Perfusion estimation in the peripheral vasculature using C-arm x-ray systems", in *2011 IEEE Nuclear Science Symposium Conference Record (NSS/MIC 2011, Valencia, Spain)*, pp. 2918–2921, 2011.

Inventions Disclosure:

- K. J. Engel, **M. Giordano** "Digital Subtraction Angiography with a spectral X-ray method", Philips Intellectual Property & Standards GmbH, ID 293648, 2010.

Curriculum Vitae

Marco Giordano is born in Rome, Italy, on August 8, 1981. In 2007 he received a M.Sc degree (cum laude) in Electronic Engineering from 'La Sapienza' Università degli studi Roma, with a thesis on optimization methods for fMRI data analysis which he developed at the Department of Cognitive Neuroscience of Maastricht University.

After the rewarding experience in Maastricht, he decided to continue working in research and obtained a Ph.D position at Philips Research Aachen, under the Marie Curie Host Fellowship for Early Stage Researchers Training. The Ph.D position was in collaboration with the Image Science Institute - UMC Utrecht, where he was enrolled as an external Ph.D student. During his Ph.D period at Philips, Marco worked on software methods to estimate tissue perfusion from X-ray angiographic images. His work consisted in the implementation of algorithms for segmentation, registration, image processing, optimization and solution of inverse problems. In February 2012, Marco joined the Image Sciences Institute to complete his Ph.D by testing his methods on clinical data acquired with an angiographic C-arm system. The results of his work are described in this thesis.

After completing his Ph.D. thesis, in November 2012 Marco joined Pie Medical Imaging BV as a product manager for cardiovascular software applications.

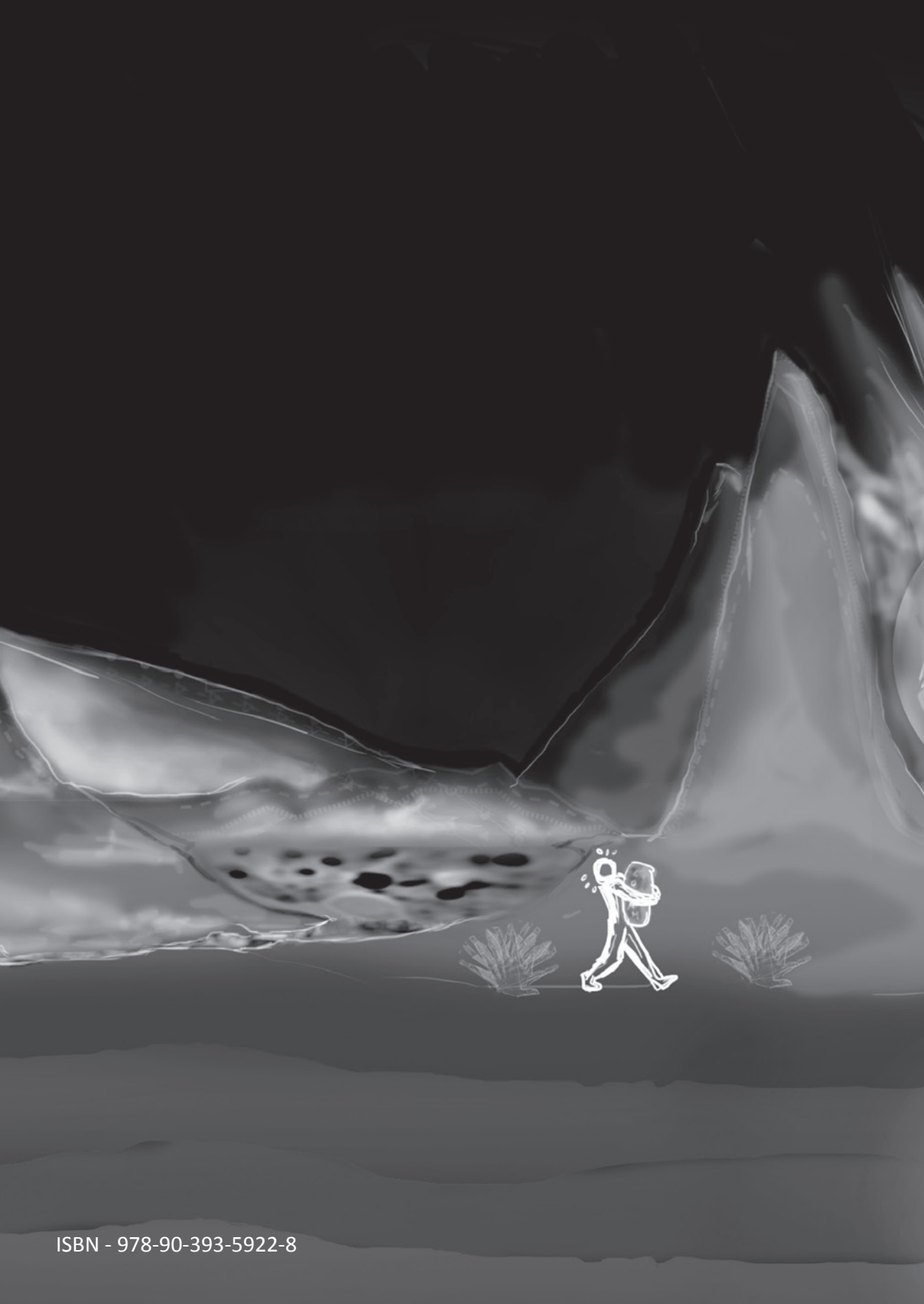

ISBN - 978-90-393-5922-8